Kinetically controlled growth of InN thin films by MBE and their structural, optical and electronic properties

A Thesis

Submitted For the Degree of

DOCTOR OF PHILOSOPHY

in the Faculty of Science

by

Malleswararao Tangi

CHEMISTRY AND PHYSICS OF MATERIALS UNIT
JAWAHARLAL NEHRU CENTRE FOR ADVANCED SCIENTIFIC RESEARCH
Bangalore – 560064, India

SEPTEMBER 2014

Dedicated To My Parents

DECLARATION

I hereby declare that the matter embodied in the thesis entitled "**Kinetically controlled growth of InN thin films by MBE and their structural, optical and electronic properties**" is the result of investigations carried out by me at the Chemistry and Physics of Materials Unit, Jawaharlal Nehru Centre for Advanced Scientific Research, Bangalore, India under the supervision of Prof. S. M. Shivaprasad and that it has not been submitted elsewhere for the award of any degree or diploma.

In keeping with the general practice in reporting scientific observations, due acknowledgement has been made whenever the work described is based on the findings of other investigators. Any omission that might have occurred by oversight or error of judgement is regretted.

Malleswararao Tangi

CERTIFICATE

I hereby certify that the matter embodied in this thesis entitled "**Kinetically controlled growth of InN thin films by MBE and their structural, optical and electronic properties**" has been carried out by Mr. Malleswararao Tangi at the Chemistry and Physics of Materials Unit, Jawaharlal Nehru Centre for Advanced Scientific Research, Bangalore, India under my supervision and that it has not been submitted elsewhere for the award of any degree or diploma.

Prof. S. M. Shivaprasad
(Research Supervisor)

Acknowledgements

I was fortunate to come across and take help from many knowledgeable and skilled persons during the course of my Ph. D. Like any other thesis present thesis also finds contribution from great number of people. So I feel this section is a great opportunity to acknowledge few of them who supported me in my research journey.

First of all, I would like to thank my thesis supervisor Prof. S. M. Shivaprasad for his patient guidance, enormous support and encouragement throughout all stages of this work. Frankly speaking, I knew very little about III-nitride research when I was admitted at JNCASR and joined in Prof. S. M. Shivaprasad's research group. I am very thankful to Prof S. M. Shivaprasad, under whose wonderful guidance I am motivated towards scientific research and I thank him for introducing me to the III-nitride research community and MBE. His experimental skills helped me a lot in completing my thesis work. The amount of freedom I got during this stay is very helpful and greatly appreciated. It is a great pleasure to be a part of the alumni of JNCASR, which is established by world famous scientist Bharat Ratna Prof. C. N. R. Rao. I would like to thank Professor C. N. R. Rao for his unstinting encouragement and support.

I would like to thank the present and past Chairman of CPMU Prof. S. Balasubramanian and Prof. G. U. Kulkarni for all the support. I also express my sincere gratitude to Prof. Ranganathan, Prof. K. S. Narayan, Prof. Shobhana Narasimhan, Prof. Umesh V. Waghmare, Dr. Ranjan Dutta and Prof. S. M. Shivaprasad for 1 year course work, where I gained basic concepts of theoretical and experimental materials science, which have been very useful for my Ph. D work.

I am indebted to Dr. Jithesh Kuyyalil, Dr. Praveen Kumar for all the help and discussions for the initial experiments. I thank Arpan De for helping me in some MBE experiments. I greatly appreciate the patience and diligent effort of Srinath sir for

technical support in maintaining MBE system. I would like to thank Somashekhar, Dr. Basawaraj, Mahesh, Vasu, Selvi, Srinivas, Kishore, Prajwal and Jagdeesh for all the technical help. I would also like to thank all the staff members of Admin, Accounts, HRD group, and Purchase section and Mr. Jaychandra (Sr. AO) for their co-operation and support.

I would like to thank all my lab mates Dr. Jithesh Kuyyalil, Dr. Praveen Kumar, Dr. Manoj Kesaria, Satish Shetty, Varun Thakur, Arpan De, Shivakumar, Sanjay Nayak, Abhijit Chatterjee, Sreedhar, Darshana, Sharvani, Ankit, Prasanth, Sandeep, and Dr. K. K. Nagaraja for giving such a happy atmosphere to work and for all the help. It was great to have very resourceful and helpful lab mates. I enjoyed their company. I express my sincere heartfelt thanks to Anu madam for caring us and for the homely food.

I would like to thank all the HCU faculty especially Prof. A. K. Kapoor, Prof. D. N. Rao, Prof. A. Chatterjee and Dr. S. Dhara for wonderful teaching which inspired me towards higher studies. I would also like to thank all the lecturers and teachers from DRN degree college, Gnanajyothi Jr college, Narasannapeta and ZPH school, kotabommali. My sincere thanks goes to lecturers Rajendra Naidu, Ramanayya, school teachers- Satyalingam, lakshmi and Ratnalaraju.

I am very grateful to my parents, without their will power and determination my entire education would have been not possible. I greatly appreciate their patience, perseverance, hard work, and the ability to keep moving forward, even in hard times. My special and sincere thanks goes to Sankar bava, his kind help and suggestions are greatly appreciated. I have lot of people to thank, who made my dream come true especially my grandmother Applasuramma, Uncles- Sailu, Apparao, Suryanarayana, Venkatrao, Aunts- Laxminarayna, Rama, Lakshmi, Guna and Cousins- Sankar, Neelakantam, Rama, Raghu, Janakiram, Kishore, Rajitha, Sekhar, Vinod, Avinash and Simhadri for being very friendly with me all the time, and lot of Friends- Bhaskar, Suri, Jithesh, Praveen, Naidu, Sowjanya, Srikanth, Priyanka, Krishna, Govinda, U Kiran, Laximinarayana, Ramesh, S Chalam, Durga, Hari, Dasari, Paandu, Narendra, Sandeep, Badram and Ramchandrarao.

Also I would like to thank Department of Science and Technology (DST), India for providing me JRF/SRF fellowship to carry out my Ph. D. work.

Synopsis

For optoelectronic applications that need to span the entire solar spectrum and for high brightness white LEDs, alloys of III-nitrides have shown great promise. Due to problems in synthesis of InN, in the past, the potential has been reinforced only recently after the substantiation of its actual narrow band gap to form III-nitride alloys. In addition to opto-electronic applications, indium nitride is expected to be utilized in the fabrication of high performance electronic devices, as it exhibits smaller effective mass and consequently very high peak, saturation velocities and electron mobility. In spite of these remarkable properties, InN is the least studied and least understood material among III-nitrides due to major synthesis problems arising due to its low dissociation temperature and high vapor pressure. This has in the past led to significant ambiguity in the literature concerning the basic material parameters measured for InN. The formation of high crystalline quality films is still challenging, and thus hinder the efficiency of $In_{0.4}Ga_{0.6}N$ light emitting diodes due to issues like the green droop. In order to understand the unusual synthesis dependent properties of InN thin films, we have performed several systematic experiments to optimize various growth parameters such as flux and growth temperature on Sapphire and Si substrates. The formed InN films are probed by using several complementary characterization tools to understand the various reasons for the variation of band gap (high to low) and surface charge induced downward band bending of InN. While optimization of growth on sapphire is of commercial importance, growth on Si surfaces is challenging. Si surfaces exhibit scientifically fascinating metal induced surface reconstructions with rich structural and electronic properties. These super structural templates where the unit cell dimensions integrally match with that of III-nitrides, enable us to grow good quality InN films at considerably low temperatures, when grown on these intermediate layers. In order to reduce dislocation density in InN epilayers and enhance electron mobility, these films and nano rods are grown on GaN Nano Wall Network

(NWN) by improvising the Nano-ELOG epitaxy. The work presented in this thesis is organized in the following chapters:

Chapter 1 gives an introduction to the motivation and the challenges encountered in group III-nitride research, and their various applications. The origin and effects of point defects and dislocations which essentially result from the growth conditions and lack of native substrates, respectively, are discussed. Primary mechanism involved in the growth of thin films, nucleation of islands and growth modes are explained. A complete overview of the thesis structure also is presented in this chapter.

Chapter 2 gives the historical background for InN growth, and describes the properties of InN. It provides a comprehensive literature survey till date, mainly focusing on the ambiguity in the band gap and surface charge accumulation of this material. It also presents a brief overview of the electron mobility of InN thin films grown by various methods by various groups.

Chapter 3 provides the details of the experimental techniques employed, such as the Plasma Assisted Molecular Beam Epitaxial (SVTA-USA) growth system, *in-situ* characterization techniques (RHEED, RGA, Ellipsometer, Flux gauge, Atomic Absorption Spectroscopy and Cathodoluminescence) associated with it and Electron Beam Physical Vapor Deposition (EBPVD) system which is used to evaporate metals for electrical contacts. Additionally the details of the various *ex-situ* characterization tools (FESEM, AFM, XRD, TEM, XPS, PL and Optical absorption) used to acquire all the results reported in this research work are also given.

Chapter 4 presents the systematic optimization of various MBE growth parameters for InN growth, such as In and Nitrogen flux and growth temperature on bare c-sapphire substrate. The analysis of optical, structural and electrical properties of the formed films are presented. The effect of several suggested reasons in the literature such as oxides, oxinitrides, stoichiometry and quantum size effects on the observed high band gap of InN are evaluated for our films. This chapter identifies nitrogen related native point defects as a reason for unintentional degenerate doping of InN thin films using both XRD and XPS analysis.

Chapter 5 details the study of InN layers formed on GaN epilayers at different growth

temperatures, to understand the reasons behind low and high band gap observed. The band gap variation experimentally observed is studied by considering non-parabolic conduction band approximation in band filling theoretical calculations. It also includes the study of surface charge induced downward band bending upto 1eV for InN films using XPS valance band analysis. Poly-crystalline samples having high band gap do not exhibit any band bending. XPS core-level analysis suggests that the In adatoms act as donor like surface states which are the reasons behind this accumulation of charge on the film surface.

Chapter 6 evaluates the growth of InN films on silicon surfaces. Metal induced Si reconstructions are used as growth templates by a method we introduce and call as Super Lattice Matching Epitaxy. This chapter discusses the sequence of steps to obtain super structural phases on Si(111) by sub-monolayer In coverages, by using *in-situ* RHEED. The growth of high quality single crystalline InN layers on In metal induced surface reconstructions on Si(111) at relatively low growth temperatures. Growth of InN on Si(111)-1×1 and 7×7 reconstructions is carried out at different substrate temperatures. Improved crystalline quality is achieved by growing InN on these optimized low temperature intermediate buffer layers.

Chapter 7 presents the attempts which are made to reduce dislocation density in the overgrown InN epilayers. The chapter discusses the growth of high mobility 1μm thick InN films that are formed on GaN epilayer and on GaN Nano Wall Network (NWN) templates. Low dislocation density is achieved (7.5×10^{9} cm^{-2})for the InN epilayers which are grown on GaN NWN by employing Nano ELOG growth process. It also provides the growth of self assisted, dislocation free and high mobility InN nano structures on GaN NWN under certain growth conditions. This chapter explains the method used for performing Hall measurements on single isolated InN nano rod. Obtained mobility values for the InN epilayers (2121cm^{2}/V-sec for 1μm thick film) and nano rods (4453 cm^{2}/V-sec) at reduced dislocation density. The obtained mobility values for the InN films are the highest among reported literature values, to the best of our knowledge. Role of defects in limiting experimental mobility values is studied by considering various scattering mechanisms at charged point defects, dislocations and phonons.

Chapter 8 summarizes briefly the contents of the present thesis, lists the highlights

and draws conclusions from the observed results. Overall, the thesis is a systematic approach to understand InN formation, inherent defects and means to reduce to obtain high quality and reliable material. We have methodically narrowed growth paths towards high structural, optical and electrical quality thin films with very high electron mobility values. This chapter also gives a brief outlook for the future work.

Contents

Acknowledgements **i**

Synopsis **iii**

Contents **x**

List of Figures **xiii**

List of Tables **xiv**

Acronyms **xv**

1 Introduction and Motivation **1**

1.1 Introduction 1

1.2 Group III - nitrides: A brief history 3

1.3 Motivation 4

1.3.1 InN: Introduction and applications 4

1.4 Applications of InN 6

1.4.1 Optical applications 6

1.4.2 LED applications 7

1.4.3 Laser applications 7

1.4.4 THz applications 8

1.5 Substrates 9

1.6 Mosaic model 11

1.7 Structural defects 12

1.7.1 Point defects 13

1.7.2 Dislocations 14
1.7.3 Planar and Volume defects 15
1.8 Thin film nucleation and growth 15
1.8.1 Growth modes 17
1.9 Organization of the thesis 19

2 Literature overview 21
2.1 Growth and properties of InN 21
2.1.1 InN: Historical background 21
2.1.2 Structural properties 24
2.2 Growth parameter dependence 25
2.3 Band gap issue 28
2.4 Surface electron accumulation 30
2.5 Overview of InN mobility 32

3 Experimental techniques 35
3.1 Growth: Molecular Beam Epitaxy 35
3.1.1 Effusion cells 37
3.1.2 Nitrogen Plasma Source 38
3.1.3 Residual Gas Analyzer 39
3.2 Electron Beam Physical Vapor Deposition 40
3.3 Reflection High Energy Electron Diffraction 41
3.4 X-ray photoelectron spectroscopy 43
3.4.1 XPS data analysis 46
3.5 High Resolution X- ray diffraction 48
3.5.1 HRXRD setup and scans 49
3.5.2 Diffraction geometries for 2θ-ω scan 52
3.6 Optical bandgap: Transmission measurements 52
3.7 Photoluminescence and Catholuminescence spectroscopy 53
3.8 Hall measurements 54
3.8.1 Van der Pauw geometry 56
3.9 Atomic Force Microscopy (AFM) 58
3.10 Field Emission Scanning Electron Microscope (FESEM) 59

4 Optimization of parameters for InN growth on bare c-sapphire 61

4.1 Dependence of crystal orientation on substrate temperature 62

4.1.1 Introduction 62

4.1.2 Experimental details 63

4.1.3 Results 63

4.1.4 Surface and bulk crystallinity of the films 63

4.1.5 Cathodoluminescence: Band gap 66

4.1.6 Discounting the role of quantum size effects on band gap 68

4.1.7 XPS: Composition and stoichiometry of InN 69

4.2 Role of native defects in the nitrogen flux dependence of carrier concentration 72

4.2.1 Results and Discussions 73

4.2.2 Strain measurements and possible native point defects 75

4.2.3 Optical absorption measurements: high band gap 78

4.2.4 XPS: Nitrogen related native point defects 80

4.2.5 Inferences 83

5 Optical band gap and surface charge accumulation 85

5.1 Introduction 86

5.2 Experimental details 89

5.3 Optical band gap: need of non parabolic conduction band 89

5.3.1 Structural characterization 89

5.3.2 Optical band gap measurements 93

5.4 Surface charge accumulation and band bending 100

5.4.1 Removal of physisorbed surface contaminants: Low Energy Ar^+ sputtering 100

5.4.2 In*3d* core-level deconvolution: Presence of In adatoms on the surface 101

5.4.3 XPS valence band spectra analysis 102

5.5 Inferences 105

6 InN growth on In induced superstructure phases of Si(111)-7×7 107

6.1 Introduction 107

6.2 Experimental 109

6.3 InN/In induced reconstructions of Si(111) 110

6.3.1 Evolution of In induced superstructures of Si(111) surface 110
6.3.2 Structural characterization 111
6.4 Lowering of growth temperature of epitaxial InN 115
6.5 Inferences 126

7 Role of defects in limiting the electron mobility of InN 127
7.1 Introduction 127
7.2 Experimental Details 130
7.3 Results: Electron mobility of InN epilayers 131
7.3.1 Broadening of ω-scans: A measure of dislocation density 135
7.4 Electron mobility of self-assembled and dislocation free InN nano rods . . 139
7.4.1 Morphological, structural and optical characterization 139
7.4.2 Hall and transport measurements on a single InN NR 145
7.5 Native point defects and dislocations as scattering centers 147
7.5.1 Charge neutrality condition 147
7.5.2 Matthiessen's rule 149
7.6 Inferences 151

8 Conclusions 153
8.1 Summary and Conclusions 154
8.1.1 Unintentional doping in InN: Band gap controversy 154
8.1.2 Surface charge accumulation 156
8.1.3 Super Lattice Matching Epitaxy of InN on Si(111) 156
8.1.4 Towards high mobility InN films 157
8.2 Highlights of the work 160
8.3 Future directions 160

Bibliography 174

List of Publications 175

List of Figures

1.1 Relation between lattice constant and band gap energy 2
1.2 Velocity-field characteristics of wurtzite GaN, InN, AlN 5
1.3 III nitride unit cell rotated by 30° w.r.t sapphire unitcell 10
1.4 Hetero-epitaxially grown mosaic epilayers 11
1.5 Two dimesional representation of point defects 13
1.6 (a) and (b) for screw and edge type dislocations 14
1.7 Schematic diagram of different processes involved during thin film nucleation and growth 16
1.8 growth modes: FM, VW and SK 17

2.1 Decomposition curve for InN 22
2.2 Crystal structures of zincblende and wurtzite InN 24
2.3 Schematic for MB effect and reported InN band gap values 29
2.4 Position of Charge Nuetralilty Level in semiconductors 31
2.5 Literature survey of mobility and carrier concentration 32
2.6 Mobility plotted versus preperation methods and substrates 33
2.7 Mobility plotted versus carrier concentration 34

3.1 Fig (a) shows our MBE growth system 36
3.2 Fig shows SVTA schematic diagram 38
3.3 Fig shows schematic diagram of RGA 39
3.4 Fig shows schematic diagram of PVD: e-beam evaporation 41
3.5 The 3D sketch shows the directions of the elastically 42
3.6 The schematic diagram of XPS 43
3.7 Fig shows the schematic diagram of the photoemission process 45

3.8 XPS core level oxygen 1s spectra showing Shirley 47
3.9 Fig shows schematic diagram of HRXRD 49
3.10 Scans in reciprocal space 50
3.11 PL recombination transitions in semiconductor 54
3.12 Fig shows schematic diagram for hall measurements 55
3.13 A common geometry for Van der Pauw Hall 56
3.14 A schematic of AFM 58

4.1 *in-situ* RHEED diffraction pattern observed for samples 64
4.2 XRD pattern for samples grown at different temperatures 65
4.3 The ω-scans for the InN films grown at 400 and 450 °C 66
4.4 *in-situ* Cathodoluminescence spectra observed for samples 67
4.5 FESEM images of the samples grown at a) 400°C, b) 450 °C, and c) 500 °C 68
4.6 XPS In (*3d*) core-level spectra obtained for samples 70
4.7 The percentage composition of oxygen and ratio of In to N 71
4.8 FESEM images for the InN film grown at N-flux of 2, 4, 6 and 8 sccm . . 74
4.9 XRD θ-2θ scans for the films 76
4.10 shows the plot of inplane vs out of plane strain 77
4.11 Native Point Defects (NPDs) in InN material 78
4.12 Absorption (squared) and MB curve plots 79
4.13 XPS N1s core level deconvolution 81
4.14 the integral intensity ratio of defect peaks to InN peak 82

5.1 AFM images for the InN film grown on GaN 90
5.2 HRXRD $2\theta - \omega$ scans for the films 91
5.3 SAED pattern obtained on 400 °C grown sample 92
5.4 ω scans for the films 93
5.5 PL, Absorption measurements on samples A, B, C and D 94
5.6 Different reported experimental band gaps for InN from literature 98
5.7 Survey scan and O1s core level 100
5.8 XPS studies of the In$3d_{5/2}$ core level obtained on treated InN thin film . 101
5.9 XPS valence band spectrum for sample A-D 102
5.10 Band bending diagram, band bending values plotted vs carrier concentration 103

6.1 Desorption curve and reconstructions: Auger residual thermal desorption curve for In/Si(111)-7×7 system 110
6.2 Surface morphology and structure: FESEM and RHEED (inset) images . 111
6.3 XRD patterns for samples A through C 112
6.4 The schematic for the unit cell relationships of InN and different In induced superstructural reconstructions 113
6.5 unit cell relationships of InN with In induced superstructural reconstructions 114
6.6 Top view FESEM images and RHEED for the InN films 116
6.7 FESEM images and RHEED for the samples B1 and B2 117
6.8 HRXRD 2θ-ω and ω scans 119
6.9 Hall mobility and HRXRD rocking curve FWHM values 121
6.10 AFM rms surface roughness plotted versus Hall mobility 122
6.11 PL spectra obtained for samples A2, A5, B2 and B1 123
6.12 shows the survey scan and inset is the high resolution Si core level 124
6.13 shows PL band edge emission values and XPS In to N ratio 125

7.1 FESEM top view of the films InN/GaN epilayer and InN/GaN NWN . . 131
7.2 Theoretical Moss-Burstein curve along with our experimental data points 132
7.3 Mobility values plotted versus thickness of the formed films 134
7.4 HRXRD 2θ-ω scans for symmetric and asymmetric reflections 135
7.5 The ω-scans acquired on symmetric and asymmetric reflections 136
7.6 extrapolated on-axis and off-axis ω-scan broadening values 137
7.7 FESEM and distribution of NRs in GaN NW cavities 140
7.8 RHEED pattern for InN NRs 141
7.9 symmetric and asymmetric 2θ-ω scans for InN NRs 142
7.10 Bright and dark field TEM images for InN NR 144
7.11 CL emission and optical absorption spectra for InN NRs 145
7.12 InN NR having four Pt contacts and schematic representation 146
7.13 Plot shows energy dependent effective mass of electron 150
7.14 Plot shows the mobility as a function of carrier concentration 151

8.1 carrier concentration vs bandgap for all the films discussed in the thesis . 159

List of Tables

1.1 Parameters of III-V nitride and other semiconductors 9

1.2 Lattice mismatch values of III-nitrides on c-sapphire 10

2.1 Literature: various growth conditions and properties of InN 26

5.1 Different experimentally measured parameters: resistivity, ... 104

6.1 Defines the notations for samples prepared by various routes 115

6.2 Different experimentally measured parameters: AFM roughness, ... 120

7.1 Different experimentally measured parameters for samples A-H 138

8.1 Consolidated values of carrier concentration and band gap for all the samples used in this thesis 158

Acronyms

AES	Auger Electron Spectroscopy
AFM	Atomic Force Microscopy
BE	Binding Energy
BEP	Beam Equvivalent Pressure
BPE	Branch Point Energy
CBM	Conduction Band Minimum
CL	Core level
CL	Cathodoluminescence
CNL	Charge Nuetrality Level
CPS	Counts Per Second
CVD	Chemical Vapor Deposition
DFT	Density Functional Theory
DOS	Density Of States
EEELS	Electron Energy Loss Spectroscopy
ELOG	Epitaxial Lateral Overlayer Growth
ESCA	Electron Spectroscopy for Chemical Analysis
FESEM	Field Emission Scanning Electron Microscopy
FM	Frank van-der Merwe (growth mode)
FWHM	Full width at Half Maximum
HREELS	High Resolution Electron Energy Loss Spectroscopy
HRXRD	High Resolution X-ray Diffraction
HT	High Temperature
HVPE	Hidride Vapor Phase Epitaxy
IMFP	Inelastic Mean Free Path

IL	Intermidiate Layer
LD	Laser Diode
LED	Light Emitting Diode
LEED	Low Energy Electron Diffraction
LME	Lattice Matching Epitaxy
LT	Low Temperature
MBE	Molecular Beam Epitaxy
ML	Monolayer
MOVPE	Metal Organic Vapor Phase Epitaxy
PVD	Physical Vapor Deposition
PL	Photoluminescence
RHEED	Reflection High Energy Electron Diffraction
RMS	Root Mean Square
RT	Room Temperature
SAED	Selected Area Electron Diffraction
SAG	Selective Area Growth
SCCM	Standard Cubic Centimeter per Minute
SK	Stranski-Krastonov (growth mode)
STM	Scanning Tunneling Microscopy
TEM	Transmission Electron Microscopy
UHV	Ultra High Vacuum
VW	Volmer- Weber (growth mode)
VBM	Valence Band Maximum
XPS	X-ray Photoelectron Spectroscopy
XRD	X-Ray Diffraction
ZPE	Zero Point Energy
0D/1D/2D/3D	Zero-Dimensional/One-Dimensional/ Two-Dimensional/Three- Dimensional
μ	Mobility
n	Carrier concentration
E_F	Fermi Level
ρ	Resistivity

Chapter 1

Introduction and Motivation

This chapter describes some of the fundamental characteristics of III-nitride semiconductors that make them technologically important, are described in the chapter. In particular, InN as a promising material among the III-nitrides and the origin of various defects incorporated during thin film formation, which essentially arise due to the lack of native substrates, is discussed. Primary mechanism involved in the growth of thin films, nucleation of islands and growth modes are explained.The chapter also presents the scope and organization of the thesis.

1.1 Introduction

The excitement brought by the science and technology of III-V compound semiconductors is well described in several books[1–4] and review articles[5–8], published. As shown in Fig 1.1, the nitride semiconductors AlN, GaN and InN are direct band gap materials with energy gaps of 0.63eV (InN), 3.4 eV (GaN) and 6.2 eV (AlN). Being isostructural and possessing similar valance states they enable band gap engineering which enables the formation of ternary alloys whose band gaps cover the entire range of visible spectrum and sufficiently in the infrared and ultraviolet (UV) regions, i.e. continuously variable from 1965 to 200 nm (0.63eV to 6.2eV). This makes them ideal candidates for optoelectronic devices operating anywhere within this wavelength range including for visible light emitters, UV lasers, IR-detectors, full spectrum solar cells, HEMTs etc. Major developments in wide gap III-V nitride semiconductors have led to the commercial

production of Light Emitting Diodes (LEDs) emitting from red to near UV. Especially the introduction of bright blue GaN-based LEDs by S. Nakamura[9,10] paved the way for full color displays and to obtain white light source for illumination. Most importantly, when LEDs are used in place of incandescent light bulbs, they provide not only higher brightness and longer lifetime, but also consume about 10-20% of the power for the same luminous flux. Therefore, III-nitride LEDs have great potential to be the next-generation illuminating source. The range of applications of nitride-based LEDs is extremely wide; standard green to violet LEDs are used in traffic lights, full colour displays, automotive panel instruments, and any kind of lighting. To attain global energy security, photovoltaic technology of solar cell has become a hot research field. Although significant progress has been achieved,[11] improving the conversion efficiency is still the main task. One approach is to make the solar cell to absorb as wide solar spectrum as possible by using multi-layers of alloys of InGaN having direct bandgap which covers the most of the solar spectrum, from 0.65 to 3.4 eV, by adjusting the In content as shown in Fig 1.1. Thus, there is substantial potential in developing high-efficiency full-spectrum-response solar cells, by using tandem stacks of III-nitride-based materials[5].

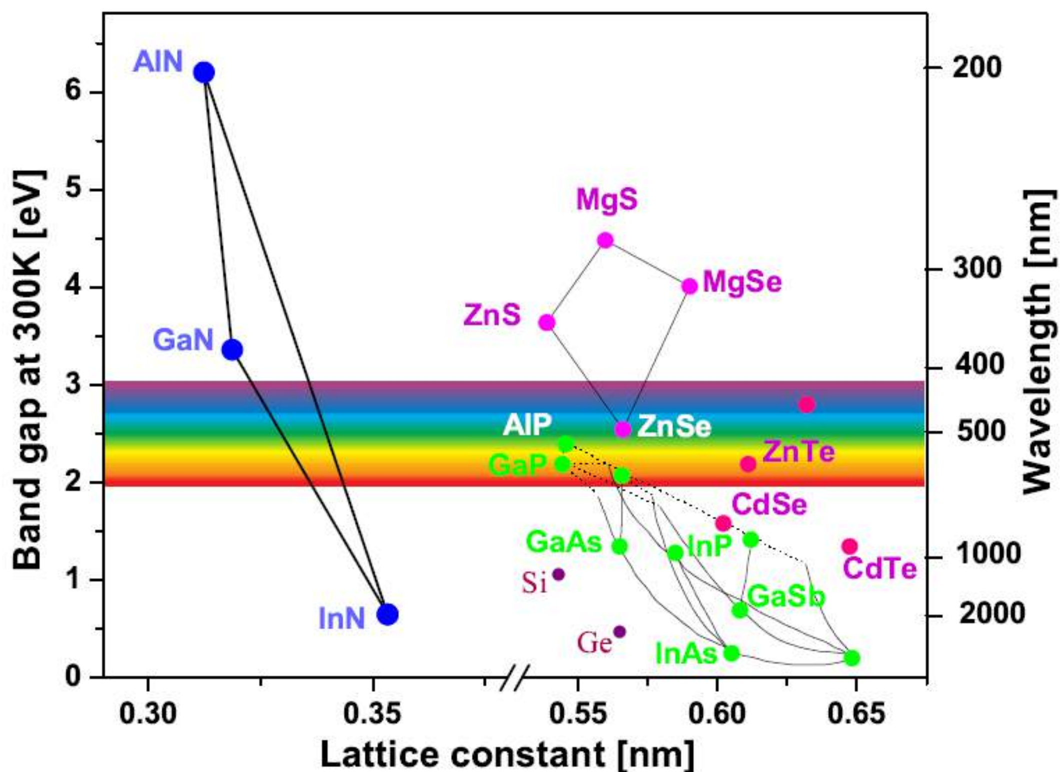

Figure 1.1: shows the relation between lattice constant and band gap energy for the III-nitrides and other various semiconductors at room temperature.[12]

The III nitride based devices are in a contrast to the (Ga,Al)As based LEDs (1.5 - 2.2 eV) or (Al,Ga,In)P based LEDs (1.3 - 2.5 eV) which cover only the IR to yellow region (Fig 1.1). On the other hand, in comparison to silicon (Si), germanium (Ge), III arsenides, phosphides (GaAs, GaP and InP) or zinc selenide (ZnSe) based material systems, group III- nitrides have a higher bond strength and melting point that result in chemical and physical stability, which make them suitable for use with high electric currents, for intense light illumination, high thermal conductivities, high radiation hardness, larger avalanche breakdown fields, larger piezoelectric constants, and larger room temperature electron mobility. These discerned properties make them suitable for high-frequency and high-power optical and electrical devices which can be used in harsh environments like automotive engines, space, and avionics.

1.2 Group III - nitrides: A brief history

Group III-nitride semiconductors have been studied for more than half a century. Among them, InN is least studied and GaN is the most investigated materials in the literature. In 1928, Tiede *et al.*[13] first reported AlN growth, later in 1938 Juza *et al.*[14] reported the synthesis of GaN which formed by flowing ammonia over hot gallium and InN from $InF_6(NH_4)_3$ reduction. These initial studies were intended to analyze the fundamental band gap measured from optical properties and relate it to the lattice parameters obtained from XRD measurements for these materials. And then 30 years later, Maruska *et al.*[15] first grew GaN epi layers having band gap at 3.39eV by vapour phase deposition on sapphire substrates, followed by the deposition of GaN epitaxial layers were deposited using hydride vapour phase epitaxy (HVPE) in the 1960s. Following this report, in 1971 blue LEDs based on GaN:Zn/n-GaN structures were prepared by Pankove *et al.*[16] on vapour phase grown GaN which relied on hot carrier injection from avalanche breakdown to generate holes. Despite the subsequent advances in growth, preparation of p-type GaN remained difficult due to the high defect density of the available heteroepitaxial films. In 1989, by employing a two step growth method, Amano *et al.* succeeded in growing good quality p-type Mg:GaN epi-layer on c-sapphire with a low temperature AlN buffer using metal organic vapour phase epitaxy (MOVPE).[17] Research carried out at Japanese company Nichia Chemical Industries by Nakamura *et*

al. used Mg doping to achieve p-type material which helped in preparing the brightest blue LEDs[9,10]. As a consequence, high power InGaN LEDs for white, blue and green light emission with expected lifetime of 10^5 hours were announced and marketed by the same company in 2002. Since then, several remarkable attempts have been made to investigate laser diodes and even high electron mobility transistors (HEMT) using the III nitride compounds and their alloys. During the 1990s, it was demonstrated that HEMTs are possible due to the accumulation of 2D electron gas at $Al_xGa_{1-x}N$/GaN interface resulting from the strain induced and spontaneous piezoelectric polarization effects.[18] In 2001, Kuzmk[19] suggested to use the ternary InAlN in place of AlGaN in order to avoid the devices degradation due to strain relaxation, since by changing the Al to In ratio the strain could be varied while maintaining the high electron sheet density. Later on, strain has been completely removed by growing InAlN/GaN lattice matched heterostructures, which is explained in detail by Jain *et al.*[20] and Bhuiyan *et al.*[21]

1.3 Motivation

1.3.1 InN: Introduction and applications

Among III-nitrides, InN is an enormously potential material for electronic and optoelectronic devices because of its outstanding material properties such as lowest effective mass ($0.04m_0$), narrowest band gap (0.63 eV), highest predicted electron mobility (4400 cm^2/V-sec) and high peak and saturation velocities (10^7 cm/sec). In spite of these fascinating properties, InN has remained the least studied and understood material among III-nitrides, since the preparation of high quality epitaxial InN material is challenging due to its low dissociation temperature ($\approx$ 550 °C), high equilibrium vapor pressure of nitrogen over the InN films during growth and lack of suitable (native) substrate material. Thus, the complexity in preparing high quality InN films using different experimental techniques, has led to a wide spectrum of reported fundamental properties like band gap values that range from 0.6 to 2.2 eV in the literature.[22,23] The high band gap values observed earlier, have been largely attributed to be resulting from the incorporation of indium oxide, hydroxide, or oxynitride and related complexes as these films were grown using low vacuum growth techniques like rf-sputtering.[24] Recently, due to the emergence

advanced growth techniques, high quality single crystalline InN films have been prepared. Over the last two decades, a major advance in InN research was made, when the growth of good quality single crystalline films of InN by MBE on sapphire substrates was reported, whose the band gap energy was claimed to be ≈ 0.67±0.05 eV[25–27]. Since then, the number of publications in the area of InN research have been significantly increased.

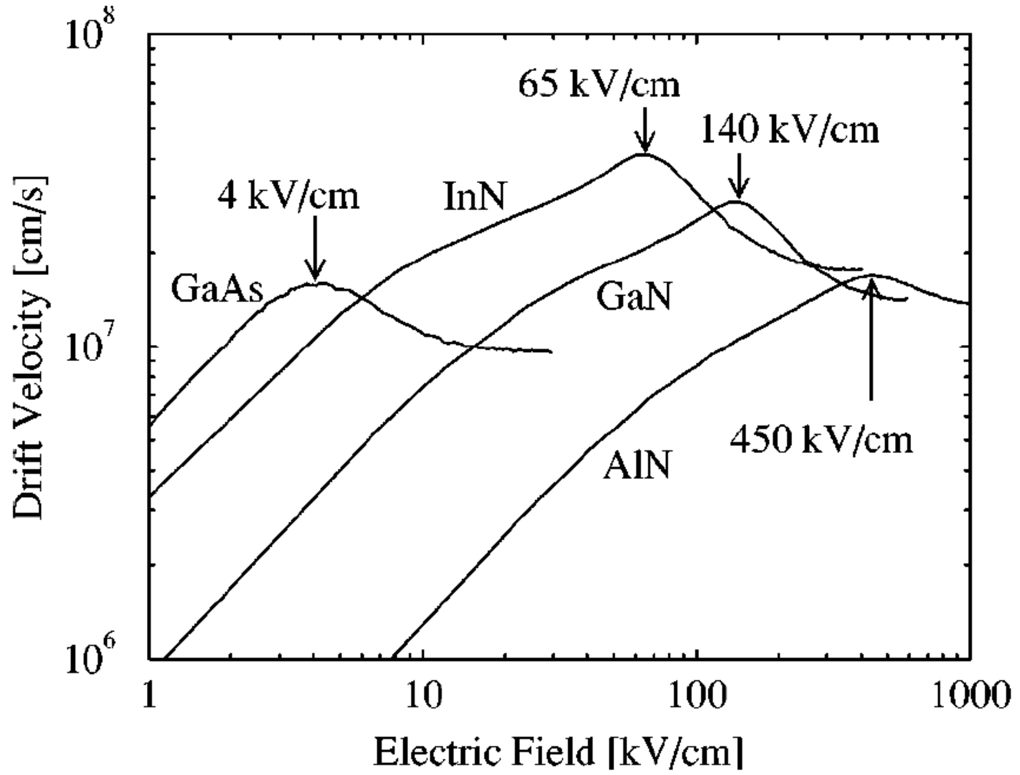

Figure 1.2: Velocity-field characteristics of wurtzite GaN, InN, AlN and zincblende GaAs.[28]

As a consequence of its lowest effective mass for electrons, InN exhibits the highest mobility and high saturation velocity among III-nitrides. The theoretically estimated maximum mobilities of InN and GaN at 300 K are 4400 and 1000 cm^2/Vs, respectively, while at 77 K the limits are beyond 30,000 and 6000 cm^2/Vs, respectively.[29] The electron transport in wurtzite InN studied by an ensemble Monte Carlo method,[28,30,31] showed that InN exhibits an extremely high peak drift velocity at room temperature, with saturation velocity much larger than that of gallium arsenide (GaAs) and gallium nitride (GaN). Fig 1.2 is the velocity-field characteristics associated with wurtzite GaN, InN, AlN, and zincblende GaAs, which shows that the respective critical field at which the peak drift velocity was achieved. InN achieves the highest steady-state peak drift velocity of 4.2×10^7 cm/s at 65kV/cm which contrasts with the case of GaN, 2.9×10^7 cm/s, AlN, 1.7×10^7

cm/s, and of GaAs, 1.6×10^7 cm/s. It is also reported[31] that the transport characteristics of InN are superior to those of GaN and GaAs, over a wide range of temperature from 150 to 500 K and a doping concentration up to 10^{19} cm^{-3}. The transport characteristics were shown to be relatively insensitive to variations in temperature and doping concentration, unlike in GaAs. This suggests that there may be distinct advantages offered by using InN in high frequency centimetre and millimetre wave devices. The transient electron transport, which is the dominant transport mechanism in submicron-scale devices, was also studied in InN,[28] and found that it exhibits the highest peak overshoot velocity which lasts over the longest distance when compared with GaN and AlN. It was predicted that InN-based field-effect transistors (FET) have an extremely high speed with a cut-off frequency of over 1 THz for 0.1 mm gates. Thus, the properties of InN show that it is a highly potential material for the fabrication of high-speed, high-performance hetero junction FETs, with several applications.

1.4 Applications of InN

The superior optical and electrical properties of group III-nitride compound semiconductors lead to the fabrication of advanced device structures. The tunable III nitride alloys having variable In composition, and thus band-gaps, made them potential candidates for state-of-the-art electronic and optoelectronic devices, that operate over a wide range of the electromagnetic spectrum. A higher band gap is preferred for microwave transistor devices, while smaller band gap are also required for a full solar spectrum cell based on InGaN.

1.4.1 Optical applications

In 1962, the importance of Electronic Lighting Technology and communication was realized with the invention of first light emitting diode (LED),[32] and consequently, light amplification by stimulated emission (LASER) using semiconductors.[33,34] This led to drastic revolution in semiconductor technology, by the production of bright light emitters used in optical fibre networks, data storage (Compact-Disc Technology) and document printing (Laser printers). But LEDs based on GaAs operate only in the red to yellow

portion of the spectrum as discussed in section 1.1. Though, SiC or II-VI semiconductors were used in making LEDs, due to their indirect band gap they do not emit with enough intensity. The first blue LEDs based on the III-V nitrides were made commercially available by Nichia in early 1994, and paved the path for high brightness optical devices. Since then, much research has been accomplished on III nitrides comprising the Al-Ga-In-N alloys that show great promising for next generation LEDs and Lasers.

1.4.2 LED applications

As shown in Fig 1.1, ($Ga_{1-y-x}Al_y\ In_x$)N alloys system span a wide range of direct band gap energies from 0.6 eV to 6.2 eV which correspond to wavelengths ranging from near infrared to deep ultraviolet,lead to high quantum efficiency and faster switching speeds. The first blue/green light emitting diode structure based on InGaN, consisted of a 3 nm layer $In_{0.2}Ga_{0.8}N$ sandwiched between p-type AlGaN and n-type GaN, all grown on sapphire substrate.[35] White LEDs of 30-40 lumens/watt efficacy have been developed recently by coating GaN LED with yellow phosphorus which produces light that appears white,[36] but is not as efficient as the commercial fluorescent light sources which give 70-80 lumens/watt. Combining red light emitting diodes with blue/green ones having the same power and brightness can produce full colour displays and efficient white lamps. Achieving a red light emitting diode based on InGaN structures depends on indium rich InGaN heterostructures. Researchers at IBM demonstrated an InN nanowire LED, which emits infrared light, demonstrating the future possibility of ideal for optical communication between devices on microchips, that would speed up computers drastically. If the III-nitride nanowires can be tuned to emit red, green and blue light, an all-nanowire LED could be manufactured on the same substrate, making LEDs cheaper and possessing greatly improved performance.

1.4.3 Laser applications

Fabrication of high quality III-nitride LEDs enables the fabrication of semiconductor lasers that operate at desired light wavelengths from ultraviolet to green. The advantage of blue GaN/InGaN lasers with shorter wavelength (405 nm) over a red laser (605 nm) is that it allows five times more storage capacity (25 GB). Blue-ray disc technology was recently adopted over traditional DVDs, by world lead in consumer electronics (including

Apple, Dell, HP, JVC, LG, Mitsubishi, Samsung, Sharp, Philips, Pioneer and Sony Corp.) which enabled high density recording and rewriting.[37] The opening of a variety of potential markets such as blue-ray is only the beginning of the enormous applications possible by this technology. Though it is evident that it is possible to mix the Al, Ga, and In in appropriate ratios to make ternary and quaternary alloys such as ($Ga_{1-y-x}Al_y$ In_x) N enabling, in principle, to make semiconductor lasers that emit light from the deep ultraviolet with a photon energy of 6 eV, to the infrared with photon energy of 1 eV, only a much narrower range of operation from the near ultraviolet (3.5 eV) to the green (2.4 eV) has been demonstrated. The performance issues that are related to the crystal growth itself limit further development. InN one dimensional (1D) nanostructures, such as nanowires, nanorods, nanotubes and nanobelts currently appear to be the most attractive structures due to the easier growth in single crystal forms without defects, with lasing properties being expected. Hu *et al.* reported the investigation of infrared lasing in high quality single crystalline InN nanobelts grown by MOCVD,[38] which can be considered a major advance in the nanophotonics which can impact imaging in chemistry, biology, and optical communications.

1.4.4 THz applications

These are many applications in the terahertz region of the electromagnetic spectrum (300 GHz to 30 THz), which corresponds to the sub-millimetre wavelength range between 1 mm and 10 μm, in the form of sensor and sources (emitter, generators etc.). However, the main challenge in terahertz applications is the lack of suitable terahertz sources and detectors. One potential way to extend terahertz detection beyond the 3.2 THz is to utilize the properties of InN and indium-rich InGaN alloys and heterostructures, which can lead to advanced THz detector and emitter devices, operating at temperatures higher than 77K and having higher sensitivity.[39,40] Furthermore, the ferromagnetic behavior of transition metal doped indium rich InGaN can enable unique enhancements of the absorption rates, and hence the photo response, under an applied magnetic field. Studies on InN show it to be a good material for optically excited THz emission.[39,41] Monte Carlo simulations of InN, GaN and AlN showed that high frequency power generation in a constant electric field occurs for the whole sub millimetre range (0.25THz-4THz)

around the liquid nitrogen temperature.[42] The possibility of THz radiation generated from InN films was observed by Ascazubi *et al.*, and Chern *et al.* showed that if the carrier concentration of InN films can be reduced by an order of magnitude, InN will surpass InAs as the most efficient semiconductor THz emitter.[39,41] However, since the material quality of InN obtainable now is inferior, this potential of THz generation and sensing using InN films is not exploited.

1.5 Substrates

Various substrates, such as sapphire, Si , SiC, GaAs, etc have been used for III-nitrides growth due to the lack of native nitride substrates. Among these substrates, because of the reasons like cost, availability, stability, feasibility of *in-situ* and *ex-situ* cleaning, and also the possibility of nitridation of its surface, the most commonly used substrate for InN growth is sapphire, though the lattice mismatch between InN and sapphire is as high as 29%. On the other hand Si is also considered attractive because of its integratability in the mature electronic industry and availability of high quality, low cost, and large diameter wafers. However, it is difficult to grow high quality InN directly on these substrates because of lattice mismatch as and the difference in thermal expansion coefficients.

Table 1.1: Parameters of III-V nitride semiconductors and most commonly used substrates.[2,43]

Material	Crystal	Melting	Lattice constant (Å)		Lattice Mismatch (*approx.* %) w.r.t			Thermal expansion $10^{-6}K^{-1}$	
	structure	point (K)	a	c	GaN	InN	AlN	$\parallel \vec{a}$	$\parallel \vec{c}$
InN	Wurtzite	1373	3.5378	5.7033	-11	0	12.0	3.09	2.79
GaN	Wurtzite	2573	3.1850	5.1880	0	11	2.3	3.17	5.59
AlN	Wurtzite	3273	3.1110	4.9800	2.3	13.7	0	4.20	5.30
Al_2O_3	Rhombohedral	2303	4.7650	12.9820	16	29.2	13.3	5.00	9.03
SiC	Wurtzite	3103	3.0806	15.1173	-3.1	14.8	-0.98	4.30	4.70
GaAs	Zincblende	1513	a=b=c=5.653		20	11.7	-	6.03	
Si	Diamond	1687	a=b=c=5.431		21	-7.8	19	2.61	

While cooling down after the growth, the substrate and the film will relax in significantly different ways depending on the differences in their thermal expansion coefficients. To overcome the problems that originate from mismatch induced defects, many methods like low temperature intermediate buffer layers, nitridation, Epitaxial Lateral Overlayer Growth (ELOG), Selective Area Growth (SAG) have been employed. Thus, in heteroepitaxial growth, not only the difference in lattice parameters but also thermal behaviour of the substrate and the epitaxial layers induce deleterious effects in the films formed.

Table 1.2: Lattice mismatch values of III-nitrides on c-sapphire along $< 11\bar{2}0 >$ and $< 10\bar{1}0 >$ directions.[25]

	$[11\bar{2}0]_{III-nitride} \parallel [11\bar{2}0]_{c-sapphire}$	$[10\bar{1}0]_{III-nitride} \parallel [11\bar{2}0]_{c-sapphire}$
InN	-25.4%	+29.2%
GaN	-33.0%	+16.0%
AlN	-34.6%	+13.3%

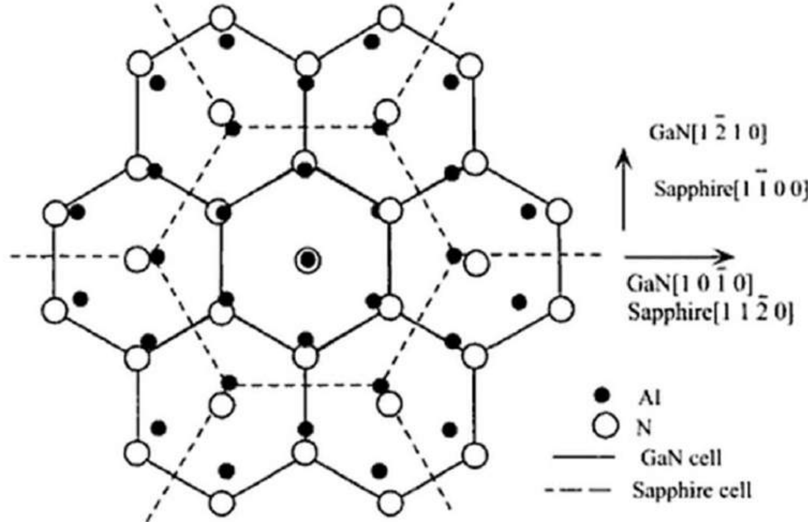

Figure 1.3: Projection of 30° rotated III-nitride unitcell on sapphire unitcell.[2]

In our studies, we have found a novel structural surface modifications on silicon that involves the initial formation of various stable metal induced superstructural phases, which are been used to grow good quality InN material. We have investigated nitride layers that are grown on c-sapphire and Si(111) substrates. In Table 1.1, the lattice parameters, lattice mismatch and thermal expansion coefficients for the nitrides and

commonly used substrates are listed. The main criteria to choose a suitable substrate for InN growth is the least lattice mismatched one which can be measured by the misfit parameter $f_m = (a_{substrate} - a_{film})/a_{substrate}$, where $a_{substrate}$ and a_{film} are the lattice constant for the substrate and the film, respectively (Table 1.1). In general III-nitrides have the tendency to grow 30° rotated *w.r.t* the sapphire unit cell and thus misfit parameter is modified accordingly as $f_m = (a_{substrate} - 2a_{film}cos\theta)/a_{substrate}$. Table 1.2 shows the lattice mismatch values in the two orientations for different nitrides with sapphire substrate. For InN on c-sapphire magnitude of lattice mismatches in the two epitaxial directions is very close in magnitude (either compressive or tensile strain), and thus there is an equal probability for InN to grow in both the epitaxial directions, tending to make it polycrystalline. Fig 1.3 depicts the arrangement of the atoms when over grown III nitride layer is rotated by 30° with respect to sapphire unitcell.

1.6 Mosaic model

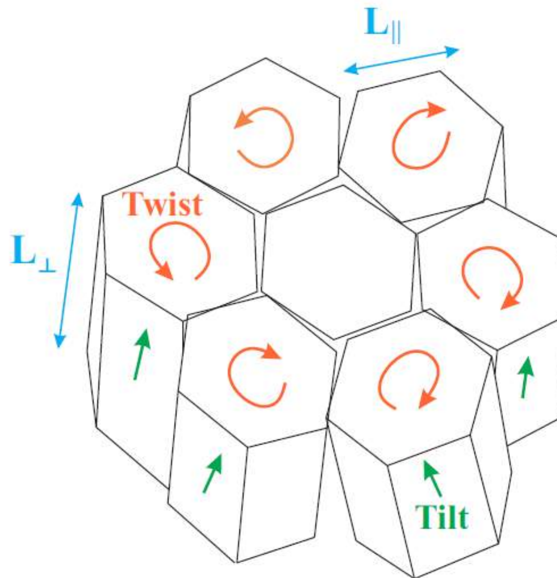

Figure 1.4: Hetero-epitaxially grown mosaic epilayers having lateral ($L_{\parallel}$), vertical ($L_{\perp}$) coherence lengths, crystal tilt and twist.

Heteroepitaxial films with large lattice mismatch to the substrate commonly exhibit a high density of threading dislocations (TD), which evolve from the coalescence of neighboring misoriented islands affecting the microstructure and crystalline quality of the InN epilayer. A mosaic model[44] is widely used to describe the epilayer microstructure

in which the in-plane and out-of-plane rotations of grains are quantified by the mosaic twist and tilt, respectively. In this model, the layer is assumed to consist of single crystals, called mosaic blocks with certain mean vertical and lateral dimensions. Since the crystallites are assumed to be free of dislocations, they can coherently scatter the x-rays, and their dimensions are called vertical and lateral coherence length.

These terms are related to directions perpendicular and parallel to the growth plane, respectively. For systems with defects mainly running parallel to the surface normal, the vertical coherence length is related to the thickness of the layer, tilt angle, α_{tilt}, or out-of-plane misorientation; twist angle, α_{twist}, or inplane misorientation; lateral coherence length, $L_{\|}$; and the vertical length ($L_{\perp}$) depends on the thickness of the layer, in case of thin films.[45] These four characteristic parameters are accessed using high resolution x-ray diffraction.

1.7 Structural defects

As it has been discussed in earlier sections, heteroepitaxial growth having different lattice parameters and thermal expansion coefficients of substrate and overgrown layer is usually strained, and varies with layer thickness. Initially film grows pseudomorphically for thickness below a critical value (t_c), Which means that both lattice parameters of substrate and film are equal with a high strain. On the other hand, for $t > t_c$, films attain relaxed values of lattice parameters by accommodating structural defects and the residual strain is either tensile ($a_{substrate} > a_{film}$) or compressive ($a_{substrate} < a_{film}$). The InN growth is very sensitive to the substrate temperature and other growth parameters and also the subsequent cooling can result in a combination of biaxial and hydrostatic strain states, that result from in-plane lattice mismatch and the incorporation of the point defects, respectively. These residual strain states can be calculated by measuring the lattice parameters via x-ray diffraction measurements.

The structural defects that are present in III-nitrides usually are point, line, planar and volume (0D, 1D, 2D and 3D) defects which have a deleterious effects on their optical and electrical properties.

1.7.1 Point defects

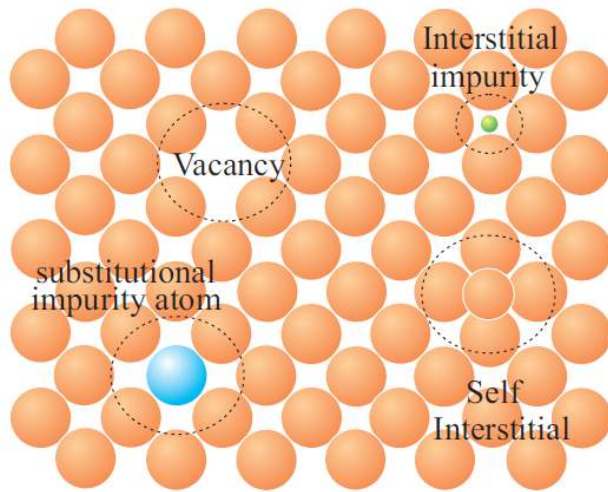

Figure 1.5: Two-dimensional schematic representation of point defects: vacancies, self-interstitial, substitutional and interstitial impurity atoms.

The number of point defects N_{pd} for a given material increases with temperature according to $N_{pd} = Nexp(\frac{-E_f}{k_BT})$, where N is total number of atomic sites, E_f is energy required for the formation of a defect in the crystal lattice, T is absolute temperature in Kelvin and k is Boltzmann's constant. The simplest of the point defects is a vacancy, from an atomic lattice site (Fig 1.5). All crystalline solids contain vacancies and, in fact, it is not possible to create a material that is free of these defects. The necessity of the existence of vacancies is explained using principles of thermodynamics; to increase the entropy (i.e., the randomness) of the crystal. A self-interstitial is an atom displaced from its crystal site and occupies interstitial site, a small void space that under ordinary circumstances is not occupied. This kind of defect is also represented in Fig 1.5. In close-packed metals, this defect introduces relatively large distortions in the surrounding lattice because the atom is substantially larger than the interstitial position in which it is situated. Consequently, the formation of self-interstitial has low probability of formation and thus exists in very small concentrations, which are significantly lower than for vacancies. Impurity point defects are found in solids, of which there are two types: substitutional and interstitial. For the substitutional type, impurity atoms replace or substitute for the host atoms,[46] and in the interstitial type, impurity atoms occupy interstitial sites between the host-lattice sites.

In compound semiconductors, antisite defects can be created by atoms occupying opposite sublattice sites. For instance in the case of InN, In atom moves on to the N site and forms In antisite (In_N) and vice-versa mechanism gives N antisite (N_{In}). Frenkel defects are nearby pairs of vacancies and interstitials, and Schottky defects are

vacancy pairs created by the simultaneous removal of a two opposite atoms in compound semiconductors. For InN, isolated and complexes of In and N point defects have been investigated.[47–49] The native point defects (NPDs) in N-rich (N/In > 1) InN are N_i, N_{In} and In_v with formation energy values ≈ 3.0eV, 5.2eV and 6.4eV; whereas for In-rich (In/N > 1) InN, the NPDs are V_N, In_N and In_i with formation energies ≈ 1.4eV, 4.7eV and 5.3eV, respectively.[50] Point defects often contribute to an increased background doping[51] and reduce the mobility of the free carriers in the semiconductors.[52]

1.7.2 Dislocations

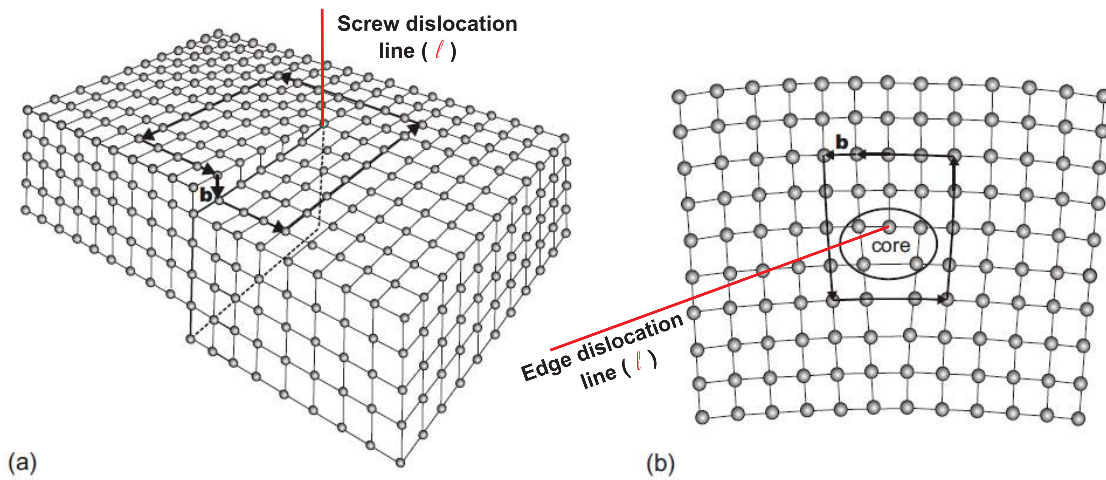

Figure 1.6: (a) screw-type dislocation for which the Burgers vector $\vec{b}$ is parallel to the dislocation line $\vec{\ell}$. (b) edge-type dislocation with Burgers vector $\vec{b}$ perpendicular to the dislocation line $\vec{\ell}$.[53]

A dislocation is a linear or one-dimensional defect around which some of the atoms are misaligned, which can greatly affect the material properties. A dislocation is usually represented by an oriented dislocation line $\vec{\ell}$, and characterized by its Burgers vector $\vec{b}$, describing displacements introduced in the crystal. Dislocation lines are characterized by the Burgers vector, found by doing a loop around the dislocation line and noticing the extra interatomic spacing needed to close the loop.

Based on the relationship of $\vec{\ell}$ and $\vec{b}$, three dislocation types are distinguished (see Fig 1.6): a *pure screw*-type dislocation with $\vec{\ell} \parallel \vec{b}$. In this case, (Fig 1.6a) all along the line, a quarter of the crystal is sheared for instance downward by the amount of lattice parameter. The *edge*-type dislocations ($\vec{\ell} \perp \vec{b}$), which corresponds to the insertion of an extra half plane in the crystal between two adjacent lattice planes. The end of

the additional half plane is the dislocation line and b is the lattice vector that virtually connects the atoms along the line (Fig 1.6b). The last one is a *mixed*-type dislocation ($\vec{b} \not\perp \vec{\ell} \not\parallel \vec{b}$) which is a combination of one screw and one edge dislocation lines[54].

In the hexagonal lattice, there are three possible Burgers vectors for perfect dislocations a, c, and a+c, and depending on their line directions, the corresponding dislocation may have respectively an edge, screw or mixed character. For instance, in the nitride epitaxial layers a dislocation is either edge or of mixed type when its line is in the basal plane and it becomes of edge type when it propagates inside the epitaxial layer, where it becomes a threading dislocation TD (ℓ=[0001]). A particular case is the a+c dislocation which is always a TD in such layers, and therefore of mixed type. Indeed, the c dislocation is always screw as a TD, but it may become edge type when its line bends in the basal plane for instance in case of epitaxial lateral overgrowth.[8]

The density of threading dislocation can be measured directly by transmission electron microscopy, which is destructive. Alternatively, nondestructive x-ray diffraction is a widely applied method to evaluate the crystalline perfection of epitaxial layers, and the density of dislocations can also be estimated by acquiring rocking curve broadening values.[55]

1.7.3 Planar and Volume defects

The **planar** defects are *grain* boundaries - separate crystals with same crystal structure but different orientations, *twin* boundaries - two separate crystalline regions that are, structurally, mirror images of each other, and *stacking faults* - are created by a fault in stacking of the hexagonal c-planes which are observed in non-polar and semi-polar material[56]. The other type of defect that exists in solid crystals is the **volume** defects which is much larger than the defects discussed earlier. These include voids, cracks, foreign inclusions, pores, and other phases.

1.8 Thin film nucleation and growth

The individual atomic processes responsible for adsorption and crystal growth on surfaces are illustrated in Fig 1.7 where atoms or molecules arrive onto a substrate. The

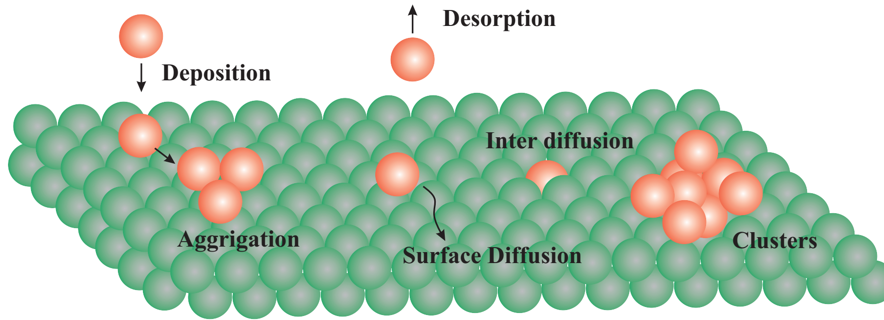

Figure 1.7: Schematic diagram of different processes involved during thin film nucleation and growth.

primary mechanism in the growth of thin films as well as surface nanostructures from adsorbed species is the transport of these species to and on a flat terrace, involving random hopping processes at the substrate atomic lattice, or desorption from the substrate (re-evaporation). On adsorption, they diffuse on terraces to meet other adatoms, resulting in nucleation of aggregates or attachment to already existing islands to form clusters. Diffusion onto the surface, or inter diffusion can be significant under certain growth conditions, which is thermally activated; that is, diffusion barriers need to be surmounted when moving from one stable (or metastable) adsorption configuration to another.

The formation of islands and the attachment of atoms to existing structures and clusters are important in the formation of self-assembled (SA) islands (dots). When a diffusing adatoms find each other, they can nucleate and form an island after they reach a critical cluster size. Adatoms that directly impinge to on an island can either incorporate into the island or lead to the next layer growth, depending on the surface potential and energy. As the island continue to grow further, and possibly migrate, they can find other islands and coalesces into larger islands.

As is typical for such processes, the diffusivity D – the mean square distance travelled by an adsorbate per unit time – obeys an Arrhenius law; this holds for atoms as well as rigid organic molecules. If we now consider a growth experiment where atoms or molecules are deposited on a surface at a constant deposition rate F, then the ratio D/F determines the average distance that an adsorbed species has to travel to meet another adsorbate, either for nucleation of a new aggregate or attachment to an already formed island. The ratio of deposition to diffusion rate D/F is thus the key parameter characterizing growth kinetics. If deposition is slower than diffusion (large values of D/F),

growth occurs close to equilibrium conditions; that is, the adsorbed species have enough time to explore the potential energy surface so that the system reaches a minimum energy configuration. If deposition is fast relative to diffusion (small D/F), then the pattern of growth is essentially determined by kinetics; individual processes, notably those leading to metastable structures, are increasingly important. Metallic islands are controlled by growth kinetics at small D/F values, while semiconductor nanostructures usually grow at intermediate D/F and their morphology is determined by the complex interplay between kinetics and thermodynamics.

1.8.1 Growth modes

A classification of growth modes has been proposed by Ernst Bauer in 1958. At the nucleation stage, the film starts to grow in one of these three basic modes;[57] illustrated schematically in Fig 1.8. Generally, there are three main MBE heteroepitaxial growth modes that are dictated by the lattice mismatch, the surface energy, and the interfacial energy. The Frank van der Merwe (FM) growth mode is a layer-by-layer growth mode, where ad-atoms attach preferentially to surface sites. In the Volmer Weber (VW) growth mode ad-atom/ad-atom interactions are strong and clusters of ad-atoms are formed upon the surface. The Stranski-Krastanow (SK) growth mode occurs when the first few layers grow in a 2D fashion and then the island growth takes over as the strain of the layers is reduced.[58]

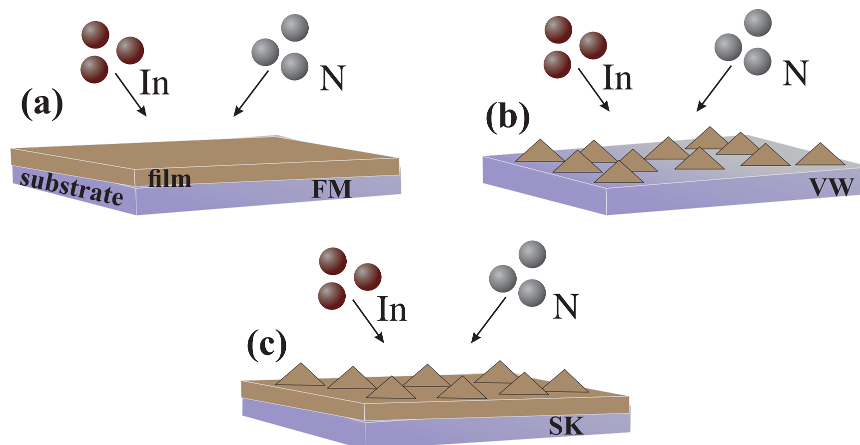

Figure 1.8: Schematic of different possible growth modes: (a) Frank-van der Merwe, (b) Volmer-Weber and (c) Stranski-Krastanov.

Frank-van der Merwe mode (FM)

If the lattice mismatch is small and the surface energy of the epitaxial layer and the interfacial energy is less than the surface energy of the substrate, the epitaxial growth mode will be FM mode. Two dimensional (2D) growth occurs when the adatoms of the film are strongly attracted to the substrate. Therefore, the first adatoms condense on the substrate surface and form a complete monolayer (Fig 1.8a) with very little strain. Subsequently, the next adatoms constitute the following monolayers and the growth takes place layer by layer. This is the ideal case, and it happens when the two materials have very similar characteristics (symmetry, lattice parameters, surface energies, growth temperatures), and more frequently in metal-metal heteroepitaxy.

Volmer-Weber mode (VW)

If the lattice mismatch is large and the surface energy of epitaxial layer is greater than the surface energy of the substrate, the epitaxial growth will be through the VW mode, which yields island growth, also known as three-dimensional growth mode. It occurs when the impinging atoms (adatoms) forms clusters on the substrate which then grow into individually islands. In this growth mode the bonds between the adatoms are stronger than the bonds between the adatoms and the substrate surface (Fig 1.8b). This mode will govern the heteroepitaxial growth when the two materials have completely different symmetries, surface energies, large lattice mismatch, usually prevalent in metal-insulator systems.

Stranski-Krastanov mode (SK)

For moderate lattice mismatch the initial growth is layer by layer, and strain due to the lattice mismatch is accumulated with increasing thickness of the epilayer. When the thickness of the 2D layer reaches a critical level, the strain will be released by the formation of small islands. As epitaxial material is added, these small islands will continue to grow until they are fully ripened. This process characterizes the hybrid SK growth mode. This is an intermediate case: after forming the first monolayer, or a few monolayers and when subsequent layer by layer growth becomes energetically unfavourable, the

growth continues in the form of islands (Fig 1.8c). The lattice mismatch between film and substrate induces a strain in the film and can explain the transition from 2D layer to 3D islands growth modes, as commonly seen metal-semiconductor interfaces.

InN is the least studied and least understood material among III-nitrides due to major synthesis problems arising due to its low dissociation temperature and high vapor pressure. This has in the past led to significant ambiguity in the literature concerning the basic material parameters measured for InN. In order to understand the unusual synthesis dependent properties of InN thin films, we have performed several systematic experiments to optimize various growth parameters such as flux and growth temperature on Sapphire and Si substrates. The chapter 2 presents brier literature overview which includes the reasons for the variation of band gap (high to low), surface charge induced downward band bending and low experimentally obtained electron mobility of InN. In order to understand these ambiguous properties MBE grown InN films are probed by using several complementary characterization tools which will be discussed in Chapter 3. While optimization of growth on sapphire is of commercial importance, growth on Si surfaces is challenging. Si surfaces exhibit scientifically fascinating metal induced surface reconstructions, having the unit cell dimensions integrally match with that of III-nitrides, enable us to grow good quality InN films at considerably low temperatures, when grown on these intermediate layers. In order to reduce dislocation density in InN epilayers and enhance electron mobility, these films and nano rods are grown on GaN Nano Wall Network (NWN) by improvising the Nano-ELOG epitaxy.

1.9 Organization of the thesis

The work presented in this thesis is systematically organized into chapters as follows.

Chapter 1 is the introduction to challenges encountered in group III nitride research. The difficulties that arise due to material properties, growth conditions by formation of native point defects and dislocations limit the attainment of ideal parameters such as mobility of the formed InN layers are described. A complete overview of the thesis structure also presented in this chapter.

Chapter 2 presents the literature overview available till date that focus on the formation

of InN layers and the ambiguous results obtained for fundamental properties of InN such as band gap and electron mobility.

Chapter 3 deals with the brief description of growth and characterization techniques used to acquire all the results reported in this research work, especially in context of how they serve as a reference to interpret and understand of the experimental investigations better.

Chapter 4 provides the results of the systematic optimization of various growth parameters of InN layers on bare c-sapphire. This chapter also discusses various reasons for the observation of high band gap and unintentional degenerate doping of InN thin films. Further, it consists of the analysis of the basic optical, structural and electrical properties measured on the formed films.

Chapter 5 deals with the detailed study of growth of InN layers on GaN epilayers deposited at different temperatures, to understand the reasons behind the high and low band gap. It also includes the study of surface charge induced downward band bending which results from the In adatoms related surface states.

Chapter 6 introduces the growth of InN onto low index Si surfaces, by considering Si reconstructions as growth templates. The chapter also focuses on the growth of single crystalline InN layers on In metal induced surface reconstructions on Si(111) at relatively low growth temperatures, a concept we introduce and named as Super Lattice Matching Epitaxy.

Chapter 7 presents our attempts to reduce dislocation density in the overgrown InN epilayers. It also discusses the growth of high mobility InN layers that are formed on GaN epilayer and on GaN Nano Wall Network templates. It also describes the growth and mobility measurements in dislocation free InN nano structures formed on GaN Nanowall templates.

Chapter 8 lists the highlights of the present work, concludes the results of the present thesis work and gives an outlook for the future work in this direction.

Chapter 2

Literature overview

This chapter provides the historical background for InN growth, and describes the growth, structure and properties of InN. It provides a comprehensive literature survey till date, focusing on issues related to the ambiguity in the band gap and surface charge accumulation of this material. It also presents a brief overview of the measured electron mobility of InN thin films grown by various methods by various groups. This review served as the motivation to undertake the present work and showed the outstanding issues in the field that needs to be presented.

2.1 Growth and properties of InN

2.1.1 InN: Historical background

Research on InN was initiated in 1938 when synthesized powder samples were analyzed by X-ray diffraction in order to determine the crystallographic properties of this material, when Juza and Hahn[14] obtained InN from decomposition of $InF_6(NH_4)_3$ at 600 °C. Due to lack of native III-nitride substrates, InN is grown heteroepitaxially on various substrates such as Sapphire, GaAs,[59] SiC[60] and GaP[61], etc. However, the most Though, mostly used substrate is c-sapphire because of its structural compatibility, wafer availability, temperature stability, transparency, etc. The state of the art InN films have been grown by various epitaxial techniques such as Molecular Beam Epitaxy (MBE),[62] Metal Organic Vapour Phase Epitaxy (MOVPE),[63] and Hydride Vapour Phase Epitaxy (HVPE).[64]

Till 1988, evaporation and RF-sputtering were the techniques used to grow InN.[65,66] Single crystalline InN was reported by Matsuoka *et al.*[67] and Wakahara *et al.*[68] for the first time in 1989 using MOVPE, and the first MBE-attempt was reported by Hoke *et al.*[69] As InN dissociats at relatively lower temperature ($\approx$ 550 °C) than other III-nitrides, MBE is the best growth technique over MOVPE for obtaining high quality material. The main advantage of MBE growth of InN over other techniques is that nitrogen can be activated using plasma irrespective of the substrate temperature. In the case of MOVPE/MOCVD, pyrolysis of NH_3 demands very high substrate temperature, where InN dissociates easily and results in a bad quality material with the formation of In droplets on film surface[21]. Moreover, InN growth is very difficult among III-nitrides due to extremely high equilibrium vapour pressure of nitrogen and the lack of lattice-matched substrates as discussed in earlier section 1.5.

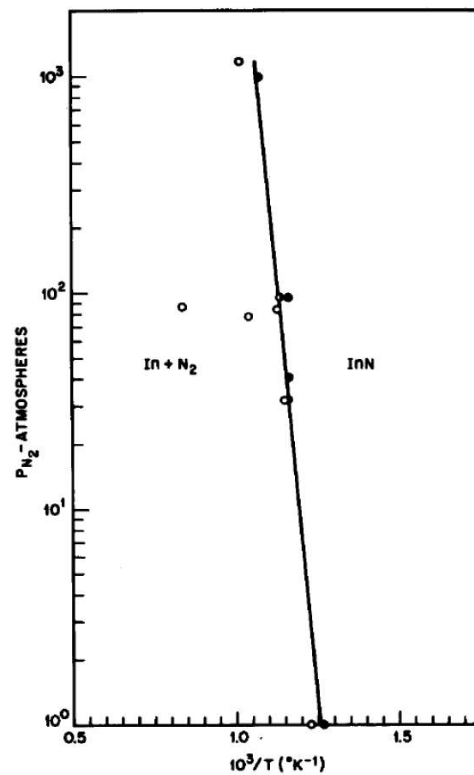

Figure 2.1: Phase relations of InN shown by decomposition curve separating InN and In+N_2 phase fields. Open circles represent experimental conditions where metallic indium was observed. Shaded circles indicate that InN was stable, while half shaded circles indicate that both In and InN are present.[70]

In the 1970's, McChesney *et al.* reported the dissociation pressure of InN as extremely high and stated that the formation of InN may require interaction of indium metal with

atomic or other excited nitrogen species at high temperature high pressures.[70] They showed that the phase relation of InN results in a P-T^{-1} relation as depicted Fig 2.1 according to

$$\Delta H_F = -\frac{1}{2} R \frac{dlnP_{N_2}}{d(1/T)} \quad (2.1)$$

where ΔH_F is reaction enthalpy (Kcal/mole), R is gas constant, P is dissociation pressure and T is temperature. In which the dissociation pressure rises very steeply towards higher nitrogen pressure. Another report by Trainor and Rose in 1974 argued that partial pressure of atomic nitrogen, rather than diatomic nitrogen, is a more fundamental parameter describing thermal equilibrium.[65] The thermal stability studies of InN indicated that InN samples decomposed in a few minutes leaving an indium residue in N_2 (at standard pressure) at 500 °C during the annealing process. However, if the InN samples were heated to 500 °C in nitrogen pressure (10^{-3} torr) InN would not decompose. The stability of InN films can be achieved by thermal dissociation of N_2. Trainor and Rose found the fundamental band edge for InN films to be 1.7 eV and their absorption study suggested that InN is a direct band gap semiconductor, due to the similarity in the shape of fundamental absorption edge to that of GaN. InN samples grown on sapphire by reactive evaporation had a Hall mobility of 20 cm^2/Vs and carrier concentration $\approx 10^{20}$ cm^{-3}. They also suggested that higher quality films could be achieved by growing the films at higher temperatures (600 °C) and lower growth rates. Hovel and Cuomo[71] produced polycrystalline InN films grown on sapphire and silicon substrates by RF sputtering with reasonably good electrical properties (Hall mobility =250 ± 50 cm^2/Vs, and n-type carrier concentration 5.8×10^{18} cm^{-3}) by reactive radio frequency (RF) sputtering. The InN films appeared dark red and possessed a resistivity in the range of 10 Ωcm. Marasina *et al.*[72] utilized chemical vapor deposition to produce InN epitaxial layers with an electron concentration of 2×10^{20}-$8\times10^{21}cm^{-3}$ and a mobility of 50-30 cm^2/Vs. They reported that the disassociation of InN rapidly occurred at 600 °C, and there was no deposition of InN layers above 670 °C and for lower growth rates.

In the 1980's the properties of InN films grown via metallic Indium in a nitrogen environment were mainly studied by Tansley and Foley, who reported an electron mobility as high as 5000 cm^2/Vs and a low background carrier concentration in the InN film ($5\times10^{16}cm^{-3}$). Those results were early indicators of the potential of InN for high mobility

FET devices. However, the optical absorption data of InN samples prepared by reactive RF sputtering indicate an optical absorption edge at 1.89 eV. Recently [73], epitaxial single-phase InN films are grown on (0001) sapphire in the temperature range of 400-600 °C by microwave-excited metal organic vapor phase epitaxy (MOVPE) using $(CH_3)_3In$ and pure atomic nitrogen or excited nitrogen species supplied by microwave discharge of N_2. It was shown that (0002) InN layers could be grown on (0001) sapphire at temperatures around 500 °C.

More recent publications, mostly describing molecular beam epitaxy (MBE) InN layers, indicate a lower energy band gap, initially reported at around 1.1 eV [74] (Mg-doped InN samples), but later progressively lower values of 0.9 eV [75] and then 0.8-0.7 eV [25,76] were reported. Recently, a band gap value of 0.65eV [77] has been proposed. These studies include growth by MOVPE and MBE on different substrates and underlying layers over a wide range of growth conditions. The highest mobility and lowest background concentration reported upto now are 2000 cm^2/Vs and $3.6\times10^{17}cm^{-3}$ for $\approx$1.2 μm InN layers grown by MBE.[78,79] The first growth of InN at high pressures was made by Dietz *et al.* in a High Pressure Chemical Vapor Deposition (HPCVD) system developed at Georgia State University.[80]

2.1.2 Structural properties

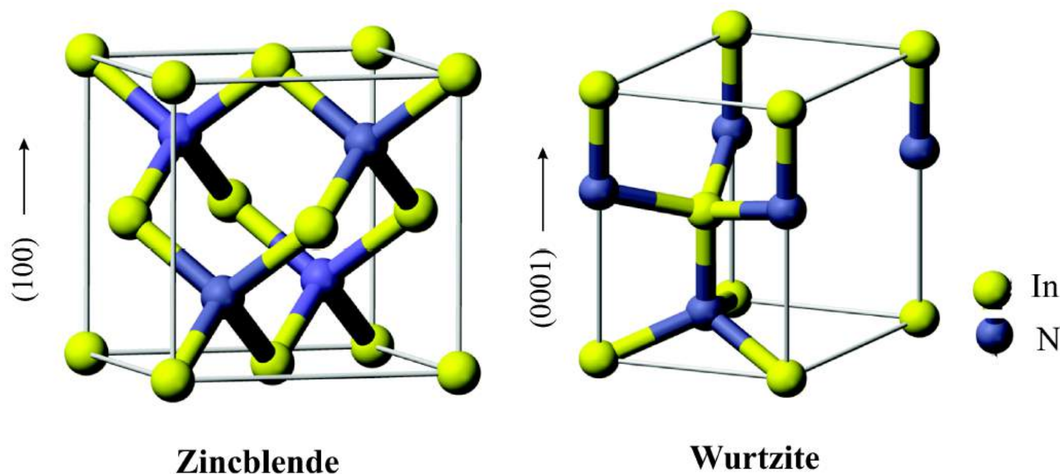

Figure 2.2: Crystal structures of zincblende and wurtzite InN.†

It is essential to know and characterize the crystal structure of the InN in order to improve the quality and performance of the InN based device structures. X-ray diffraction

†http://en.wikipedia.org/wiki/Zinc_sulfide

(XRD) is a versatile non-destructive technique, which reveals detailed information about the chemical composition and crystallographic structure of any natural and manufactured material. The crystal and microstructure of InN films, which may include dislocations, grain boundaries etc., are typically investigated by X-ray diffraction and transmission electron microscopy (TEM) while, Rutherford back scattering spectrometry (RBS) measurements are used to assess film stoichiometry, Low energy electron diffraction (LEED) is a technique used to analyze the crystal structure of the surface. By using all the structural characterization techniques mentioned above, it has been shown in the literature that the crystal structure of indium nitride epitaxial layers is similar to that of GaN films prepared under similar conditions. InN can crystallize in three different structures, wurtzite, zincblende and rock salt, similar to that of other nitrides. Thermodynamically, the stable crystal structure is the hexagonal wurtzite structure. However, InN can also be obtained in the cubic zincblende structures when grown on (001) crystal planes of cubic substrates like silicon and GaAs. The wurzite structure has a hexagonal unit cell and thus two lattice constants c and a, and contains six atoms of each type. The zincblende structure has a cubic unit cell, containing four indium atoms and four nitrogen atoms. In both cubic and hexagonal crystal structures, each indium atom is coordinated by four nitrogen atoms and each nitrogen atom is coordinated by four indium atoms as shown in the Fig 2.2. The main difference between the cubic and the hexagonal structure is that they have a different stacking sequence of the closest packed diatomic planes.

The lattice constant values of InN may be influenced by the growth conditions, impurity concentrations, and the film stoichiometry. Juza and Hahn[14] first reported the crystal structure of InN to be wurtzite having lattice parameters a = 3.53 Å, and c = 5.69 Å. These values are quite close to a = 3.5480 Å, c = 5.7600 Å reported by Tansley & Foley[81], and a = 3.544 Å, c = 5.718 Å reported by Osamura *et al.*[82]

2.2 Growth parameter dependence

The mobility, carrier concentration, band gap values and other growth parameters of the InN thin films which are grown by using different growth techniques on various substrates and by employing various growth schemes are listed in the Table 2.1.

Table 2.1: Literature overview of various growth conditions and properties of InN

Year	Substrate	Growth Method	Mobility (cm^2/V-sec)	n (cm^{-3})	d (μm)	T_s (°C)	E_g (eV)	Ref.
1972	Sapphire, Silicon	RF sputt.	250	$5\text{-}8\times10^{18}$	20-5	500	high Eg	71
1974	Sapphire	e-beam evap.	20	5×10^{18}	-	380	high	65
1980	Sapphire	RF sputt.	20	5×10^{18}	-	-	1.7-2.85	83
1984	Silicon or Glass	RF sputt.	5000	5×10^{16}	0.1-2	-	high	66
1988	Glass and Quartz	Mag. sputt.	10	6×10^{20}	0.6	127	1.7	84
1994	-	Theory	4400	1×10^{17}	-	-	-	29
1999	InN buffer/N/Sapphire	MBE	700	5×10^{19}	0.7	350-500	-	85
2000	AlN/Sapphire	MEE-MBE	500	3×10^{18}	0.2	360 - 590	-	86
2000	InN buffer/Sapphire	PAMBE	600	$\sim1\times10^{20}$	-	470	2	87
2001	GaN/N/Sapphire	MOMBE	500	8.8×10^{18}	0.3	475-525	-	88
2001	InN buffer/Sapphire	ECR-MBE	1700	5×10^{19}	1	470	0.89	74
2001	AlN/N/Sapphire	MEE-MBE	805	5.1×10^{18}	0.12	460	-	89
2002	InN buffer/N/Sapphire	MBE	1900	8×10^{18}	0.3-0.7	450-470	0.9	75
2002	InNbuffer/N/Sapphire	MBE	600	2.8×10^{19}	0.22	550	1.89	90
2002	AlN/Sapphire	MBE	1055	3.5×10^{18}	0.45	460	-	91
2002	GaAs	Mag. sputt.	40	4×10^{20}	1.53	400	1.9eV	92
2002	InN buffer/N/Sapphire	MBE	830	1×10^{19}	0.6	550	-	93
2002	InN buffer/N/Sapphire	RF-MBE	-	3.8×10^{19}	0.3	460-550	0.78eV	94
2002	GaN/Sapphire	MBE	2050	3.5×10^{17}	0.2-7	-	-	76
2002	AlN/Sapphire	MBE	615	5.48×10^{18}	0.12-1.0	360 -590	0.78eV	27
2002	GaN/Sapphire	MOVPE	250	1×10^{19}	0.5	400-600	1.9eV	95
2003	Sapphire	MBE	700	10^{18}	-	450-650	0.7-2eV	96
2003	GaN/Sapphire	MBE	1400	1.6×10^{18}	0.25	300-500	-	97
2003	InNbuff/N/Sapphire	MBE	1130	4.9×10^{18}	1.5	460-550	0.75eV	25
2003	N/Sapphire	MOVPE	730	5.8×10^{18}	0.5	450-650	0.7-0.9eV	98
2003	GaN(250nm)/Sapphire	MBE	2050	3.5×10^{17}	7.5	-	0.64-0.74	99
2003	GaN/Sapphire	MBE	-	5×10^{17}	1	-	-	100
2003	InN buffer/GaN	MBE	1380	1.6×10^{18}	0.25	480	0.6-0.7	101
2003	InN/AlN	MBE	780		0.5-0.8	500	1.9	102
2004	InN/GaN	MOVPE	1100	1×10^{19}	< 0.5	450	0.78	103

Year	Substrate	Growth Method	Mobility (cm^2/V-sec)	n (cm^{-3})	d (μm)	T_s (°C)	E_g (eV)	Ref.
2004	AlN/Sapphire	MBE	1113	2.1×10^{18}	0.8	-	-	104
2005	AlN/N/Sapphire	MBE	2000	3.6×10^{17}	12	460	0.67	78
2005	InN/InGaN/AlN/Sapphire	MBE	2050	3.5×10^{17}	7.5	470	0.6	105
2005	Sapphire	RPECVD	182	7.6×10^{19}	3.7	440	0.9	106
2005	GaN/AlN/Sapphire	MBE	1000	high 10^{17}	2	-	0.7	107
2006	N/Sapphire	RFMBE	1130	3×10^{18}	2-3	300-600	0.77	108
2006	GaN/Sapphire	MBE	2200	3×10^{17}	7	-	-	109
2006	GaN/Sapphire	MBE	2370	low 10^{17}	4.4	530	0.62	110
2006	AlN/Sapphire	MBE	1500	-	0.8	380	-	111
2006	InN buffer/N/Sapphire	MBE	1070	5.2×10^{18}	0.75	550	0.74	112
2006	GaN/AlN/Sapphire	MBE	1000	1×10^{18}	0.5	-	-	113
2006	GaN/AlN/Sapphire	MBE	2000	low 10^{17}	1.2	-	-	114
2006	-	Theory	14000	1×10^{15}	-	-	-	115
2006	-	MBE	2000	1×10^{18}	-	-	0.67	116
2006	InN buffer/Sapphire	MBE	1000	$5\text{-}8.9\times10^{18}$	0.8	380		117
2006	AlN/Sapphire	MBE	690	6.8×10^{18}	0.3	520	0.69	118
2007	GaN/Sapphire	MEE-MBE	1140	1.3×10^{18}	1	380	-	119
2007	GaN or AlN/Sapphire	MBE	≈200	1×10^{19}	1.5	-	0.69	120
2007	GaN/Sapphire	MOCVD	1300	4.6×10^{18}	0.5	575	-	121
2008	GaN/Sapphire	PAMBE	1904	1.94×10^{18}	1	450	0.65	122
2008	AlN/Sapphire	MOCVD	1400	7×10^{18}	0.8	510-570	0.76	123
2009	GaN/Sapphire	MBE	1910	5×10^{17}	0.7	400-480	0.67	124
2009	GaN/Sapphire	PAMBE	1300	6.1×10^{18}	0.54	-	-	125
2010	GaN/AlN/Si	MBE	1208	1.35×10^{19}	2	425	-	126
2010	InN/Sapphire	MOCVD	457	9×10^{18}	0.35	520	-	127
2010	GaN/c-SiC	MBE	1420	4.8×10^{17}	2	550	-	47
2012	GaN/Sapphire	MBE	3280	1.47×10^{17}	5	500 -380	-	128
2014	InNbuffer/AlN/N/Sapphire	MBE	1780	1.7×10^{18}	1	540	0.69	129

2.3 Band gap issue

The material properties of InN change dramatically with the growth techniques employed and thus the understanding of this novel semiconductor still remains very poor. During the last decade, there have been several conflicting reports on the band gap of InN; values have varied between 0.6 and 2 eV in different papers.[24,25] Bagayoko and Franklin[130] presented an overview of two groups of experiments that provided different values of the band gap of wurtzite InN. Experiments in the first set, (before year 2000) yielded band gap values of 1.9-2.0 eV, while the later second set gave band gap values of 0.7-1.0 eV, depending on the free carrier concentrations. Samples studied by in the second set, mostly grown by molecular beam epitaxy, were believed to be of much higher quality than those of first set that mostly investigated RF sputter grown polycrystalline films. Inushima *et al.*[74] determined that the band gap of InN grown on sapphire by MBE was between 0.89 and 1.46 eV at respective electron concentrations of 5×10^{19} cm^{-3} and 2×10^{20} cm^{-3}. Kadir *et al.* studied samples of InN grown by metal-organic vapor phase epitaxy (MOVPE), and they reported that the band gap Eg for the InN samples is $\sim$ 0.7 eV.[131] Recently, the Hydride Vapor Phase Epitaxy (HVPE) growth technique has received attention because it is a useful method for growing thick layers of group III-Nitrides.[132,133] Cathodoluminescence (CL) spectrum measurements of single crystalline (0002) InN grown by HVPE exhibit a strong peak at 0.75 eV. In conclusion, InN films grown by Molecular Beam Epitaxy (MBE)[26,27], HVPE and MOVPE[134] revealed that the band gap energy of InN is about 0.7 eV.

Until recently, the band gap energy of $\approx$ 0.7 eV was considered as the fundamental narrow band gap due to measurements by infrared photoluminescence (PL) and optical absorption of InN grown by MBE, MOCVD, and HVPE. However, the growth of high quality InN layers and related indium rich III-N alloys remains difficult due to InN stoichiometric instabilities, limited carrier concentration and low dissociation temperatures, leading to inconsistent and process dependent material properties.[1] Nevertheless, Butcher *et al.*[106] have shown that In:N stoichiometry affects the apparent band gap of the InN film very strongly, and evaluation of stoichiometry variations in InN films (MBE grown and Remote Plasma Assisted Chemical vapor deposition (RPECVD))

suggests that these films should not to be treated as homogenous materials. For instance, the electron carrier concentration dependence of the optical absorption edge for epitaxial material does not follow the Moss-Burstein effect for InN samples grown by different techniques.[135,136]

In degenerate narrow direct bandgap semiconductors the direct transitions, which take place from the valence band maximum to above the Fermi level that situated deep inside the conduction band as the levels below it are completely occupied, result in Moss-Burstein effect or band filling effect which is schematically shown in Fig 2.3(a). This effect can be understood by means of optical absorption measurements. The absorption coefficient (α) is determined from transmission measurements, using the expression $\alpha(E) = C(E - E_g)^{1/2}$ where E_g is the bandgap of the material. The direct optical band gap is determined by the standard procedure of plotting the squared absorption coefficient versus energy and then by extrapolating the linear leading edge to the zero value of the squared absorption coefficient.[137] Fig 2.3(b) shows the apparent change in the band gap of InN materials grown by different techniques.

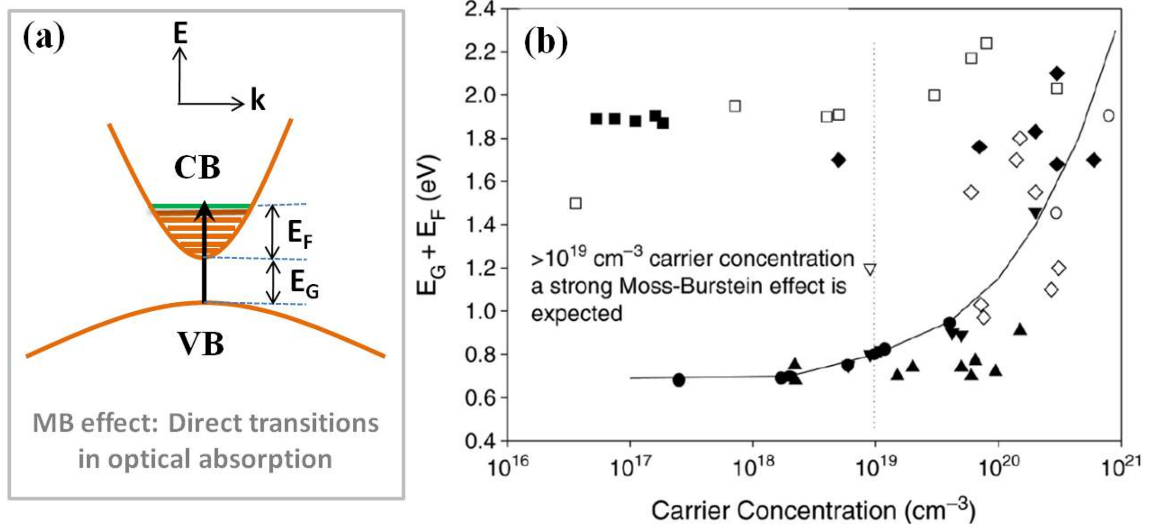

Figure 2.3: (a) shows the schematic for direct transitions that take place in optical absorption due to Moss-Burstein effect and (b) shows various reported band gap values for InN in literature. Continuous curve represents the theoretical prediction of Moss-Burstein effect.[23]

The reported high bandgap values with low carrier concentration from the earlier work by Tansley and Foley[81] using RF-sputtering, but since have not been reproduced in the literature. There is a possibility of continuous alloying or mixture of indium oxide

and indium nitride, which as per effective medium theory can result in an in-between bandgap value. It has been shown that indium oxide shows a very weak dependence of bandgap with carrier concentration as seen in Fig 2.3(b) by Tansley and Foley. Alevi et al.[138] have used their data of the bandgap variation with carrier concentration for their HPCVD grown InN/GaN/Sapphire samples, and show that the fundamental bandgap of InN is about 1.20eV, which is higher than the recent reported value.[22] A parabolic conduction band has been used in many reports to derive the Moss-Burstein shift. A carrier concentration dependent effective mass resulting from non-parabolic conduction band has been much argued for InN[139] which is based on the experimental observation that effective mass varies with carrier concentration. It has been observed that, depending on the crystallinity of the samples, the carrier concentration changes and hence effective mass can be varied. For narrow band gap semiconductors, since the conduction band edge gets modified because of the interaction between valence and conduction bands, later on a non-parabolic conduction band calculated using **k.p** band structure evaluation method solving Kanes two band **k.p** model[140].

2.4 Surface electron accumulation

Surface electron accumulation is observed to be an intrinsic property of the InN epitaxial layer. Recently, this surface electron accumulation phenomenon on InN layers has attracted much attention because the high density of electrons on the surface is important for formation of Ohmic contacts. However, the main cause of electron accumulation on the InN surface and how it is related to the surface atomic configuration are still not clear. We can find several explanations for surface electron accumulation on semiconductor surfaces reported in the literature. Electron accumulation layers at the semiconductor surfaces have been observed through techniques that include high resolution electron energy loss spectroscopy[141], angle-resolved photoemission spectroscopy[142] and electron tunneling spectroscopy.[143] Surface electron accumulation is not only observed in InN layers but also observed in InAs, InSb and recently In_2O_3.[145,147] The main reason for surface electron accumulation on InAs layer is the donor like intrinsic surface states whose energy spectrum is determined by the surface reconstructions.[148] Initially, researchers observed this surface charge accumulation on InAs surfaces and

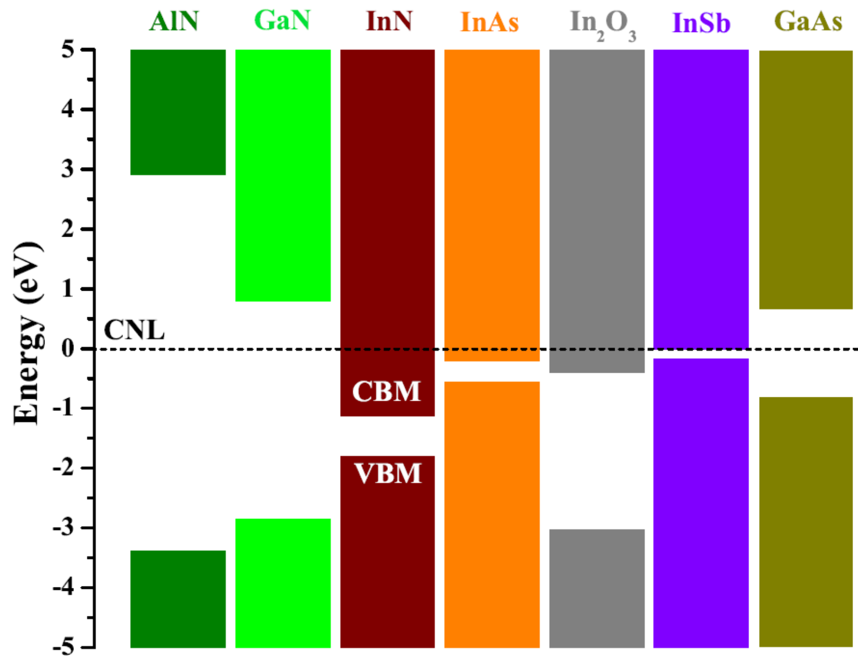

Figure 2.4: The position of the conduction band minimum (CBM) and the valence band maximum (VBM) *w.r.t* the charge neutrality level (CNL) for AlN, GaN, InN, InAs, In_2O_3, InSb and GaAs. For InN, InAs, In_2O_3 and InSb, the CNL is situated in the conduction band.[144–146]

later on InN and on single crystalline undoped In_2O_3 surfaces and attributed it to native surface defects. Other reason is that when the charge neutrality level (CNL) situates above the conduction band minimum (CBM), charge accumulates on the surface. The Fermi level stabilization or Charge Nuetrality Level positions for InAs, InN, and In_2O_3, InSb are reported to be ≈0.2 eV, ≈1.2 eV, ≈0.4eV and ≈0.06eV respectively, above the conduction band minimum, where as, for other semiconductors it lies within the band gap (below the conduction band minimum)[144,145], as shown in the Fig 2.4. Yamaguchi *et al.* have reported that electron accumulation on InAs/GaAs depends on the layer thickness and is induced by the quantum size effect.[149] They also have suggested that the dislocations due to lattice mismatch at the InAs/GaAs interface may also be responsible for surface electron accumulation. The phenomenon of surface electron accumulation on InN layers was first observed by Mahboob *et al.* by using (HREELS).[150] According to their report, an intrinsic surface electron accumulation layer is found to exist and is explained in terms of a particularly low -point conduction band minimum in wurtzite InN. The electron accumulation is a consequence of ionized donor type surface states pinning the surface Fermi level above the conduction band minimum. Piper *et al.*[114]

have calculated energy positions of -point, conduction band minimum and valence band maximum of AlN, GaN and InN with respect to the branch point energy and concluded that the conduction band minimum lies far below the branch point energy and is the cause of electron accumulation in InN layers. Experimentally, surface electron accumulation has been observed for both polar and non-polar surfaces, while it was absent on *in-situ* cleaved non-polar InN surfaces.[151,152] D. Segev and C. G. Van De Walle have reported that the cause of electron accumulation on polar InN is In-In bonds leading to occupied surface states above the conduction band minimum.[153] In recent results from angle resolved photoelectron spectroscopy of InN, it has been reported that the electrons in the accumulation layers reside in discrete quantum well states, defined perpendicular to the film surface.[154] By using electron tunneling spectroscopy, Veal *et al.* also have reported the native electron accumulation layer at the surface of n-type InN.[143]

2.5 Overview of InN mobility

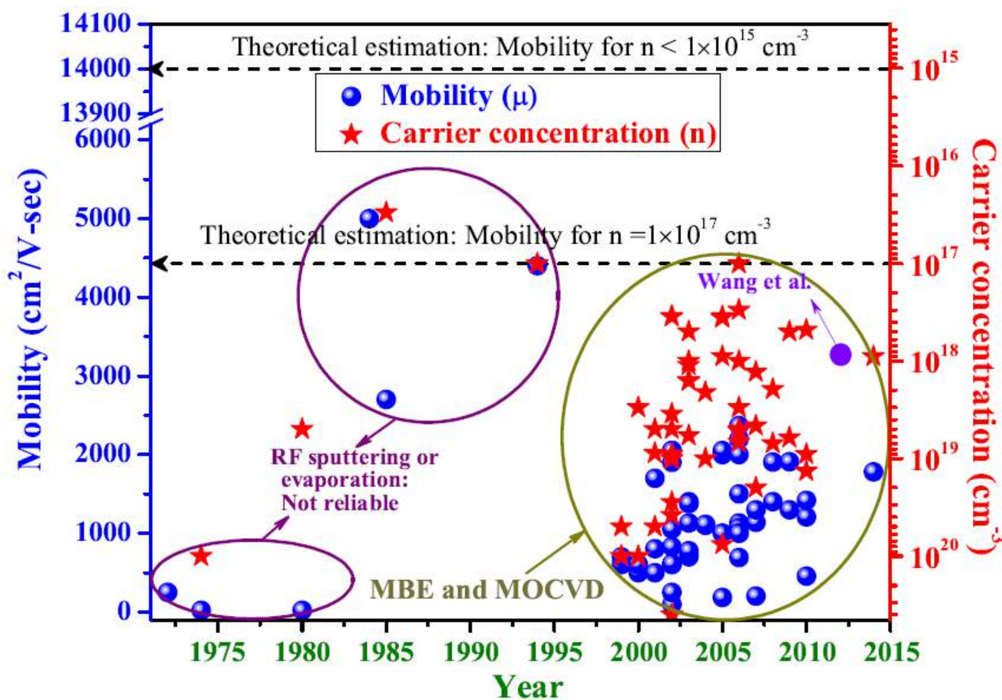

Figure 2.5: Fig shows literature survey of mobility and carrier concentration in the last few decades.

In order to understand year wise improvement of electron mobiltiy and concentration measurements of InN thin films grown by various techniques, the values from literature are listed in Table 2.1 and consolidated into year versus mobility and carrier concentration

plot as shown in the Fig 2.5. Until late 1980's, very few data points where the InN thin films were grown by rough vacuum techniques like sputtering and evaporation existed. However, these films exhibit very high electron mobility and low carrier concentration than the state of art of the films, which were later not reproduced in the literature. Unfortunately, these points are not reliable since the films not grown under high vacuum conditions and there is a huge probability of the incorporation of oxygen and other impurities which do not yield high quality InN material as discussed in many reviews and articles[21,23,116]. In the 1990's owing to the advancement in the growth techniques such as MBE and MOCVD, researchers have achieved reasonably high mobility and low carrier concentration values. Using MBE, growth of high quality InN material is possible, though there are many difficulties in synthesis as discussed in the previous chapter. Till date highest mobility reported in the literature is 3280 cm^2/V-s, by Wang *et al.*[128] where films of 5μm thickness at reduced dislocation density are grown on GaN buffer by employing a gradient growth temperature. However, theoretically estimated mobility is still far away from the experimentally obtained values. The theoretically estimated mobility values are ≈4400 and ≈ 15000 cm^2/V-s for the carrier concentration values of $\approx 1 \times 10^{17}$ and $< 1 \times 10^{15} cm^{-3}$ respectively[115], which are represented in the Fig 2.5 by dashed arrows. Thus, still there is a huge opportunity to improve the material quality towards the theoretically predicted mobility.

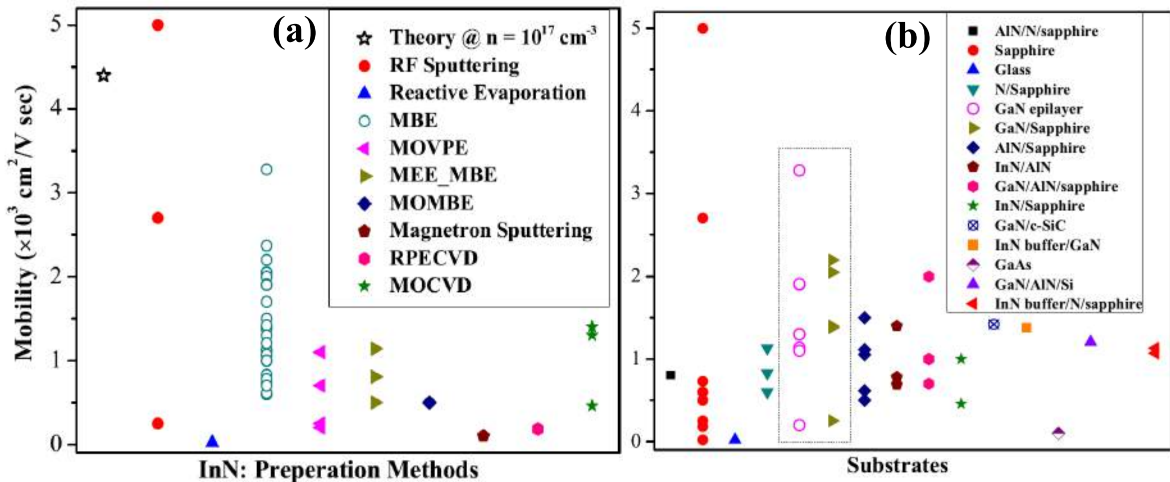

Figure 2.6: Fig shows literature survey of Mobility plotted versus (a) preparation methods and (b) substrates used for InN growth.

Fig 2.6(a) shows literature survey (summarized in Table 2.1) of Mobility plotted versus preparation methods, which infers that the most of InN films in the literature are grown by

MBE and a few films by other methods like MOVPE and MOCVD. For InN growth, MBE is the most preferable and convenient technique since the substrate temperature here is completely independent of the nitrogen source unlike other methods. Also since MBE growth takes place in UHV base pressure conditions, oxygen incorporation and consequent ambiguity in understanding fundamental properties can be discounted. The reported electron mobility is as high as 3280 cm^2/V-s for the films grown by MBE (excluding the irreproducible RF sputtered films), whereas films grown by other methods could attain mobility values upto ≈1500 cm^2/V-s. From the Fig 2.6(b), it is clear that most of InN films were grown on GaN thick epi or thin buffer layers. The high mobility values are obtained for the films grown on GaN/sapphire substrates which could be due to the less lattice mismatch between InN and GaN (see Table 1.1). The InN films grown on AlN also show high mobility but not as higher than the films grown on GaN templates.

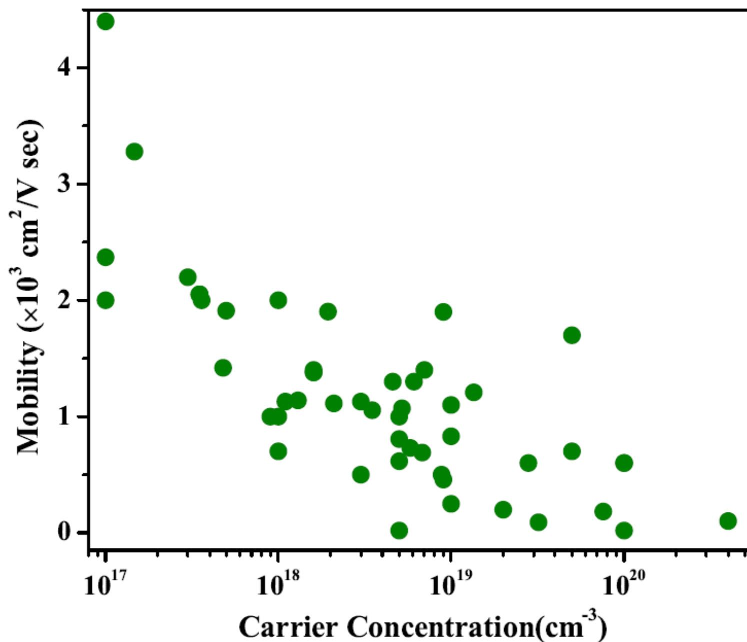

Figure 2.7: Fig shows literature survey of Mobility plotted versus carrier concentration.

To further examine the relationship between the Hall electron mobility and carrier concentration of InN films, all the Hall data from Table 2.1 are summarized in Fig 2.7, which include the data of InN films grown with different buffer-layer treatments, growth methods and varied substrate temperatures. From Fig 2.7, it is clear that in order to achieve InN films with higher mobility, the carrier concentration should be less than $2{\times}10^{17}$, and thus more attention is needed to understand the origin of the unintentional background doping of InN[86].

Chapter 3

Experimental techniques

Since our motivation of this work is to understand the dependence of the properties of InN films on the growth parameters, we use the sophisticated MBE growth technique and then several characterization methods. This chapter provides the basic information of the various experimental methods used in this study and provides the physical background of the apparatus used for both synthesis and characterization.

3.1 Growth: Molecular Beam Epitaxy

Epitaxy comes from a Greek root (epi- above and taxis- in ordered manner), and means deposition of a single crystalline film on a single crystalline substrate, such that there is a geometrical relationship between the two respective unitcells, such deposited films are called as the epitaxial films or epitaxial layers or epilayers. Epitaxial films can be grown from precursors that are in the form of either gas, liquid or solids. Since the substrate acts as a seed crystal, the overgrown layer takes on a lattice structure and orientation identical or closely related to that of the substrate. In this epitaxial growth, the layer can be deposited on a substrate of the same or different composition, which are called as homo or heteroepitaxial growth processes, respectively.

At Bell Telephone Laboratories, Alfred Y. Cho used the term MBE[155] in 1970 after extensive work on epitaxial films by Davey and Pankey[156], Shelton and Cho, and Arthur[157]. MBE growth includes the interaction of a single or multiple molecular or

atomic beams at the surface of a heated crystalline substrate, in an ultra-high vacuum chamber maintained at the base pressure of ∼10^{-11} torr. At this pressure the mean free path of the ambient gas particle is approximately 40 km and thus provides a clean environment for deposition and film formation. The low background pressure also provides the best available purity, because the arrival rates of contaminants are significant orders of magnitude less than typical chemical vapour deposition conditions. Unlike other deposition techniques, MBE growth provides impurity-free, high quality films with abrupt layer interfaces.[158] Fig 3.1(b) is a schematic of a typical MBE system.[159]

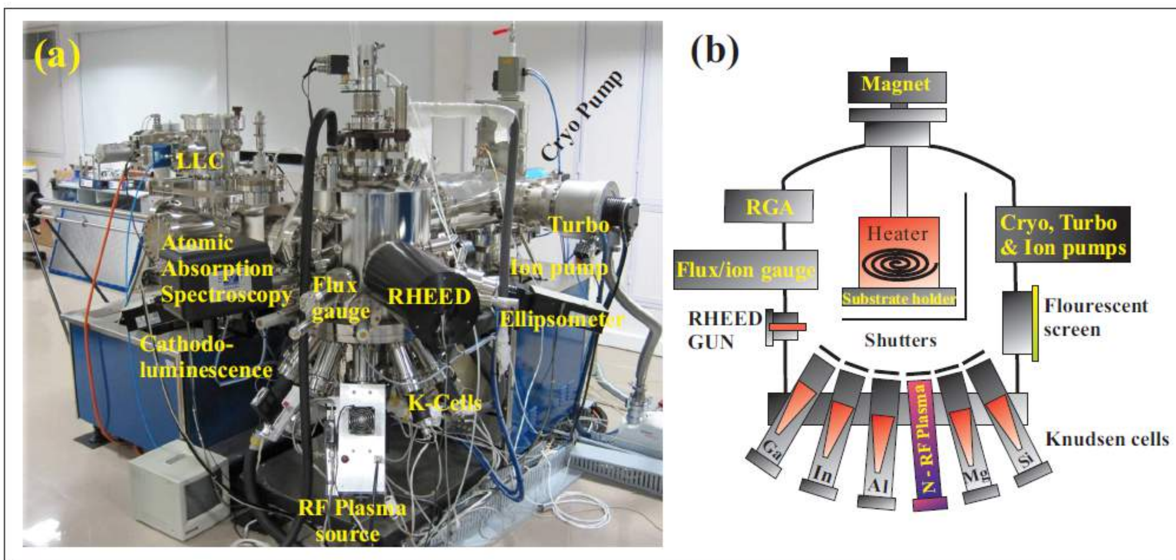

Figure 3.1: (a) shows MBE growth system used to grow III-nitride thin films and (b) shows the schematic diagram for the growth chamber, *modified figure.*[159]

Fig 3.1(a) and (b) show nitride PAMBE (SVTA-USA) system at JNCASR and a schematic of the growth chamber. The system is evacuated by turbo, ion and cryo pumps (cryo and turbo pumped exclusively during the growth) which results in a base pressure of high 10^{-11} Torr as measured using Bayard Alpert type ionization gauge. The main chamber consisting of a cryo panel around it, is cooled with LN_2 which prevents degassing of atoms from the chamber walls, thus also acting as a cryo pump. The growth manipulator which can heat the substrate upto 1200 °C, is cooled by water during growth. The rotations of growth manipulator is controlled by the magnet assembly attached to a motor. This motor controller is equipped with an ON/OFF switch and a knob that is used to adjust the speed from 0-60 rpm. Samples can be transferred in and out of the system through the turbo connected load-lock chamber. The preparation

chamber has a water-cooled sample heating/degassing facility up to 700 °C and also has a cathodoluminescence facility. Active nitrogen radicals are supplied by a radio frequency inductively coupled plasma source. III group (In, Ga and Al) and dopant (Si and Mg) metallic species are supplied by effusion cells. Shutters placed in front of the III-V sources permit direct control of the epitaxial growth surface at a monolayer level by changing the incoming beam with the opening and closing of the shutter. Growth can be monitored *in-situ* by a reflection high energy electron diffraction (RHEED) Staib Instruments system. Upto 3 inch substrates can be mounted on the growth stage achieving a growth uniformity of $<1\%$ over the diameter of 2.8 inch. Growth temperature can be controlled by a high temperature heater capable of temperatures $\approx$ 1200 °C. The substrate temperature is monitored by a thermocouple and a pyrometer. Growth temperatures were calibrated using a silicon/aluminum eutectic using the pyrometer. Flux rates are frequently calibrated using Accu Flux atomic absorption system, Flux gauge and QCTM which are assembled in growth chamber. The operation of the MBE system can be carried out through the panel control board as well as computer automation. The absence of carrier gases as well as the ultra high vacuum environment allows the growth of high purity thin films. In case, any part of MBE is reassembled for troubleshooting purpose, the system has to be baked at 200 °C for atleast 48hrs to remove water and other contamination, before film deposition.

3.1.1 Effusion cells

Water cooled standard effusion cells (Knudsen cells) were used to supply indium, gallium, aluminum, silicon and magnesium flux. Crucibles were made up of pyrolytic boron nitride and prior to the loading of charge, were outgassed at 1400 °C. High purity 99.9999% metal ingots are used in the cells. Once loaded with metal, all effusion cells were again briefly outgassed to approximately 10% above the maximum intended operating temperature with both the K-cell and substrate shutters. The flux from effusion cells is well calibrated by a quartz crystal thickness monitor (QCTM), Accu Flux monitor and Flux gauge. A QCTM is a water cooled quartz crystal placed close to the growth position in the MBE system. Flux can be calibrated by monitoring the change in characteristic oscillation frequency of the crystal due to increase in mass while deposition.

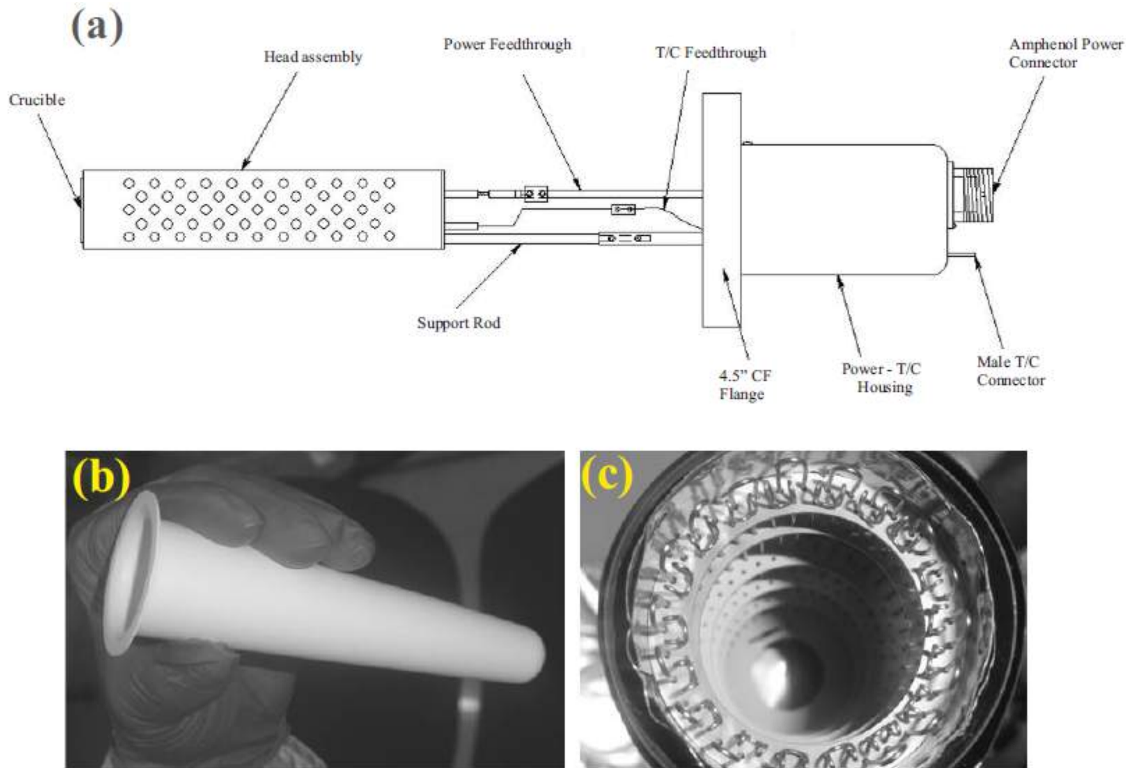

Figure 3.2: shows SVTA schematic diagram of (a) Effusion cell, (b) photo copies of PBN crucible where charge is loaded and (c) Effusion cell heater.

This technique was used to quantify fuxes for In, Ga, Al, Si and Mg in this system using the appropriate tooling factor. These flux rate (F) values are well matched with the theoretical values that are obtained using the following equation.[160]

$$F(cm^{-2}s^{-1}) = 4.7 \times 10^{20} \times \frac{p(Torr)}{\eta} \times \frac{T(K)}{M(amu)}^{1/2} \tag{3.1}$$

where p is the pressure reading of the ion gauge, η is the ionization efficiency given by the empirical relation $\eta \approx 0.6(Z/14) + 0.4$, where Z is the number of electrons in atom or molecule, the quantities T and M are the effusion cell temperature and the atomic (or molecular) mass of the beam species.

3.1.2 Nitrogen Plasma Source

As the common form of nitrogen is inert at achievable growth temperatures, a plasma or ion source is required to activate the N_2 molecule. The primary source used in this work was a radio frequency inductively coupled plasma source (RF-ICP). All nitrogen

which flowed into the RF-ICP was filtered by a Aeronex Gate Keeper nickel inert gas filter, and the flow was moderated by a 0-10 sccm mass flow controller. Nitrogen is controllably leaked into the cavity via an inlet, and the water cooled coil couples the RF signal into the cavity via a magnetic field which is most intense at the centre of the cavity. The alternating field accelerates charged particles which collide further with other species and a plasma is formed. Typically the source was operated at RF powers of 150-450 W and a flow rate of 2-8 sccm for film growth. The forward and reflected powers can be varied, and there is also a deflection plate that can be used to deflect other charged species.

3.1.3 Residual Gas Analyzer

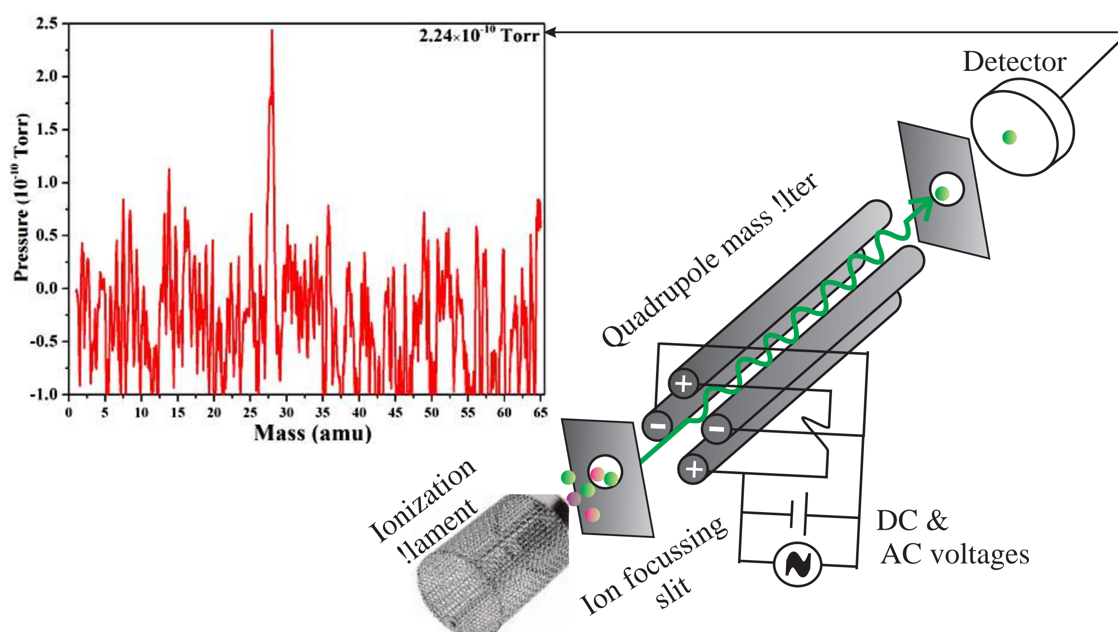

Figure 3.3: shows schematic diagram of RGA [161] and RGA scan of the background vacuum obtained in our spectrum, before the commencement of film growth.

Mass spectrometers use the difference in mass-to-charge ratio (m/e) of ionized atoms or molecules to separate them from each other. Operation of a quadrupole mass spectrometer used in our studies, consists of a long-life, dual thoriated-iridium (ThO_2/Ir) filament as source of electrons. An electron from the beam knocks an electron off the background residual gas molecules to create ions, that are directed into a quadrupole mass filter consisting of four parallel metal rods arranged as in Fig 3.3. Two opposite rods have an applied potential of (V_{dc}+Vcos(ωt)) and the other two rods have a potential of -(V_{dc}+Vcos(ωt)), where V_{dc} is a DC voltage and Vcos(ωt) is an AC voltage. The applied

voltages affect the trajectory of ions traveling down the flight path centered between the four rods. For given DC and AC voltages, only ions of a certain mass-to-charge ratio pass through the quadrupole filter and all other ions are deflected out of their original paths. A mass spectrum is obtained by monitoring the ions passing through the quadrupole filter as the voltages on the rods are varied[161], either by varying ω and holding V_{dc} and V constant, or varying V_{dc} and V (V_{dc}/V is fixed) for a constant ω. A Faraday cup for lower vacuum and a channeltron for higher vacuum are used as detector, allowing partial pressure measurements from 10^{-5} Torr to 5×10^{-11} Torr. The Faraday cup is a metal cup that is placed in the path of the ion beam and attached to an electrometer, which measures the ion-beam current. For increased sensitivity and faster scan rates multichannel, continuous-dynode electron multiplier (Channeltron) is employed. The ion separation power of a mass spectrometer is described by the resolution, which is defined as: $R = \frac{m}{\Delta m}$, where m is the ion mass and Δm is the difference in mass between two resolvable peaks in a mass spectrum. For example, a mass spectrometer with a resolution of 1000 can resolve an ion with a m/e of 100.0 Kg/C from an ion with an m/e of 100.1 Kg/C.

Inset in Fig 3.3 shows the typical RGA spectrum that is acquired in our system while the gate vlaves for all the pumps were opened at the base pressure of growth chamber is high 10^{-11} Torr. Only the presence of a peak at 28 amu is seen, as a result of residual CO and N_2, and indicates the cleanness of the background atmosphere.

3.2 Electron Beam Physical Vapor Deposition

We have also employed an e-beam PVD system for depositing metals onto the III-nitride films in the e-beam evaporation process, the source material is placed in a crucible and a filament below the crucible is heated. By applying a large voltage and magnetic field, electrons are drawn from the filament are made to focus as a beam on the source material. The beam is swept across the surface of the source material to heat all of the material. Advantage of this technique over other physical vapor deposition techniques is evaporating the high melting point materials and to maintain composition of alloys and compounds. In this work, e-beam evaporation technique is frequently used to deposit In

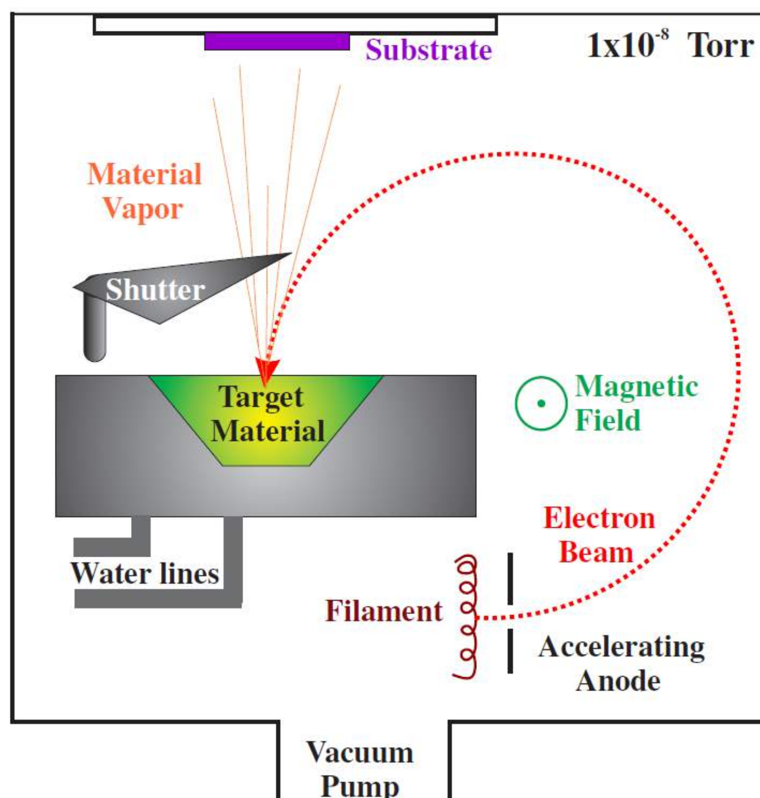

Figure 3.4: shows schematic diagram for e-beam evaporation

or Ag (or any other) metal contact pads to perform electrical measurements.

Characterization techniques

3.3 Reflection High Energy Electron Diffraction

RHEED is a very powerful *in-situ* real time growth monitoring technique. MBE system used for this work has a Staib RHEED system consisting of a high energy electron gun capable of a focussed 10 kV beam energy and a phosphor coated screen with recording camera on the opposite side of the chamber to capture the RHEED pattern, as shown in Fig 3.5. Using RHEED, growth rate, growth mode, surface crystallinity and strain relaxation information can be accessed. This technique utilizes the grazing angle (1-2°) incidence of the high energy electron beam (Fig 3.5a) in which the wavelength of the electrons is comparable to typical atomic spacings (0.1-1 nm) and therefore is a surface sensitive tool. The electrons reflect off different atomic planes, within the first several nanometres of the film and interfere, constructively and destructively to form a

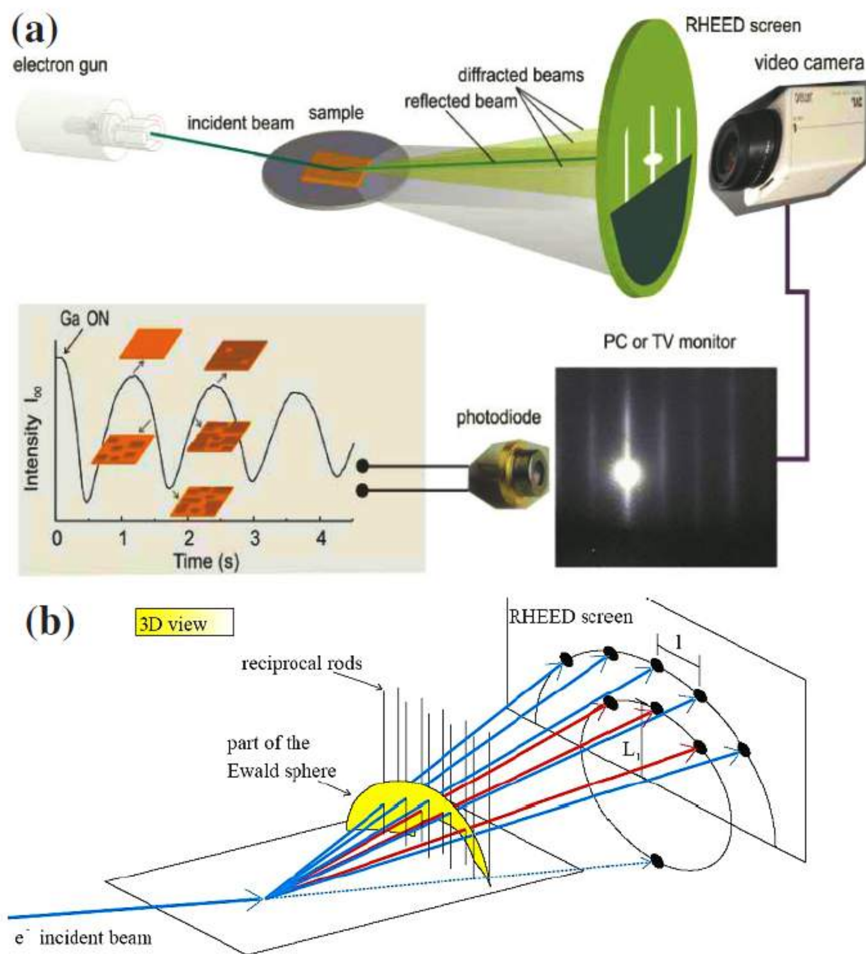

Figure 3.5: (a) The schematic of the RHEED including the representation of the growth rate in mono-layers in terms of the oscillations.[162] (b) shows the 3D representation of the elastically scattered electrons in real space[163] which hit a fluorescent screen in certain spots, along Laue circles (0 in red and 1 in cyan). The pattern depend on the roughness and morphology of the film surface.

diffraction pattern on the phosphor screen. From this diffraction pattern (or RHEED pattern) one can infer structural and morphological properties about the growing crystal. The extensive research in the understanding how different features within RHEED patterns relate to film properties is thoroughly reviewed by Braun[164,165]. Typical RHEED pattern of single crystalline surfaces are dominated by a combination of reciprocal lattice streaks and Kikuchi lines. The shadow edge signifies where the beam is blocked by the film/substrate, and the separation of this and the direct beam represent the angle of incidence of the beam impinging on the film. Typical spot sizes for the electron beam are ≈100 μm, and the spacing of the reciprocal lattice streaks is inversely proportional to the spacing of the atomic planes taking part in diffraction. Whether the streaks appear

continuous or broken can be used to assess the roughness of the growth front, where streaky reciprocal lattice features indicate that the film is smooth on a nm scale and the patterns are due solely to reflection/diffraction. If however, the reciprocal lattice features appear spotty then it indicates there is roughness on the nm scale, through which some electrons are transmitted through surface features and cause an interference pattern (spotty reciprocal lattice features). The growth rate can be determined from RHEED intensity oscillations, for which the period corresponds to one monolayer of growth which is clearly shown in Fig 3.5(b). The surface roughness, and therefore the growth mode, may be discerned from the nature of the RHEED pattern. In this thesis RHEED is primarily used to determine the crystalline nature of the film surface, e.g. poly or single crystal, atomically flat or rough, and to study how strain is accommodated as growth progresses.

3.4 X-ray photoelectron spectroscopy

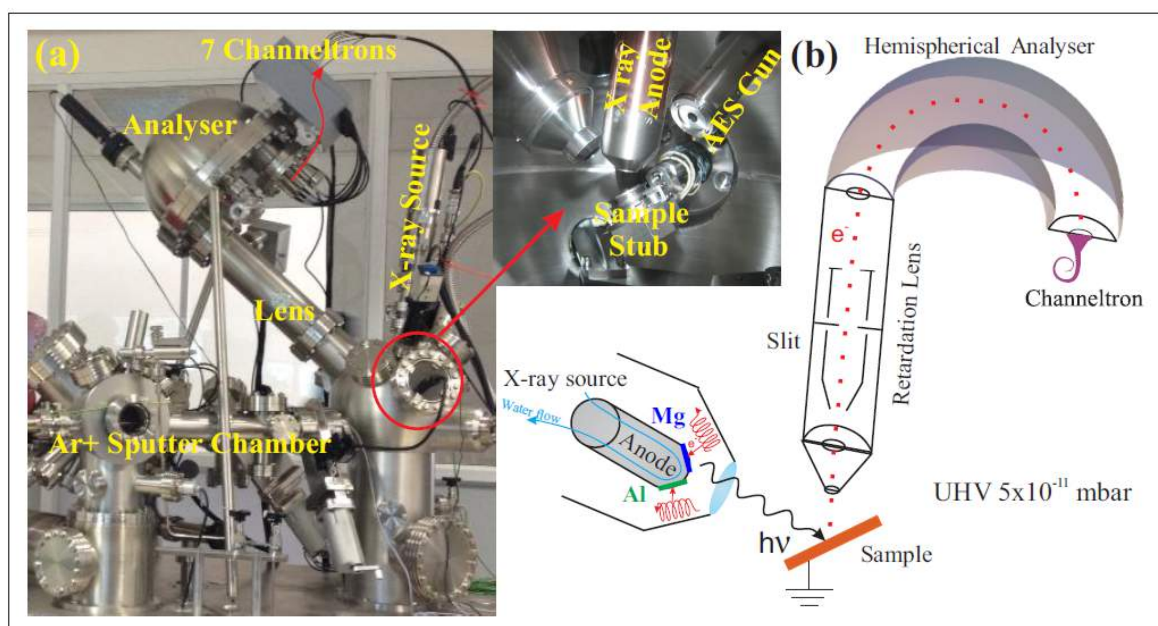

Figure 3.6: shows the XPS system that used for this work and a schematic diagram.

XPS has been widely used to investigate the chemical composition and oxidation state at the sample surface, after it was introduced in the mid 1960s by K. Siegbahn and his research group at the University of Uppsala, Sweden.[166] The basic working principle of

X-ray photoelectron spectroscopy (XPS) or Electron Spectroscopy for Chemical Analysis (ESCA) is photo electric effect outlined by Einstein in 1905. Fig 3.6 shows the Omicron XPS system, in which we have carried out the experiments. XPS is able to detect most of the elements except hydrogen and helium, because of their low sensitivity. For the x-ray sources employed in surface chemical analysis, one normally uses Al or Mg as an anode material, having energy of 1253.6 eV and 1486.6 eV, for Al and Mg, respectively. since most of the core levels are in the 0-1000eV range. The most intense lines are called $K_{\alpha 1}$ and $K_{\alpha 2}$, but often the doublet is viewed as one line and called $K_{\alpha 12}$. The electrons, which are generated by thermionic emission process from a proximal tungsten filament, accelerate on to the high voltage (≈15kV) anode that is coated either with Al and Mg and generates the X-ray photons as shown in Fig 3.6b, concentric hemispherical analyzer (CHA) which acts as a band-pass filter is employed (Fig 3.6) for the collection of the photoelectrons generated, with high resolution. A retarding electrostatic lens-system is placed in front of the hemispheres in order to focus the electrons into the analyzer and to change the angular acceptance or retard the electron energy. The electrons passing through the retarding lens system reach the HSA, which has two concentric hemispheres held at different potentials, and only electrons with kinetic energy within the band of pass energy E_p can pass the analyzer.

Photoemission principle states that if an atom absorbs a photon, an electron from the core shell of the atom will be ejected out from the atom, provided that the photon energy is greater than the sum of that electron binding energy (BE) and the work function (Φ) between Fermi level (E_F) and Vacuum level (E_V). The typical photoemission in the XPS process is shown schematically in Fig 3.7. The resultant kinetic energy, KE, of the photoelectrons and Auger electron with reference to the Fermi level, will be given in Eqn 3.2.

$$KE = h\nu - BE - \Phi \tag{3.2}$$

Although it is the kinetic energy of the outgoing photoelectrons is measured experimentally, spectra are usually displayed on a binding energy scale to allow easy elemental identification. If hν and Φ are known, the measured KE would allow us to obtain the BE of characteristic core levels in the sample. Since each element has unique set of core levels, kinetic energies, this can be used to identify elements from the XPS

spectrum. Chemical shifts in peak position due to charge transfer in different elements provide valuable information on the valence state of elements, The spectra around the Fermi level, also gives useful information of the occupied states in the valence band.

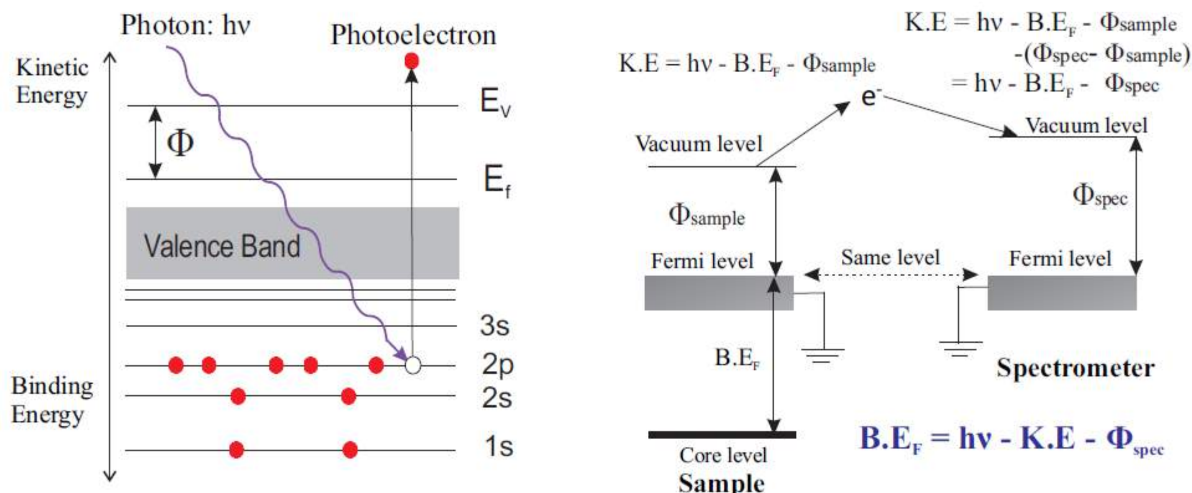

Figure 3.7: shows the schematic diagram of the photoemission process. The vacuum level (E_V) is the energy of an electron at rest (zero kinetic energy) in a vacuum far away from neighbouring particles such that it has no interaction with them. The work function (Φ) of a solid is defined as the minimum energy to remove an electron from the highest occupied energy level in the solid to the vacuum level.

Since special charge compensation techniques are applied, a charging potential for an insulator or semiconductor sample is taken into account. We have employed several ways of using binding energy references. For metallic compounds the Fermi edge is a suitable binding energy reference. A submonolayer gold film is deposited on a sample in order to use the Au(4f) peak as a binding energy reference. C(1s) for graphitic carbon is also employed for internal binding energy calibration. Other suitable reference peaks can be used as well[167,168]. The width ΔE of an XPS peak is defined as a full width at half-maximum (FWHM) of the peak after background subtraction. The width is a combination of several contributions:

$$\Delta E = [\Delta E_n^2 + \Delta E_p^2 + \Delta E_a^2]^{1/2} \tag{3.3}$$

where ΔE_n is the natural width of a core level, ΔE_p is the spectral width of photon source radiation, ΔE_a is the analyzer resolution. Additionally, the peak can be broadened by sample inhomogeneity or by differential charging.[169] The shape of a core-level photoelectron peak depends on a peak type as well as on the insulator or metallic nature

of the sample, and several overlapping components due to the coexistence of different chemical states of the same element. The shape of a peak corresponding to a single chemical component can be determined separately for every chemical compound.[170] The peak shapes are deconvoluted into the Gauss-Lorentz (Voigt) profiles by the Doniach-Sunjic and will be discussed in section 3.4.1. The stoichiometry of the sample surface can be estimated from the area ratio of the XPS peak and the general formula for the XPS peak area[171] is:

$$I = n\ f\ \sigma\ \theta\ y\ \lambda\ A\ T \tag{3.4}$$

where n is the atomic concentration of the element, f is the X-ray flux, σ is the photoelectronic cross-section for the atomic orbital of interest, θ is the angular efficiency factor for the instrumental arrangement, y is the efficiency in the photoelectric process for formation of photoelectrons of the normal photoelectron energy, λ is the mean free path of the photoelectrons in the sample, A is the area of the sample from which photoelectrons are detected, T is the detection efficiency for electrons emitted from the sample. The stoichiometric ratio of two elements A and B can be determined from the peak areas:

$$\frac{n_A}{n_B} = \frac{(I_A/\sigma y \lambda T)_A}{(I_B/\sigma y \lambda T)_B} = \frac{I_A}{S_A} \tag{3.5}$$

Where S_A and S_B are the atomic sensitivity factors for the elements for respective electron transitions, are tabulated and listed in literature.[171] Thus, if the surface has n number of elements then a generalized expression for determination of the atomic fraction (relative percentage composition) of any constituent in a sample can be written as:

$$X_e = \frac{I_e/S_e}{\sum_{i=1}^{n} I_i/S_i} \times 100\% \tag{3.6}$$

where the summation represents over all the constituents of the surface.

3.4.1 XPS data analysis

An X-ray photoelectron spectrum of a solid-state sample always contains a background, which is formed by inelastically scattered photoelectrons. To estimate the peak shape and the stoichiometry from an experimental spectrum, first the background should be

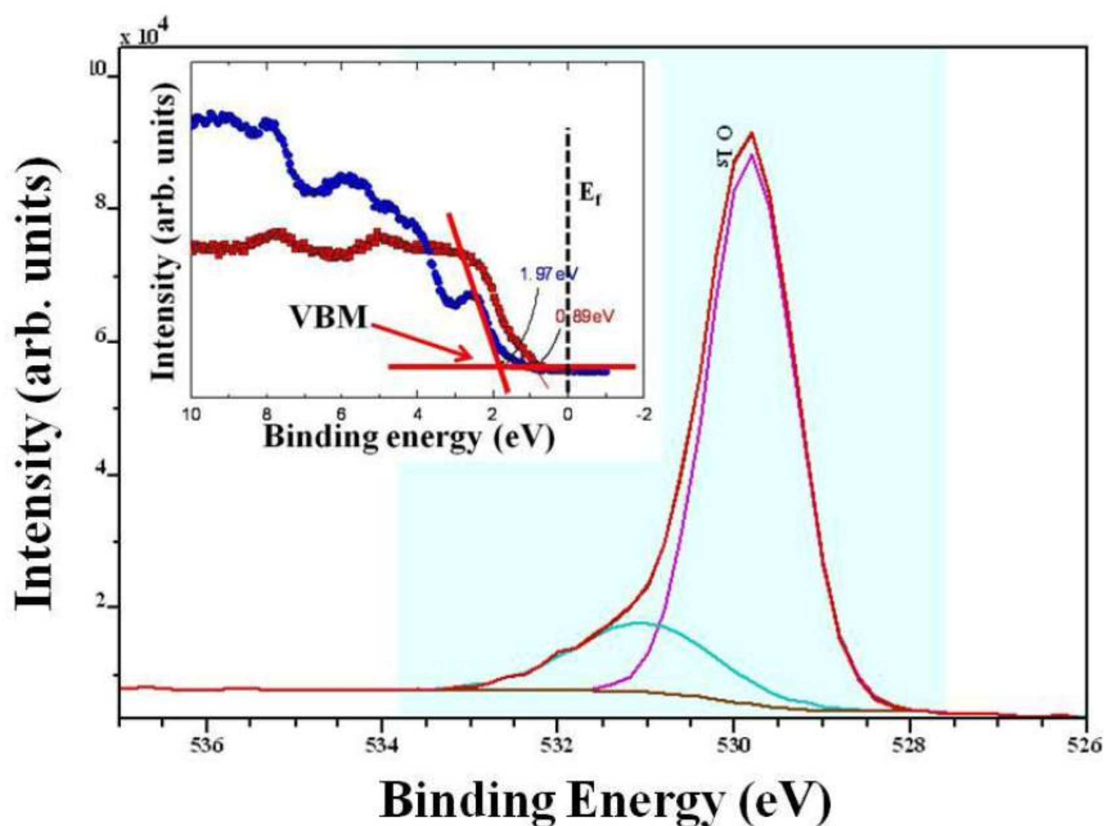

Figure 3.8: XPS core level oxygen 1s spectra showing Shirley background and peak deconvolution. Inset shows a schematic of valence band spectra showing valence band maximum (VBM).[172]

subtracted to determine the accurate peak position (binding energy, or B.E.) and the peak area, with the later being important for quantification. There are currently three background subtraction methods available[173]. (1) Linear is a simple subtraction method based on the assumption that the background corresponds to a straight line connecting the start and end points of the peak. (2) Shirley background assumes that intensity of the background is proportional to the peak area on the lower B.E. side of the peak. According to Shirley the subtraction of the background shape depends on the assumptions of a constant energy spectrum of scattered photoelectrons and a constant scattering probability in the peak region[174]. When the high B.E. end of the peak has a higher intensity value than the low B.E. end, the Shirley background typically gives a curved S shape, which is shown as the brown line in Fig. 3.8. (3) The Tougaard option is a complex background which is calculated from empirical energy loss functions. It works well on pure clean metals with wide energy range but is not very useful where only a small scan range has been acquired. Throughout our study, we use Shirley-type background

subtraction[174].

XPS peaks may consist of a number of overlapping peaks, often of different peak shapes and intensities. In this situation, peak deconvolution is required to separate overlapping peaks in a spectrum as shown in Fig. 3.8 Our XPS spectral deconvolution is achieved in Fityk and Xpspeak open source software packages. The shapes of the peak (height, width, Gaussian/Lorentzian function, etc.) are automatically varied until the best fit to the observed spectrum is achieved, considering physical aspects like peak position and FWHM etc. As mentioned earlier, another potential use of XPS is valence band measurements,[175] where we can identify the position of the Fermi level with respect to valence band maximum (VBM) and some surface and interface states as shown in the inset to Fig 3.8.

3.5 High Resolution X- ray diffraction

X-ray diffraction involves probing a crystal with x-ray radiation having a wavelength (λ) close to the crystal lattice spacing, as shown in figure. These x-rays are scattered by the electron cloud surrounding each atom in the crystal, yielding constructive interference between the scattered x-rays when the path difference AB (nλ) is equivalent to 2d sinθ.[176,177] This is the basis of Bragg's law, which relates the spacing between the 'planes' of atoms from which diffraction is occurring (d) to the angle (θ) at which the incident monochromatic beam must probe the plane to give constructive interference:

The simplest kind of X-ray diffraction arrangement is the double crystal diffraction scheme which consists on a monochromator crystal and a sample crystal from which the diffracted intensity signal is registered depending on the angle of rotation of the sample, further analyser crystals, makes it possible to resolve with high resolution the angular distribution of the beam diffracted by the sample. High resolution refers to a low λ dispersion of the used x-ray beam ($\Delta\lambda/\lambda$= 10^{-5}-10^{-4}), a limited beam divergence ($\Delta\omega$ = 0.001-0.008°) and a very good 2θ resolution ($\Delta\theta$ = 0.001-0.003°). Such a diffraction scheme is called triple-axis diffraction setup as shown in Fig 3.9.

In order to understand the bulk structural and crystalline quality and also the strain state of the layer, via measuring the lattice parameters of the InN, high resolution X-ray

diffraction measurements using a triple axis diffractometer are necessary. Additionally, dislocation density and nature of dislocations are is also obtained by measuring tilt and twist angular spread in InN epitaxial layers.

3.5.1 HRXRD setup and scans

The x-ray diffraction measurements were carried out using a Brucker D8 diffractometer, which consists of the following: **1** X-rays are generated by bombarding a metal (Cu)

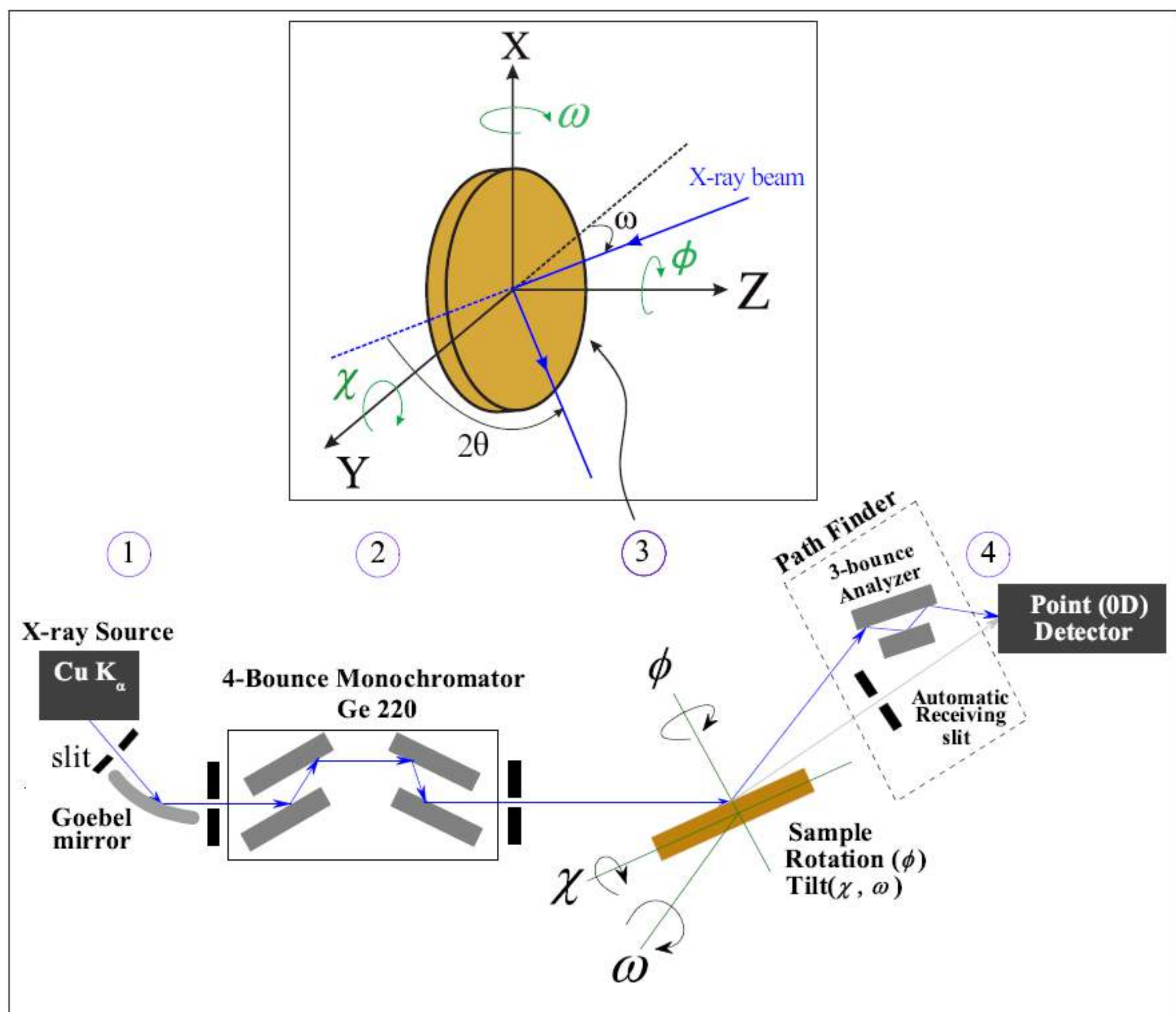

Figure 3.9: shows schematic diagram of HRXRD and inset represents the geometry of the goniometer with possible translations and Eulerian Craddle angles of rotation [53,178,179].

with electrons in an evacuated ceramic tube with an x-ray mirror placed after the x-ray source to collect the photons emerging from the line focus of the tube within an acceptance angle, forming an intense parallel beam with a very low divergence.

2 Four-bounce Ge 220 monochromator is used to obtain a monochromatic parallel incident beam with a x-ray wavelength corresponding to $CuK_{\alpha 1}$ (λ= 1.54056 Å) and reaching a maximal resolution $\Delta\lambda/\lambda = 10^{-5}$.

3 A goniometer (shown in inset) where the sample under investigation is mounted, enables translations along X, Y and Z, and also Eulerian tilt-χ and azimuthal-ϕ rotations are possible for a mounted sample. Here, χ is defined as the angle between sample surface and the plane of interest (in the 0-90° range) and the angle ϕ, ranging from 0 - 360°, measures the azimuthal rotation around the surface normal of the sample. The incident ω and diffracted 2θ angles are defined respectively between the X-ray source and the sample and between the incident beam and the detector angle.

4 The Pathfinder is a scintillation point detector. The scattered-beam path can be directed through two different optics: the automatic receiving slit or the Ge(220)×3 Analyzer.

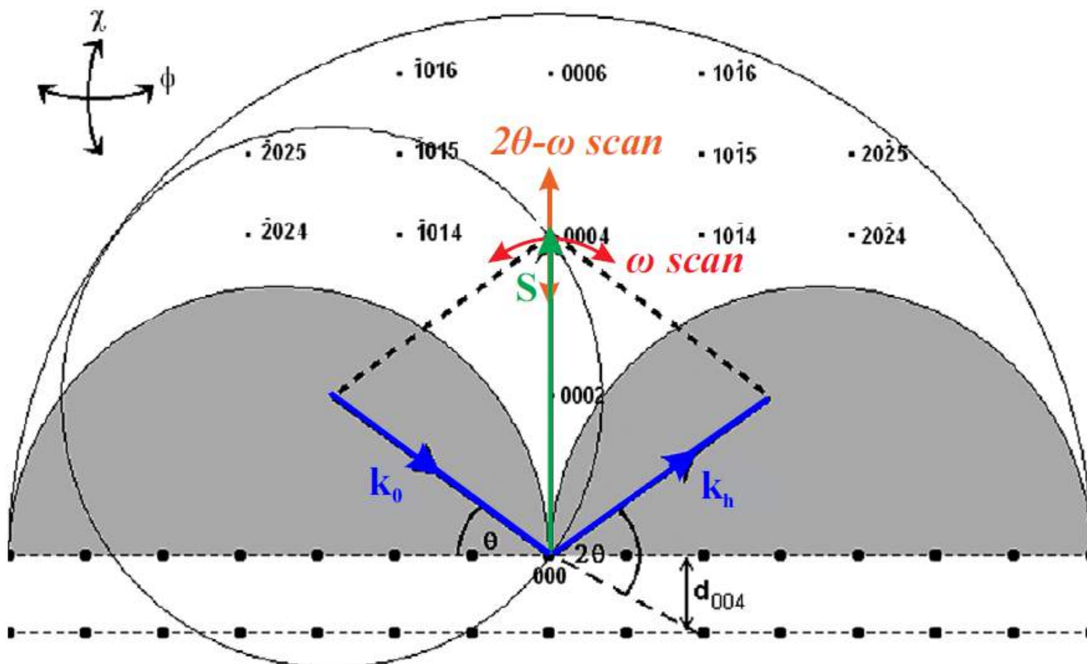

Figure 3.10: A section through reciprocal space for an [0 0 0 1]-oriented InN film. Regions of reciprocal space where the sample blocks a beam are shown in grey (inaccessible). Here, the vectors k_0 and k_h have the length $1/\lambda$ (where λ = 1.54 Å); the vector **S** has a length of $1/d_{0004}$ and is perpendicular to the (0 0 0 4) plane. The Ewald sphere is shown here as a circle, cutting the 0 0 0 4 reciprocal lattice spot. Some spots are absent as they have an intensity of zero.[178]

The different kinds of scans possible with the HRXRD, which provide a wealth of

information about the sample, are as follows:

Detector scan: Align 2θ position of detector to see the X-ray beam that stems directly either from source or diffracted from crystal planes.

Z scan: After translating the sample to proper X and Y positions, Z height can be optimized in such a way that the sample bisects the X-ray beam.

ω **scan or rocking curve:** The detector remains stationary and the sample is rotated about the ω axis. In reciprocal space, S (scattering vector) as shown in Fig 3.10, traces an arc centred on the origin. The length of S stays the same, but its direction changes (related with the tilt and twist angles).

2θ - ω scan: The sample (or the x-ray source) is rotated by ω and the detector is rotated by 2θ with an angular ratio of $1:2$, is the standard scan type for powder diffraction. In reciprocal space, S moves outwards from the origin. The length of S changes, but its direction remains the same and depends on the offset. For 2θ - ω scans, the x-axis is in units of 2θ. When there is no offset and $\theta = \omega$, it is a symmetrical scan (θ-2θ) which is vertical in reciprocal space.

ω **- 2θ scan:** Simply a 2θ-ω scan, but with ω on the x-axis, is the standard scan type for reflectivity and high-resolution work. The scattering vector is moved radially. This requires a coupled movement of the sample (ω) and the detector (2θ). In reciprocal space, q moves outwards from the origin. The length of q changes, but its direction remains the same and depends on the offset = θ - ω. In this case, the orientation of the probing q vector has the same tilt angle with respect to the sample surface normal during the whole measurement. In the special case of $\omega = \theta$, the scan runs parallel to the normal surface (offset = 0 and tilt angle = 0).

2θ scan: The sample and source remain stationary and the detector is moved. S traces an arc along the circumference of the Ewald sphere, where both the length and the direction of S change.

ϕ **scan:** Rotation of the sample about the ω axis (usually in the plane of the sample). The length of S stays the same, but the sample is moved, bringing the reciprocal lattice spot through S so that the direction of S changes with respect to the sample.

χ **scan:** Similar to ϕ scan, except that the sample is rotated about the χ axis (plane of the sample rotated with respect to the incoming x ray beam).

3.5.2 Diffraction geometries for 2θ-ω scan

Symmetric: In this geometry, planes parallel to the sample surface are investigated. the angle ω and 2θ of incoming and outgoing beams with respect to the sample surface are simultaneously varied, where ω=θ.

Asymmetric: An asymmetric 2θ-ω scan can be performed for the planes having tilt (τ) with respect to the sample surface. As in the case of a symmetric scan, the detector is placed at an angle of 2θ with respect to the incoming beam. The incoming beam, however makes an angle of ω with respect to the sample surface. Since $\omega=\theta\pm\tau$, grazing incidence (-) or grazing exit (+) 2θ-ω scans can be collected in this asymmetric geometry.

Skewsymmetric: An alternative way of getting the asymmetric scan is in the skew-symmetric geometry, where the sample is tilted over a fixed angle around the χ axis instead of the ω axis. The rest of the procedure to acquire the 2θ-ω scan in skewsymmetric geometry is same as symmetric scan.

Detailed information of above scans and geometries are available in Speakman's MIT SOPs.[180] In this work, HRXRD has been extensively used to extract the following information,

i) The crystalline nature of the film and its epitaxial relation with the substrate.

ii) The a and c lattice parameters of the samples to calculate the residual strain (absolute lattice parameters).

iii) The tilt and twist mosaic angular spread of the crystallites to determine the screw and edge dislocation density, respectively.

3.6 Optical bandgap: Transmission measurements

The band gap of InN films grown in this study is measured through a simple transmission spectroscopy.[181] In this technique, using a beam splitter, this incident light is divided

into two rays of equal intensity which fall on two identical detectors and the sample is inserted in the path of one of the two beams. The ratio of the intensities recorded by two detectors is plotted as a function of energy (E) of the probing light. The intensity of light transmitted through a film of thickness d is,

$$I_t(E) = I_0 exp(-\alpha(E)d) \tag{3.7}$$

where I_0 is intensity of incident beam and $\alpha(E)$ is the absorption coefficient of a given film. Absorption coefficient of a semiconductor is described by the following equation,

$$\alpha(E) = C(E - E_g)^n \tag{3.8}$$

where E_g is the bandgap, C is the constant and the value of the exponent n denotes the nature of the transition; for instance, $n = 1/2$ for direct transitions and $n = 2$ for indirect transitions. A Tauc plot[182] is a convenient way of displaying the optical absorption spectrum of a material pioneered by J. Tauc, who proved that momentum is not conserved even in a direct optical transition.[183] This plot shows the quantity $h\nu$ (the energy E of the light) on the abscissa and the quantity $(\alpha h\nu)^n$ on the ordinate. The resulting plot has a distinct linear regime which denotes the onset of absorption. Thus, extrapolating this linear region to the abscissa yields the energy of the optical band gap of the material. However, if the material in question does not have a single phase, it is likely not to have a single distinct absorption onset, which corresponds to a more gradually-sloping curve in the Tauc plot. Room temperature transmission measurements were performed with a Perkin Elmer system with near-infrared-visible-UV spectrometer (Lamda 900) scanning spectral range between 200nm and 2500nm, where emission from a mercury lamp source was used to provide the spectral range.

3.7 Photoluminescence and Catholuminescence spectroscopy

Photoluminescence occurs when excited electrons upon the photon stimulation recombine with holes or traps and a photon is emitted.[184] A suitable laser or filtered light

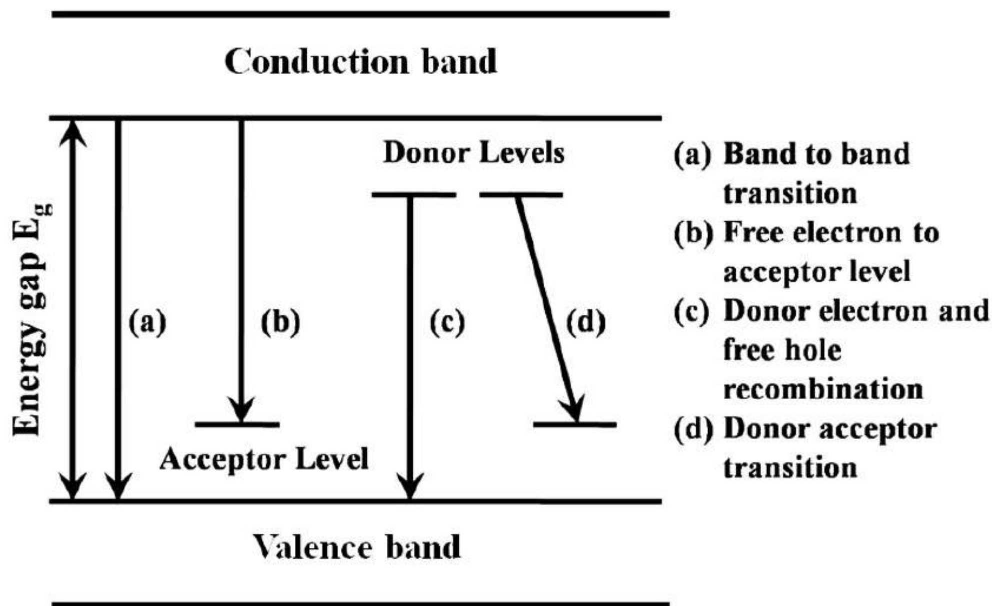

Figure 3.11: shows the basic recombination transitions in semiconductor during the process of photoluminescence.

from mercury lamp that has a photon energy output higher than the band gap of the semiconductor is incident on the surface of the sample, which will generate electron hole pairs. Those electron hole pairs will recombine, often through a radiative transition back to the ground state of the atom. Some of the observed recombination pathways are presented in Fig 3.11. Information about the band structure, donor and acceptor levels, defect types, impurities, crystalline quality, and defect densities in the material system can be extracted by measuring the wavelength of the emitted photon. We have used HORIBA JOBIN YVON *i*HR320 PL system with mercury lamp as the source of light and the required excitation wavelength is generated using optical grating.[185] In cathodoluminescence, energetic electrons are used as excitation source. Cathodoluminescence is an optical and electrical phenomenon whereby a beam of electrons, unlike PL photon source, is generated by an electron gun which impacts on a luminescent material causing the material to emit photons.

3.8 Hall measurements

Single field Hall effect measurements are performed to measure the resistivity, bulk carrier concentration and mobility of semiconducting thin films. The geometry of Hall

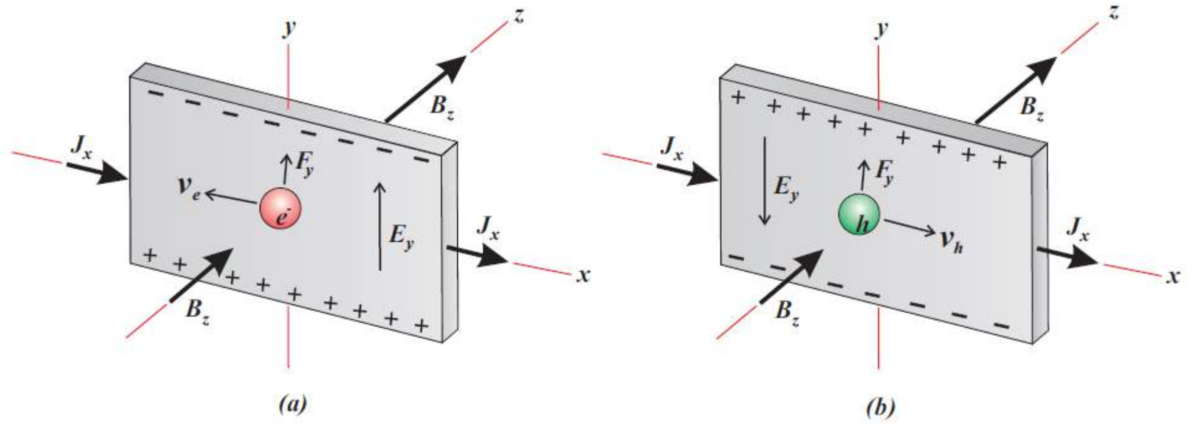

Figure 3.12: shows schematic diagram where the forces on the charge carriers in a semiconducting slab in a magnetic field give rise to hall voltage across the width of the slab.[186]

effect measurements is depicted in Fig 3.12. An electric current is passed through the semiconducting thin film via contacts at either end while a magnetic field $H = (0, 0, H_z)$ is applied perpendicularly to both the surface and the electric current J_x. Due to the Lorentz force $F_y = -e(\mathbf{E} + \frac{\mathbf{v}\times\mathbf{H}}{c})$, the transverse electric field $E = (E_x, E_y, 0)$ perpendicular to the direction of current flow launches[146,177] the equation of motion of an electron as given below. In the case of steady state, current is independent of the time, and therefore p_x and p_y will satisfy the following equations

$$0 = -eE_x - \omega p_y - \frac{p_x}{\tau} \tag{3.9}$$

$$0 = -eE_y + \omega p_x - \frac{p_y}{\tau} \tag{3.10}$$

where $\omega = \frac{eH}{mc}$

multiply these equations with $-ne\tau/m$, which result in

$$\sigma_0 E_x = \omega\tau j_y + j_x \tag{3.11}$$

$$\sigma_0 E_y = -\omega\tau j_x + j_y \tag{3.12}$$

electron and hole contributions to the transverse current respectively are

$$j_y(e) = ne\mu_e(\frac{\mu_e H}{c}E_x + E_y) \tag{3.13}$$

$$j_y(h) = ne\mu_h(\frac{-\mu_h H}{c}E_x + E_y) \tag{3.14}$$

here $\omega\tau c = \mu H$

Hall field E_y is determined by requirement that the net transverse current in y-direction is zero which means $j_y(e) + j_y(h) = 0$ and thus,

$$0 = (ne\mu_e^2 + pe\mu_h^2)(H/c)E_x + (ne\mu_e + pe\mu_h)E_y \tag{3.15}$$

net current in x-diretion is

$$j_x = (pe\mu_h + ne\mu_e)E_x \tag{3.16}$$

therefore

$$E_y = E_x H \frac{p\mu_h^2 - n\mu_e^2}{p\mu_h - n\mu_e}.\frac{1}{c} \tag{3.17}$$

Hall constant

$$R_H = \frac{E_y}{J_x H_z} = \frac{1}{ec}.\frac{p\mu_h^2 - n\mu_e^2}{(p\mu_h - n\mu_e)^2} \tag{3.18}$$

If electrons are dominant carriers in a semiconductor then above equation simplyfies to

$$R_H = -\frac{1}{ne} \tag{3.19}$$

3.8.1 Van der Pauw geometry

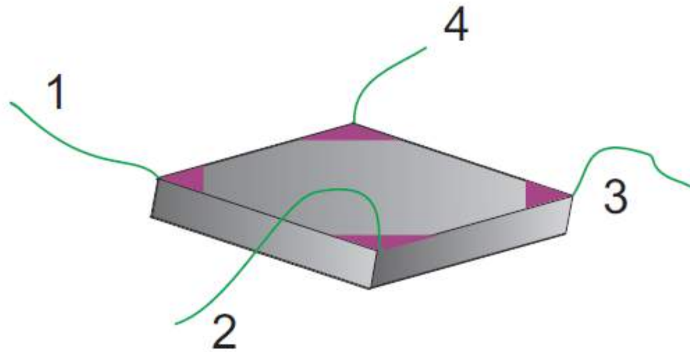

Figure 3.13: A common geometry for Van der Pauw Hall measurements.

A typical geometry used for measurements of the sheet resistance and Hall voltage of a sample, and that used in this work, is the van der Pauw geometry, shown schematically

in Fig 3.13. If a current is passed between contacts 1 and 2, I_{12}, and a voltage measured across contacts 3 and 4, V_{34}, the resistance

$$R_{12,34} = \frac{V_{34}}{I_{12}} \tag{3.20}$$

Van der Pauw[187,188] showed that, for flat continuous lamina of arbitrary shape, the sheet resistance R_s satisfies

$$exp(-\pi R_{12,34}/R_s) + exp(-\pi R_{23,41}/R_s) = 1 \tag{3.21}$$

allowing the sheet resistance to be determined from simple electrical measurements. From the reciprocity theorem, $R_{12,34} = R_{34,12} = R_{21,43} = R_{43,21}$, these quantities can be averaged to yield a much more accurate value of the sheet resistance, canceling out any offset voltages. In a similar way, the reciprocity theorem can be used to yield accurate values of the Hall voltage.[189,190] A current can be applied between a set of contacts on opposite corners, for example I_{13}, in the presence of either a positive or negative magnetic field, and a Hall voltage is measured between the other two corners, for example $V^{\pm}_{24}$, where $\pm$ denotes the polarity of the magnetic field. The average Hall voltage is then given from

$$V_H = \frac{V^+_{13} - V^-_{13} + V^+_{24} - V^-_{24} + V^+_{31} - V^-_{31} + V^+_{42} - V^-_{42}}{8} \tag{3.22}$$

Using each set of currents and voltages, for the Hall voltage and sheet resistance measurements, it is therefore possible to obtain an accurate value for the sheet density and mobility of the sample.

Hall effect measurements reported in this work were performed using an Ecopia HMS-3000 Hall effect measurement system. Indium contacts are made to the samples in the van der Pauw geometry discussed above. The system includes a 0.58 T permanent magnet, and the polarity of the field is changed by rotating the magnet through 180°. The system can pass a current up to 20 mA. Hall effect measurements were only made if a linear I-V curve was obtained, indicating Ohmic contacts had been formed to the material. During measurements, the sample sits in a container that can be filled with liquid nitrogen for

performing measurements at 77 K.

3.9 Atomic Force Microscopy (AFM)

AFM provides information on the quality of the surfaces in terms of root-mean-square (rms) roughness, but also on the morphology and the average grain size. The AFM principle in the contact mode is based on the measurement of a short-range interaction between the sample and the probe, which depends on the distance between them. Typical tips used in this work are pyramid-shaped silicon tips with opening angles around 10 °-15° near the apex and with a maximum radius of 5 nm, providing images with a lateral resolution of ≈ 5 nm. The tip mounted at the end of a cantilever is scanned across the surface of the sample, which moves up and down over its topography. The displacement caused by the atomic forces of the features at various positions on the surface can be measured to create an image.[191] The AFM measures the van der Waals force between the tip and the surface; this may be either the short-range repulsive force (in contact-mode) or the longer-range attractive force (in non-contact mode). There are three scanning modes associated with AFM, namely; contact mode, non-contact mode, and tapping mode. Contact mode is the scanning mode in which the tip is in contact with the surface and

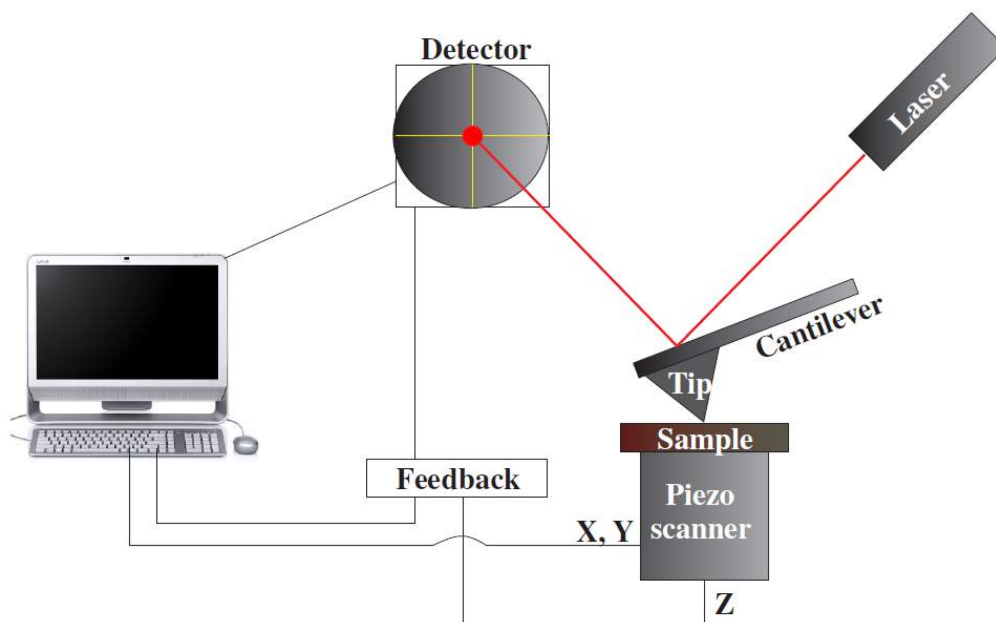

Figure 3.14: A schematic representation of AFM.

the image is obtained by repulsive forces between tip and the sample. In tapping mode,

the image is obtained by the tip, which just taps the surface for small periods of time. In non-contact mode, the tip oscillates above the surface, and the image is obtained from the attractive forces between the tip and the sample. The tip is scanned over a surface with feedback mechanisms that enable the piezo-electric scanners to maintain the tip at a constant force (to obtain height information) or height above the sample surface (to obtain force information). As the tip scans the surface of the sample, the focused laser beam is deflected off the attached cantilever into a position sensitive dual photodiode system. Feedback from the dual photodiode system and the control software enables the tip to maintain either a constant force or constant height above the sample. The surface morphology including rms surface roughness of the InN and GaN layers in this thesis was analyzed using a Dimension 3100 SPM (Veeco, USA) in both contact and non-contact modes. The tapping mode is usually used to scan fragile samples. This mode is preferred in the case of group III nitrides, not to protect the sample but the tip, since they are materials much harder than the silicon tips.

3.10 Field Emission Scanning Electron Microscope (FESEM)

In Field Emission Scanning Electron Microscope (FESEM), the image is formed by scanning an electron beam across a sample and collecting the secondary electron signal from the beam-sample interaction, which is used to control the intensity of the spot on a cathode ray tube which is scanning in synchronization with the beam on the sample.[192] Electron accelerating voltages ranging from 0.5 to 30 kV and image spatial resolution down to 1 1/2 nm. Tilting of the sample is also possible to obtain a cross-sectional view. Because the probe used for imaging is an electron beam, some interesting contrast mechanisms (and signals) can be produced. The appearance of the image is usually as though the sample was "illuminated" by the detector being used to form the image, up to the point of "shadows" while dark spots can be from surface contamination. In order to perform FESEM measurements, an electrical path is needed to avoid the electron accumulation on the samples. If this path is not present, the impinging electrons can negatively charge its surface, leading to the screening of the sample to new incoming

electrons. In this work, cross section images with a surface view are carried out by FESEM from FEI Netherlands. These images give information about the type of growth (columnar or compact) and allow the estimation of the layer thickness to calculate the growth rate.

Chapter 4

Optimization of parameters for InN growth on bare c-sapphire

In this chapter we present the optimized parameters for InN growth and address several issues related to the band gap and degeneracy of films. We carefully design two sets of experiments for the growth of InN using MBE and analyze the results using several complementary characterization tools. The issue of variable band gap values for InN films grown on c-sapphire has been addressed in this work.

In the first section, α-InN films have been deposited in nitrogen rich conditions at different substrate temperatures on bare Al_2O_3 (0001), by Plasma Assisted Molecular Beam Epitaxy. The results show that single crystalline wurtzite InN films are formed, but their orientation depends on the substrate temperature. The band gap measured on these samples (1.78eV) is explained by the Moss-Burstein shift on these degenerately n-doped samples.

We address the carrier concentration, strain and bandgap issue of InN grown on c-sapphire at different N-flux by Molecular Beam Epitaxy and characterized by several complementary characterization tools. By using X-ray diffraction and X-ray photoelectron spectroscopy, we demonstrate that the strain in InN films is related to point defects like nitrogen interstitials and nitrogen antisites. We invoke the role of minimal hydrostatic strain and biaxial strain in the InN film attributed to the interstitial

nitrogen atoms, which is partially compensated by the strain induced by the nitrogen-antisites. We find that the variation in absorption edge can be attributed to defect induced carrier concentration and that nitrogen interstitials and nitrogen antisites act as donors that yield the respective absorption edge and Moss-Burstein shift. This chapter is a step towards the ability to form low carrier concentration strain relaxed films and attaining the intrinsic band gap value for this technologically important material.

4.1 Dependence of crystal orientation on substrate temperature

4.1.1 Introduction

As discussed earlier, inspite of its outstanding properties, required for optoelectronic and photonic applications, among other group III nitrides InN is the least studied due to difficulties in producing good quality InN films, resulting from its low dissociation temperature, the high equilibrium vapor pressure of nitrogen and also unavailability of suitable lattice matched substrates[193]. One of the most important electronic properties of InN, which is much debated by researchers, is its band gap. With the synthesis of high mobility, low carrier concentration, polycrystalline, RF sputtered films by Tansley and Foley in 1986[81], the band gap of wurtzite InN was accepted to be 1.89eV, but more recent results have shown much lower values[23], with initial reports indicating a value of 1.1eV[74], which has progressively reduced to lower values of 0.90 eV[26], 0.80-0.7eV[25,27,194] and 0.65-0.6eV.[77,195] Observation of higher band gap has been attributed to several reasons such as strong Moss Burstein shift, quantum size effects, oxygen inclusion and stoichiometry changes[49,75,196,197]. For the low band gap the reasons include defects, non-stoichiometry, film non-uniformity and Mie-resonances[139,197]. However, the full range of reported experimental observations is not fully understood and thus, the issue needs to be addressed by a spectrum of complementary characterization performed on samples prepared under controlled growth parameters.

In this chapter, we revisit the plausible reasons for the high band gap of InN grown on bare c-plane sapphire using a Plamsa Assisted-Molecular Beam Epitaxy (PA-MBE)

system equipped with accurate flux and temperature measurement and a combination of *in-situ* and *ex-situ* characterization tools. MBE has the distinct advantage over other methods like Metal Organic Chemical Vapor Deposition (MOCVD) since the substrate temperature can be independently chosen irrespective of the nitrogen source. One of the important reasons for the observed band gap of InN, which has not been considered seriously, is the influence of deviation from stoichiometry. Thus, along with other plausible reasons we perform systematic XPS analysis to probe the influence of stoichiometry on the band gap of InN. We show here that crystallinity of InN films results from the carefully chosen kinetic growth conditions and do not influence the observed band gap value.

4.1.2 Experimental details

Before loading into the chamber c-sapphire substrates, provided by Semiconductor Wafer Inc having miscut of ≈0.4°, were rinsed in acetone and out-gassed at 500 °C for one hour in the preparation chamber. Further out-gassing is performed at 800 °C in the growth chamber for 30min so that the streaky RHEED diffraction pattern characteristic of clean sapphire (0001) surface is obtained. In first set, we have chosen three substrate temperatures, 400 °C, 450 °C and 500 °C for the growth of InN, monitored by a K-type thermocouple and an optical pyrometer. In second set, N_2 flux rates for the InN films grown in this experiment are 2, 4, 6 and 8 sccm (standard cubic centimeter per minute) with a Radio Frequency (RF) plasma forward power of 375W.

4.1.3 Results

For the present study we have grown InN film at three temperatures viz. 400 °C, 450 °C and 500 °C using MBE on bare c-plane sapphire without any substrate surface pre-nitridation or having any buffer layers.

4.1.4 Surface and bulk crystallinity of the films

We have used *in-situ* RHEED to determine the surface crystallinity of the grown samples. Fig 4.1 consists of the respective RHEED pattern for samples grown at 400 °C,

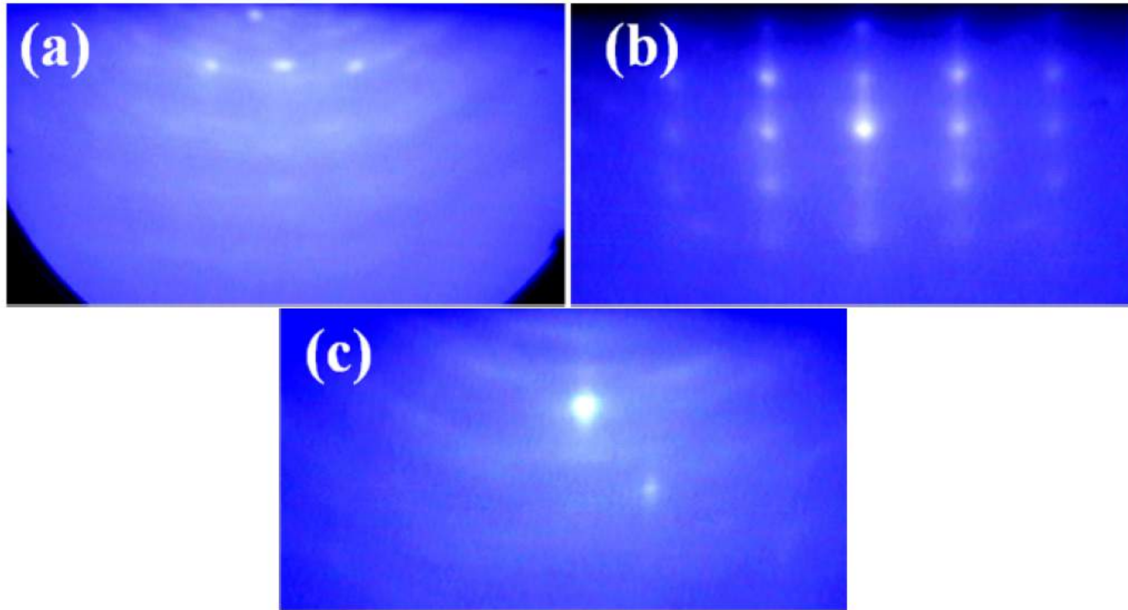

Figure 4.1: (a-c) show *in-situ* RHEED diffraction pattern observed for samples grown at 400 °C, 450 °C, and 500 °C, respectively.

450 °C and 500 °C. The RHEED pattern in Fig 4.1 a shows spots superimposed on a faint ring pattern which shows that the film surface grown at 400 °C is predominantly polycrystalline in nature. From the RHEED pattern shown in Fig 4.1b for the 450 °C, we observe a dominant spotty pattern with weak streaks, which is an indication of the transmission through the features of a rough single crystalline film. The absence of any circular streaks as seen in Fig 4.1a indicates the absence of polycrystallinity in this sample. The RHEED pattern for the 500 °C sample shown in Fig 4.1c is similar to that observed for the 400 °C sample, where spots are superimposed on faint ring like pattern, which indicates polycrystalline nature of the sample surface. Thus, our RHEED study shows that among the different temperatures studied, the surface region of the sample grown at 450 °C is single crystalline, while others show polycrystallinity. This can be due to a surface effect or different orientation of growth of single crystalline features.

Thus, X-ray diffraction measurements performed and the θ-2θ pattern are shown in Fig 4.2(a-c) for InN films grown at 400 °C, 450 °C and 500 °C, respectively. As observed by RHEED, x-ray diffraction also shows that the sample grown at 450 °C is single crystalline in nature. In the case of this InN film two diffraction peaks (0002) and (0004) are observed, in addition to the (0006) reflection from the sapphire substrate, at diffraction angles (2θ), 31.2°, 65.27°, and 41.66° respectively. Absence of other reflections confirms that at 450

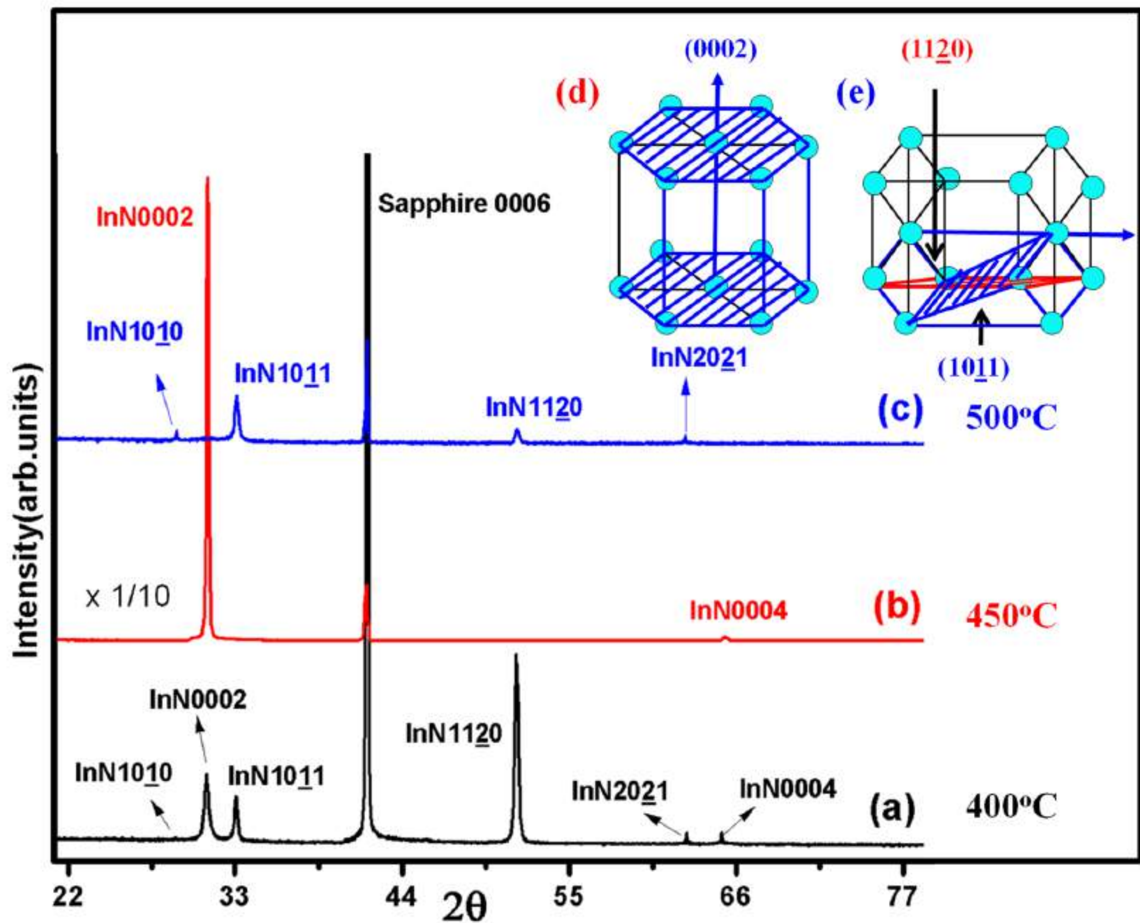

Figure 4.2: XRD pattern for samples grown at different temperatures a) 400 °C, b) 450 °C, and c) 500 °C, respectively. Inset to the figure, Fig 4.2d and Fig 4.2e show the wurtzite unit cell of InN with c-axis parallel and perpendicular to that of substrate for 450 °C and 500 °C growth temperatures.

°C single crystalline wurtzite InN (α-phase) grains are formed parallel to the c-axis of the sapphire substrate. At the slightly lower growth temperature of 400 °C, besides the on-axis peaks (0002), (0004) and the sapphire (0006), we observe peaks at 33.09°, 51.6° and 62.66°, which correspond to the off-axis crystal planes of wurtzite InN($10\bar{1}1$), InN($11\bar{2}0$) and InN($20\bar{2}1$) respectively, as shown in Fig 4.2a. At the higher temperature of 500 °C, Fig 4.2c, we observe that on-axis reflections are completely absent in this sample. The sample shows peaks of InN($10\bar{1}1$), InN($11\bar{2}0$) and InN($20\bar{2}1$) apart from the sapphire (0006) peak. We observe that the reflections observed on samples grown at 450 °C are completely absent in 500 °C sample and vice-versa, whereas the 400 °C grown sample has all the reflections. A schematic of the corresponding planes for the main reflections in the two cases is shown in Fig 4.2(d) and (e). The figure clearly indicates that while InN grows with its c-axis parallel to the c-axis of Al_2O_3 at 450 °C, at 500 °C InN grows

with its c-axis parallel to the a-b plane of substrate, while at 400 °C both orientations coexist. Thus, 500 °C grown sample is not polycrystalline as indicated by RHEED but shows a different orientation of the wurtzite InN growth with respect to the substrate. Our study clearly demonstrates that the crystalline orientation of the sample is strongly dependent on subtle changes in the substrate temperature.

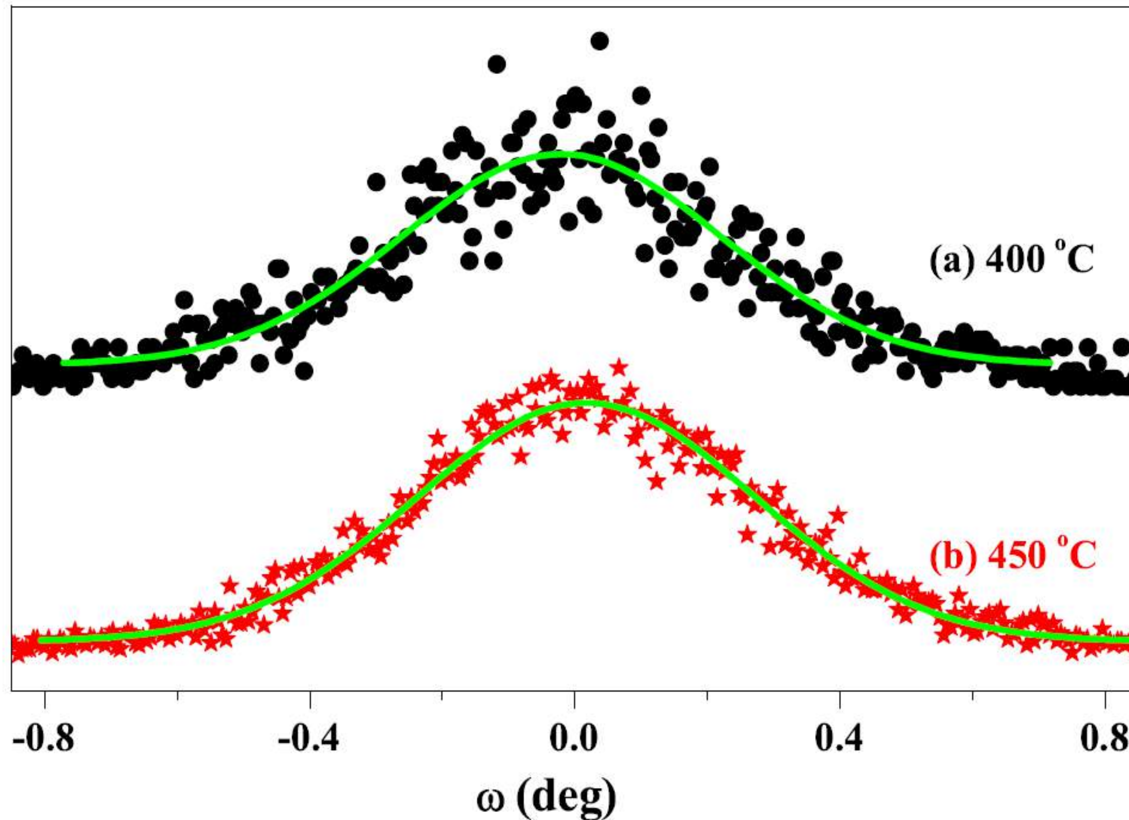

Figure 4.3: (a) and (b) show the ω-scans for the InN(0002) reflection of the films grown at 400 °C and 450 °C, respectively. Solid lines are Gaussian fits for the data points.

Fig 4.3 shows the ω-scans acquired on InN(0002) having FWHM values of 42.1 and 35.6 arc-mins for films grown at 400 °C and 450 °C, respectively, which show relatively the good crystalline quality of the α-InN film formed at 450 °C. The combination of RHEED and XRD studies thus show that 450 °C is the optimum temperature for InN growth, with c-orientation parallel to that of the bare sapphire substrate.

4.1.5 Cathodoluminescence: Band gap

To address issues related to the varied band gap values reported in literature, we probe the band edge emission using cathodoluminescence measurements. Most of the

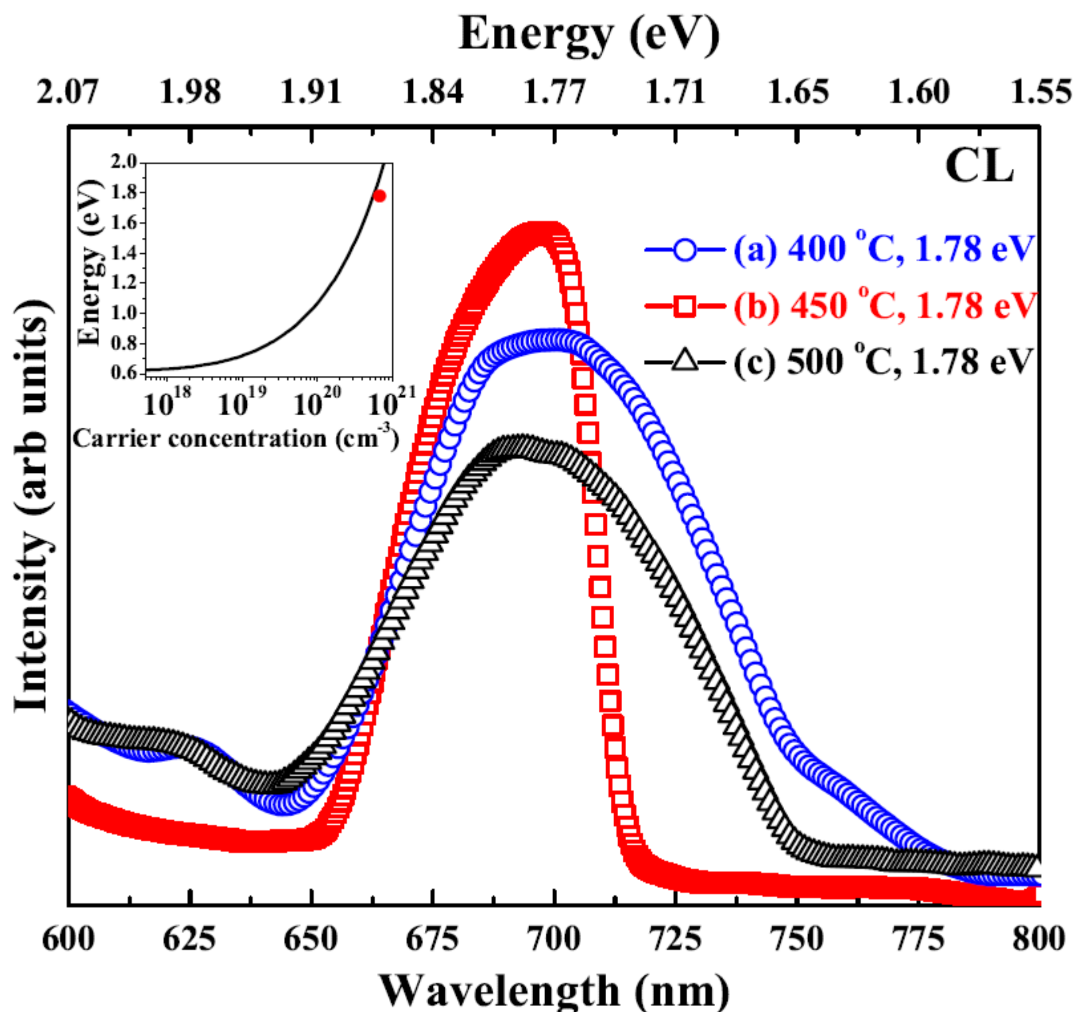

Figure 4.4: *in-situ* Cathodoluminescence spectra observed for samples grown at a) 400 °C, b) 450 °C, and c) 500 °C, respectively. Inset to the figure shows the theoretical curve for the variation of the band edge with carrier concentration, along with the value determined in this study.

band gap data available in the literature for InN have been obtained using absorption measurements[198]. Hamberg and Granqvist have shown that band gap broadening results in an under-estimation of the measured band gap values for samples with carrier concentration above 10^{19}cm^{-3}.[199] Strong change in refractive index near the band gap edge limits the use of absorption squared plots to estimate band gap values. The first observation of PL in the case of InN film came only in 2002[200], which may be due to the poor quality of the materials synthesized earlier. We have observed cathodoluminescence with a strong band edge emission on our samples ascertaining the good quality of the films grown. Cathodoluminescence spectra measured at room temperature on our samples are shown in Fig 4.4. Fig 4.4(a-c) show CL spectra from InN samples grown at 400 °C, 450

°C and 500 °C respectively. All the samples show emission at nearly 1.78eV, similar to the high band gap value reported by Tansley and Foley[81], and the FWHM of the three samples grown at 400 °C, 450 °C and 500 °C are respectively 160meV, 104meV and 170meV. Recent MBE studies have attributed the observed high band gap value to the polycrystallinity of the sample[75]. However, since all the samples studied here show similar high band edge values and are of single α-phase, it can be inferred that by our combined *in-situ* RHEED and XRD studies, the polycrystallinity of grown α-InN films does not have any influence on the observed high band gap. The inset in Fig 4.4 will be discussed later.

4.1.6 Discounting the role of quantum size effects on band gap

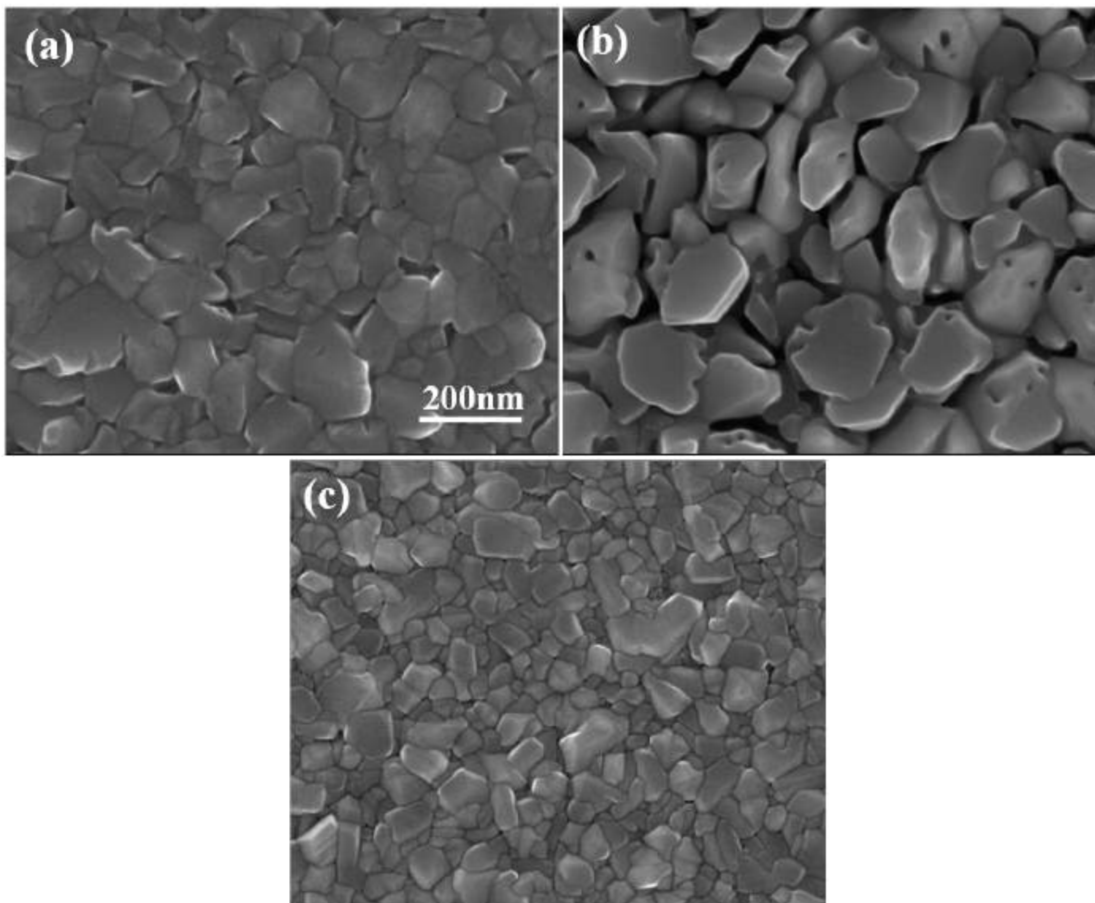

Figure 4.5: FESEM images of the samples grown at a) 400°C, b) 450 °C, and c) 500 °C, respectively.

Since the observed high band gap for InN has sometimes been assigned to quantum size effects[75] determined by the grain sizes. We have mapped the surface morphology of the

grown films by FESEM which is shown in Fig 4.5a, 4.5b and 4.5c for samples grown at 400 °C, 450 °C and 500 °C, respectively. Line scans showing roughness of the FESEM images are also shown on the micrographs. From Fig 4.5a, for growth at 400 °C, it is clear that surface morphology of this sample consists of large grains forming a quasi-continuous film. To verify this core-level XPS study is performed. At 450 °C, the FESEM image shown in Fig 4.5b consists of large and well separated grains. Fig 4.5c shows the FESEM image of the InN film grown at substrate temperature of 500 °C where it is apparent that the film consists of a large numbers of grains of various sizes, but are smaller in size compared to the other two temperatures. Thus, the three samples grown at different temperatures with different grain sizes show the same band edge emission suggesting same InN phases. We see that the observed average grain size is about ≈100nm which is quite large for any quantum size effect to have any appreciable influence on the band gap value.

4.1.7 XPS: Composition and stoichiometry of InN

Formation of oxynitride/oxide at grain boundaries has also been suggested to be a factor that enhances band gap[49]. To address this, we sputter clean the surface with low energy Ar+ ions before performing any XPS measurements to remove atmospherically adsorbed contaminants and results of our samples are shown in Fig 4.6. The figure consists of normalized In *3d* core level peak from InN samples grown at 400 °C, 450 °C and 500 °C, deconvoluted into (shown only for 400 °C sample) components arising from different contributions of In bonding with In, N, O, hydroxide, etc.[201]. From the figure it is clear that InN film grown at 400 °C has broader In $3d_{5/2}$ peak as compared to those grown at higher temperatures. This In $3d_{5/2}$ peak is de-convoluted into Gaussian components (Fityk-HWHM is ≈0.7eV) from InN contribution and that from indium oxide or indium oxynitride related contributions at 443.5eV and 444.7eV binding energies[201], respectively. The integrated area of In−O peak (30661) is roughly half of that of the In−N peak (56723). Since at 400°C growth temperature the formation of indium oxide can be neglected[202], the extra component can be attributed to the presence of oxynitride in this film. We do not see any oxynitride related peak in XRD pattern, suggesting that it is amorphous and could be at the grain boundaries, as reported earlier[49]. Oxygen in the InN films has been attributed to the exposure of samples to atmosphere, where they adsorb at

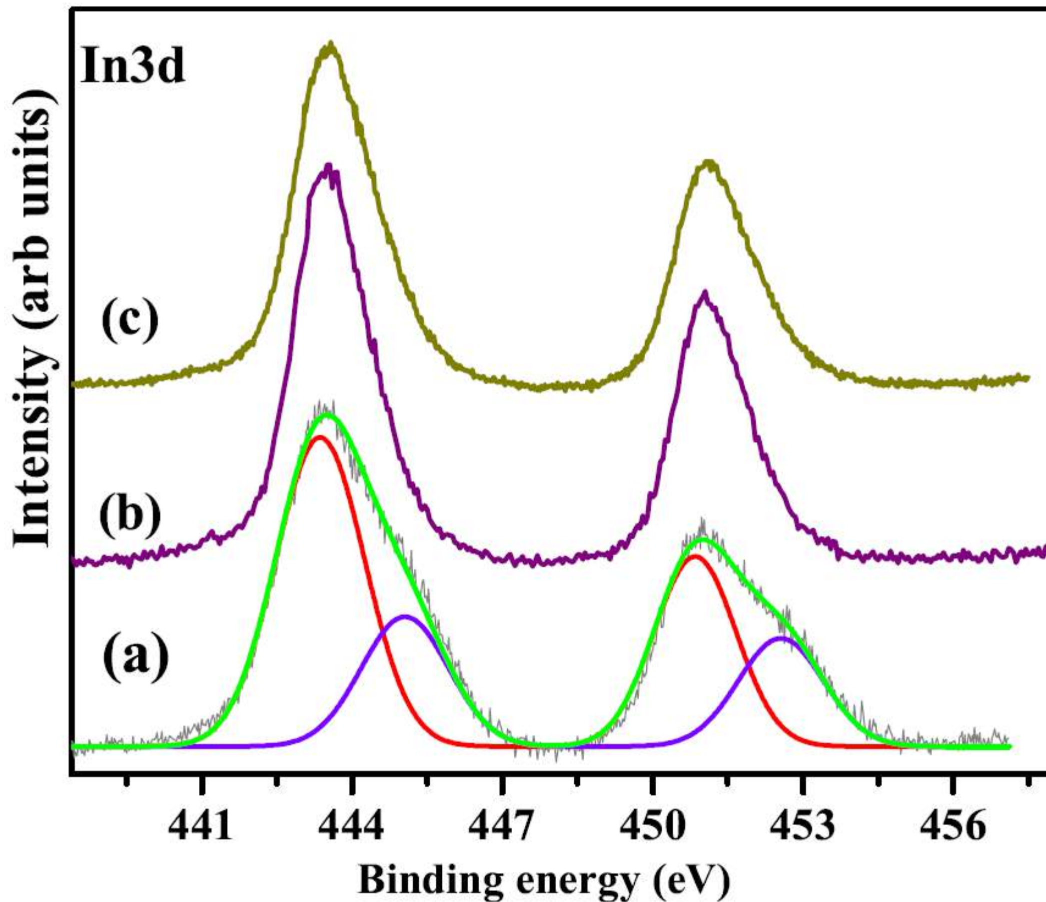

Figure 4.6: XPS In (*3d*) core-level spectra obtained for samples grown at a) 400 °C, b) 450 °C, and c) 500 °C, respectively.

grain boundaries and form oxynitrides[23] or by the diffusion of oxygen from the sapphire substrate to the InN layers[202]. We have ensured by Mass Spectrometry that there is no oxygen ($< 10^{-15}$ torr partial pressure) in the MBE growth chamber. Fig 4.7 shows the relative percentage composition of oxygen (on alternate y-axis) by measuring the core level XPS peaks[203] plotted versus growth temperature. Fig 4.7 indicates that sample grown at 400°C has 20% oxygen and at higher temperatures the percentage of oxygen is zero. Absence of oxygen in samples grown at 450 °C and 500 °C with well-separated granularity also suggests that the source of oxygen may not be from the ambient. Oxygen might be resulting from the diffusion from the substrate to InN layer at this particular temperature 400 °C. However, films grown at 450 °Cand 500 °C dont show the formation of oxide/oxynitride. The reaction of In and N atoms at higher temperature can be faster than diffusion of oxygen atoms to the surface of the over grown film. In Fig 4.7, we have plotted the ratio of In to N computed from the XPS survey scan, which clearly shows that

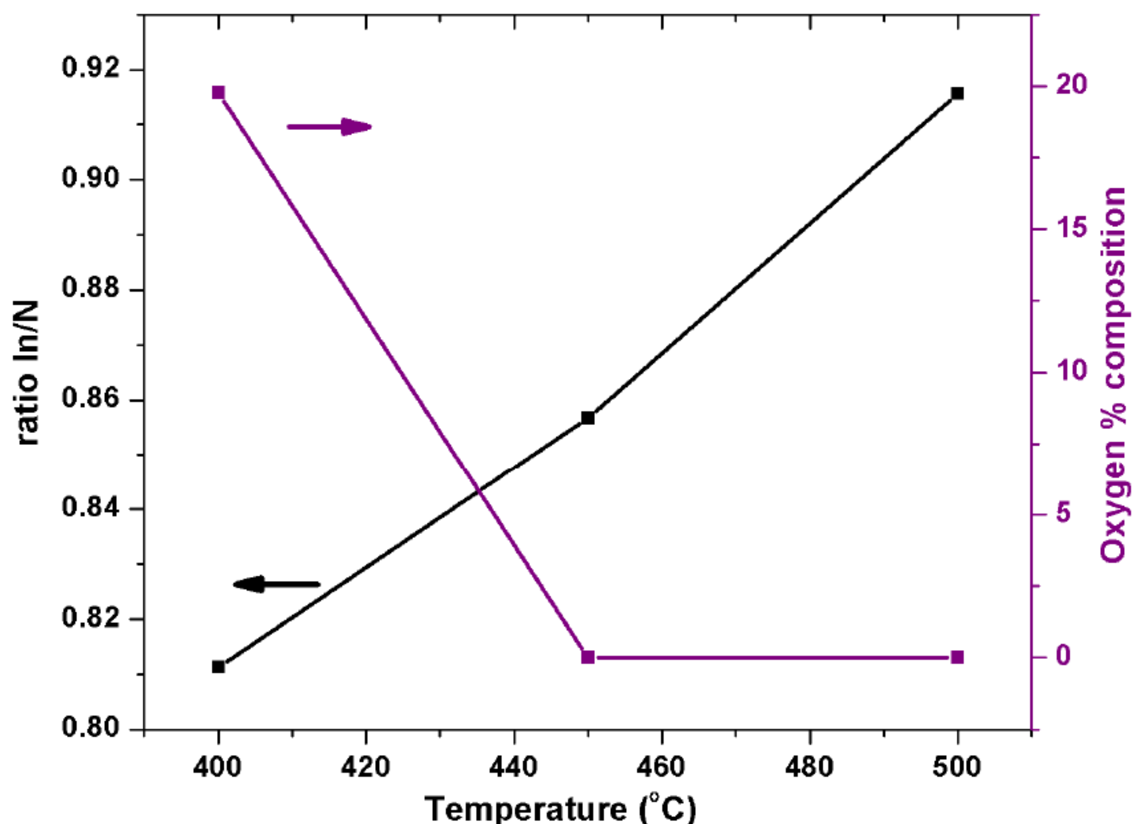

Figure 4.7: shows the percentage composition of oxygen and ratio of In to N at different growth temperatures.

all the as grown samples are N rich. Since MBE is a non-equilibrium growth technique involving kinetic influences, such a nitrogen rich stoichiometry is possible and hence can be considered to be the source of background doping. Fig 4.7 shows that, with increase in temperature, the ratio of In/N increases but the band edge emission remains at 1.78eV, irrespective of the variation in the stoichiometry, again reiterating the presence of a single InN wurtzite phase. Since we see oxygen by XPS and the bandgap is not changed, we believe the oxygen is only at grain boundaries.

A number of reports have attributed the observed high band gap of InN to Moss-Burstein shift [194,196] which occurs when carrier concentration exceeds the conduction band density of states forming the Fermi level in the conduction band. As a result, electrons fill the bottom of the conduction band and the band gap measured is higher. Hall measurements of our InN films yield the carrier concentration of unintentional n-doping to be high $10^{20} cm^{-3}$. The theoretical prediction by W. Walukiewicz et al. [116] (shown in the inset of Fig 4.4) for the above mentioned carrier concentration should give a band

gap of ≈1.78eV, which matches quite well with our measured value. Thus, our studies suggest that among the different factors suggested in the literature Moss-Burstein effect can explain the observed band gap in our degenerately n-doped InN films. Though at such a high background doping level one may expect alloying effects, since we do not observe any core-level shifts, such effect can be discounted[23].

4.2 Role of native defects in the nitrogen flux dependence of carrier concentration

Though the observation of the variation of bandgap values of InN has been attributed to oxygen incorporation[21] and In inclusion,[204] the observation of a strong Moss-Burstein shift[24] has successfully explained the observed values.[139,205,206] Studies by Kadir *et al.* have shown that increase in bandgap can be due to Moss-Burstein shift and the presence of 1% to 3% hydrostatic strain in InN films.[207] Butcher *et al.* examined the extent of this shift in high and medium carrier concentration material 5×10^{19} to 5×10^{20} cm^{-3} and proposed that the band gap is much higher than the recently accepted value of ≈0.64eV, due to non-stoichiometric nitrogen rich conditions resulting in strained films.[136] Biaxial strain arises due to the lattice mismatch between substrate and overlayer, while hydrostatic strain is mainly due to the presence of native point defects like vacancies, interstitials and antisites in the films.[208] In the case of InN, it is not yet clear whether interstitials or antisites cause the observed high background dopant concentration. Earlier, first principle calculations predicted that formation energies for nitrogen related defects (nitrogen interstitials - N_i) in n-type InN are very high (≈6eV),[209] but recent calculations and experimental results have proposed values ≈3eV[210] and ≈0.5eV[211] for nitrogen rich InN. The formation energies for other NPDs in N-rich and In-rich InN films are given in Section 1.7.1. Molecular beam epitaxial growth is kinetically driven and operates away from thermodynamic equilibrium, yielding deviations from stoichiometry due to subtle changes in growth parameters like substrate temperature, flux rates of species etc.[106,212] Among these different growth parameters, the effect of substrate temperature on the properties of InN has been well elucidated in the literature.[68,86,94,213] As described earlier, the effect of substrate temperature on the various properties of InN

is studied and the optimized the growth temperature to obtain good quality material on bare c-sapphire substrate is found to be 450 °C.[214] MBE growth of InN, in absence of substrate modifications and intermediate layers like nitridation, buffer-layers and epi-layers, provides strained films owing to the high lattice mismatch (≈25%) between c-sapphire and grown InN overlayer. Thicker films will lead to strain relaxation as the effect of strain, which originates from native point defects at interface, become negligible at increased thickness.[104] To produce InN films with low carrier concentration and lesser strain, they are usually grown on modified c-Sapphire substrates, on which intrinsic properties like band gap are measured.[215] To understand the reason behind the ambiguous properties, InN films should be grown on bare c-sapphire to avoid the formation of alloys[25,216], at intermediate layers. A systematic investigation of the effect of nitrogen flux rate on nitrogen related point defects induced strain and consequently on the band gap of InN, is described below.

4.2.1 Results and Discussions

Fig 4.8(a), (b), (c) and (d) show the FESEM plan view images of InN films grown on c-sapphire at different nitrogen flux rates of 2, 4, 6 and 8 sccm, respectively. The images show that, except for the film grown at 2 sccm, all the films have non-continuous granular surface morphology and the surface roughness increases with increase in nitrogen flux rate. RMS values of surface roughness for $5\times5\mu m^2$ scanned area for sample A to D by AFM are 47, 14, 21 and 35nm respectively. As seen in Fig 4.8(a), the sample grown at 2 sccm has large grains connected with flat and smooth surfaces consist of deep trenches that results in its high surface roughness. Low N-flux permits enhanced surface diffusion of In atoms resulting in a strain relaxed large connected network structure. The corresponding inset shows a predominantly streaky RHEED pattern, taken along $< 11\bar{2}0 >$ direction, characteristic of an atomically smooth crystalline surface. Fig 4.8(b) shows closely packed grains with less roughness compared to the other films. The inset shows the streaky plus spotty RHEED pattern, due to electron transmission through the crystalline 3D grains with flat tops. Fig 4.8(c) shows the FESEM image for the sample grown at a flux rate of 6 sccm having an average grain size of 100 nm and has higher roughness (RMS of 21nm) than that grown at 4 sccm (14 nm RMS). This high roughness may be due to N-rich

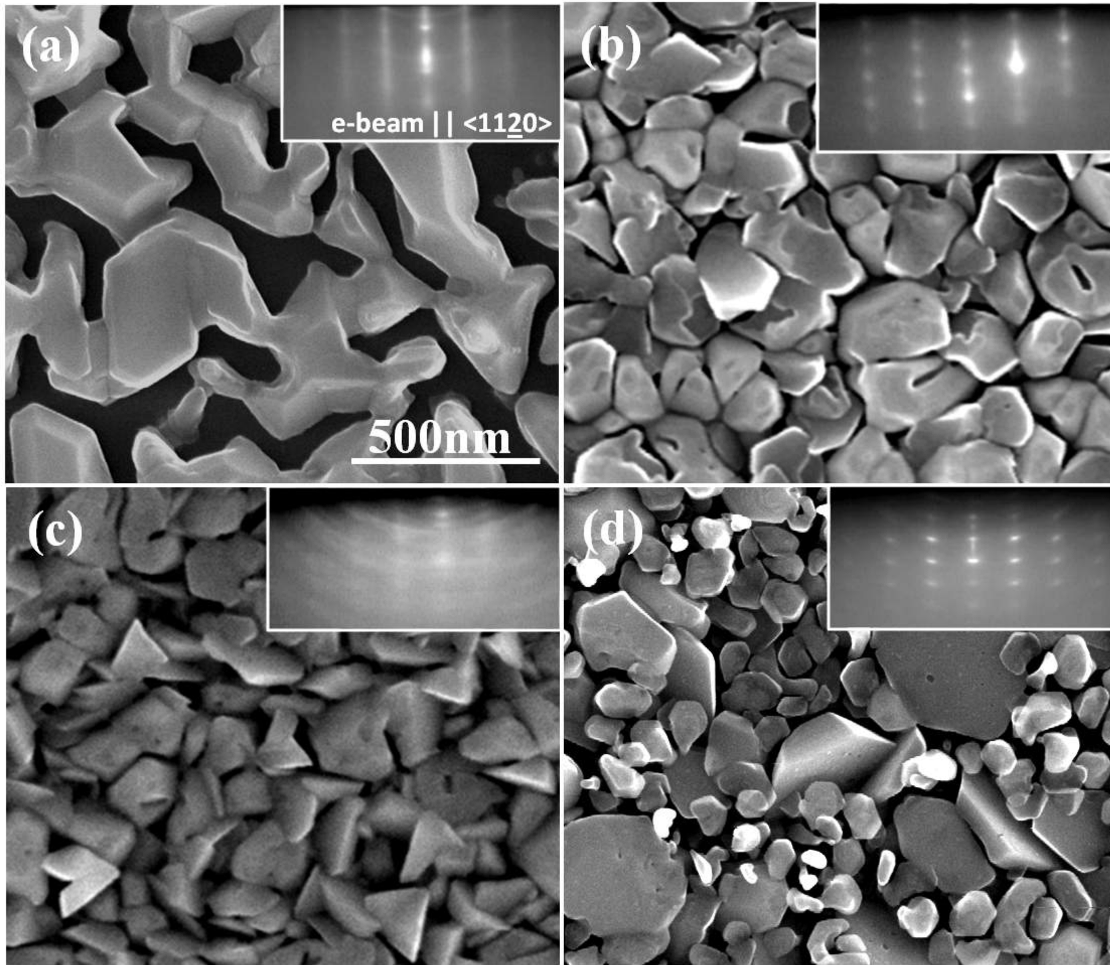

Figure 4.8: (a), (b), (c) and (d) show the FESEM images for the InN film grown at different N-flux of 2, 4, 6 and 8 sccm respectively and corresponding insets show respective RHEED pattern. Here RHEED is taken with e-beam $\parallel < 11\bar{2}0 >$.

conditions in which nucleation density increases due to reduced migration of In atoms and higher nitridation probability, resulting in smaller 3D island growth. The inset of Fig 4.8(c) shows a weak spotty plus amorphous ring pattern manifesting the polycrystalline nature of the film. Fig 4.8(d) shows the FESEM image for sample grown at 8 sccm nitrogen flux and has higher roughness compared to the films grown at 4 and 6 sccm, again resulting from migration restricted epitaxy with increasing N-flux. At this high flux rate (8sccm) as seen in the figure, grains with a wide distribution of sizes and shapes grow, with the average grain size being about 80 nm. The corresponding inset in Fig 4.8(d) shows the RHEED pattern with elongated spots superimposed on amorphous ring pattern depicting a relatively higher polycrystallinity of the 3D crystallites of the film. The formation of relaxed network structures and compact 3D island structures observed in the FESEM images indicate that tensile or compressive in-plane strain in our InN

films may be negligible. Averaged Line-scans of the RHEED pattern along < 0001 > and < $11\bar{2}0$ > directions, give a value of c/a to be 1.61 for sample grown at 4 sccm, while for the sample grown at 8 sccm the c/a ratio is 1.60.[217] Since the lattice parameter for ideally relaxed InN give a c/a value to be 1.61,[218] it can be seen in FESEM that InN films grown in our experiments have relaxed percolation structures with 3D island growth. Thus, FESEM and RHEED studies show network structures with atomically smooth surface at lower N-flux rates and rough polycrystalline 3D island morphology for the films grown at higher N-flux rates. At the very low flux rate (2 sccm) we do not have a continuous smooth film, but we observe a flat connected network structure with trenches. Overall, it can be seen that RHEED and FESEM studies suggest 4 sccm to be the optimal N_2 gas flow rate to obtain relatively good quality InN on bare sapphire substrate.

4.2.2 Strain measurements and possible native point defects

θ-2θ vs log of intensity scans by XRD measurements on these samples are shown in Fig 4.9(a-d) for the InN films grown at flux rates 2, 4, 6 and 8 sccm, respectively. Log of intensity is chosen for Y-axis, to accentuate low intensity peaks. From the XRD pattern it can be noticed that all films have wurtzite structure. Among all samples, InN films grown at 2 and 4 sccm nitrogen flux rates show dominant c-oriented peaks of InN(0002) and InN(0004) at $\approx$ 31.5° and 65.5° along with substrate Al_2O_3(0006) peak at $\approx$46.7° respectively. This is in accordance with the results of RHEED and FESEM discussed earlier for the same samples. In addition to these c-orientations, the film grown at 2 sccm has a very low intensity peak at $\approx$33.3° which is ascribed to InN($10\bar{1}0$). In case of InN films grown at 6 and 8 sccm nitrogen flux rates, in addition to the on axis planes InN(0002), InN(0004) we observe off axis planes InN($10\bar{1}0$), InN($10\bar{1}1$),InN($10\bar{1}2$), InN($11\bar{1}0$), InN($10\bar{1}3$), InN($11\bar{2}2$) and InN($20\bar{2}2$) at $\approx$29.3°, 33.3°, 51.7°, 57.1°, 61.8°, and 69.7°, respectively. However, films grown at 6 and 8 sccm have higher intensity single crystalline c-oriented peaks compared to the off axis components, suggesting that they are weakly polycrystalline in nature, in consonance with RHEED and FESEM results described earlier. The calculated c and a lattice parameters from InN(0002) and off axis high intensity peaks (averaged over all off-axis orientations) are A(5.686Å, 3.538Å), B(5.692Å, 3.534Å), C(5.675Å, 3.534Å) and D(5.675Å, 3.533Å) for InN films grown at 2,

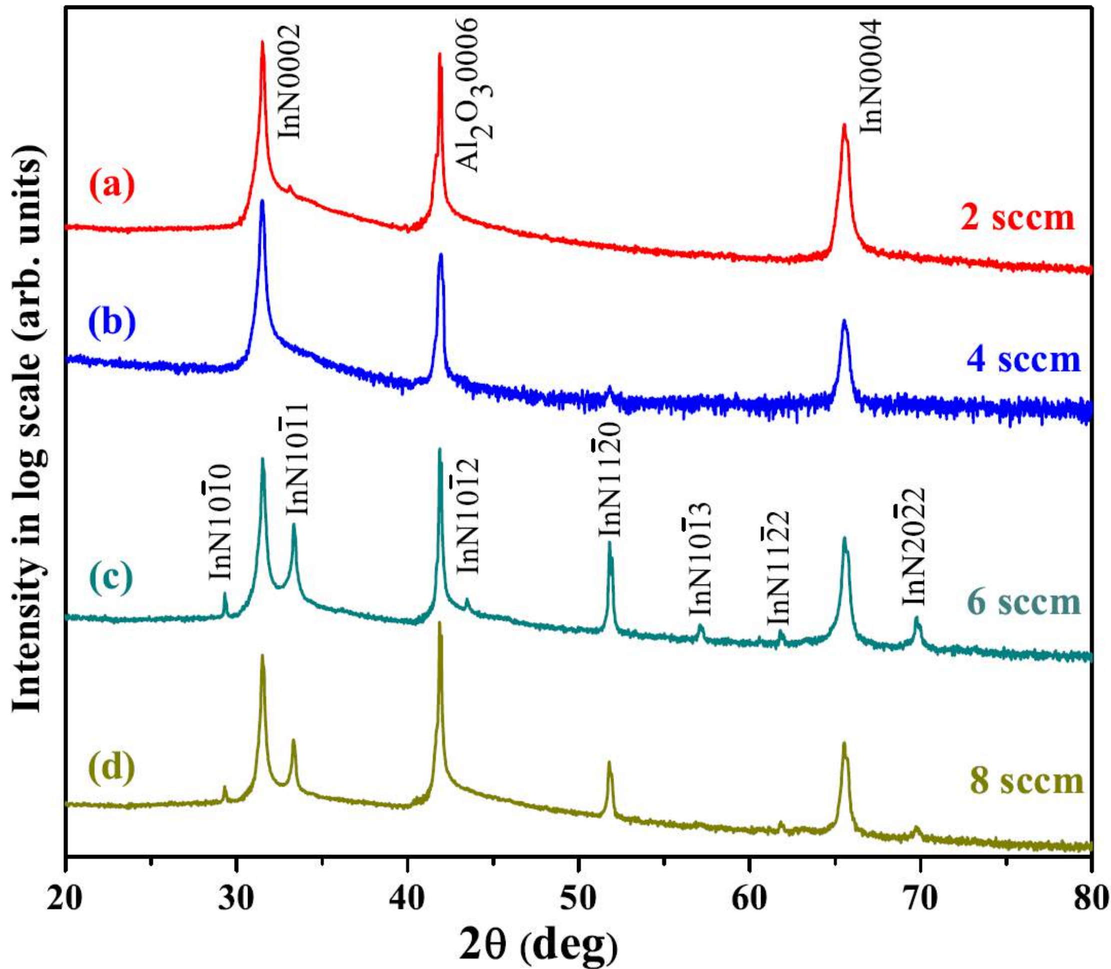

Figure 4.9: (a), (b), (c) and (d) show the XRD θ-2θ scans for the films grown at 2, 4, 6 and 8 sccm respectively.

4, 6 and 8 sccm, respectively.

Fig 4.10 consists of dashed and solid lines calculated for pure hydrostatic and biaxial strains, arising due to native defects in the overlayer and lattice mismatch between overlayer and substrate, respectively.[207,208] In the inset, open circles represent literature values obtained for films by MBE growth[218,219] while the solid circles are for MOVPE grown hydrostatically and biaxially strained InN films.[207] The inset shows that the lattice parameters calculated for our samples (solid triangles) show a small negative strain (compressive). This minimal biaxial strain can be attributed to the relaxed network structure and 3D island growth mode. As shown in Fig 4.11, the possible native defects in InN are nitrogen vacancies (V_N), indium vacancies (V_{In}), nitrogen interstitials (N_i), indium interstitials (In_i), nitrogen on indium sites (nitrogen anitsites:N_{In}) and indium on nitrogen sites (indium anitisites: InN). Since the size of nitrogen atom (56 pm) is smaller

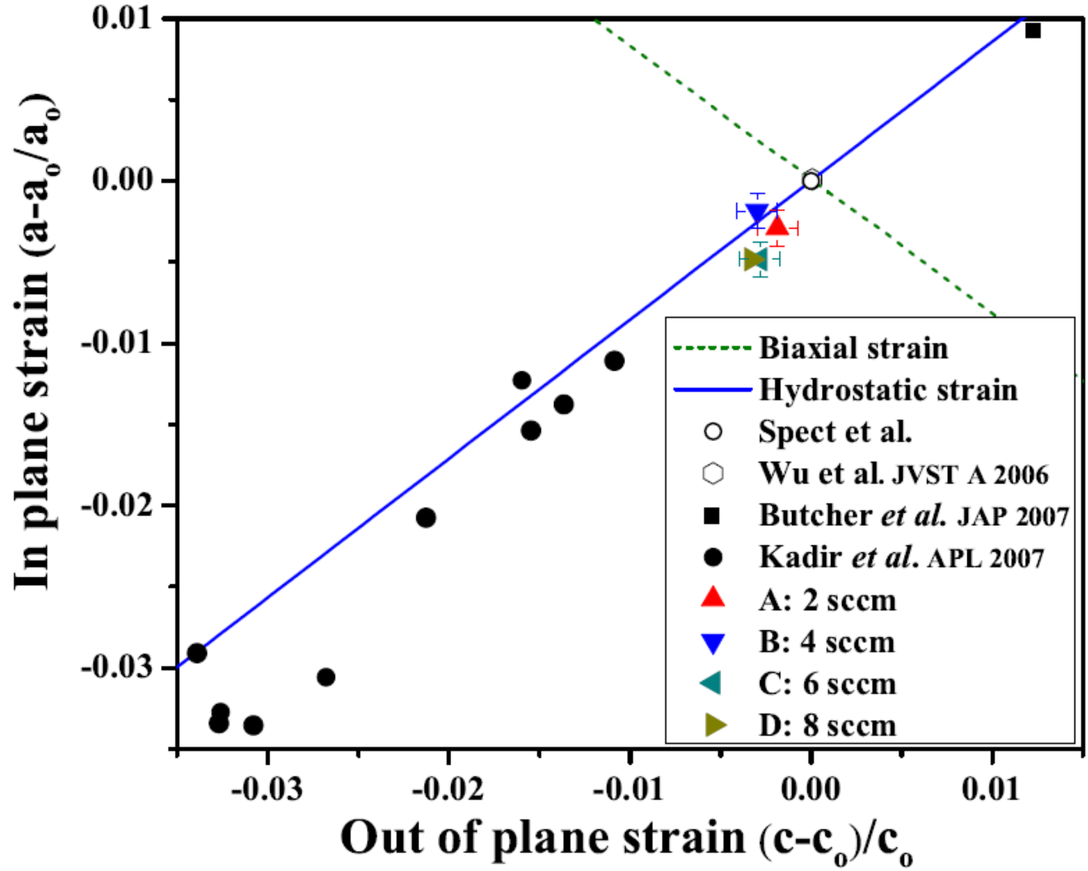

Figure 4.10: shows the plot of inplane vs out of plane strain. The solid and dashed lines indicate pure hydrostatic and biaxial strains and solid triangles show calculated strain values from XRD pattern. Open symbols show literature values of MBE grown films,[218,219] while solid circles are for MOVPE grown InN films.[207] solid square is for the rf sputter grown film by Butcher et al.[136]

than that of indium (156 pm), nitrogen antisites (N_{In}) and vacancies (V_N, V_{In}) reduce the unit cell volume whereas indium antisites (InN) and interstitials (N_i, In_i) increase the unit cell volume of the wurtzite InN. Here, since the measured lattice parameters are less than the relaxed values of c=5.706Å, a=3.537Å,[218] we can infer that our InN films have V_{In}, V_N or N_{In} defects. It has been shown earlier that presence of oxygen will lead to positive strain (tensile strain) in the InN films[208] due to the formation of crystalline indium oxide in the film, manifested as In_2O_3 related peaks in XRD pattern. Since our films are grown in an oxygen free environment (with oxygen partial pressur $<10^{-14}$ torr as measured by RGA) and we do not observe any In_2O_3 related peaks in the XRD pattern, we can discount any oxygen incorporation in the films. Thus, it is clear that the films grown at lower nitrogen flux rates 2 and 4 sccm are mono crystalline in nature, whereas the films grown at higher flux rates of 6 and 8 sccm are weakly polycrystalline. As in the

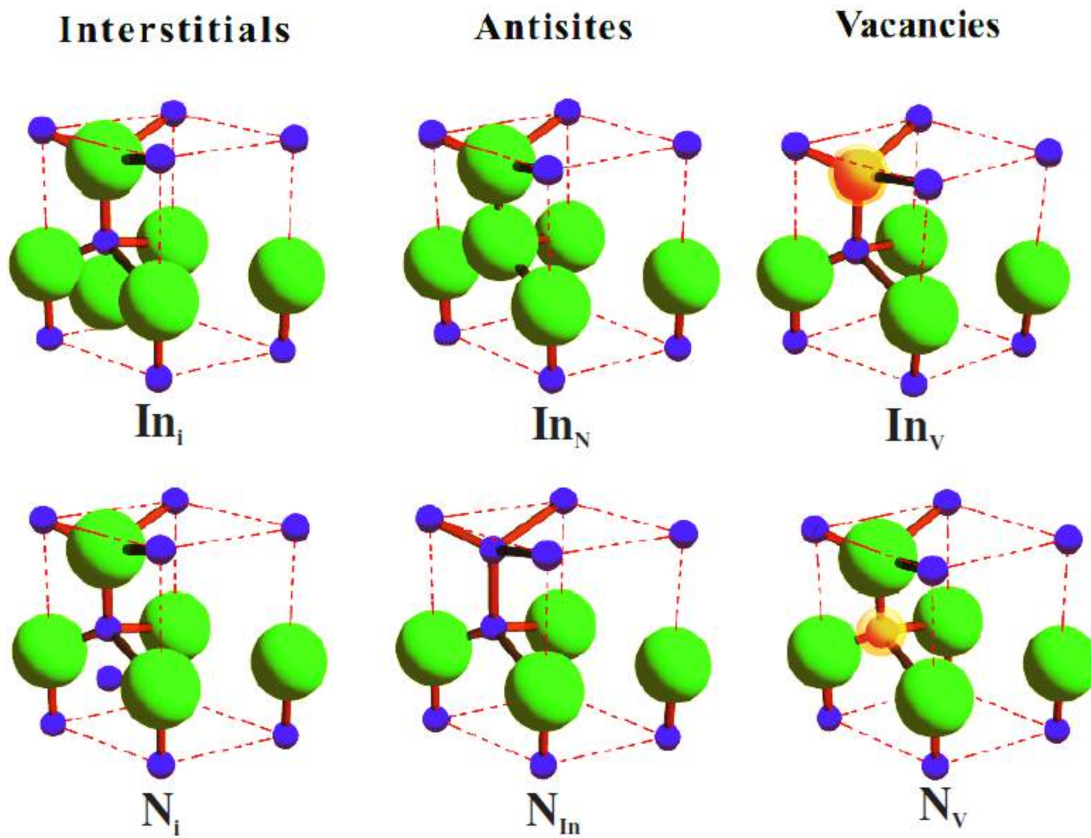

Figure 4.11: Possible Native Point Defects (NPDs) in InN material

RHEED and FESEM observations, XRD results again suggest 4 sccm as the optimal N flux rate for obtaining high quality InN films.

4.2.3 Optical absorption measurements: high band gap

Fig 4.12(a), (b), (c) and (d) show the optical absorption behavior of the InN films grown at 2, 4, 6 and 8 sccm, respectively. The absorption coefficient is determined from transmission measurements in UV-VIS and near infrared regions, using the expression $\alpha = \frac{1}{d}\ln\frac{1-R}{T}$ where R is reflectivity, T is transmittivity and d is sample thickness.[220] The direct optical bandgap is determined by the standard procedure of extrapolating the linear part of the squared absorption coefficient.[137] Fig 4.12 shows that the InN films grown at 2, 4, 6 and 8 sccm nitrogen flux show increasing absorption edge values at 1.29, 1.62, 1.72 and 1.93eV, respectively, and the free carrier absorption appears around 0.7eV.[105] These values of the absorption edge are larger than the current consensus bandgap value of 0.64eV[22] and smaller than the sputter grown InN bandgap values of

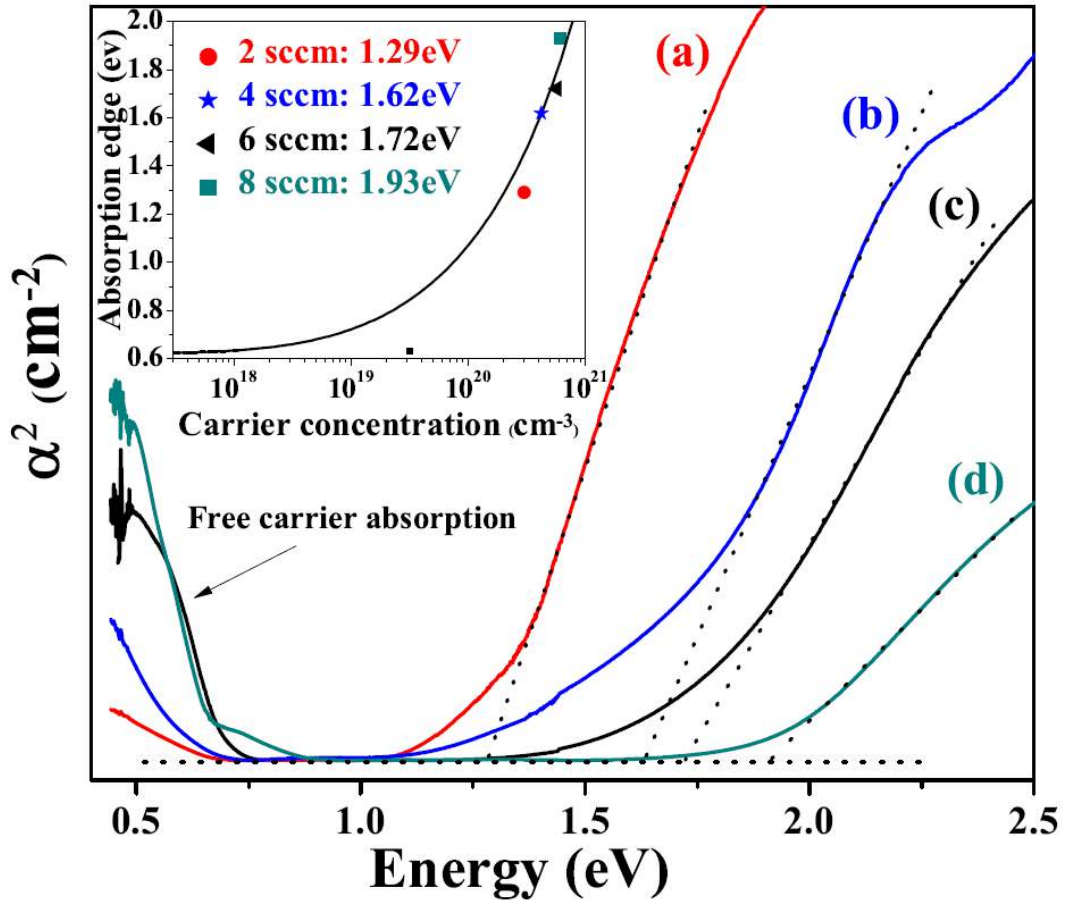

Figure 4.12: (a), (b), (c) and (d) show absorption (squared) plots for films grown at N-flux rates of 2, 4, 6 and 8 sccm, respectively. The inset shows theoretical Moss-Burstein shift curve along with our experimental points.

1.89eV.[81] We have determined the carrier concentration by Hall measurements for InN films grown at 2, 4, 6 and 8 sccm to be 3.1×10^{20}, 4.3×10^{20}, 5.7×10^{20} and 6.1×10^{20}cm^{-3} respectively. Thus, the increase in the intensity of free carrier absorption as seen in Fig 4.12 with increasing flux rate can be attributed to the increase in unintentional degenerate n-doping. As evident from Fig 4.8, since the grain sizes (80-100 nm) of all films are larger than the Bohr exciton radius (8 nm) of InN films,[221] the consequences of quantum size effects on variation in absorption edge of InN[222] can be neglected. Since the XRD and XPS results show the absence of In_2O_3 in our films, the increase in bandgap due to oxide formation can also be discounted. Another argument for the band gap variation is the Moss-Burstein (MB) effect, which accounts for the variation of absorption edge with carrier concentration in the degenerate doping limit. The inset to Fig 4.12 shows the Moss-Burstein shift curve plotted by assuming a non-parabolic conduction band and an intrinsic bandgap value of 0.64eV.[22,215] Our experimental data plotted in the inset

show that the absorption edge follows MB shift according to the respective degenerate concentrations. Thus, the variation in the absorption edge with N-flux can be attributed to the carrier concentration.

Earlier studies by Kadir *et al.* have attributed the increase in bandgap value of InN films due to Moss-Burstein shift and presence of 1% to 3% hydrostatic strain in InN films.[207] Since we observe a minimal strain of 0.5% in our films, the observed variation of band edge with carrier concentration can be solely due to the Moss-Burstein shift.[24] Butcher *et al.* re-visited the extent of Moss-Burstein shift in high carrier concentration InN material and proposed that the band gap of InN are much higher (>1eV) than the recently accepted value (≈0.64eV). He relates this to the different kinds of defects present and correlates it to nitrogen rich non-stoichiometric N:In ratios by Elastic Recoil Detection analysis.[136,212] In our XPS experiments, the N:In ratio determined from XPS survey scans are 1.08, 1.14, 1.19 and 1.27 for films A-D respectively,[203] there appears to be effect of excess nitrogen on the band gap of InN. Thus, the increase in the carrier concentration with the N flux can be due to the presence of extra nitrogen as point defects in the samples that can influence optical and electrical properties.

4.2.4 XPS: Nitrogen related native point defects

To understand the contribution of excess nitrogen to unintentional doping, we have performed core-level XPS measurements of N(1s). The variation in high binding energy component in N(1s) core level can be ascribed to variation in electronic structure due to nitrogen related point defects.[136] We have analyzed the acquired XPS N(1s) core level data, by Shirley background subtraction and deconvolution into Voigt components to observe any defect related manifestations. Fig 4.13 shows the deconvoluted N1s core level for films grown at 8 sccm showing components related to In-N bonding at 395.6 eV, atomic nitrogen peak at 397.9 eV and a defect related peak at 396.9 eV. An asymmetric tail observed at higher binding energies of the peak is attributed to the inelastic scattering of the core electrons due to a surface charge accumulation layer, which is observed on InN surfaces.[223,224] From Fig 4.13 it is clear that integral intensity of defect peaks in all our samples is higher than atomic nitrogen peak, showing the significant role of defects in our samples.

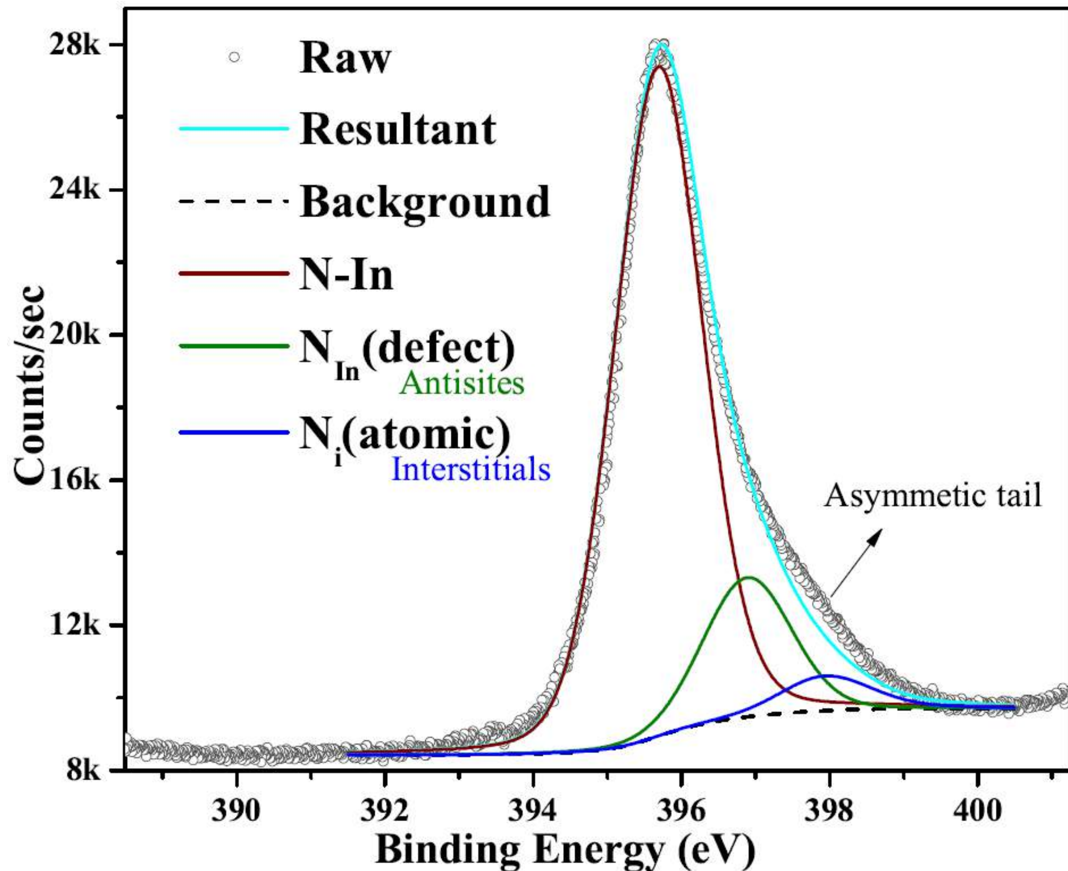

Figure 4.13: shows the deconvoluted XPS N1s core level for the sample grown at 8sccm.

From XRD strain measurements discussed earlier, the possible native defects can be nitrogen vacancy (V_N), In vacancy (V_{In}) or nitrogen antisite (N_{In}). Positron annihilation measurements performed on InN films concluded that the absence of nitrogen vacancies in InN films is not the reason for unintentional conductivity for InN, and in general for group III nitrides.[225] The increase of carrier concentration with increase in flux rate in our absorption and Hall studies and also N:In ratio values (>1) calculated from XPS survey scan permit us to exclude the presence of nitrogen vacancies in our MBE grown InN films. Though V_{In} causes reduced lattice volume, these shallow acceptors cannot explain the high carrier concentration observed in InN films. Since researchers[212] have experimentally confirmed by UV Raman spectra the presence of V_{In} at the interface in InN films, and provided evidence of excess nitrogen that can exist in the form of interstitial nitrogen, molecular nitrogen or nitrogen antisite. Thus, we can infer that the atomic nitrogen species, identified by XPS core-level analysis, may be present as nitrogen interstitials.

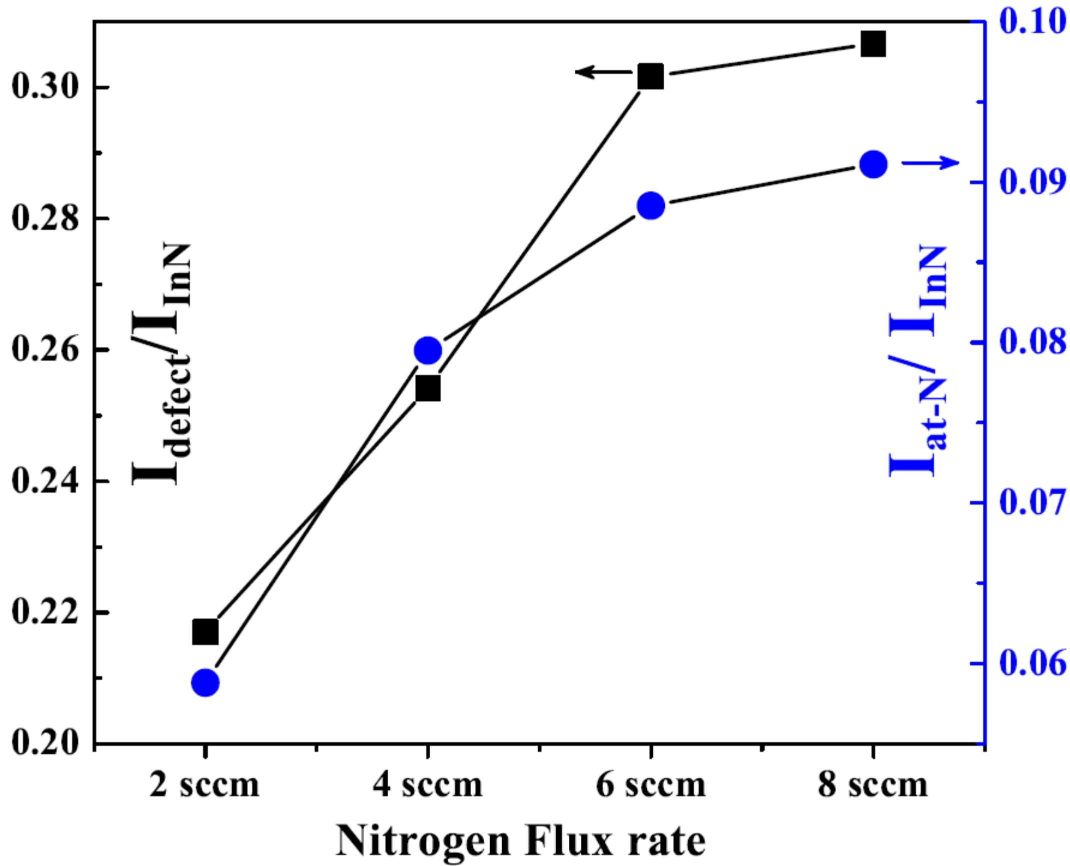

Figure 4.14: shows the integral intensity ratio of defect peaks to InN peak plotted versus N-flux rate. The solid squares and circles represent ratio of integral intensity of nitrogen interstitial and antisite defect to InN peaks respectively.

N on an In site is an unfavorable configuration with a formation energy 5eV. But experimental studies show that these are possible in growth that occurs in non-equilibrium conditions. Thus, nitrogen antisite is the thermodynamically most stable defect than nitrogen interstitial in nitrogen rich InN films.[211,212] Our results indicate that the mobile nitrogen species which occupy the In vacancies (V_{In}) may form the N anti-site defect. It has to be noted that the presence of N interstials will increase the lattice volume with lattice parameter larger than relaxed parameters. We speculate that the increased lattice volume due to nitrogen interstitials could be compensated by the reduction in lattice volume due to nitrogen antisites, resulting in minimal hydrostatic strain in InN films as seen in Fig 4.10. Since the integral intensity ratio of defect or atomic nitrogen to InN peaks increases with N-flux, as shown in Fig 4.14, the observed antisite N_{In} and nitrogen interstitials N_i in our InN films could be contributing to the high carrier concentration. Previous calculations[209,210] assuming a thermodynamic equilibrium, have proposed high

formation energy for nitrogen interstitials in InN, but as MBE or any epitaxial growth occurs far away from equilibrium, such formation energies can be much smaller.[211]

4.2.5 Inferences

To identify the factors that have been attributed in the literature to explain the high band gap observed for InN grown on bare sapphire, we have grown InN films by MBE and probed them by complementary techniques. All the samples grown at 400 °C, 450 °C and 500 °C are crystalline (wurtzite) α-InN and show a band edge emission at 1.78eV, irrespective of the growth temperature. Our results indicate that factors like quantum size effect, non-uniformity and presence of oxynitrides can be discounted as plausible reasons for the high band gap value. We demonstrate that single crystalline wurtzite InN can be grown on bare sapphire and its c-axis orientation depends strongly on substrate temperature. The optimum temperature for the growth of single crystalline c-oriented InN film on sapphire substrate is identified to be 450 °C. At 500 °C the c-axis of InN is parallel to the substrate a-b plane but at 450 °C we observe it to be parallel to the substrate c-axis. At still lower temperature of 400 °C, single phase InN consisting of both orientations of growth is observed. We infer that crystal orientation and In/N stoichiometry do not influence the band gap of InN. On these nitrogen rich InN films we conclude that strong Moss-Burstein effect can explain the observed high band gap.

Our results show that the films grown at lower N-flux yield a rough, connected network structure while high flux rate promotes polycrystalline 3D island growth. At all the flux rates studied, wurtzite InN films are formed, and we observe 4 sccm as the optimal flux rate to obtain good quality InN films. Absorption measurements showing the variation in absorption edge from 1.29 to 1.93eV as N-flux is varied from 2 to 8 sccm, are analyzed in light of various possible reasons viz oxygen incorporation, quantum size effect, Moss-Burstein shift and non-stoichiometry. We infer that the Moss-Burstein shift as the possible reason for band edge variation with carrier concentration, supporting the recent consensus on the intrinsic bandgap value of ≈0.64eV for InN. Our data shows that unintentional dopant density increases with N flux, indicating the role of nitrogen related point defects as a source of background dopants. The minimal compressive hydrostatic strain from XRD studies enables us to exclude nitrogen vacancies as possible background

dopants. Our analysis suggests that N-interstitials and antisites are the possible donor like defects in the PA-MBE grown InN films. Thus, experiments to optimize the various other MBE experimental growth parameters like plasma power and In flux, so as to reduce the native defects and consequently the carrier concentration, to improve the quality of InN formed on bare c-plane sapphire substrates, are performed and results presented in the next Chapter.

Chapter 5

Optical band gap and surface charge accumulation

This chapter focuses on the role of unreacted indium on the band gap of InN and role of In adatoms on near surface downward band bending. The issue of ambiguous values of the band gap (low to high) of InN thin film in the literature has been addressed by careful experimentation.

We have grown wurtzite InN films by PA-MBE at different growth temperatures (in the range of 400 - 470 °C) GaN epilayer/c-sapphire substrate, and characterized by complementary structural and chemical probes, that yielded films with various morphology and crystallinity and thus different optical properties. The band-gap values are determined by optical absorption and PL studies. Absorption edge is found to depend on the Hall carrier concentration as per the Moss-Burstein relation. Mie resonance as a reason for low band gap value (≈0.74eV) and also the formation of Indium oxides and oxynitrides as the cause for high band gap value (≈1.54eV) are evaluated. The charge accumulation and magnitude of near surface band bending is also studied on InN thin films by knowing the surface and bulk Fermi level position with respect to the valence band maximum using X-ray photoelectron spectroscopy and optical absorption measurements, respectively.

5.1 Introduction

InN has remained a puzzling material and a common consensus has not been arrived at regarding the reported crystallinity dependent material parameters such as effective mass and band gap owing to its low dissociation temperature.[22] The complexity and ambiguity has led to a wide spectrum of reported band gap values from 0.6 to 2.2eV, using different experimental techniques.[22,23] The higher band gap value observed has been largely argued to be resulting due to the presence of indium oxide, hydroxide, or oxynitride and related complexes.[24] Shubina *et al.* have attributed, the low band edge PL emission of 0.7-0.8eV, to Mie resonances due to the presence of In metallic clusters segregated at the grain boundaries which lead to the modification of the dielectric constant of the material.[204] In their XRD pattern the peak at 33° (2θ) has been attributed to the presence of metallic In clusters. However, K. M. Yu *et al.* have assigned the XRD feature at 33° to the presence of polycrystalline wurtzite InN d($10\bar{1}1$) crystallites, as they could not observe other metallic In interplanar distances either by XRD or SAED.[107] The origin of the band gap variation has been attributed to stoichiometry, quantum size effects, polycrystallinity, film non-uniformity, formation of alloys and also to the unintentional dopants in the host material.[23] Recent experimental results, largely not exclusively based on MBE, support a lower band gap value. Since the full spectrum of reported band gap values is not completely understood, assigning a band gap to InN is still elusive. The main reason that complicates the comparison of results is the lack of systematic studies on samples grown under same growth conditions and characterized by several complementary tools.

The previous chapter addressed the cause for the high band gap of InN on sapphire by studying the dependence of its properties on growth temperature.[214] Our systematic investigation suggested that presence of oxygen, stoichiometry, polycrystallinity and quantum size effect do not bear upon the high band gap observed for InN. Complementing this, the present work is an attempt towards being able to assign a proper band gap value of InN, by carefully designing an experiment to grow InN at four different substrate temperatures on GaN epilayer under the same growth conditions. We have chosen Molecular Beam Epitaxy for InN growth since growth temperature can be independent of the N_2 source and in an oxygen free UHV environment. With this approach, we

evaluate several proposed reasons in the literature for the band gap variations of InN and correlate the variation in the carrier concentration and band gap with the crystallinity of the material and with respect to the Moss-Burstein shift.

Epitaxially grown InN films comprise of a surface charge accumulation layer that pins the Fermi level well above the conduction band minimum which hinders device performance. First principle calculations have shown that the origin of Fermi-level pinning on InN and GaN polar and non-polar surfaces is the presence of metal adlayers on surfaces.[153] In case of GaN, Fermi level is pinned at ≈0.7eV below the conduction band minimum, where as for InN it happens at ≈1.2eV above. In case of narrow band gap semiconductors like InN and InAs, the Fermi level pins above the conduction band minimum since its value at Γ-point is much lower than the conduction band edge at other k-points, as revealed by band structure calculations.[141] This pinning has also been observed experimentally by energetic particle irradiation on group III-nitrides (InN, GaN) and on In rich alloys (InGaN). Defects induced by this irradiation result in saturated carrier concentration which permits the Fermi-level to stabilize in the vicinity of the branch point energy,[226] where the valence band like character switches to conduction band like behavior.[227] If the branch point energy is well above (below) the conduction band minimum, then the surface states act as donors (acceptors) which result in downward (upward) surface band bending, originated by the charge accumulation layer (depletion layer).[150,227] Anomalous downward band bending observed in InN has been attributed to the large difference in electro-negativity between In and N atoms, causing difficulty in the formation of high resistive InN films.[144] Indium adlayers on as grown InN films result from its low dissociation temperature which is even lesser than that of the native indium oxide, hence solely annealing at high temperatures may not be useful to get stoichiometric InN surfaces.[228,229] Electron accumulation on surfaces makes it very difficult to measure the electrical properties of the underlying stoichiometric InN layer and also can reduce device performance. Evidence for the presence of charge accumulation layer has been provided by several techniques like (high resolution electron energy loss spectroscopy) HREELS,[141] electrolyte based Capacitance Voltage, contact resistance,[226,230] XPS measurements[152] and theoretically by solving Poissons equation within the modified Thomas-Fermi approximation.[141] However, the physical origin of

this phenomenon is not yet unambiguously clear, and has been attributed not only to the presence of donor like surface states,[227] but also polarity of surfaces.[152,153,231,232] Experimentally, surface electron accumulation has been observed for both polar and non-polar surfaces[114] while it was absent on *in-situ* cleaved non-polar InN surfaces.[152] Initially, researchers observed this surface charge accumulation on InAs surfaces and later on InN and on single crystalline undoped In_2O_3 surfaces and attributed it to native surface defects.[142] The Fermi level pinning positions for InAs, InN and In_2O_3 are reported to be at ≈0.2eV, ≈1.2eV and ≈0.4eV, respectively,[145] above the conduction band minimum.

It is important to point out that the accumulated surface charge may be solely related to the In(4d) electrons. However, recently, reports by Chang *et al.* and Zhao *et al.* have shown the absence of surface Fermi level pinning on non-polar lateral surfaces of intrinsic c-oriented non-tapered InN nano wires,[231,232] which highlights the role of morphology in this observation. Researchers working on surface electron accumulation have used hydrogen irradiation and HCl followed by annealing for cleaning the InN surfaces,[141,224,229] which itself can result in electron accumulation,[224,233] low energy nitrogen ion bombardment also has been previously shown to create near surface donor defects that resulted in Fermi level stabilization,[113] and thus causing ambiguity in understanding this phenomenon.

Surface charge accumulation could be one of the reasons for experimentally obtained lower mobility values. Still there is a room to improve the experimental mobility of InN. Hence, careful experiments needs to be performed by varying basic parameters like growth temperature, In flux and thickness. Here, we try to understand the reasons that cause electron accumulation on surfaces of InN films formed at different temperatures and magnitude of the band bending is measured for mono and polycrystalline degenerate InN films using both XPS and optical absorption studies. The InN films are cleaned by using inert low energy Argon ions by which there is no preferential sputtering of the nitrogen and thus no III-V bond breaking.[234] The value of band bending resulting from this space charge on InN surfaces is determined by XPS-valence band and optical absorption spectra, and is observed to be dependent on the morphology and carrier concentration of the formed films.

5.2 Experimental details

InN thin films A, B, C and D presented here were grown by Radio Frequency Plasma Assisted Molecular Beam Epitaxy system (RF-PAMBE, by SVTA, USA) on a 2μm thick GaN epilayer formed on c-Sapphire (grown by Hydride Vapor Phase Epitaxy) at substrate temperatures of 400 °C, 430 °C, 450 °C and 470 °C, respectively. InN growth is carried out in a narrow regime of growth temperature as InN is very sensitive to the growth temperature because of its low dissociation temperature. N_2 flux rate for all the InN growth is 4.5sccm with a Radio Frequency (RF) plasma forward power of 375W. Optical band gap values are obtained from Photoluminescence studies. For valence band analysis, stoichiometry and composition measurements, *ex-situ* X-ray Photoelectron Spectroscopy (XPS) has been performed with a relative composition detection better than 0.1%, and energy resolution of 100meV at 90% peak, calibrated by observing the Fermi level position of a clean Au foil electrically connected to the sample surface. Before performing XPS measurements, InN thin films were sputter cleaned by an optimized low energy (0.5keV, 2μA) Ar^+ ions, to remove physisorbed adventitious carbon and oxygen resulting from atmospheric exposure, without affecting their crystalline quality and surface composition.

5.3 Optical band gap: need of non parabolic conduction band

5.3.1 Structural characterization

We have performed several complementary experiments to understand the subtle relation between surface morphology, composition and structure of InN films formed at different substrate temperatures in a narrow (400 °C - 470 °C) range. Fig 5.1(a-d) show the AFM surface morphology scans with their respective RHEED pattern for InN films grown on GaN epilayer at 400 °C, 430 °C, 450 °C and 470 °C, respectively. The AFM images are acquired at different scales to view the fine features according to surface smoothness of the formed films. Fig 5.1(a) is for film formed at 400 °C and shows a granular surface morphology with 60-70nm 3D islands, whose RHEED inset shows a

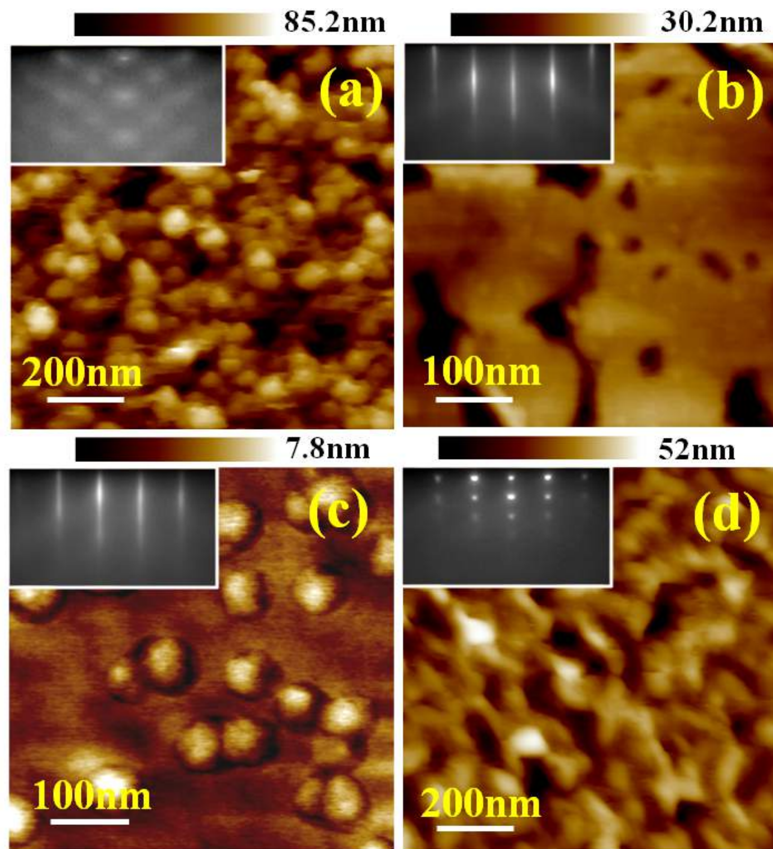

Figure 5.1: (a), (b), (c) and (d),show the AFM images for the InN film grown on GaN epi-layer at 400 °C, 430 °C, 450 °C and 470 °C respectively, and values for gradient color bars above each image depicts height contrast of the features. The insets show respective RHEED pattern taken with e-beam $\parallel < 11\bar{2}0 >$.

diffused spotty pattern due to the transmission of the electron beam through the 3D features. Fig 5.1(b) and (c) are for films grown at 430 °C and 450 °C, and show flat InN films with a few depressions in (b) and a few (10^7cm^{-2}) 50-60nm nano-metric objects dispersed on them in (c). Insets of Fig 5.1(b) and (c) show sharp streaky RHEED pattern which indicate the flatness of their surfaces and their single crystalline nature. Fig 5.1(d) is the AFM topography of the film grown at 470 °C which has a rough surface with deep trenches, manifesting as a spotty RHEED pattern. Color bars on top of the respective images in Fig 5.1 show height contrast of the features and the RMS surface roughness values measured by AFM for samples E to H are 17.3, 7.2, 4.6 and 10.9nm, respectively. The higher surface roughness for the films E and H is due to the poor crystal quality (discussed later) at lower temperature and relatively more dissociation of InN at higher temperature, respectively. Thus, the films grown at the low (400 °C) and high (470 °C) temperatures result in higher surface roughness while those formed at intermediate

temperatures of 430 °C and 450 °C, display a flat morphology.

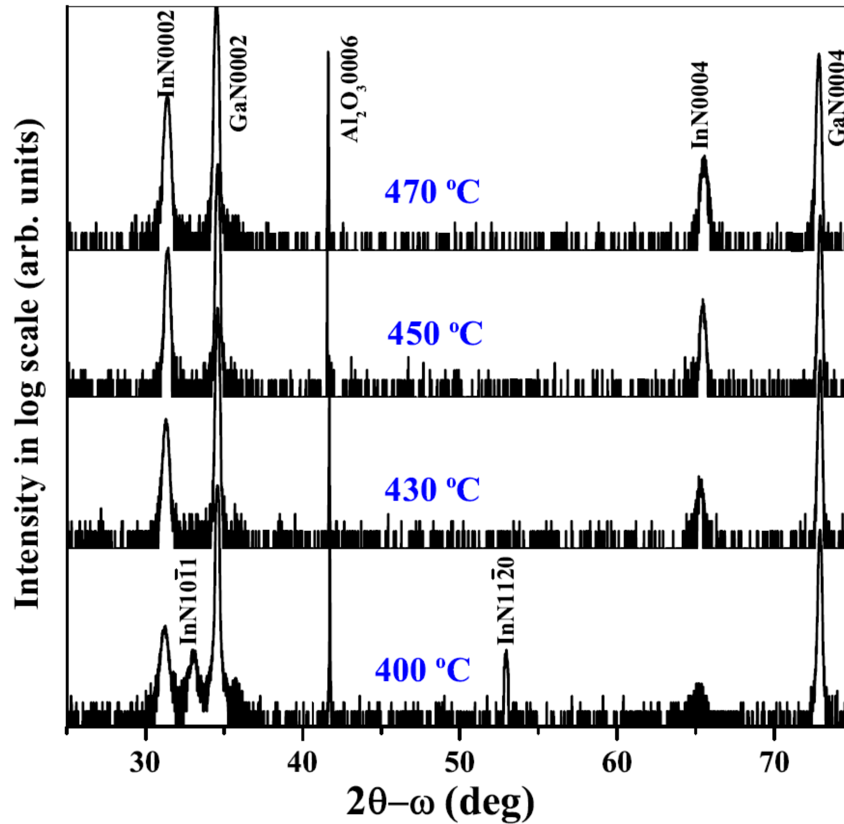

Figure 5.2: shows the HRXRD $2\theta - \omega$ scans for the films grown on GaN epi-layer at 400 °C, 430 °C, 450 °C and 470 °C.

Fig 5.2 shows the HRXRD measurements made with respect to Al_2O_3(0006) reflection at 41.68° as reference plane, to reveal the crystal structure of the InN films, where a logarithmic Y-axis is plotted to identify weaker signals from the off-axis planes. The top and bottom spectra correspond to typical 2theta-omega (2θ-ω) scans obtained for InN films grown on GaN epilayer at 450 °C and 400 °C, respectively. The pattern show that all the epitaxial films grown posses single crystalline wurtzite structures by indentifying the c-oriented peaks: InN(0002) at 31.28° and InN(0004) at 65.30°, along with GaN epilayer and c-Sapphire related ones: GaN(0002), GaN(0004) and Al_2O_3(0006) at 34.50°, 73.50° and 41.68°, respectively.

In the case of sample A in addition to the on-axis planes InN(0002), InN(0004) we observe less intense extra peaks at 33.2° and 52.6° which we attribute to off axis wurtzite planes InN(10$\bar{1}$1) and InN(11$\bar{2}$0), respectively.[107] This suggests that sample A along with predominant c-oriented crystallites also have a few crystals with other orientations,

resulting in a weak polycrystalline component of the film which was also clearly observed by RHEED. We find sample C which shows a band edge of about 0.74eV, has no peak around 33° in the XRD pattern, while samples A shows a peak at 33.18° which, we assign to the orientation $(10\bar{1}1)$ of wurtzite InN. As discussed earlier Shubina *et al.*,[204] had attributed this peak to metallic In which lead to low absorption edges due Mie-resonances and infrared emission resulting from interface states between metallic In cluster and InN boundary. But our data shows that sample having this XRD feature at around 33.18° show high band gap (≈1.54eV), whereas sample C which has a low band edge value of ≈0.74eV (Fig 5.5) does not have this peak. Though peaks, In(101) at 32.96° and InN$(10\bar{1}1)$ 33.18° are difficult to resolve. Since there are no other metallic In related reflections and that we dont observe low band gap value on sample A, we unambiguously ascribe the feature to InN wurtzite crystallites having $(10\bar{1}1)$ growth orientations.[107] The absence of $(10\bar{1}1)$ orientation or metallic In related contribution in sample B, C and D indicates that these samples are single crystalline in nature. Thus, the study clearly excludes the role of any metallic In in determining the band gap of InN film. It can also be noted that the presence of oxygen in the growth environment will result in the formation of crystalline indium oxide in the film which will be manifested as diffraction peak in XRD. We do not observe any oxide related peak in XRD pattern. Thus, HRXRD shows that the film grown at the lower temperature of 400 °C is polycrystalline with no evidence for the presence of crystalline indium metal or indium oxide phase on the surface.

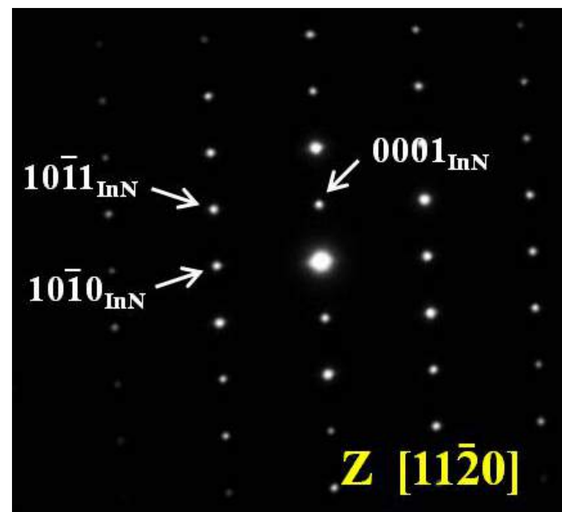

Figure 5.3: shows SAED pattern obtained on 400 °C grown sample

In order to check the presence of amorphous In in the grown samples, Selective Area

Electron Diffraction (SAED) studies are performed. The ring like pattern and the other spots related to amorphous and single crystalline In, respectively, are not observed in SAED pattern, as seen in Fig 5.3, which infers clearly that there is no presence of either single crystalline and amorphous Indium in the formed InN thin films.

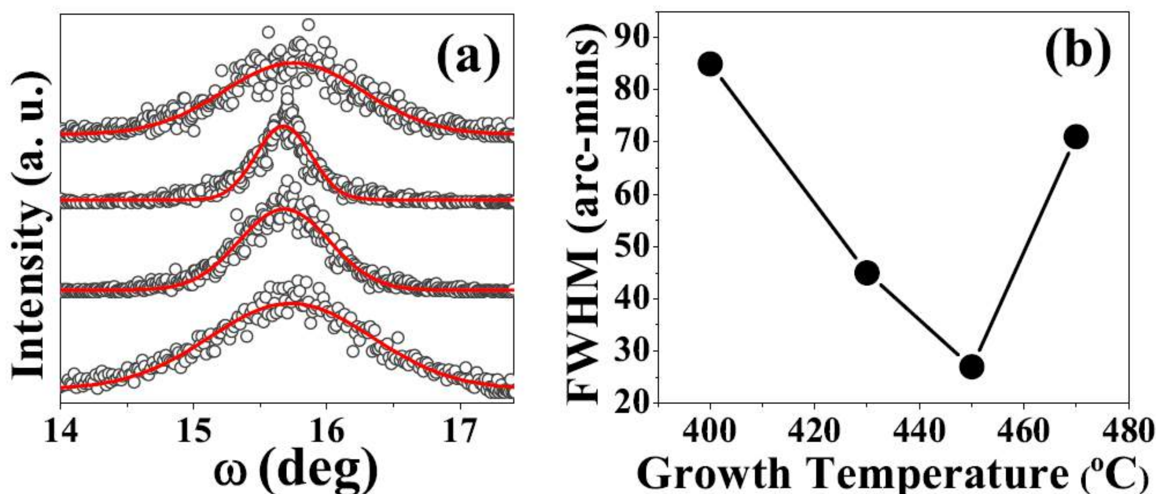

Figure 5.4: (a) shows the ω-scans (bottom to top) for the InN(0002) reflection of films grown on GaN epi-layer at 400 °C, 430 °C, 450 °C and 470 °C. Solid red lines are Gaussian fits for the data points. (b) shows FWHM values ω plotted versus growth temperature.

Fig 5.4 shows the ω-scans around InN(0002) reflection having FWHM 85, 45, 27 and 71 arc-mins, respectively. (b) plots the variation of the InN(0002) peak FWHM values versus growth temperature. Higher FWHM values are seen for films grown at low and high temperatures of 400 °C and 470 °C, while the films grown at the intermediate temperatures 430 °C and 450 °C show better crystalline quality. This corroborates well with the observations made by AFM micrographs and the RHEED pattern discussed earlier.

5.3.2 Optical band gap measurements

Single field Hall measurements were performed in the Van der-Pauw geometry at room temperature to estimate the electron concentration of the films as a) 4.0×10^{20}, b) 5.2×10^{19}, c) 2.4×10^{19} and d) 1.5×10^{20}cm^{-3}, differing with the different resistivity values of the films. The variation in carrier concentration is according to the crystal quality. Mobility values for respective carrier concentrations are 55, 70, 75 and 63cm^2/V-sec.[86] These high carrier concentration and low mobility values are reasonable for InN

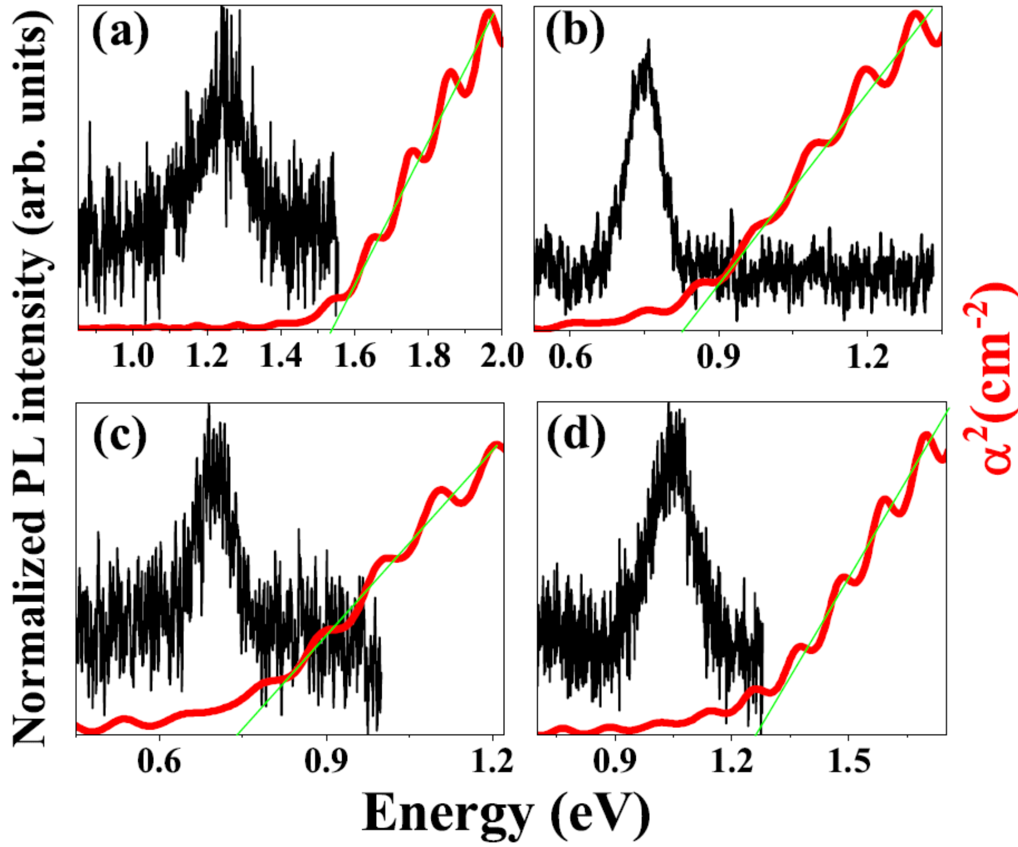

Figure 5.5: (a)-(d) show the normalized PL band-edge emission and absorption squared plots for the samples A, B, C and D films.

films having thickness of ≈300nm. Reported high mobility values in the literature are due to the higher thickness of the formed films and different growth schemes employed.[78,86,128]. The first observation of PL for InN film was reported only in 2002,[26] due to the poor quality of InN films synthesized earlier. In this study, we have observed photoluminescence with a strong band edge emission even at RT[105,118] in our samples, ascertaining the good quality of the films grown. The insets (a)-(d) show normalized PL spectra (Y-axis) and absorption squared plots (alternate Y-axis) for InN films grown at a) 400 °C, b) 430 °C, c) 450 °C and d) 470 °C. The band edge emission values obtained by PL for the samples and are 1.25, 0.75, 0.70 and 1.05eV with FWHM values of 160, 85, 72 and 130meV, respectively which increase with increasing carrier concentration.[105,235] The absorption coefficient is determined from transmission measurements, using the expression $\alpha = \frac{1}{d} \ln \frac{1-R}{T}$ where R is reflectivity, T is transmittivity and d is sample thickness.[220] The direct optical band gap is determined by the standard procedure of extrapolating the linear part of the squared absorption coefficient.[137] The interference

fringes seen in the absorption curve are due to Fabry-Perot oscillations.[236] Absence of these oscillations in our earlier reported absorption spectra[215] is due to relatively nonuniform thickness of the GaN epilayer that is used as buffer,where the interference effects are destroyed.[237] As shown in the inset, obtained absorption edge values for samples a-d are 1.54±0.05, 0.82±0.05, 0.74±0.05 and 1.25±0.05eV, respectively, and are higher than the recent consensus value of 0.63eV[195] due to the respective charge carrier concentration in the films.[205]

In case of heavily doped narrow bandgap semiconductors with non-parabolic conduction band, for instance in InN, the optical transitions in Photoluminescence are because of the recombination between electrons in the conduction band which has the Fermi level deep inside it and valence band heavy holes. Any conduction band electron from Fermi level to conduction band minimum (CBM) can take part in this process, whereas in optical absorption only direct transitions can take place from the valence band minimum (VBM) to the Fermi level in conduction band. As a result PL emission exhibits at the lower energy than the absorption edge.[22] Absorption studies are a good measure of the position of the bulk Fermi level and thus Moss-Burstein shift. Plotting the values of band edge values from optical absorption and carrier concentration from Hall in Fig 5.6, reveals a good agreement with the Moss-Burstein curve, where the shifts in absorption edge energies are attributed to strong band filling effects resulting from unintentional degenerate doping.[76,205]

Literature shows unintentional dopant density values up to $\approx 2\times10^{21}\text{cm}^{-3}$ in InN from various sources[23] which has been attributed to the presence of oxygen, hydrogen, excess nitrogen and to nitrogen vacancies, but a conclusive agreement has not yet been arrived at.[23] Also, the influence of InN crystallinity on the background doping level is yet to be addressed. Beginning with Trainor and Rose in 1974, there have been several attempts to correlate the band gap variation with carrier concentration.[65] The generally accepted Moss-Burstein shift[205,206] occurs when the carrier concentration becomes larger than the conduction band edge density of states and the measured absorption edge shows higher values than the actual band gap of the material. Tansley and Foley used an empirical fit to suggest that high band gap InN materials show a weak dependence on carrier concentration.[238] Later Davydov *et al.* calculated the Moss-Burstein shift taking into

account parabolic conduction band represented by the equation (5.1).[239] Their theoretical curve using an effective mass value of $0.1m_0$ was shown to adequately describe the band gap variation.

$$E_C(k) = E_G + \frac{\hbar^2 k^2}{2}\left(\frac{1}{m_v} + \frac{1}{m_c}\right) \tag{5.1}$$

where E_G is the direct band gap energy, $\hbar$= reduced Planck's constant, $k = (3\pi^2 n)^{1/3}$, m_v and m_c are electron effective mass at CBM and VBM. However, in a later study the same calculation is found to severely overestimate the observed band gap values.[98] Another successful attempt to elucidate the band gap variation of MBE grown samples was carried out by Wu *et al.*, who used both parabolic and non-parabolic conduction band to evaluate the shift, though it was found that the former method with an effective mass of $0.07m_0$, over-estimates the shift.[76,139] For narrow band gap semiconductors, since the conduction band edge gets modified because of the interaction between valence and conduction bands, a non-parabolic conduction band calculated using **k.p** band structure evaluation method was employed. They calculated the conduction band dispersion by solving Kanes two band **k.p** model,[140] as follows:

$$E_C(k) = E_G + \frac{\hbar^2 k^2}{2m_0} + \frac{1}{2}\left(\sqrt{E_G^2 + 4E_p\frac{\hbar^2 k^2}{2m_0}} - E_G\right) \tag{5.2}$$

where, E_G is the direct band gap energy, m_0 is the rest mass of electron and E_p is an energy parameter related to the momentum matrix element, $\frac{2}{m_0}\ |\langle S|P_x|S\rangle|^2$. Based on experimental results they have assumed a band gap value of 0.7eV and the value of E_p (=10eV) was deduced by the fit of experimentally obtained effective mass variation with carrier concentration.[76] Though the predicted curve explains well the MBE results, we find that data obtained from samples grown using other experimental techniques (discussed later) fall well below the curve. For the high carrier concentration material with low band gap, this has led to the argument that low band gap value is the result of defect level emission.[23] Different theoretical predictions for the Moss-Burstein shift available in the literature have been mainly derived based upon limited observations or

have considered only samples grown solely using MBE. But a consideration of several data by all techniques in the literature is essential to evaluate the goodness of fit and to assign the band gap variation to the Moss-Burstein shift. It is also to be noted that effective mass, a key factor in the device performance and a potential parameter in deriving the Moss-Burstein shift, is also endowed with a range of reported theoretical values from $0.06m_0$ to $0.59m_0$ [90] and experimental values from $0.04m_0$ to $0.24m_0$.[22] Since the Kane matrix element is independent of compounds, the variation of effective mass with band gap is linear, and this for InN with low band gap requires low effective mass.[240] However, the occurrence of the high band gap in InN (1.9eV) with an effective mass of $0.11m_0$ falling on the linear curve has led to an ambiguous situation.[240]

To study the dependence of band gap variation with carrier concentration, we have performed Hall measurements on the four samples.[105] Results of our measurements (star symbols) along with various experimental measurements reported in the literature are consolidated in Figure 5.6.[22,23,98] It can be seen that there is an order of magnitude reduction in the carrier density in the low band gap samples B and C compared to larger band gap samples A and D. Our results and the experimental growth condition does not support oxygen as a plausible source of background dopant in our samples and could be due to other suggested dopants in the literature such as nitrogen related point defects.[49] For InN growth on bare sapphire substrate the lattice mismatch in the two epitaxial directions viz. $[11\bar{2}0]$InN $\parallel$ $[11\bar{2}0]$sapphire and $[10\bar{1}0]$InN $\parallel$ $[11\bar{2}0]$sapphire are -25.4% and +29.2% which is much closer to each other in absolute magnitude compared to other III nitrides on bare sapphire which, for example, for GaN are respectively equal to -33.0% and +16.0%.[25] where sample B, C and D show relatively high quality single crystalline smooth films. The weak polycrystalline nature of sample A with their rough surfaces also suggest increased defects owing to orientational grain boundaries resulting from the growth direction other than in c-axis. For sample A we have observed reflections corresponding to other orientations of growth viz. InN$(10\bar{1}1)$ and InN$(11\bar{2}0)$ which will lead to form interfacial defects. Observing the considerable scatter in the reported band gap values from various sources, shown in Figure 5.6, we have carried out a non-linear curve fit of the experimental data to the Levenberg-Marquardt algorithm which is based on chi-square minimization.[241,242] We observe from Figure 5.6 that there are reported

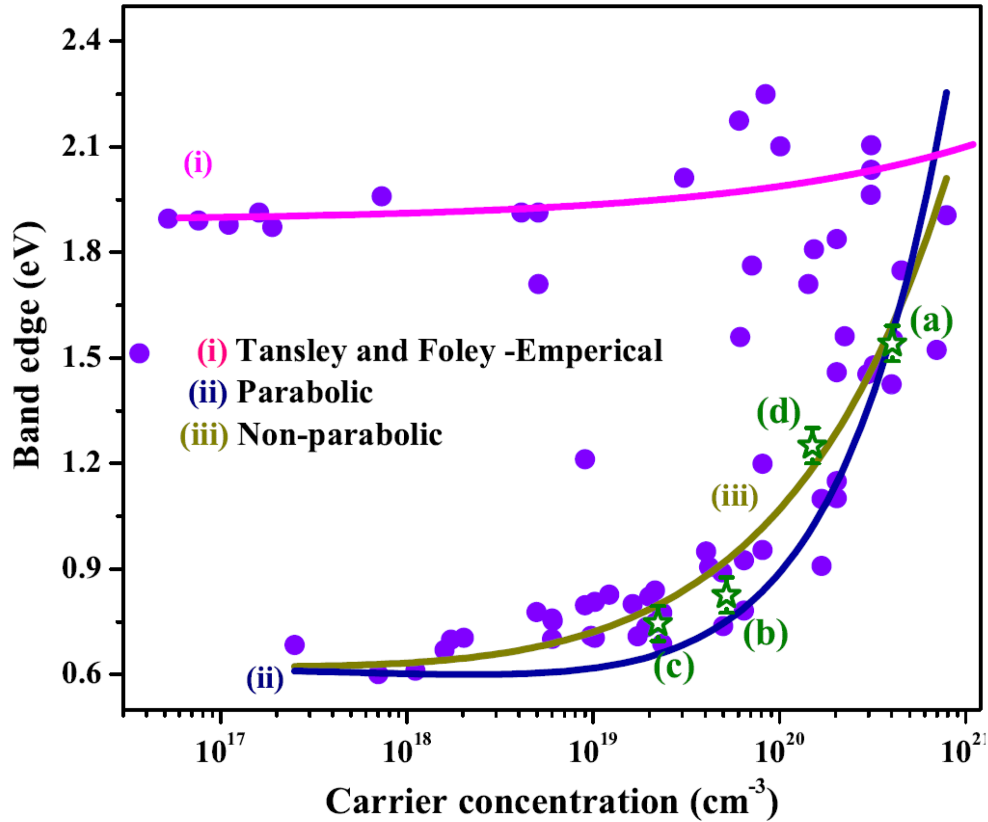

Figure 5.6: Different reported experimental band gaps for InN from literature[22,23,98] and present experiments, along with Moss-Burstein shift calculations: (i) Tansely Foley empirical data, (ii) assuming parabolic conduction band and (iii) assuming non parabolic conduction band. The star symbols (a-d) are from the present experiments.

high band gap values with low carrier concentration from the earlier work by Tansley and Foley[238] using RF-sputtering, but, have not been reproduced in the literature since. There is a possibility of continuous alloying or mixture of indium oxide and indium nitride, which as per effective medium theory can result in an in-between band gap value. It has been shown that indium oxide shows a very weak dependence of band gap with carrier concentration[96] as seen in Figure 5.6 for the fit by Tansley and Foley. This prompts us to exclude these experimental values from the following analysis. M. Alevi *et al.*[138] have used an empirical exponential fit to their data of the band gap variation with carrier concentration for their HPCVD grown InN/GaN/Sapphire samples, and show that the fundamental band gap of InN is about 1.20eV. Since the trend of the data points presented in Figure 5.6 shows clearly that the Moss-Burstein curve for InN follows an exponential form, we have fit an exponential function to the available data points. Chi-square minimization for this empirical exponential function shows a good agreement with the data and yields a band gap value of 0.7eV, which is higher than the

recent reported value.[22] As discussed in the introduction, a parabolic conduction band has been used in many reports to derive the Moss-Burstein shift. We have performed a non-linear fit to the data, assuming parabolic conduction band with effective mass (m*) as the fitting parameter. The hole effective mass in the valence band is assumed to be that of free electron and the band gap value is fixed to the recently accepted value of 0.64eV. Effective mass obtained from this fit is about ≈0.15m_0 which is higher than most of the reported values.[22] Also it can be seen that the best fit obtained after chi-square minimization for parabolic conduction band assumption shown in Figure 5.6, underestimates the shift especially in case of band gap data for low carrier concentration material, suggesting the need for a non-parabolic conduction band for InN. As described earlier, a carrier concentration dependent effective mass resulting from non-parabolic conduction band has been much argued for InN[139] which is based on the experimental observation that effective mass varies with carrier concentration. We have observed that, depending on the crystallinity of the samples, the carrier concentration changes and hence effective mass can vary for the samples. We have performed a non-linear curve fit to the data shown in Figure 5.6, assuming a non-parabolic conduction band with energy parameter Ep as the fitting parameter. Using the conduction band dispersion given by Eq. (5.2), a non-linear curve fit yields a band gap value of ≈0.64eV and E_p of 9.5eV, which is close to the value deduced for E_p by Wu *et al.*[76] We find that calculation with non-parabolic conduction band yields a better fit to most of the experimental data. It has to be noted that for both the parabolic and non-parabolic calculations, we have taken into account the conduction band renormalization effects due to electron-electron interaction and electron-ionized impurity interaction, considering the dielectric constant to be 6.7,[90] without which it deviates from literature values leading to a poor fit. Observation of low band gap values well below the calculated curve for InN having high carrier concentration has led to the argument that the low band gap infrared emission results from the defect states of a high band gap InN material.[23] The equi-distribution of data points above and below the fitted curve shown in Figure 5.6 suggests that the large scatter in the values can be attributed to measurement errors in determining the band gap due to band broadening and strong change of refractive index near the band edge.[23] Thus, a low band gap value with a non-parabolic conduction band can explain the variation in the band gap values of InN.

5.4 Surface charge accumulation and band bending

5.4.1 Removal of physisorbed surface contaminants: Low Energy Ar^+ sputtering

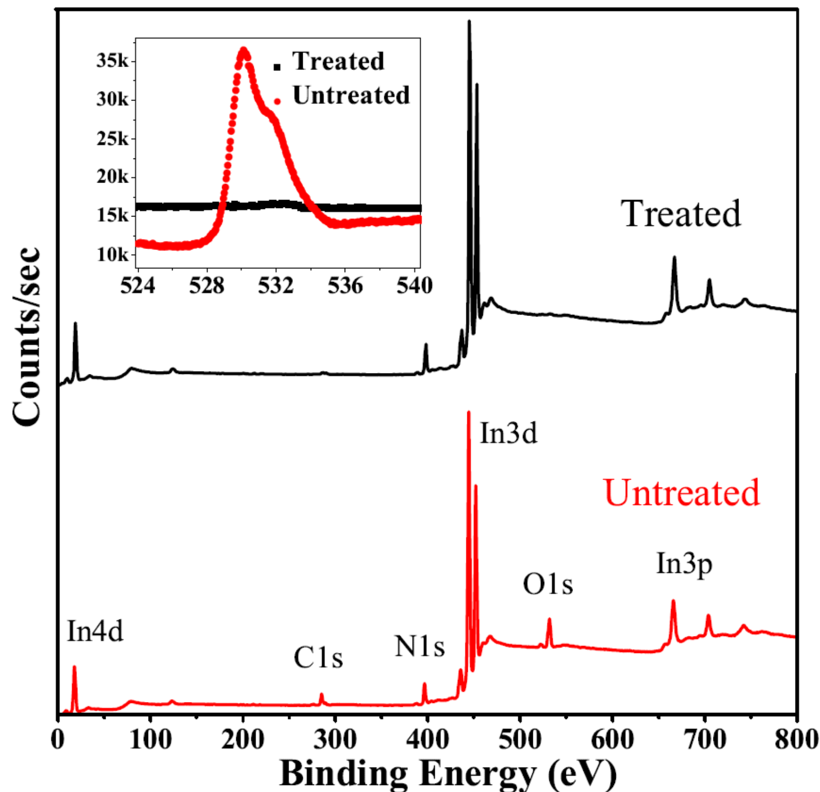

Figure 5.7: shows the survey scan and O1s core level (as inset) Ar^+ ion bombardment treated on treated and untreated film.

Inorder to remove native oxide and physisorbed contaminants resulting from atmospheric exposure, all films were sputter cleaned using low energy Ar^+ ions. Fig 5.7 shows the survey scans acquired on the film grown at 430 °C with and without cleaning. After treatment, O*1s* and C*1s* core level peaks almost vanish, which indicates the removal of adventitious carbon and oxygen. As oxygen is a surface contaminant, it does not effect on bulk band emission of the films. Slight increase in the intensity of N*1s* and In*3d* peaks on treated films reveals that there is no degradation in the film surface and composition. Inset to Fig 5.7 shows O*1s* core level on treated and untreated sample. Before ion - bombardment it exhibited two shoulders which are related to O−In bonding at lower binding energy and physisorbed oxygen at higher binding energy,[224] but in the

treated sample O*1s* signal is absent.

5.4.2 In*3d* core-level deconvolution: Presence of In adatoms on the surface

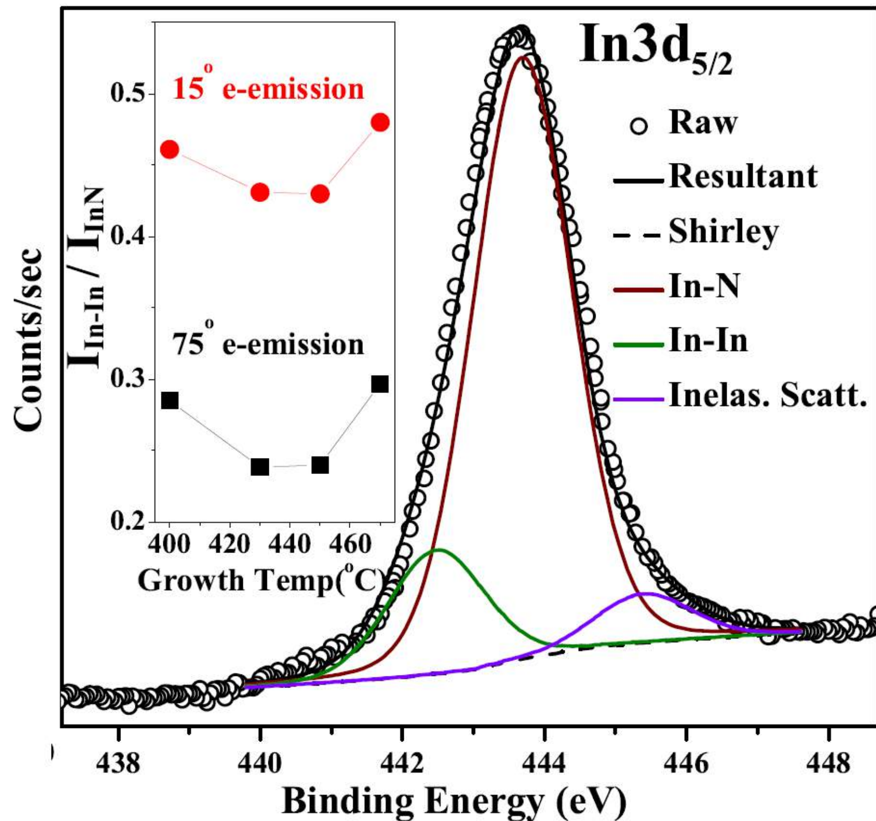

Figure 5.8: shows XPS studies of the In$3d_{5/2}$ core level obtained on treated InN thin film grown at 430 °C, deconvoluted into In−In, In−N and inelastic scattering of near surface electrons. Inset shows filled squares and circles for the integral intensity ratio of In−In to In−N components (I_{In-In}/I_{InN}) collected at 15° and 75° electron emission angles with respect to the sample plane, for films deposited at different temperatures.

To determine the surface chemical state of indium in our films, core level XPS measurements were carried out on treated InN samples, and a representative result is shown in Fig 5.8 for the 430 °C grown film. The binding energies of the respective transitions are obtained with reference to the Fermi level position, after Shirley-background subtraction. In*4d* core level is not considered for analysis, as its binding energy overlaps with that of N*2s* core level. The figure shows the deconvoluted In$3d_{5/2}$ core-level spectrum, using Voigt line shapes with 10% Lorentzian component, yields two chemical states at 443.80eV and 442.50eV, assigned to the In−N and In−In bonding,

respectively. The absence of In−O or In−O−N (indium oxynitrides) bonding related component is also evident in the In$3d_{5/2}$ core level recorded on treated InN films. The small peak , at higher binding energy(≈445.50eV) (without this peak asymmetric tail remains) can be attributed to inelastic losses to the conduction electrons in the charge accumulation layer.[224] Inset to Fig 5.8 shows the integral intensity ratio of In−In component to In−N component in In$3d_{5/2}$ core level peaks, acquired at photo electron emission angles of 15° and 75°, with respect to the sample surface plane to see the distribution of In along the depth of the sample. This ratio remains almost constant for each emission angle, but has larger value for the core-levels collected at 15° grazing angle than that at 75°, showing the surface accumulation of In adatoms on the InN films.

5.4.3 XPS valence band spectra analysis

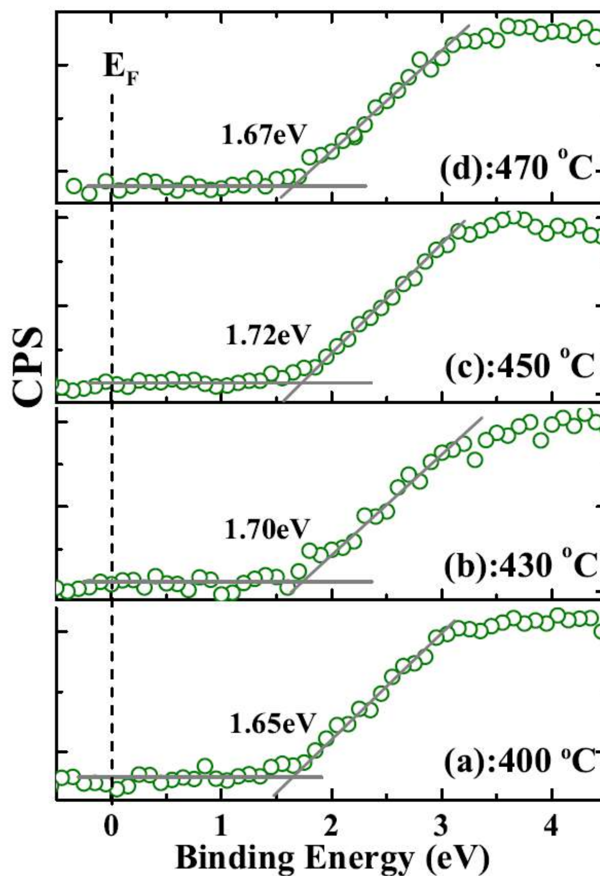

Figure 5.9: (a-d) shows photoemission valence band spectrum for the samples (A-D).

The magnitude of the surface band bending can be estimated from the energy separation between surface and bulk valence band maxima values ($VBM^{XPS}_{Surface}$ -

VBM_{Bulk}^{Abs}) determined by XPS valence band spectra and the previously described absorption measurements. Fig 5.9(a-d) shows representative valence band spectrum for the samples E-H. The values of the valence band maxima (VBM) determined by extrapolating the linear fit to the leading edge of the valence band to the base level[152] are 1.65, 1.70, 1.72eV and 1.67eV for samples A, B, C and D, respectively. A downward near surface band bending can be expected, if the surface Fermi level E_F lies well above the CBM than the bulk E_F, the schematic representation of the downward band bending is shown in inset to Fig 5.10, whereas in the case of a flat band,[228] the measured surface Fermi level position should almost align with CBM of InN at Γ-point. The measured values indicate that the Fermi level gets pinned well above the CBM nearer to branch-point energy,[152,226] which can be attributed to the universal charge accumulation phenomenon on InN surfaces.[151]

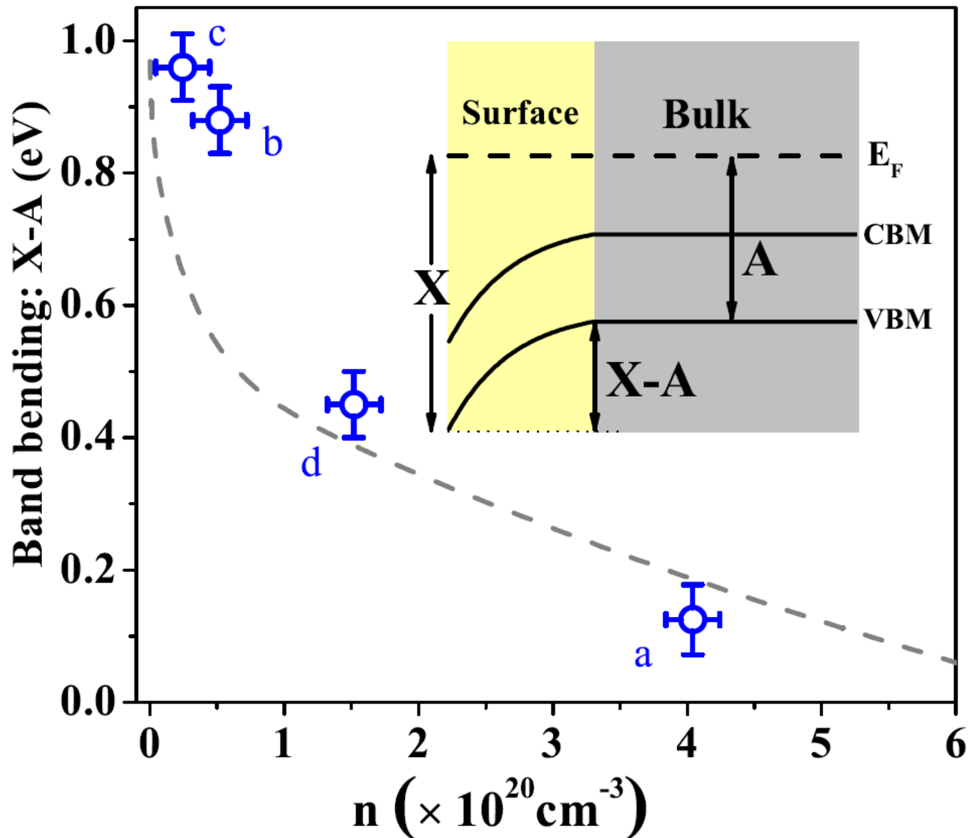

Figure 5.10: shows band bending values plotted vs carrier concentration(n), open circles are from this study and the dashed line is by King *et al.*[144]. The inset shows band diagram, X = $VBM_{Surface}^{XPS}$ and A = VBM_{Bulk}^{Abs} are Energy separations between Valence Band Maximum to Fermi level on surface and in bulk respectively, determined by XPS and absorption measurements.

In Fig 5.10 open circles represent downward band bending, resulting from this accumulation, which is plotted as a function of carrier concentration. The dashed line show B-spline fitting to the values measured by King *et al.*[144], to which our experimental data agrees well. It is clear from the plot that single crystalline InN thin films grown at temperatures 430 °C, 450 °C and 470 °C show surface band bending (0.88, 0.98 and 0.42eV), while the polycrystalline sample grown at 400 °C hardly possesses any. These values are listed in Table 5.1. The absence of downward band bending can be attributed to high band emission energy resulting from band filling effects, where the Fermi level has been pinned well above the conduction band minimum as a consequence of the Moss-Burstein shift. Mahboob *et al.* have shown that the surface charge density

Table 5.1: Different experimentally measured parameters: resistivity, carrier density, hall mobility, Absorption edge, AFM roughness, ω-scan FWHM of InN0002, Valence Band Maxima and Band bending values for samples A, B, C and D.

Sample	Resistivity ρ (Ω-cm)	Carrier density-n (cm^{-3})	Mobility μ (cm^{-2}/V-sec)	Absorption edge A (eV)	AFM roughness (nm)	ω-scan FWHM (arc-min)	XPS VBM X(eV)	Band bending $X-A$
A	2.7×10^{-4}	4.0×10^{20}	55	1.54±0.05	17.3	85	1.65	0.1
B	1.8×10^{-3}	5.2×10^{19}	70	0.82±0.05	7.2	45	1.70	0.88
C	3.4×10^{-3}	2.4×10^{19}	75	0.74±0.05	4.6	27	1.72	0.98
D	5.6×10^{-4}	1.5×10^{20}	63	1.25±0.05	10.9	71	1.67	0.42

on InN surfaces is $2.8\times10^{20}cm^{-3}$ from HREELS measurements, which is slightly less than the carrier concentration of $4.4\times10^{20}cm^{-3}$ measured in our sample A,[150] resulting in a metallic like surface and thus a flat-band. Thus, from deconvolution of In$3d_{5/2}$ core level and valence band studies, the downward band bending induced by electron accumulation can be attributed to the presence of indium adatoms which result in donor like surface states on the single crystalline InN films, while its absence in the polycrystalline films shows the equilibrium condition between surface and bulk carrier concentration.

5.5 Inferences

In summary, to study the cause for surface electron accumulation, InN films of different morphology are grown at different temperatures in ultra clean conditions on Al_2O_3(0001) substrate with a GaN buffer epilayer. We have undertaken the study realizing that the exploitation of the excellent electronic and optical properties predicted for InN is hindered due to the lack of consensus in the origin of the variation of the fundamental band gap value in literature. Characterization by various techniques show that the wurtzite InN thin films formed at low temperature (400 °C) are polycrystalline while those grown at high temperatures (430 °C, 450 °C and 470 °C) are single crystalline in nature, with the high quality film obtained at 450 °C. Complementary surface sensitive and bulk chemical and structural probes have enabled us to rule out the possibility of Mie-resonances as reason for the low band gap feature of InN and Indium oxynitride or oxide as causes for high band gap as perceived in the literature. Our studies do not suggest oxygen as a source of background dopant in InN. We comprehensively review the band gap data of InN presented in the literature. A Moss-Burstein shift based on non-parabolic conduction band is found to explain well the observed band gap variation in literature and the present work, and yields the fundamental band gap value of InN to be 0.70eV.

Thus, variation in optical band gap values acquired from absorption measurements with Hall carrier concentration is in accordance to the Moss-Burstein curve, due to strong band filling effects. X-ray photoelectron emission core-level and valence band studies reveal that the Fermi level pinning is well above the VBM ($\approx 1.8eV$) which is attributed to near surface charge accumulation from In adlayer on single-crystalline or polycrystalline InN films. The consequent surface band bending values, determined by optical absorption and XPS valence band maxima positions, are seen to be prevalent for the single crystalline InN films. A flat band is observed for the highly degenerate polycrystalline films with high band gap, when the bulk carrier concentration tends to equate the surface charge density. Thus, this study attributes the band bending which originated from In induced surface charge accumulation to the bulk carrier concentration which is related to the crysalline quality of the formed films. As our results match with earlier reports in literature, we show that low energy Ar^+ ions also can be used for cleaning

InN surfaces. The work highlights the need to find optimal conditions for stoichiometric and single crystalline thin film formation especially at the surface to make good contacts for devices and to reduce detrimental effects on the opto-electronic properties of this highly potential material.

Chapter 6

InN growth on In induced superstructure phases of Si(111)-7×7

This chapter studies the growth of InN thin films on the 7×7 reconstructed Si(111) surface, by characterizing their structural, morphological and optical properties. A novel approach by initially forming submonolayer In induced super-structures on Si(111) surface, followed by growth of InN on these modified surfaces is adopted. The results show that unit cells of the superstructures that integrally match the InN unit cell, enable the growth of high quality films that show superior structural, optical and electronic properties. We call this novel approach as Superlattice Matched Epitaxy.

6.1 Introduction

InN films possess high unintentional conductivity, which originates from dislocations, native point defects, unreacted Indium, mono-atomic hydrogen, and other guest impurities.[114,136,233,243] The residual unintentional degenerate n-type doping and the very large surface electron density ($\sim10^{20}$cm^{-3})[150] have made it extremely difficult to achieve p-type doping in InN and to accurately determine other fundamental properties such as band gap and carrier effective mass.[240] The high growth temperature, required to crack ammonia precursor, dissociates InN and thus renders CVD processes non-desirable for the growth of InN. The Plasma Assisted Molecular Beam Epitaxy (PA-MBE) growth has the advantage of employing low growth temperatures because of the high reactivity of

the nitrogen (N_2^*) plasma with the elemental In flux at the substrate surface.

At high temperatures necessary for epitaxial growth, InN tends to dissociate, resulting in poor crystal quality film[25]. Thus, there is a necessity to identify conditions and methods to grow good quality epitaxial at relatively low temperatures. Efforts for the incorporation of nitrides into the Si industry have been nominal at best, especially in the case of InN. As in the case of growth on sapphire, substrate nitridation of Si surface and growth of AlN and InN epilayers are found useful for the growth of InN films on Si substrate.[21,244,245] Though lack of a suitable substrate material is a common problem to grow good quality InN, c-Sapphire and 6H-SiC are the most commonly used substrates for InN growth with lattice mismatch values of 25% and 15%, respectively. But, the high resistivity of these substrates prevents direct electrical connection of InN devices with electronic components. On the other hand, Si(111) is an alternate substrate for InN growth due to its high abundance, low cost, good thermal conductivity, excellent crystal quality, attainability of large sized wafers, cleavability, excellent doping properties and the maturity of silicon technology.[246] In the literature, several surface modifications of the sapphire substrates, such as formation of a thin AlN intermediate layer, growth on GaN epilayers, use of low temperature InN intermediate layer and alternating low and high temperature (HT) layers have been employed[25,89,110,118,215] and significantly high electron mobility values are demonstrated.[27,86] Similar procedures have been pursued for Si as well. For instance, Grandal *et al.* reported the improvement of the InN crystal quality when HT-AlN buffer layers were used[247], Wu *et al.* studied the RF-MBE growth of InN using an AlN/ultrathin β-Si_3N_4 as buffer layer on Si and found that β-Si_3N_4 serves as an effective diffusion barrier for Si auto-doping.[248] However, these methods still rely on the use of high substrate temperature for the InN films, which itself may result in non stoichiometric films and undesirable effects of thermal expansion mismatches and Si auto-doping. Thus, in search of a novel growth scheme to grow good quality InN on Si substrate at relatively low growth temperatures than conventionally employed, we invoke the possibility of using metal induced Si reconstructions as growth templates.[249]

Semiconducting surfaces are endowed with several fascinating ordered reconstructions which exhibit rich structural and electronic properties. Several research groups, including ours have previously shown the formation of several In induced submonolayer

superstructural phases on Si(111) surfaces, viz. Si (111)-1×1-In, Si (111)-$\sqrt{31} \times \sqrt{31}$ R±19°-In, Si (111)-$\sqrt{3} \times \sqrt{3}$ R30°-In, Si (111)-4×1-In.[250,251] Based upon several experiments in UHV and using *in-situ* Low Energy Electron Diffraction (LEED) and Auger Electron Spectroscopy (AES) measurements, we have previously reported a 2D phase diagram[252] for this system that shows several kinetic pathways for the formation of these reconstructed structural phases that have different 2D lattice parameters. The present study is a demonstration of In induced stable interfacial superstructural phases on Si (111), as templates for InN growth. We employ here Plasma Assisted Molecular Beam Epitaxy as the preferred technique for InN growth, since the growth temperature chosen can be independent of the N source.

The experiments involve firstly, the formation of the In metal induced superstructural phases in the submonolayer regime, followed by growth of epitaxial InN films and characterized by complementary tools. We then correlate the 2D unit cells of the superstructure and InN overlayer in terms of Superlattice Matching Epitaxy (SME). For InN, we have shown that 0.5 ML In induced 1×1 surface reconstruction of unit cell size 3.8 Å is the best lattice matched super-structural phase on Si(111) which results in a lower lattice mismatch (8%) with that of InN unit cell of 3.53 Å. Furthering this, in this study InN growth temperature has been optimized on Si (111)-1×1 as well as Si (111)-7×7 surface reconstructions, which are now used as templates to grow superlattice matched epitaxial high quality InN films.

6.2 Experimental

We use the phase diagram for Si(111)-7×7-In system as guidance to obtain these superstructural phases in our PA-MBE system. Si(111) substrates are thermally degassed inside the preparation chamber at 600 °C for 60 min and further cleaned in the growth chamber at 800 °C for 30 min and at 900 °C for 5 min to remove the native oxide. While cooling the substrate down to room temperature, the 1×1 to 7×7 phase transition are observed at ≈ 760 °C. We adsorb about 2ML of In at RT on Si(111)-7×7 surface and anneal the surface at different temperatures in such a way that the metal desorption results in different surface reconstructions[252,253] by monitoring the evolution of the superstructures using RHEED.

6.3 In induced reconstructions of Si(111) as superlattice matched epitaxial templates for InN growth

First section of this chapter presents the InN samples grown on, 7×7, 4×1 and 1×1 surface phases and are denoted as samples A, B, and C respectively. Indium flux and N_2 flow rate are maintained same for all the samples. The InN growth temperature is chosen as low as 300 °C, since all the studied surface phases are stable at this temperature. The second section includes the optimization of the growth temperature on 7×7, and 1×1 surface reconstructions. To improve crystal quality further, these optimized templates are used as surface modified substrates.

6.3.1 Evolution of In induced superstructures of Si(111) surface

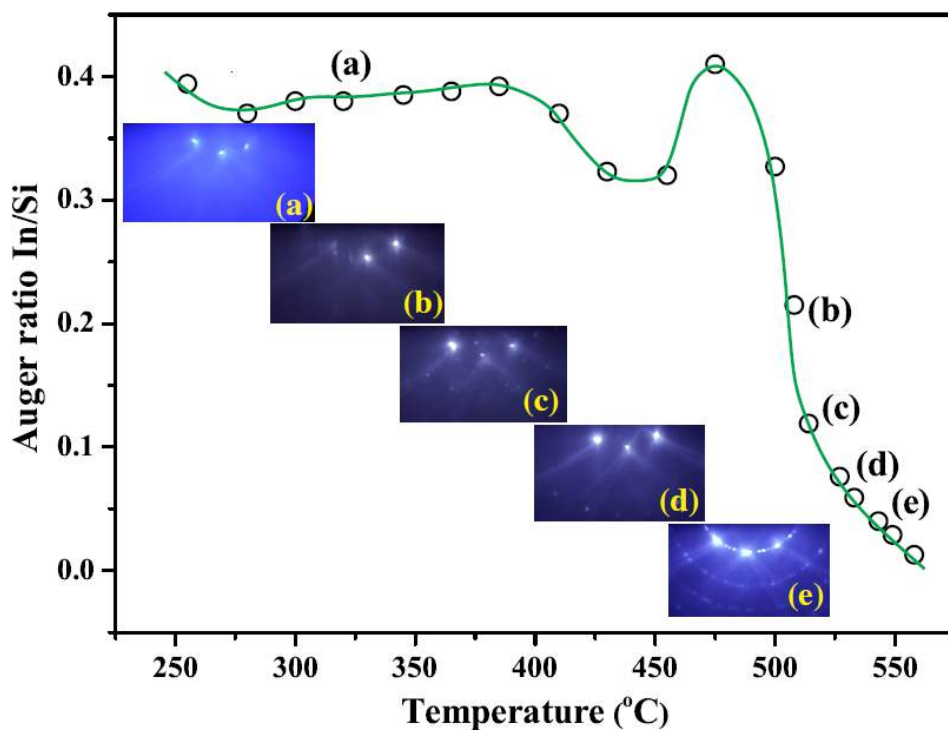

Figure 6.1: Desorption curve and reconstructions: Auger residual thermal desorption curve for In/Si(111)-7×7 system showing the appearance of different superstructural phases and their respective RHEED patterns are shown. (a) 1×1, (b) 4×1, (c) $\sqrt{31}\times\sqrt{31}$, (d) $\sqrt{3}\times\sqrt{3}$ and (e) 7×7.

The kinetic pathway is represented by the desorption curve in Fig 6.1 which plots the

In/Si Auger ratio versus annealing temperature. The Auger ratio of In MNN (404eV) peak to Si LVV (92eV) peak is plotted versus annealing temperature showing the residual thermal desorption process. The figure shows the progressive appearance of different ordered phases viz., (a) 1×1, (b) 4×1, (c) $\sqrt{31} \times \sqrt{31}$, (d) $\sqrt{3} \times \sqrt{3}$ and (e) 7×7 as In desorbs from the surface from hierarchical sites, as shown by RHEED and Auger ratio in the figure.

6.3.2 Structural characterization

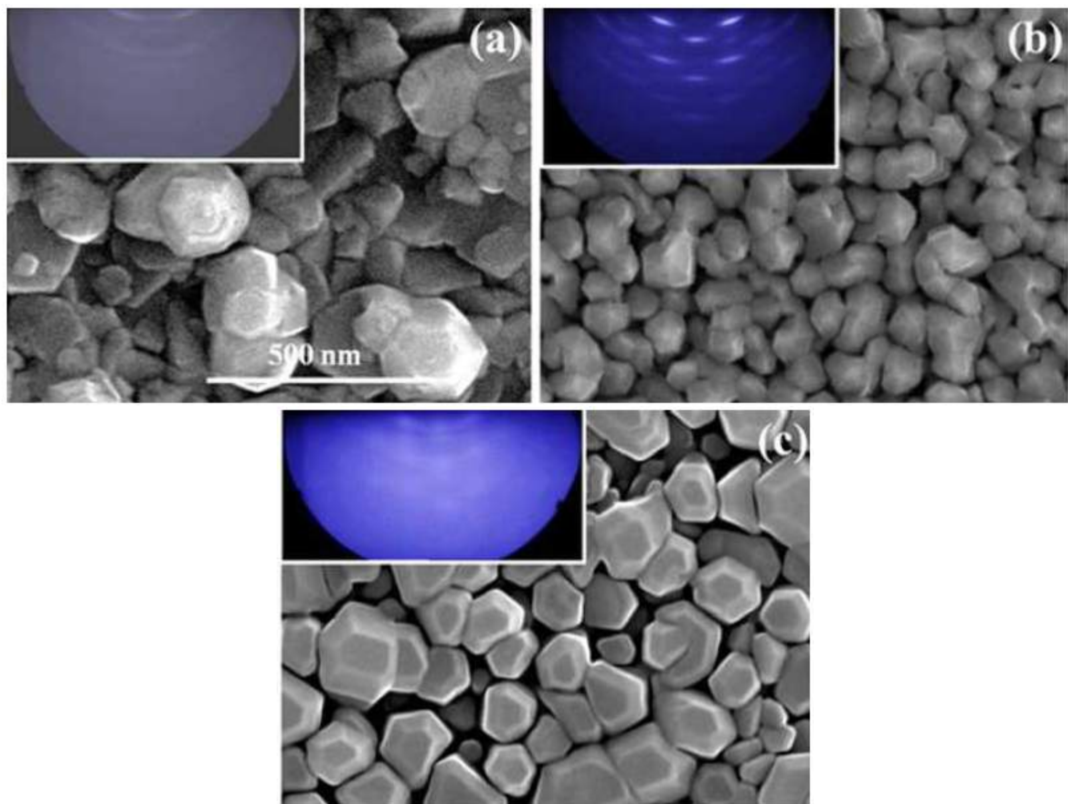

Figure 6.2: Surface morphology and structure: FESEM and RHEED (inset) images for different InN samples: (a) sample A, (b) sample B and (c) sample C.

Surface morphology of the grown InN films obtained by FESEM is shown in Fig 6.2(a-c) for samples A, B, and C, along with their respective RHEED pattern as insets. Fig 6.2(a) shows large InN crystallites of random shapes and the corresponding RHEED pattern depicts broken ring pattern, characteristic of mis-oriented or polycrystalline surfaces. Fig 6.2(b) shows the FESEM image for InN grown on 4×1 phase, which has closely packed hexagonal crystallites with average grain size of ≈100nm having pyramidal tops. The inset of Fig 6.2(b) shows corresponding broken ring RHEED pattern where the elongated

spots (arcs) have a high spot to background intensity contrast, suggesting a mis-aligned arrangement of the crystallites. The InN grown on 1×1 surface shows a morphology in Fig 6.2(c) which consists of relatively larger hexagonal grains with flat tops. Inset to Fig 6.2(c) show a RHEED pattern, which is spotty and streaky, superimposed on a faint ring background. This manifests better ordered InN crystallites formed preferentially on the 1×1 phase, as compared to films grown on other superstructures. The Root Mean Square (RMS) surface roughness of the different samples grown is measured by AFM, over a 5×5μm^2 area. Sample A shows RMS roughness of ≈35nm whereas samples B and C have a value of ≈15nm indicating that films formed on 1×1 and 4×1 surfaces, have smoother surface morphology.

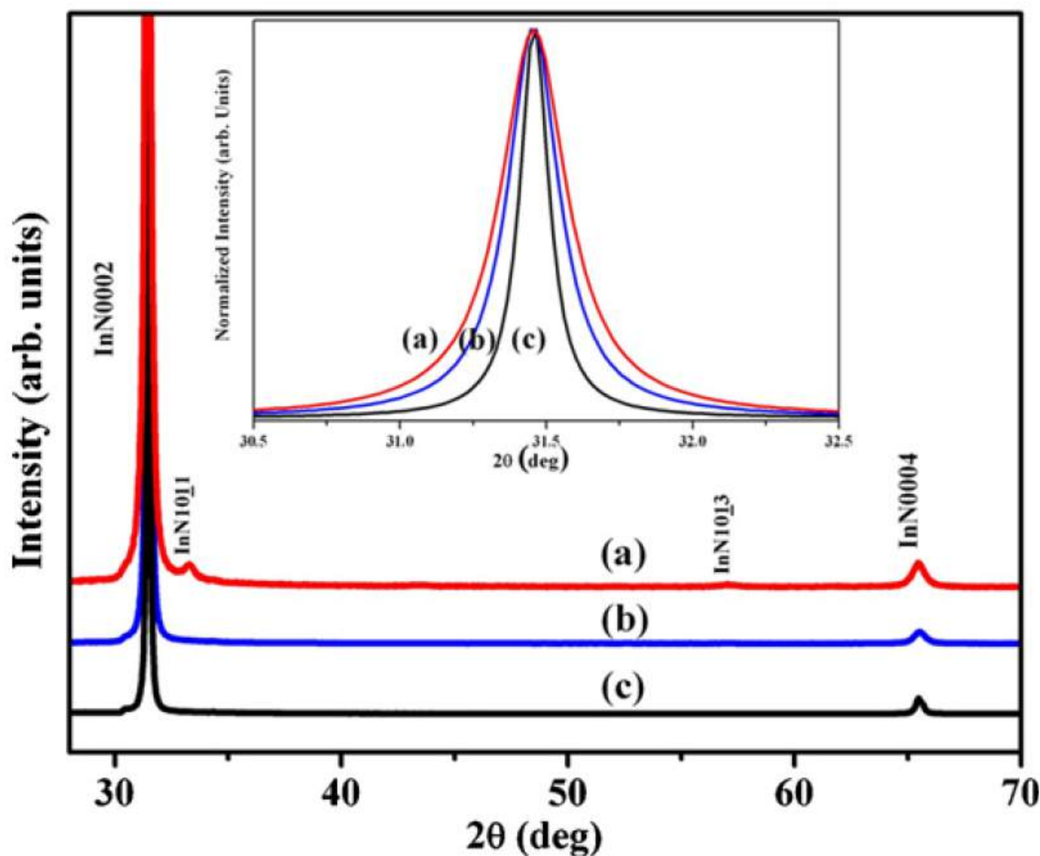

Figure 6.3: X-ray Diffraction: XRD patterns for samples A through C. Inset shows the scans of 0002 reflections for different samples. (a), (b) and (c) represent samples A, B and C respectively.

Fig 6.3(a-c) consist of the θ-2θ XRD scans for samples A, B, and C, respectively, confirming the wurtzite structure of InN films are formed. Fig 6.3(a) is the XRD pattern for InN grown on clean Si 7×7 which clearly shows crystalline InN (0002) and InN (0004) peaks at 31.33° and 65.37° respectively. The Fig 6.3(a) also shows the presence of weak

InN ($10\bar{1}1$) and ($10\bar{1}3$) reflections at angles 33.16° and 57.04°. Fig 6.3(b) and (c) are the XRD pattern for InN grown on the 4×1 and 1×1 superstructural phases which have only crystalline peaks related to InN (0002) and InN (0004). Scans of the (0002) wurtzite InN reflections on the different samples (after subtracting the contribution from the $K_{\alpha 2}$ X-ray component) are shown as inset in Fig 6.3 for samples, A through C and FWHM of the (0002) reflection for samples A shows a value of ≈1000 arcsec, whereas samples B and C have a significant lower value of ≈645 arcsec. Thus, XRD results show better crystalline quality for samples B and C.

We have measured charge carrier concentration of samples A, B, and C by Hall measurements using a magnetic field of 0.58T, as 6.3×10^{20} cm^{-3}, $3.1\times10^{20}cm^{-3}$, and $6.0\times10^{19}cm^{-3}$respectively. We can see that there is an order of magnitude reduction in the carrier concentration for InN grown on the 1×1 surface.

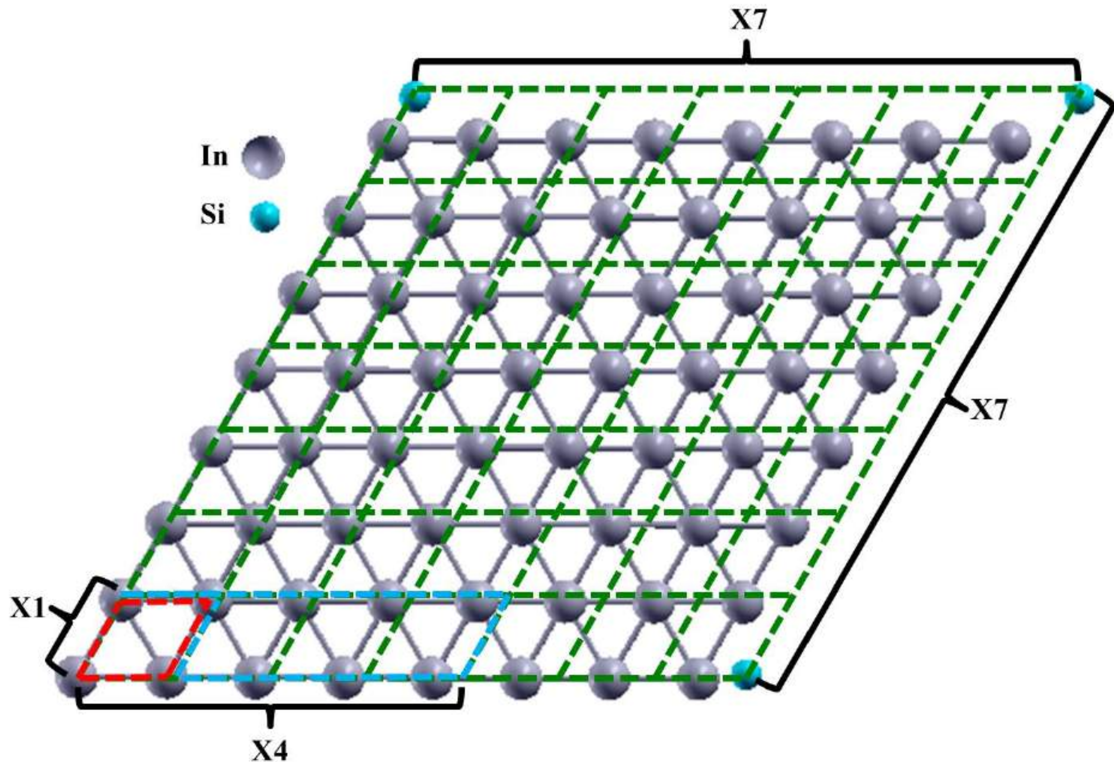

Figure 6.4: shows the schematic for the unit cell relationships of InN and different In induced superstructural reconstructions of Si(111) surface.

We have also grown InN on other reconstructions observed for the Si(111)-7×7-In system which showed poor surface morphology, structural, optical and electrical characteristics. To understand why the 4×1 and 1×1 superstructures result in

better epitaxial InN films, we calculate the 2D unit cell parameters for the different superstructural phases and evaluate their epitaxial compatibility to the InN unit cell. The in-plane lattice constant of InN and that of bulk truncated (unreconstructed) Si(111) surface are 3.53Åand 3.80Å, respectively. The InN lattice match with Si 7×7, 4×1 and 1×1 unit cells is schematically shown in Fig. 6.4. Fig. 6.5 shows the coincidence

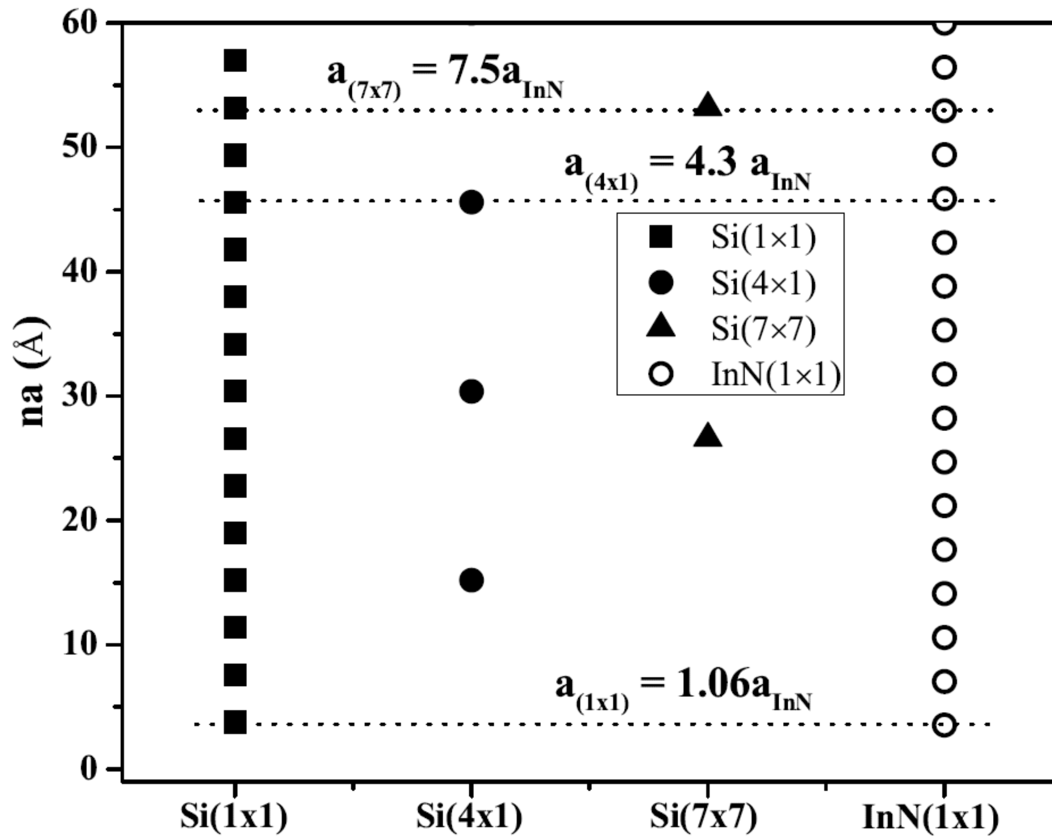

Figure 6.5: shows the coincidence, represented as dotted lines, of the integral multiples of lattice parameters (na) of the superstructural phases 1×1, 4×1 and 7×7 with that of InN.

(represented as dotted lines) of the integral multiples of lattice parameters of the super structured phases 1×1, 4×1 and 7×7 with that of InN. The maximum misfit is with the large domain (7×7), due to the matching of fifteen InN unit cells with two unit cell of 7×7. In the case of (4×1), thirteen unit cells of InN match with three unit cells of (4×1) through long edge. The 1×1 phase has almost equal lattice parameter of InN, hence the lattice matching occurs at every unit cell of InN. The fact that InN grown on the 1×1 and 4×1 In induced reconstructed surfaces on Si(111) are of superior quality, can be attributed to the relation between lattice parameters of In induced superstructures 1×1, 4×1 and 7×7 on Si(111) with that of InN lattice, and are $a_{1\times1} = 1.06a_{InN}$, $a_{4\times1}$

= 4.3a_{InN} and $a_{7\times7}$= 7.5a_{InN}, as shown in Fig. 6.5, yielding an integral-superlattice matching epitaxy of 1/1, 13/3 and 15/2, respectively. Hence, SME shows that 7×7 has higher domain mismatch with InN unit cell, whereas 1×1 and 4×1 phases form better matched template, resulting in superior InN film. Thus, we not only demonstrate a novel method to form better quality InN at a reduced temperature, but also the criticality of the nature of the interface in deciding the material quality of the films. Though the results show formation of crystallites rather than uniform InN films, on specific superstructural phases, as indicated by their superior bulk crystallinity, these films can also serve as better low temperature template for the two step growth method. However, there is a need to optimize this technique to get smooth and continuous InN thin films for high performance, stable layers.

6.4 Lowering of growth temperature of epitaxial InN by superlattice matched intermediate InN layers

In this study, InN growth temperature has been optimized on Si (111)-1×1 as well as Si (111)-7×7 surface reconstructions, which are now used as templates to grow superlattice matched epitaxial thin native intermediate layers to form good quality InN. Table 6.1 provides all the sample details, and the notation used in the study.

Table 6.1: Defines the notations for samples prepared by various routes.

Sample	Indium induced phase on Si(111)	Growth Temperature(°C)	Superlattice matched intermediate layers
A1	7×7	100	No
A2	7×7	200	No
A3	7×7	300	No
A4	1×1	100	No
A5	1×1	200	No
A6	1×1	300	No
B1	-	350	A5(30 min)
B2	-	350	A6(30 min)

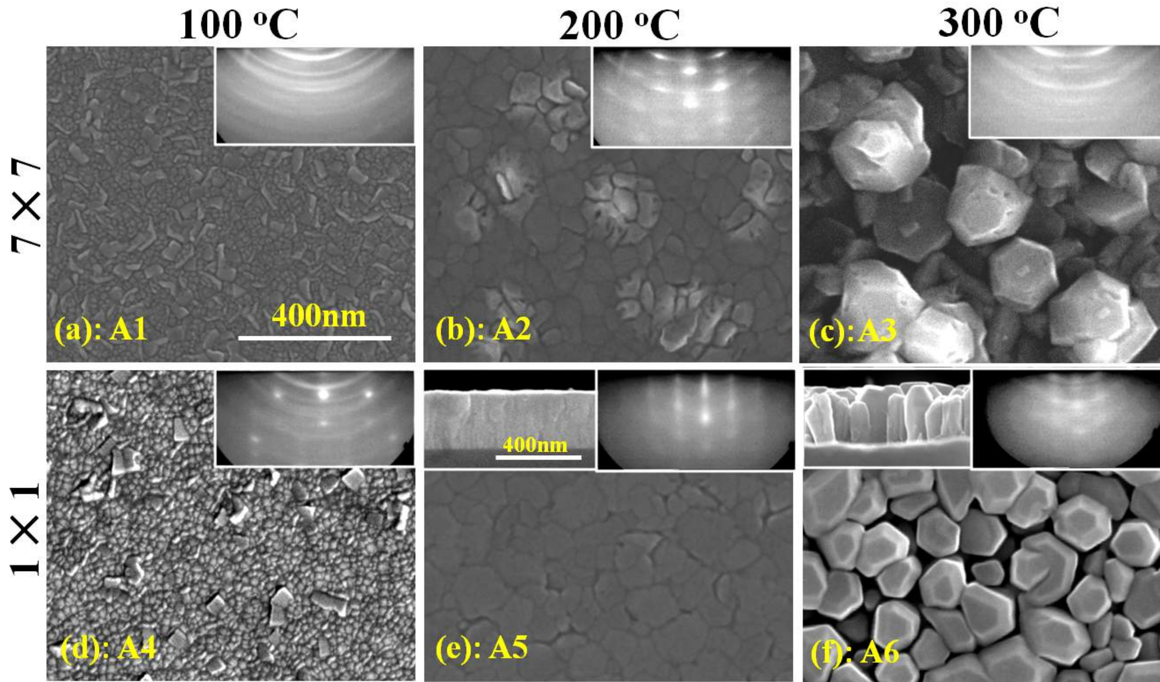

Figure 6.6: (a) - (c) show the top view FESEM images for the InN films grown on In induced Si(111)-7×7 super structural phase and 6.6(d) - (f) for the InN films grown on In induced Si(111)-1×1 super structural phase at 100 °C, 200 °C and 300 °C, respectively. The top-left insets of 6.6(e) and (f) show the FESEM cross sectional view of the films A5 and A6. The top-right insets show respective RHEED pattern taken with e-beam $\parallel < 11\bar{2}0 >$.

Fig 6.6(a) - (c) show the FESEM plan view images of InN films grown on bare Si(111)-7×7 surface at 100, 200 and 300 °C (samples A1, A2 and A3), while Fig 6.6(d)-1(f) is of InN films A4 - A6 grown on In metal induced - 1×1 reconstructed Si(111) surface at 100, 200 and 300 °C, respectively. The images show that all the films have non-continuous granular surface morphology and the surface roughness varies with growth temperature. Samples A2 and A5 grown at 200 °C on Si(111)-7×7 and 1×1 surface reconstructed phases are relatively smoother [Fig 6.6(b) and (e)] than the films grown at 100 °C and 300 °C on both the phases. RMS values of surface roughness calculated from 5×5 μm^2 scanned area for sample A1 to A6 by AFM are 12.4, 11.0, 32.0, 8.8, 4.7 and 9.2 nm, respectively. These values show that the films grown on Si(111)-7×7 have higher surface roughness than that of the films grown on better lattice-matched Si(111)-1×1 at respective temperatures[253]. Higher surface roughness values (32 and 9.2 nm) for samples A3 and A6 can be due to the enhanced surface diffusion of In atoms at relatively higher growth temperatures. The corresponding top-right insets of each image show the respective RHEED pattern, taken along $< 11\bar{2}0 >$ direction, consisting of rings, or

rings with elongated spots for samples A1 to A4, reflecting poor crystal quality and high surface roughness measured. The faint streaks for sample A5 is due to a fairly atomically smooth crystalline surface. Observation of spots alongside the streaky pattern for sample A6 is due to electron transmission through the crystalline 3D granular structure with flat tops. The Fig 6.6(e) shows less surface rms roughness with closely packed flat top grains which appear to have coalesced at this relatively lower growth temperature of 200 °C. The top-left insets to Fig 6.6(e) and (f) show cross-sectional view of samples A5 and A6, respectively. Compact and flat morphology is observed for sample A5, while A6 exhibits 3D columnar growth morphology with faint rings in its RHEED pattern due to the relative azimuthal misorientation of the crystallites.

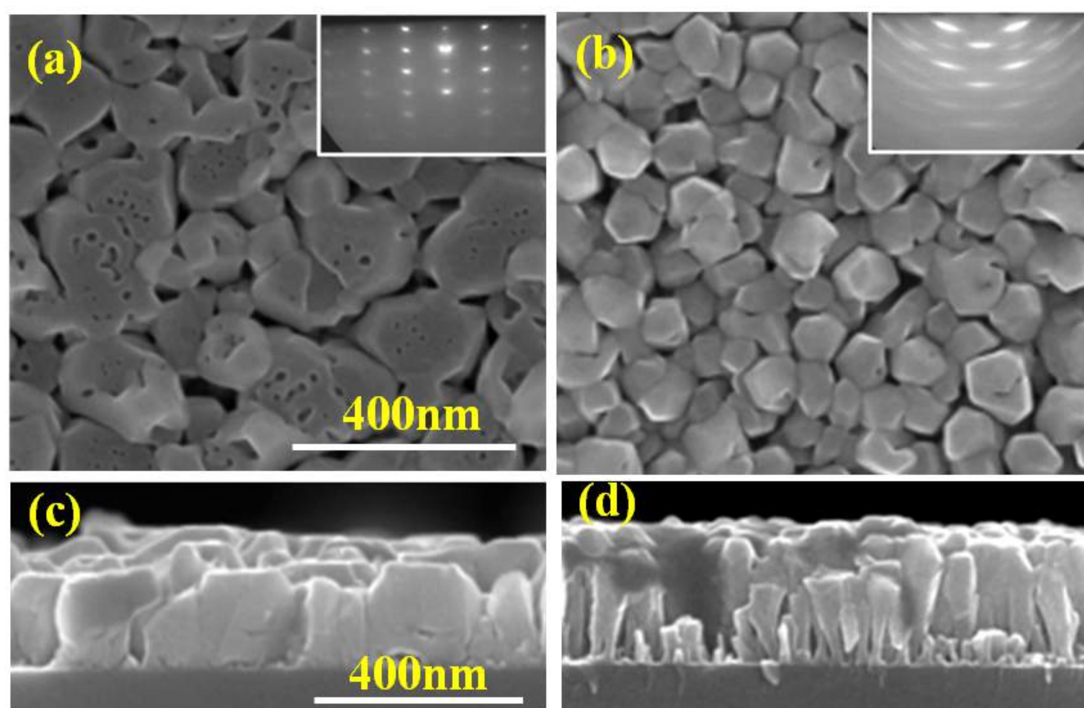

Figure 6.7: (a) and (b) show the top view FESEM images for the samples B1 and B2 respectively. 6.7(c) and (d) show the respective FESEM cross sectional view. The insets to 6.7(a) and (b) show respective RHEED pattern, taken with e-beam $\parallel < 11\bar{2}0 >$.

Among these six samples, A5 and A6 show streaky RHEED pattern and relatively smooth surface morphology and narrow FWHM values in HRXRD (discussed later). These films are now used as intermediate layers for growing InN epilayers at 350 °C to get better epitaxial films. As higher temperature is essential for better epitaxy, the second series of growth of InN has been performed at a relatively higher temperature but still 100 °C less than that used conventional methods for growing InN. In this set, for further

improvement in bulk crystalline quality of InN epilayers A5 and A6 samples grown for 30 min have been used as low temperature lattice matched epitaxial intermediate layers to grow InN epilayers at 350 °C. Fig 6.7(a) and (b) show FESEM plan view images with their RHEED pattern as insets for the samples B1 and B2 which are grown at 350 °C on top of the low temperature lattice matched epitaxial intermediate layers of thickness ≈60 nm grown at 200 °C (A5) and 300 °C (A6), respectively. The films consist of isolated granular morphology, whose average grain size for sample B1 and B2 are 200 and 70 nm and AFM rms surface roughness values for these samples are 5.2 and 8.0 nm, respectively. The spotty RHEED pattern of 6.7(a) is due to transmission of electrons through the 200 nm 3D islands, as evident from Fig 6.7(c). While the RHEED elongated spots through arcs in Fig 6.7(b) can be due to the slight misorientation of nano columns as seen in Fig 6.7(d). Thus, the InN film formed on top of 200 °C grown on the lattice matched (1×1) intermediate layer shows better surface crystalline quality than that of the film grown on top of 300 °C grown intermediate layer.

To understand the crystal structure and bulk crystalline quality of the InN films HRXRD measurements are carried out and the results are shown in Fig 6.8, which shows 2θ-ω scans that are acquired on symmetric and asymmetric planes for sample B1, respectively. In symmetric geometry, samples are aligned with reference to the strong Si (111) reflection observed at 28.4°. The film B1 is seen to be single crystalline wurtzite structure, by displaying intense c-oriented peaks, InN(0002) at 31.28° and InN(0004) at 65.30° along with substrate peaks viz. Si(111) and Si(222) at 28.4° and 58.8°, respectively, as shown in the Fig 6.8(a). Asymmetric planes are studied in skew symmetric geometry, where plane of interest is setup normal to the diffraction plane in such a way that it satisfies Bragg's diffraction conditon[254]. Fig 6.8(b) shows 2θ-ω scan for the asymmetric reflection which consists of InN($10\bar{1}1$) and InN($20\bar{2}2$) peaks at 33.40° and 69.79°, respectively. Similar HRXRD pattern are observed (not shown in figure) for remaining samples (A1 to A6 and B2) which confirm that all the grown films possess single crystalline wurtzite structure. Inset in the Fig 6.8 shows the ω-scans (rocking curves) around the InN(0002) and InN($10\bar{1}1$) reflections, and the FWHM values are listed in Table 6.2. Comparing the FWHM values for samples A5 (1.35°) and B1 (0.82°), it can be seen that crystalline quality of B1 is better than that of A5. Similar trend

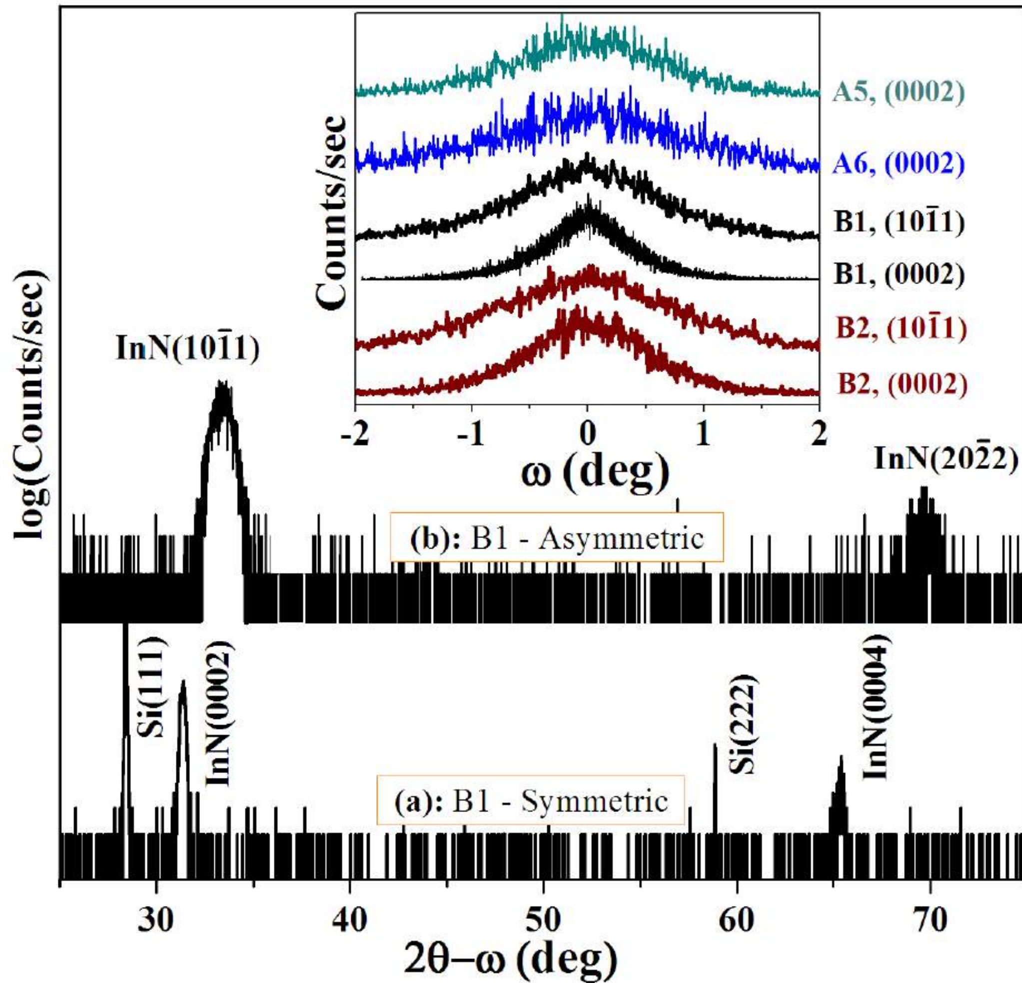

Figure 6.8: (a) and (b) show the HRXRD 2θ-ω scans that are acquired on symmetric and asymmetric reflections for film B1. The inset shows the ω-scans for the InN(0002) reflection of films A5, A6, B1 and B2, and for InN(10$\bar{1}$1) reflection of films B1 and B2, respectively.

has been observed for samples A6 and B2. The high FWHM values of 1.74 and 1.25° for samples A6 and B2 reflects the crystallite tilt, as observed in their FESEM cross sectional view and RHEED studies. The rocking curves around InN(10$\bar{1}$1) reflection for films B1, B2, A5 and A6 having the FWHM values of 1.55, 1.88, 2.10 and 2.36° (for A5 and A6, rocking curves are not shown in the inset), which are higher than the respective InN(0002) rocking curves, indicating dominating edge dislocations, resulting from twist. Thus, mosaicity is resulting from tilt and twist of the grown crystals which is less for sample B1 in comparison to other samples. As described by Lee *et. al*[254], dislocation density is calculated using tilt and twist from InN(*000l*) and extrapolated InN($h0\bar{h}0$) rocking curve broadening values, for sample B1 and is found to be $\approx 6\times10^{10}$cm^{-2}. The films grown on lattice matched intermediate layers have shown improved crystal quality

than the films grown directly on metal induced surface reconstructions Si(111)-7×7 and Si(111)-1×1. Thus, from 2θ-ω and ω-scans it is observed that the InN film B1 has the best single crystalline quality among the films grown.

Room temperature Hall measurements performed on these samples at 0.58T show that they are n-type and the corresponding carrier concentration and mobility values are listed in Table 6.2. The table also consists of the respective stoichiometry ratios obtained from XPS and band edge emission observed by PL, and will be discussed later.

Table 6.2: Different experimentally measured parameters: AFM roughness, rocking curve FWHM, hall carrier concentration, mobility and XPS % composition ratio, PL band edge emission for all samples.

Sample	AFM rms roughness (nm)	Rocking curve InN0002/10$\bar{1}$1 FWHM (deg)	Carrier concentration n (cm^{-3})	Mobility μ (cm^2/V-s)	XPS In/N ratio	PL emission (eV)
A1	12.4	3.21	7.0×10^{21}	11	1.15	-
A2	11.0	2.15	3.0×10^{20}	23	0.91	1.32
A3	32.0	2.73	6.3×10^{20}	13	0.93	2.00[a]
A4	8.8	3.12	3.0×10^{21}	17	1.13	-
A5	4.7	1.35 / 2.10	1.2×10^{20}	50	1.03	1.12
A6	9.2	1.74 / 2.36	6.0×10^{19}	47	1.00	0.74[a]
B1	5.2	0.82 / 1.55	4.2×10^{19}	75	1.00	0.72
B2	8.0	1.25 / 1.88	8.1×10^{19}	57	1.02	0.80

[a]Reference 253.

To understand the dependence of electron mobility on structural quality of films, electron mobility and rocking curve FWHM values are plotted as a function of carrier concentration for all samples in Fig 6.9. As expected, it clearly shows that mobility monotonically decreases with increasing carrier concentration. Samples that possess high mobility have good crystalline quality (lower ω-scan FWHM values). Hall measurements also reveal that sample A5 and A6 which have narrower XRD FWHM values, have better electrical properties among the first six samples A1 to A6, as listed in Table 6.2. This justifies the choice of the identical growth parameters of A5 and A6 to obtain the low temperature lattice matched intermediate layers to form improved thin films. When

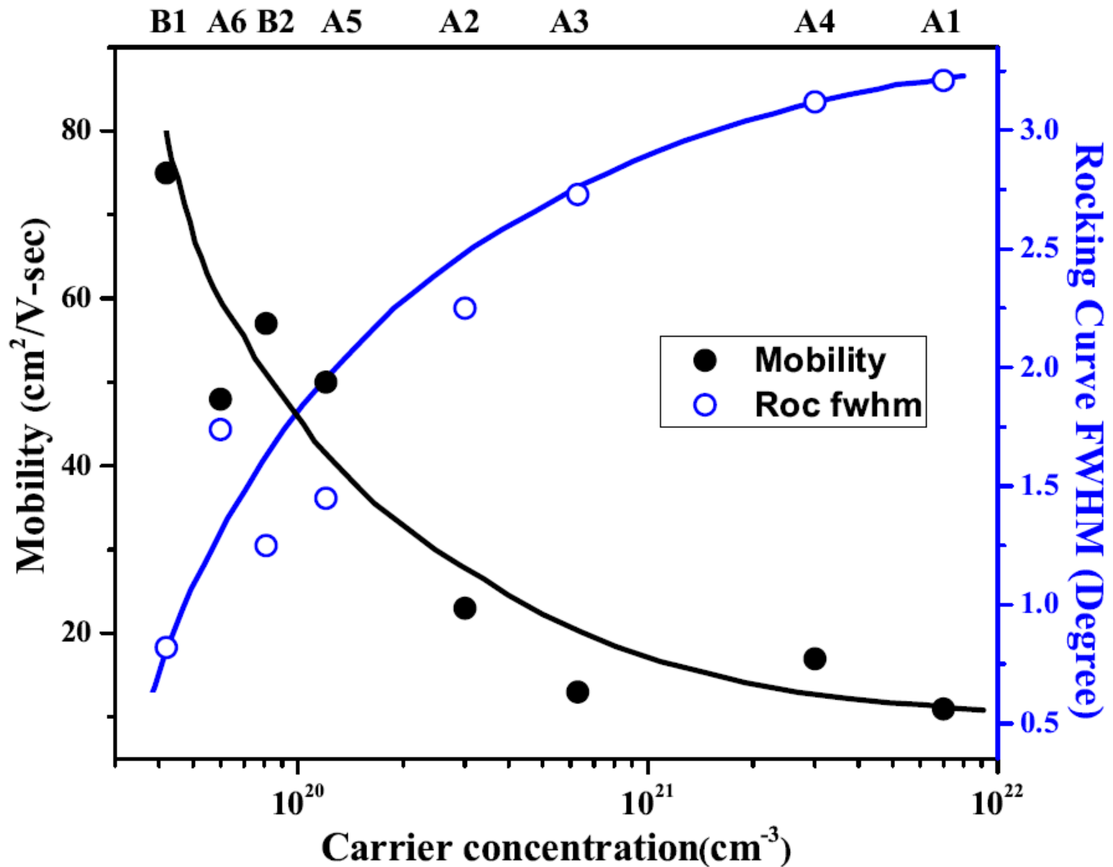

Figure 6.9: shows Hall mobility and HRXRD rocking curve FWHM values plotted as a function of Hall carrier concentration for all the grown samples, solid lines show the trend of variation in parameters.

the lattice matched intermediate layers are employed in the case of samples B1 and B2, grown at relatively high temperature (350 °C), the crystalline quality is improved as well as better electrical transport properties are obtained for these samples. Calculated TD density from HRXRD measurements for sample B1 is $\approx 6\times10^{10}$ cm^{-2}. However, since these films are highly degenerate (10^{19}-10^{20} cm^{-3}), the effect of dislocations is expected to be minimal on the mobility of electrons, due to electron screening.[128]

Fig 6.10 depicts the plot of AFM surface roughness versus mobility, which reveals that higher the surface roughness, lower the Hall mobility and samples having AFM roughness greater than 12 nm show very low mobility. The sample A5 with lower roughness (4.7 nm) is having mobility of 50 cm^2/V-sec which is lower than the mobility of the samples B1 and B2 with higher roughness values. This can be explained by the fact that A5 has relatively broader rocking curve FWHM which reveals poorer crystalline quality and hence low mobility among these three samples (A5, B1 and B2). Overall, Fig 6.9 and

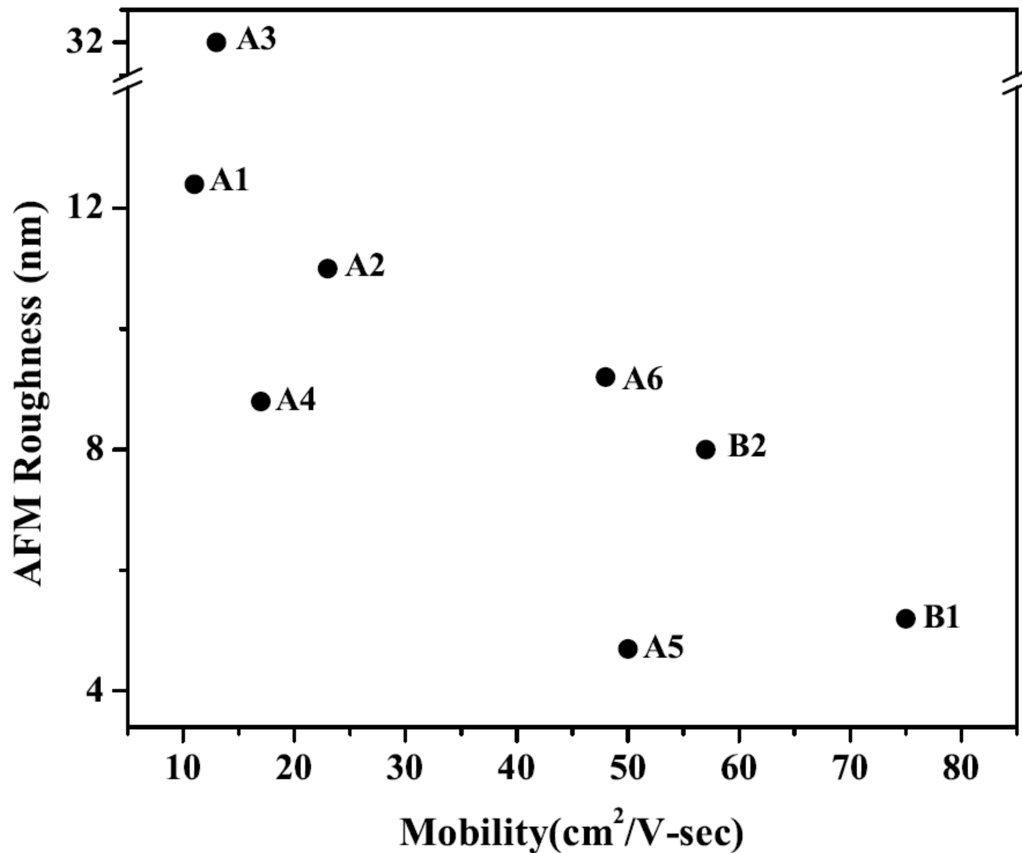

Figure 6.10: shows AFM rms surface roughness plotted versus Hall mobility.

6.10 infer that the mobility of electrons mainly depends on bulk carrier concentration and structural quality rather than surface morphology of the films. Thus, InN film B1 grown on 200 °C lattice matched intermediate layer exhibits minimum carrier concentration and narrow rocking curve FWHM along with higher electron mobility of 75 cm^2/V-sec.

The observation of PL for InN films was not reported until 2002[26] and are still rare in the literature, due to the poor quality of InN films synthesized. We observe PL emission at RT for most samples, except for A1 and A4 samples. Fig 6.11 shows the RT photoluminescence spectra obtained for samples A2, A5, B1 and B2 with band edge emission values of 1.32, 1.12, 0.72 and 0.8 eV, respectively. The PL emission values 2.0 and 0.74 eV for samples A3 and A6 are previously reported[253]. The widths of the PL emission peaks are found to increase with increasing Hall carrier concentration. Among the first series of samples (A1 to A6), the lowest band edge emission is recorded at 0.74 eV for sample A6, whereas sample A5 has the emission peak appearing at a higher value of 1.12 eV, though it consists of relatively better structural and morphological characteristics than that of A6. This can be attributed to the higher carrier concentration that raises

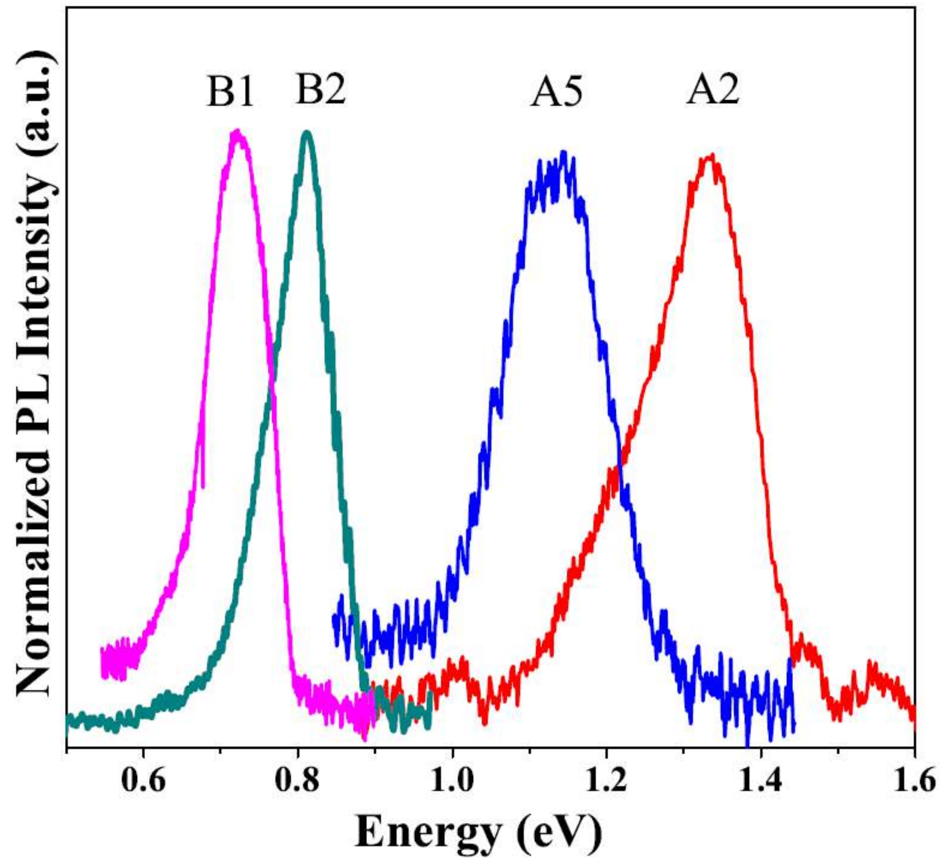

Figure 6.11: shows the PL spectra obtained for samples A2, A5, B2 and B1.

the Fermi level high into the conduction band. All these band gap values are higher than the lowest reported value (≈0.63 eV), which results in strong band-filling effects (Moss-Burstein shift) caused by high carrier concentrations[105]. Samples (A1 and A4) grown at 100 °C do not show any PL emission because of its poor morphology and structural quality, which was evident from the ring like RHEED pattern, high values of AFM rms surface roughness and wider rocking curve FWHM values. Among the samples grown with lattice matched intermediate layers, sample B1 emits at the lower values of 0.72 eV than that of sample A5. On the other hand, sample B2 has an increased band gap (0.80 eV) relative to sample A6 due to its higher unintentionally doped carrier concentration.

As the accumulation of surface charge, present due to excess In adatoms on grown InN surfaces, causes ambiguity in measuring the electrical properties and optical properties of InN thin films[255], their dependence on stoichiometry also becomes important. Before performing XPS measurements, InN thin films were sputter cleaned by an optimized low energy (0.5keV, 2μA) Ar^+ ions[234,256], to remove physisorbed adventitious carbon and oxygen resulting from atmospheric exposure, without affecting their crystalline

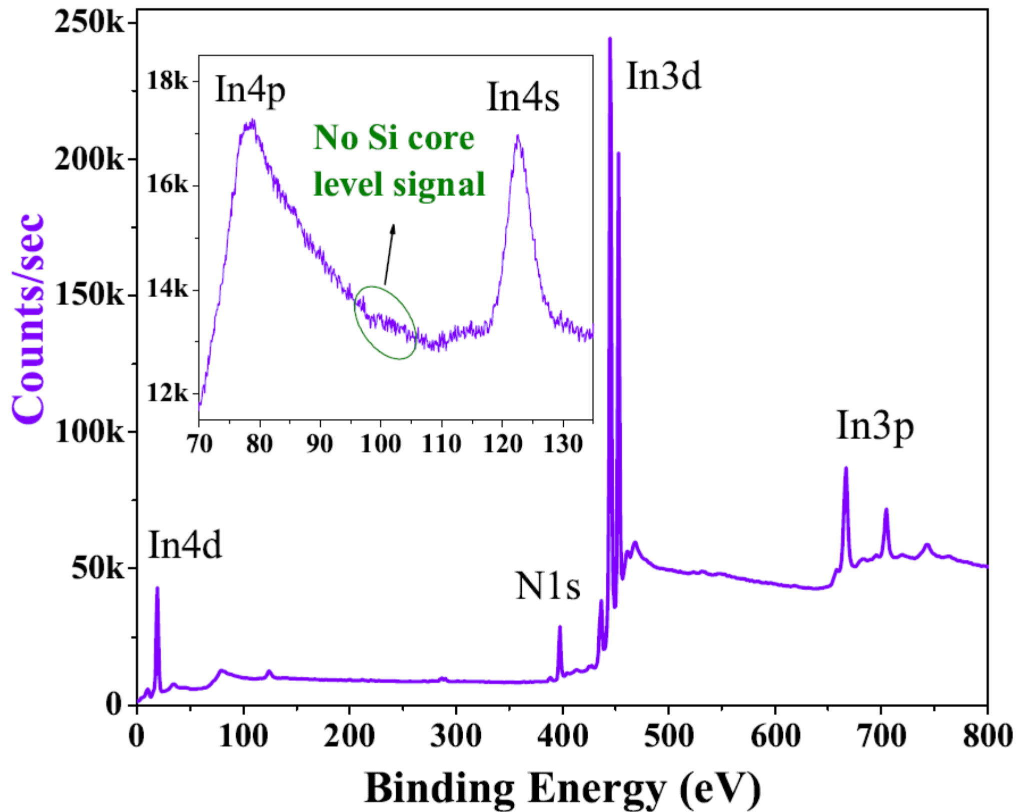

Figure 6.12: shows the survey scan and inset is the high resolution Si core level collected on sample B1, after treating with low and high energy Ar^+ ions.

quality and no III-V bond breaking. As a measure of stoichiometry, the In to N ratio calculated from XPS survey scans which are acquired on the films treated by low enery Ar^+ ions.[234,256] Fig 6.12 shows the survey scan for the film B1, where O*1s* and C*1s* core level peaks almost vanish, which indicates the removal of adventitious carbon and oxygen. Inset shows the high resolution core level studies performed for Si*2p* signal close to the interface of sample B1 upon treating with high energy (2keV, 11μA) Ar^+ ions. The absence of Si signal in the bulk of the films confirms that there is no diffusion of Si atoms into the over grown InN film from the substrate. Thus, high carrier concentration could be due to crystalline quality, donor like native point defects and stoichiometry of the formed films. However, it is clear that improvement in structural quality of InN films can be achieved by using intermediate super-lattice matched epitaxial thin InN layers grown on In induced 1×1 superstructural phase of Si(111). Fig 6.13 shows In to N ratio that is plotted as a function of carrier concentration along with the band gap values obtained from PL. The solid line shows the theoretically calculated Moss-Burstein (MB) curve using **k.p** theory by considering conduction band non-parabolicity, and normalization

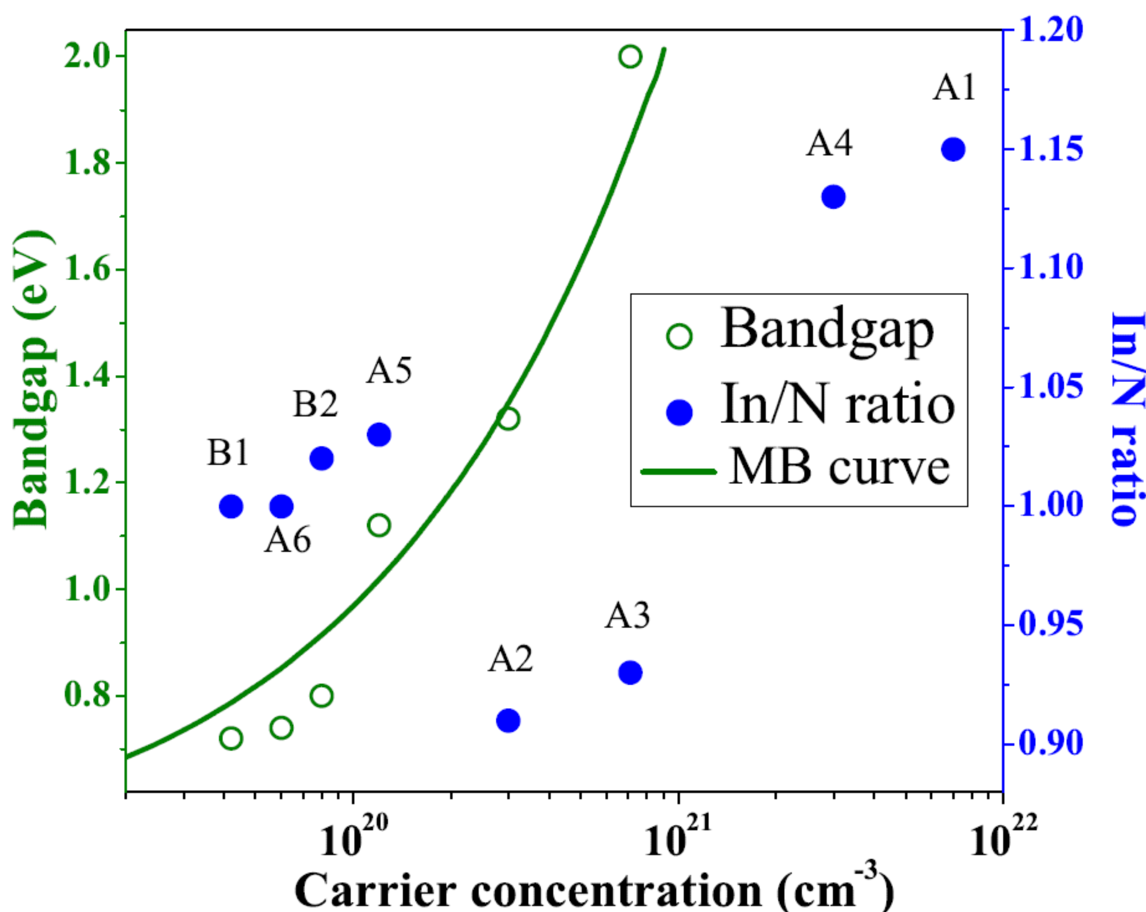

Figure 6.13: shows PL band edge emission values and XPS In to N ratio plotted as a function of Hall carrier concentration and solid line indicates the theoretical Moss-Burstein curve.

effects (electron-electron and electron-impurity interaction) using InN band gap value of 0.63 eV[76,215]. The band gap values obtained for these samples, represented by open circles in Fig 6.13, follow the trend of the MB curve. It can be seen that samples showing low band gap are having nearly stoichiometric In to N ratio whereas samples with non-stoichiometric composition either show very high band gap values (or absence of PL emission) as compared to the stoichiometric samples. As the indium tetragonal phase related peaks are not observed in X-ray diffraction measurements for all samples, presence of In metal crystallites in the bulk of the film can be excluded, and thus the observed IR emission is solely arising from InN[204]. This indicates that band filling effect alone does not determine PL emission, but stoichiometry also plays a deterministic role. This is evident from Fig 6.11 and 6.13 that InN film grown on top of 200 °C lattice matched intermediate layer (sample B1) has stoichiometric composition and has the lowest band gap of 0.72 eV.

6.5 Inferences

The careful experiments performed were directed towards obtaining improved crystal quality of InN/Si(111) with low band gap grown on native epitaxial intermediate layers at relatively low temperatures compared to conventional growth temperatures that are adopted in MBE systems for InN growth. This results in a reduced thermal expansion misfit effects and no auto doping due to diffusion of Si into the film from the substrate. This work demonstrates the optimization of growth temperature (of 200 °C) for a single step growth of InN on In metal induced superstructural 7×7 and 1×1 phases of Si(111). The results reveal that better crystalline quality of InN is achieved on the In induced Si(111)-1×1 superstructural phase due to the smallest lattice mismatch of 8% between the InN unit cell and 1×1 surface reconstruction, as compared to other observed superlattices. X - ray diffraction measurements show that all the films grown in this study are c-oriented with wurtzite crystal structure, and better crystalline quality is achieved for the film grown at 200 °C on 1×1 reconstruction. Further improvement in the crystal quality, confirmed by relatively narrower rocking curve FWHM widths, has been accomplished for the two step grown films B1 and B2, in which superlattice matched atomically epitaxial thin InN layers, grown on In induced 1×1 substrate surface reconstruction. Obtained mobility values for the samples are found to be influenced by bulk structural quality and carrier concentration. Stoichiometric and good crystalline films show lower band edge emission and the band gap values result due to the high degeneracy and non stoichiometry of the films. Absence of PL emission for samples A1 and A4 is due to poor crystal quality and high In to N ratio. PL band edge emissions are found to be varying in accordance with the band filling effects depicted by Moss-Burstein curve. Thus, our experiments not only demonstrate a method to form better quality InN at a reduced temperature, but also show that lattice matched epitaxial native surface modifications are equivalent to the use of hetero-buffers to attain good quality InN films. More studies are underway to achieve higher mobility and lower carrier concentration by optimizing growth parameters at relatively low growth temperatures to arrest the dissociation of InN and prevent Si out diffusion into the over grown InN layers by sheer kinetic control.

Chapter 7

Role of defects in limiting the electron mobility of InN

This chapter presents the characteristics of InN thin films grown on two kinds of GaN templates on c-sapphire. The results show by HRXRD that the films formed on these surfaces show reduced dislocation/defect density.

A two step kinetically controlled single-growth process for the formation of an array of InN dislocation free high mobility nano rods (NRs) on GaN nano wall network (NWN) is demonstrated. The InN films and nano rods formed on the NWN template are shown to be almost defect free and possess extremely high electron mobilities by Hall measurements.

7.1 Introduction

In addition to optoelectronic applications due to its band edge emission in the NIR, indium nitride is expected to be utilized in the fabrication of high speed electronic devices as it exhibits a small effective mass $\approx 0.04 m_0$[240], higher peak, saturation velocities and high mobility $\approx$ 4400 cm^2/V-sec at RT.[28,128,129] In order to achieve high quality InN material, there have been several efforts by employing special growth schemes in molecular beam epitaxy (MBE), metal organic chemical vapor deposition (MOCVD) and other growth techniques to obtain low carrier concentration $\sim 10^{17}$ cm^{-3}. Relatively low lattice

mis-matched intermediate layers are used to minimize the dislocations/defects resulting from ≈25% mismatch between c-sapphire substrate and overgrown InN. Heteroepitaxial InN and usually grown on a GaN epilayer, which results in films with reduced threading dislocation (TD) density in the range of 10^9-10^{11} cm^{-2}, and a low electron concentration ($< 10^{16}$ cm^{-3}). Theoretically estimated mobility value[115] for InN is ≈14000 cm^2/V-sec for carrier concentration of 1×10^{15}cm^{-3}, experimentally reported values[78,122,128,129] are only in the range of 500 – 3000 cm^2/V-sec for carrier concentration values of high 10^{18} - mid 10^{17} cm^{-3} respectively, limited by defects such as charge centers and dislocations.[257] In 2000, migration enhanced epitaxially grown 0.2μm InN films by Lu *et al.*[86], exhibited high mobility 542 cm^2/V-sec for carrier concentration of low 10^{18}cm^{-3}. Recently, Wang *et al.* have reported hall high mobility of ≈3000 cm^2/V-sec for 5μm thick InN layers with reduced dislocation density by employing a growth scheme of boundary temperature controlled epitaxy (gradient growth temperatures).[128] Prior to Wang's report, Koblmüller *et al.*, have obtained films with mobility of 2370 cm^2/V-sec for 4.4μm thick InN films using step flow growth scheme under In rich conditions[110] and Gallinat *et al.* reported mobility of 2250 cm^2/V-sec for 5.5μm thick samples.[258] The low mobility values observed in the experimental results reported, have been attributed to the scattering of electrons at the charged point defects and dislocations.[2,257] In order to reduce dislocations in the InN epilayers many efforts have been made in the literature. Dimakis *et al.* grew a 10μm thick InN layer and observed the reduction of dislocations from interface to surface.[259], Wang et al. lowered dislocation density by using a LT InN buffer on an ultra-thin *in-situ* AlN layer on sapphire substrate and obtained mobility of 1780 cm^2/V-sec for 1μm thick InN sample.[129] Kamimura *et al.* made an attempt to reduce dislocations in InN epilayers by employing epitaxial lateral over growth (ELOG) on molybdenum mask patterned sapphire substrate by MBE and achieved threading dislocation density of 10^9 - 10^{10} cm^{-2}.[195] Very recently, Seetoh *et al.* have shown improved internal quantum efficiency of InN micro crystal grown over porous GaN template by MOCVD which has been attributed to nano ELOG epitaxy which resulted in lower dislocations in the over grown InN films.[260]

On the other hand, highly reduced dislocation density is achieved by growing III-nitride materials as nano structures[261]. In recent years, formation of high quality

InN nano-columnar structures is pursued since they possess reduced dislocation density, large surface-to-volume ratio, the absence of misfit induced strain, and also since their size dependent properties can be tuned. Although, much progress has been made in the preparation of InN 2D films, synthesis of high quality InN nano crystals remains difficult. Growth of III-V NRs is generally achieved through catalyst assisted routes such as catalytic metal induced Vapor Liquid Solid (VLS) mechanism or self-catalytic V-S method, where metal droplets enable the material to solidify below the frozen liquid-solid interface[262,263]. However, use of native metal droplets results in strain, absence of epitaxy, and the remanence of an unnecessary foreign material causing deep defect levels which can degrade the optical and electrical properties[264,265]. Researchers have also extensively used Selective Area Growth (SAG) method where complex lithographic techniques are used to pattern a dielectric mask on a substrate where they form epitaxial NRs defined by the pattern[266–268]. Since lithographic processes are complex, time consuming and difficult to control doping and crystalline quality, lithography and catalyst free methods are sought after to obtain self-assembled nano-columnar arrays. We[269,270] have shown that by PA-MBE growth, spontaneous formation of self assembled GaN nanostructures on sapphire and silicon substrates under nitrogen rich conditions. By sheer kinetic control the open screw dislocations result in a self-organized GaN hexagonal Nano Wall Network (NWN) that is single crystalline, c-oriented, defect/strain free and also self-assembled hexagonal GaN nano-columns.[269]

Having shown the effect of several optimized MBE growth parameters on the properties of the InN films in previous chapters, in this chapter, we try to understand the reasons that limit the electron mobility of InN. The films are grown on a thick 2μm GaN epilayer and on GaN Nano Wall Network morphology by varying the thickness of the formed films. We have controlled various kinetic processes of growth and a very novel form of the nano-ELOG scheme is used to grow InN on GaN nano wall network/c-sapphire, without employing any lithographic routes. We are able to lower the dislocation density for 1μm thick films grown on GaN NWN. By using high resolution XRD rocking curve broadening of symmetric and asymmetric reflections, the dislocation density is measured. Thickness dependent mobility is studied. Our experiments have yielded InN thin films with RT mobility of 2121cm^2/V-sec which is higher than the best values in the literature[110,129,258]

for 1μm thick film upto now. Further, InN NRs are grown on GaN NWN under certain growth conditions to study the electron mobility for dislocation free conditions. For these faceted nanorods, our experimental hall mobility for InN NR is measured to be 4263 cm^2/V-sec which is almost equal to the maximum theoretically estimated value of $\approx$ 4400 cm^2/V-sec for a carrier concentration of 1×10^{17} cm^{-3} with dislocation density $\leq 10^7$ cm^{-2}.[257]

7.2 Experimental Details

InN thin films were grown on a 2μm thick GaN epilayer (grown by Hydride Vapor Phase Epitaxy) and on a $\approx$0.25μm thick GaN Nano Wall Network formed on c-Sapphire at substrate temperature of 450 °C for different growth durations. For GaN NW growth, Ga K-cell temperature is set to 1000 °C and the Nitrogen flux is kept at 4.5 sccm (standard cubic centimeter per minute) while Radio Frequency (RF) plasma forward power of 375W with N_2 flow rate of 4.5sccm. After this, Ga K-cell and N_2 plasma source shutters are closed while the substrate temperature is ramped down to the InN growth temperature of 450 °C. Metallic indium was supplied by a standard effusion cell at a temperature of 800 °C at a flux rate of $4.4\times10^{14}cm^{-2}s^{-1}$. InN is grown on top of the pre-formed GaN NWN at 450 °C with the same RF plasma conditions employed for GaN NW growth. The thickness values of the films are measured post deposition using Surface Profile Analyzer and cross sectional FESEM which are listed in Table 7.1. For InN Nano Rod growth on Gan NWN, metallic indium is supplied by an effusion cell at a temperature of 750 °C at a flux rate of $2.5\times10^{13}cm^{-2}s^{-1}$, by keeping other parameters same as InN epilayer growth. Some InN NRs were scratched off from the substrate and dispersed in ethanol and dropped on carbon coated Cu grid for TEM characterization. Low temperature (77K) Cathodoluminescence measurements and room temperature (RT) optical absorption studies are performed to determine the optical properties of the InN NRs. In order to perform the Van der-Pauw Hall and J-V measurements on a single InN NR, the In/Ag metal pads are deposited in E-beam evaporation in a base pressure of 2×10^{-9} Torr. The NRs scratched from the substrates are drop cast between the four In/Ag pads. Later, four contacts are made by depositing the Platinum (Pt) connecting wires between NRs and the In/Ag pads in a FESEM environment, working with the

base pressure of 5×10^{-8} Torr. The Hall mobility and carrier concentration values are measured by a 0.58T magnetic field across this configuration.

7.3 Results: Electron mobility of InN epilayers

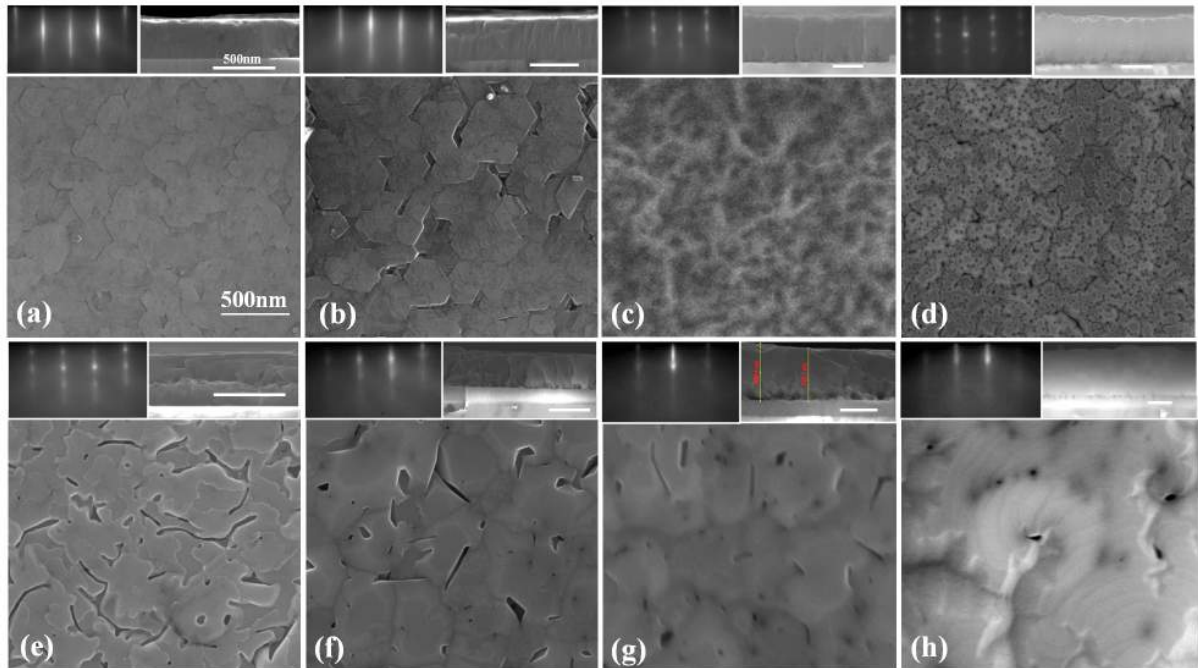

Figure 7.1: Fig. 1 (a-d) and (e-h) show the FESEM top view of the films InN/GaN epilayer and InN/GaN NWN, respectively. Insets show the RHEED pattern (right) and the FESEM cross section view (left). The top-left insets of 1(a-h) show the FESEM cross sectional view of the films and the top-right insets show respective RHEED pattern taken with e-beam $\parallel < 11\bar{2}0 >$ for samples A-H.

Fig 7.1 (a-d) and (e-h) show the FESEM surface morphology scans and their respective RHEED pattern (left) and cross sectional FESEM images (right) as insets for InN grown on GaN epilayer and GaN NWN grown at 450 °C of various thickness. Thickness values of the films are listed in the Table 7.1. As thickness of the films increases, surface roughness increases for the films InN/GaN epilayer (a-d), whereas it decreases for the films InN/GaN NWN (e-h). This is evident in the RHEED pattern where the change from streaky to spotty RHEED pattern for the films A-D, and spotty to streaky for the films E-H depicts that the smoothness of the surface improves for the films grown on GaN NWN with increasing thickness up to 1μm. Fig. 7.1(c-f) show a granular surface morphology whose RHEED is a diffused spotty pattern superimposed on faint streaks due to the transmission of the electron beam through the rough 3D surface features.

However, the respective FESEM cross sectional images show the compactness in bulk of the overgrown InN epilayers. Fig 7.1(h) shows the larger grains (> 1μm) with smooth surface morphology and the respective RHEED inset shows the sharp streaky pattern, which indicates the flatness of surface. As shown in the FESEM cross sections both the films of 1μm thick are compact. The RMS surface roughness values measured on 3×3 μm^2 scanned area by AFM for samples D and H are ≈2.1 and 4.5nm respectively, which confirms that the film grown on GaN NWN exhibits smoother surface morphology than the film grown on GaN epi-layer.

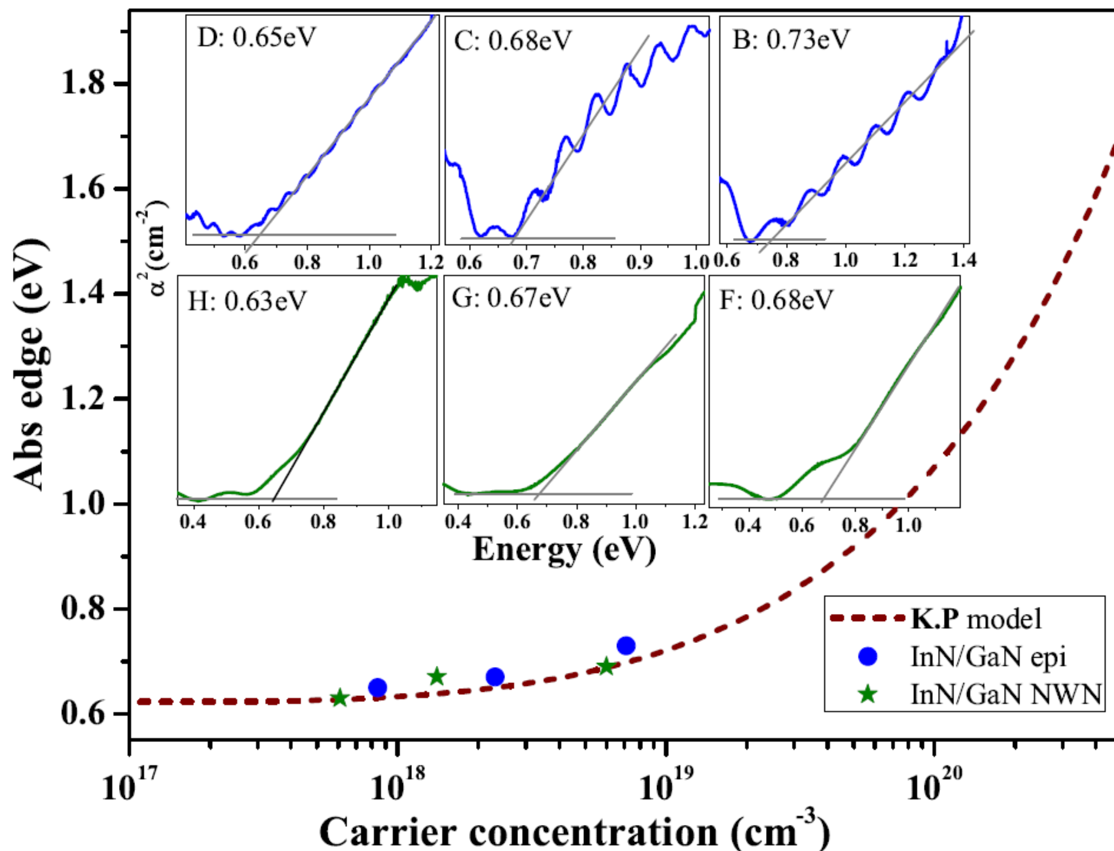

Figure 7.2: shows theoretical Moss-Burstein curve along with our experimental data points (absorption edge versus carrier concentration) obtained for the films B-D and F-H. The insets show absorption squared plots for the same films.

Single field Hall measurements were performed in the Van der-Pauw geometry at room temperature to estimate the electron concentration and mobility values of the films which are listed in Table 7.1. From Hall measurements it has been observed that the carrier concentration decreases and mobility increases with increasing film thickness for the both films InN/GaN epilayer and InN/GaN NWN. The insets in the Fig. 7.2 show absorption spectra for all the films studied. The spectra yield band-edge values of 0.65

and 0.63 eV for the 1μm thick InN films grown on the GaN epilater and the GaN NWN, respectively. Fig. 7.2 also shows the theoretically calculated Moss-Burstein curve using **k.p** theory for a non-parabolic conduction band and considering normalization effects (electron-electron and electron-impurity interactions) using the band gap value of InN as 0.63eV, along with data points obtained from Hall and photoluminescence values in the present study. The inset to Fig 7.2 shows the transmission measurements for the films B-D and F-H. The direct optical band gap is determined by the standard procedure of plotting the squared absorption coefficient versus energy in the high absorption range and then by extrapolating the linear leading edge to the zero value of the squared absorption coefficient.[137] The interference fringes seen in the absorption curve for the film InN/GaN epilayer are due to Fabry-Perot oscillations created within underlying thick GaN epilayer. The band edge values obtained for the 1μm thick films grown on NWN and epilayer are 0.63 $\pm$ 0.05 and 0.65 $\pm$ 0.05 eV respectively. The slight blue shift is observed as decreasing thickness of the formed films. The band edge values from optical absorption versus the carrier concentration obtained from Hall measurements is plotted in Fig. 7.2, the dependence reveals a good agreement of the experimental data points with the Moss-Burstein curve (solid curve), where the shifts in absorption edge energies are attributed to strong band filling effects resulting from unintentional degenerate doping.

Hall mobility (carrier concentration) values for 1μm thick samples formed on GaN epilayer and NWN are 1300 (8.4×10^{17}) and 2121 cm^2/V-sec (6.1×10^{17}cm^{-3}), respectively. Fig 7.3 shows the mobility values plotted versus thickness (upto 1.6μm). The data is obtained from the present study (solid diamond) and the literature (open triangles). The mobility is seen to increase with increasing thickness and the films grown on NWN exhibit higher mobility than that of the films grown on GaN epilayer. For 1μm thickness, the mobility value of the InN film formed on NWN show the highest mobility (2121cm^2/V-sec) than values in the literature (Table 2.1) upto now. At lower thickness, our mobility values are lower than the best literature values, since the measurements are done on samples formed by special growth schemes like migration enhanced epitaxy. Recently Wang *et al.* and Koblmüller *et al.* reported very high mobility values of 3000 and 2370 cm^2/V-sec for the films having thickness of $>4\mu$m, where they have used gradient growth temperatures and step flow growth schemes. These values are lower than the theoretically expected

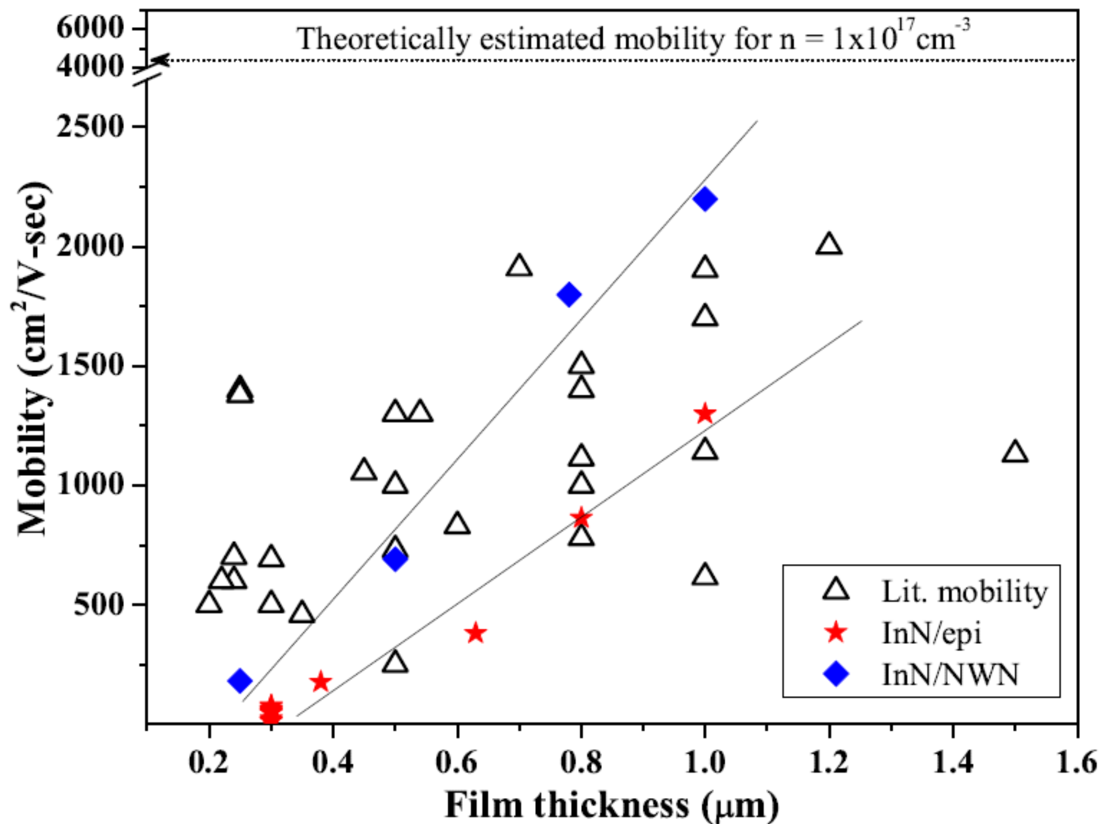

Figure 7.3: shows the mobility values plotted versus thickness of the formed films, open triangles are for the literature values (Table 2.1), filled diamonds (InN/GaN NWN) and stars (InN/GaN epilayer) are from this study. The dotted line represents the theoretically estimated mobility[115] value for the carrier concentration of 1×10^{17} cm^{-3}.

mobility ($\approx$ 4400cm^2/V sec) which suggests that there is still some remnant charged native point defects and dislocations in the films.

Fig 7.4(a-d) show HRXRD 2theta-omega scans for the film H (InN/NWN) acquired in symmetric and skew symmetric geometries for on-axis planes and off-axis planes respectively, where a logarithmic Y-axis is plotted to identify even weaker signals from the planes. Asymmetric reflections are obtained using skew symmetric geometry using pivotal benefit of HRXRD machine in such a way that the measuring geometry meets the Bragg's condition by bringing the diffraction plane normal to the plane of interest. This is possible by changing Euler angle (χ), which is the angle between the symmetric and asymmetric reflections as shown in the inset to Fig 7.4(d). Fig 7.4(a) shows the 2θ-ω scan that is obtained on the symmetric reflections InN(000l) while Fig 7.4(b-d) shows 2θ-ω scan for the skew symmetric reflections (off-axis planes) InN($h0\bar{h}l$), where h *(or)* l = 1, 2, 3, 4. The reflections InN(0002), InN($10\bar{1}4$), InN($10\bar{1}2$), InN($10\bar{1}1$), InN($30\bar{3}2$)

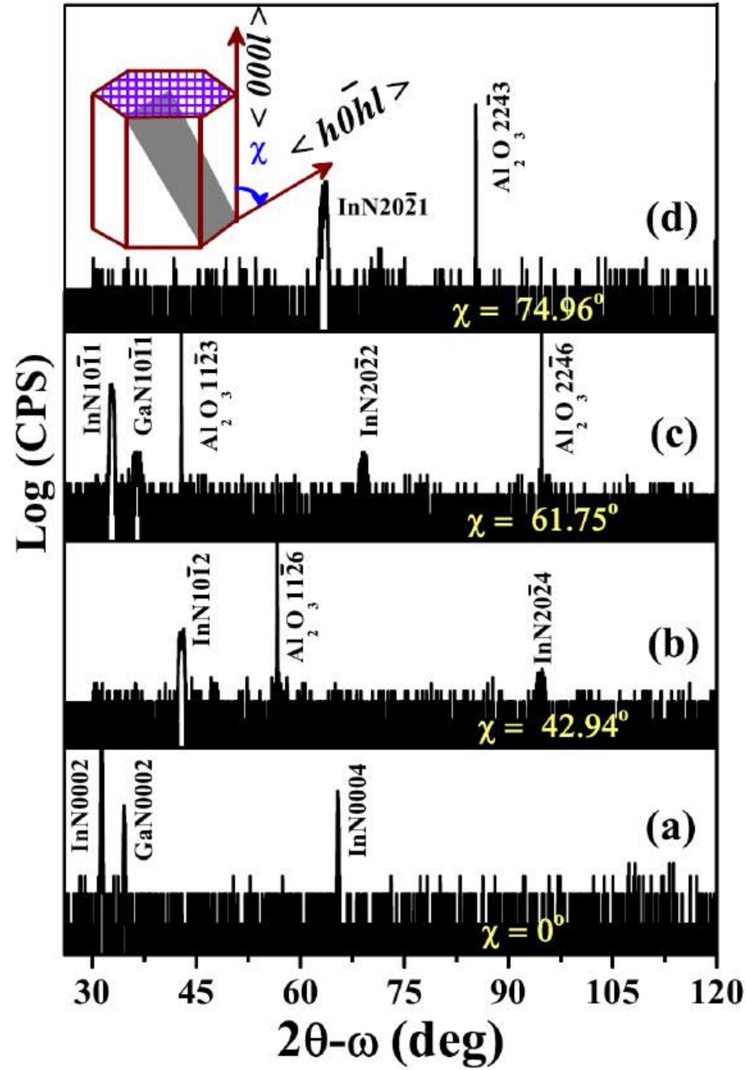

Figure 7.4: (a-d) show the HRXRD 2θ-ω scans for symmetric and asymmetric reflections obtained at the inclination angles $\chi = 0$, 42.94, 61.75 and 74.96°. Inset to (d) schematic representation for inclination angle χ between on-axis and off-axis planes.

and InN($20\bar{2}1$) are acquired, by setting up the inclination angle (χ) to the values of $\approx$ 0°, 24.0°, 42.9°, 61.7°, 70.29° and 74.9°, respectively. By knowing these peak positions inter-planar spacing (d) and lattice parameters (a, c) are determined for all the samples. These values are found to be slightly lesser than that of the relaxed values which is due to the tensile stress resulting from the presence of native point defects like indium and nitrogen vacancies in the grown samples.

7.3.1 Broadening of ω-scans: A measure of dislocation density

Fig 7.5 shows ω-scans that are acquired on off-axis and on-axis reflections for the films (C, D, G and H) grown on GaN epi layer and NWN. X ray diffraction technique measures

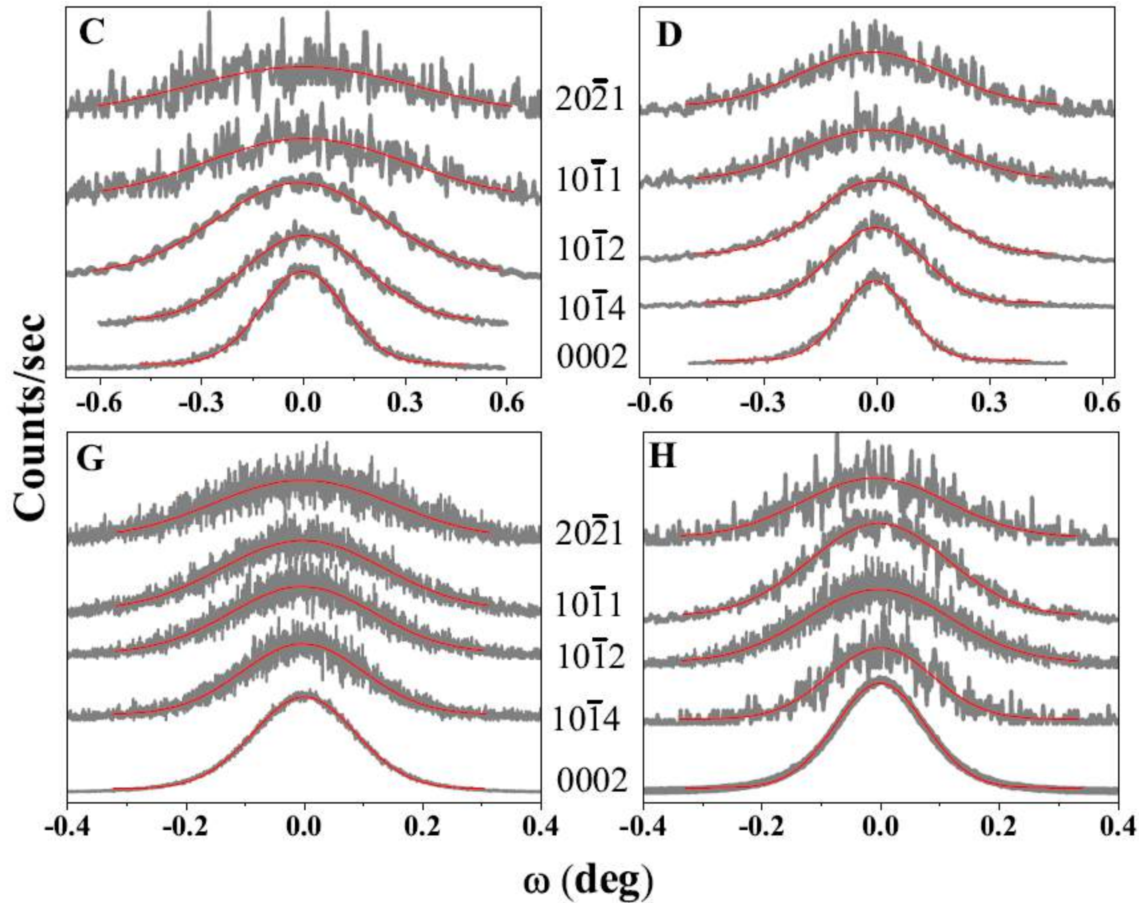

Figure 7.5: show the ω-scans acquired on symmetric and asymmetric reflections for samples C, D, G and H. The solid red lines are Gaussian fit to the data.

TD density with least error since the measurement is nondestructive, large area probing technique and less time consuming than the TEM measurements. Therefore, measuring TD density in group III-nitrides is facilitated by knowing the broadening values of the ω-scans acquired on the on-axis and off-axis planes , and eventually to evaluate the structural quality of InN films. It is well known for the III-nitrides that the out-of-plane and in-plane mosaicity (tilt and twist) of the crystallites originates even in single crystal material, due to the incorporation of threading dislocations (TDs) which are the consequences of the thermal expansion and lattice mismatch between the substrate and over grown layer. For c-oriented III-V compound semiconductors, TDs typically have line direction parallel to the <*000l*>. Tilt is related to the pure screw or mixed type TDs where Burgers vector persists along the c-direction. Thus, screw type dislocations associated with the tilt of the crystallites distort the on-axis planes which broaden on-axis $(000l)$ rocking curves. The twist is related to the edge type TDs where Burgers vector parallel to the in plane direction $<11\bar{2}0>$. Therefore, the distortion in the off-axis planes

normal to the surface is associated with edge type TDs. The values of broadening of the off-axis rocking curves are acquired in the skew symmetric geometry. Thus, many off-axis reflections are acquired with increasing lattice plane inclination and extrapolated to the lattice planes which are normal to the sample surface. Fig 7.6 shows the fit to

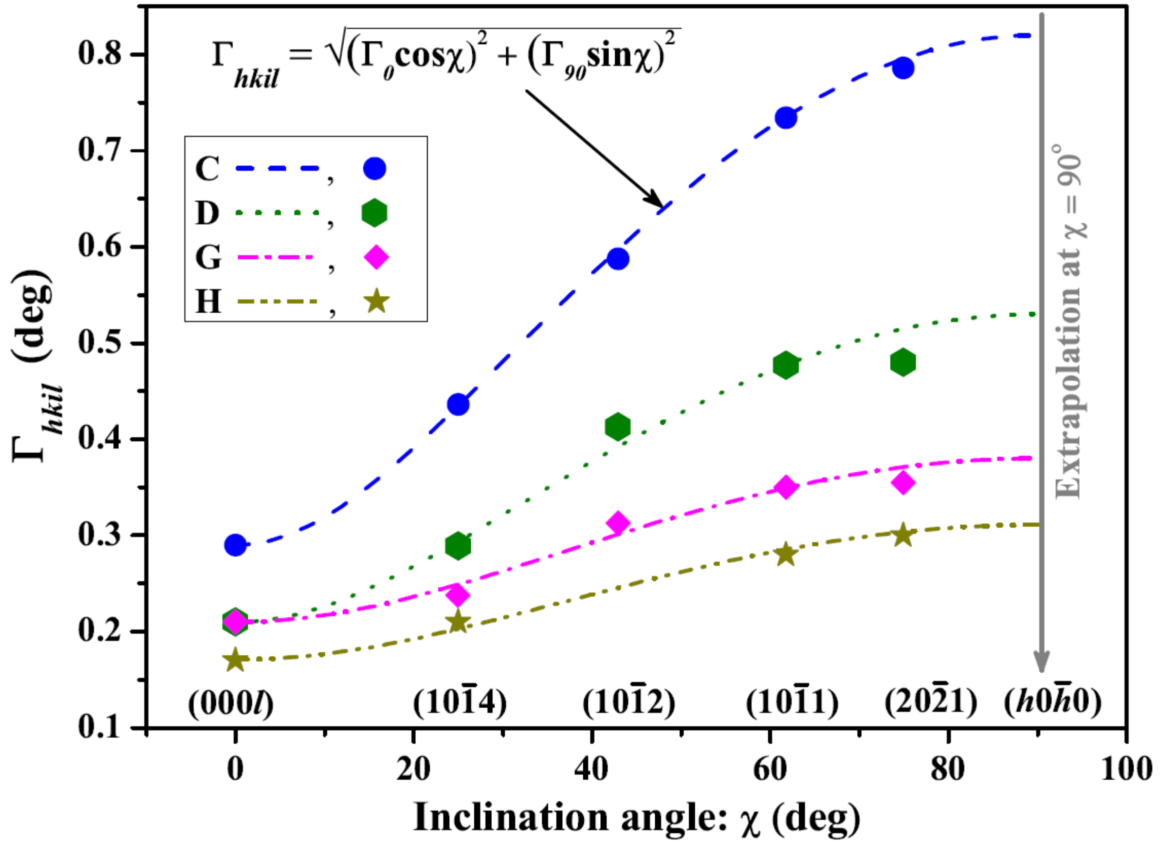

Figure 7.6: shows the extrapolated on-axis and off-axis ω-scan broadening values onto off-axis planes which are perpendicular to the on-axis planes for films C, D, G and H.

the off axis (normal to the sample surface) broadening values for all the films using the following equation (7.1) which is extrapolated to the plane normal to the sample surface at $\chi = 90°$. This method to find out twist angle was developed by Lee *et al.* by which only one symmetric and one skew symmetric rocking curve broadening values are enough to estimate the twist angle of the crystals and thus to determine the edge TDs. Thus, the twist angle (Γ_{90}) is determined by extrapolating all these FWHM values to a lattice inclination angle $\chi = 90°$.

$$\Gamma_{hkil} = \sqrt{\Gamma_0^2 \cos^2\chi + \Gamma_{90}^2 \sin^2\chi} \tag{7.1}$$

where Γ_{hkil} is the FWHM of the Bragg plane whose surface normal has an inclination angle χ with respect to the c- direction. The tilt angle Γ_0 is FWHM value of the on-axis (0002) plane. The tilt (Γ_0) and twist (Γ_{90}) values for all the samples are listed in Table 7.1. To make the measurements easier, the values of coherence length are not considered in equation (7.1), thus the error in these dislocation calculations is $< 20\%$.[254] The twist

Table 7.1: Different experimentally measured parameters: Film thickness, rocking curve FWHM, hall carrier concentration, mobility, tilt, twist and dislocation density for all samples.

Sample	Film thickness (μm)	Carrier Concentration (cm^{-3})	Mobility (cm^2/V-s)	Γ_0 / Γ_{90} (deg)	N_{screw} (cm^{-2})	N_{edge} (cm^{-2})	N_{dis} (cm^{-2})
A	0.38	1.2×10^{19}	175	0.42/1.35	3.7×10^{9}	1.5×10^{11}	1.6×10^{11}
B	0.63	7.1×10^{18}	380	0.34/0.98	2.6×10^{9}	8.2×10^{10}	8.5×10^{10}
C	0.80	2.3×10^{18}	863	0.28/0.82	1.8×10^{9}	5.6×10^{10}	5.8×10^{10}
D	1.00	8.4×10^{17}	1300	0.21/0.52	9.5×10^{8}	2.3×10^{10}	2.4×10^{10}
E	0.18	2.6×10^{19}	180	-	-	-	-
F	0.50	6.0×10^{18}	690	0.31/0.87	2.1×10^{9}	6.2×10^{10}	6.4×10^{10}
G	0.80	1.4×10^{18}	1800	0.21/0.39	9.5×10^{8}	1.3×10^{10}	1.3×10^{10}
H	1.00	6.1×10^{17}	2121	0.17/0.29	7.0×10^{8}	8.5×10^{9}	7.5×10^{9}

angle $\Gamma_{90}$is the extrapolated FWHM value for a rocking curve at lattice inclination angle of 90°. In case of compact layers having random dislocation lines, following equations are used to measure the values of screw and edge type TDs.[178]

$$N_{screw} = \frac{\Gamma_0^2}{4.36 b_s^2} \tag{7.2}$$

$$N_{edge} = \frac{\Gamma_{90}^2}{4.36 b_e^2} \tag{7.3}$$

where N_{screw} and N_{edge} are the screw and edge dislocation densities. Γ_0 and Γ_{90} are the tilt and twist angles (in radians) which are obtained as described above and, b_s and b_e are the magnitudes of the burgers vectors $\mathbf{b}_s = [0001]\mathbf{c}$ and $\mathbf{b}_e = [11\bar{2}0]\mathbf{a}/3$, respectively. Here **a** and **c** are InN lattice vectors with magnitudes 3.537 and 5.706Å, respectively. For these samples, edge dislocations are calculated to be more than screw dislocations.

As the mixed dislocation is combination of one edge and one screw components, a slight over estimation can occur in the calculation of the dislocation density. The calculated screw, edge and total (N_{dis}=N_{screw} + N_{edge}) TD values for all the samples are listed in Table 7.1. for 1μm thick films InN/epi and InN/NWN, the dislocation density values are calculated to be 2.4$\times$10^{10} and 7.5$\times$10^{9} cm^{-2}. In our study, the value of the dislocation density reduces with increasing film thickness, which confirms that more dislocations are created at interface and annihilated as the film thickness is increased. The dislocation density is further reduced for the InN films grown on the defect free GaN NWN.

7.4 Electron mobility of self-assembled and dislocation free InN nano rods

7.4.1 Morphological, structural and optical characterization

Fig 7.7(a) shows the top view FESEM image for GaN NWN template grown for 30 min on bare sapphire at 630 °C. Fig 7.7(b) and (c) are the top and tilted views of the FESEM images obtained after growing InN NRs at 450 °C on the GaN NWN template. Fig 7.7(a) shows the hexagonal network of the GaN nanowalls, with the inset showing a six fold symmetry by FFT. The image 7.7(b) clearly shows the NRs formed inside the cavities of the GaN NWN are hexagonally faceted and its sharp six-fold symmetry is evident in the corresponding FFT inset. All the rods are vertically aligned and well separated with the heights of most of these NRs being ≈ 750 nm, while a few are in the range 100 – 750 nm. This vertical growth of the InN NRs is attributed to the low sticking coefficient of In atoms on the GaN NWN at this temperature, promoting super-saturation inside the cavities[269] and nucleating GaN nano columns. Fig 7.7(c) shows the tilted view of the vertically aligned NRs that stem from the hexagonal closed loops of the network. All the NRs have identical orientation and a tapered morphology, irrespective of the heights, with similar aspect ratios. The distribution of the GaN NWN cavity and the InN NR diameters is shown in Fig 7.7(d). The bar diagram shows that the average diameter of the NR is ≈120 nm (range from 20 to 220 nm) and the average diameter of the cavities is ≈ 70nm (range from 10 to 250 nm). The InN nano rod density is ≈1.2$\times$10^{8}cm^{-2}, while

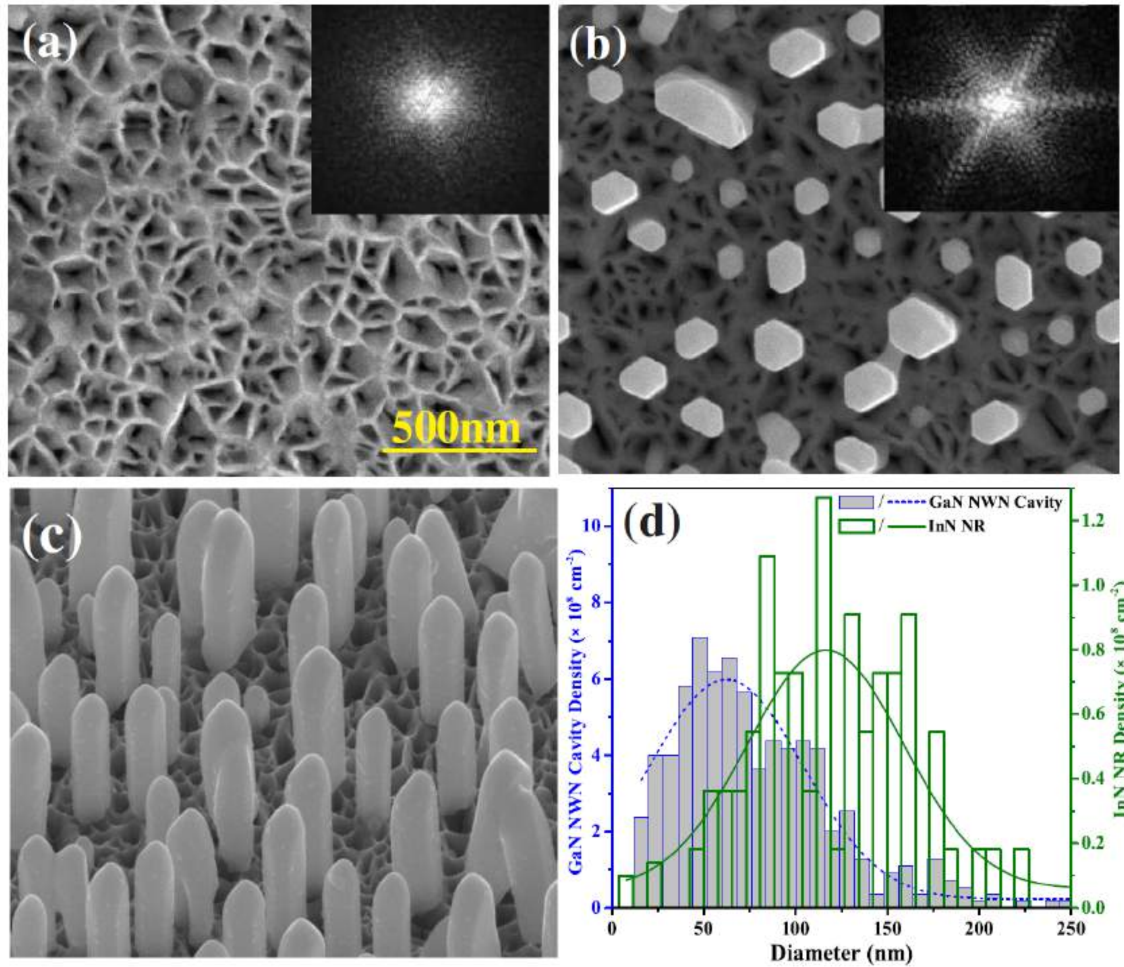

Figure 7.7: (a) and (b) show the top views of FESEM images of bare GaN NWN and after depositing InN, respectively with their corresponding FFTs as insets, while 1(c) is the tilted view of InN NRs. 1(d) is the distribution of GaN NWN cavity diameters and InN NR diameters with dotted/solid Gaussian fits to the respective distributions.

the cavity density of GaN NWN is found to be $\approx 1\times10^9$cm^{-2}, showing that only 12% of the nano cavities (>40nm) are populated with the InN NRs. Thus, the In adatoms have enough energy to move out of the smaller cavities and spend more time in the neighboring larger cavities (>40nm), where they have a higher probability of nitridation and consequent nucleation.

Fig 7.8(a-c) shows the RHEED pattern obtained during InN growth with an electron beam of 8keV kinetic energy incident along $<11\bar{2}0>$ on (a) the bare GaN NWN template, (b) 5mins grown InN NRs and (c) 3hrs grown InN NRs, respectively. Fig 7.8(a) is a spotty RHEED pattern due to the transmission of the electrons through the walls of the GaN NWN. The calculated c/a ratio from the averaged line scans (intensity profiles) taken along a* and c* reciprocal lattice vector directions (shown in Fig 7.8(c)) is ≈1.62 which

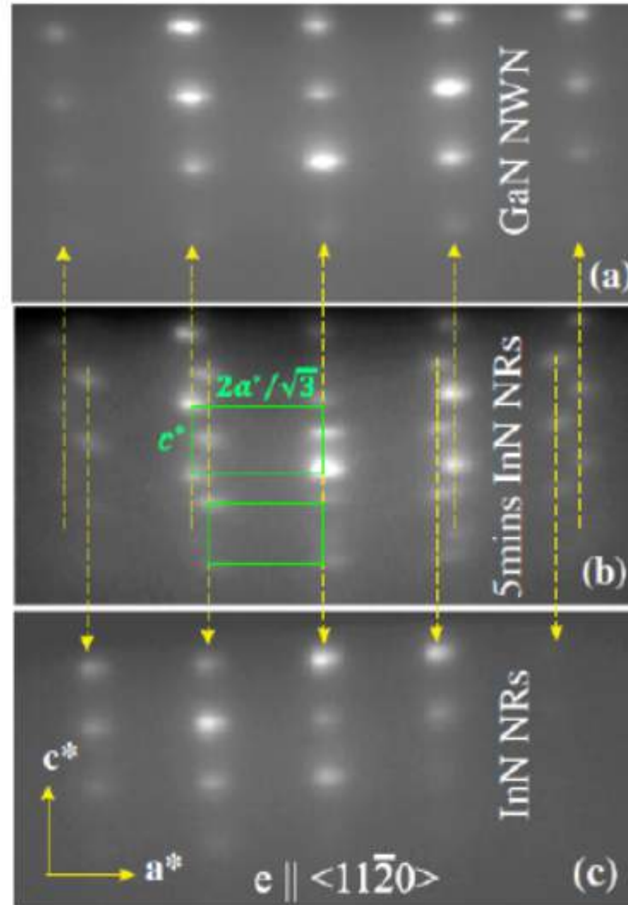

Figure 7.8: (a-c) show the RHEED pattern obtained on the GaN NW network template, 5mins grown InN NRs and post growth of InN NRs, respectively. Rectangles show the unit cells for InN (smaller) and GaN (bigger) in reciprocal space. $\mathbf{a}^*$ and $\mathbf{c}^*$ are reciprocal lattice vectors represented in Fig 7.8(c).

is characteristic of wurtzite GaN. Fig 7.8(b) shows the RHEED pattern obtained on 5mins grown InN NRs on GaN NWN, consists of an additional set of spots with the c/a ratio of 1.61 that can be attributed to the formation of wurtzite InN on top of the GaN NWN. These two sets of spots, shown as rectangles in Fig 7.8(b) for InN and GaN (lattice mismatch of 11.5 %) show that the InN NRs are relaxed and grow without any interfacial alloying. Fig 7.8(c) shows the characteristic spotty RHEED pattern of transmitted electrons through the InN NRs, as indicated by arrows in Fig 7.8(a-c), for higher coverage.

To understand the crystalline structure and quality of the InN films, HRXRD measurements are performed and the results are shown in Fig 7.9. The 2θ-ω scans, in logarithmic scale, are acquired on symmetric and asymmetric planes for InN NRs, respectively. InN NRs are seen to possess single crystalline wurtzite structure with the

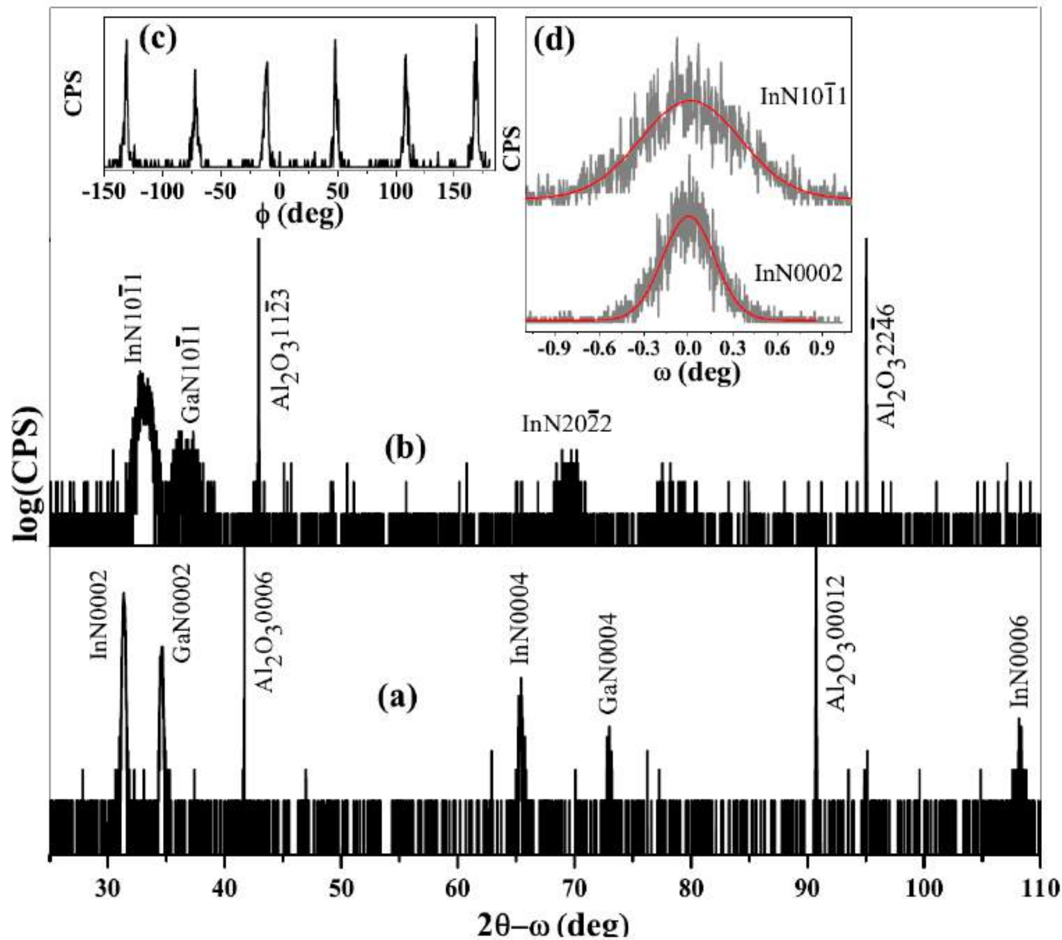

Figure 7.9: (a) and (b) show symmetric and asymmetric 2θ-ω scans acquired by HRXRD on InN(0002) and InN(10$\bar{1}$1) planes, respectively. The inset (c) shows the phi scan and (d) rocking curves acquired on InN NRs. Solid lines in (d) are Gaussian fits to the raw data points.

preferential growth direction along c-axis. The pattern Fig 7.9(a) displays intense c-oriented peaks, InN(0002) at 31.28°, InN(0004) at 65.30° and InN(0006) at 108.30° along with the GaN(0002) peak at 34.58° and the Al_2O_3 substrate (0006) and (000 12) peaks at 41.68° and 90.80°, respectively. Fig 7.9(a). Fig 7.9(b) shows 2θ-ω scan for the asymmetric reflection which consists of InN(10$\bar{1}$1) and InN(20$\bar{2}$2) peaks at 33.13° and 69.57° along with GaN(10$\bar{1}$1) peak at 36.81° and the substrate peaks viz. Al_2O_3(11$\bar{2}$3) and Al_2O_3(22$\bar{4}$6) at 42.89° and 95.11°, respectively. Absence of any peak related to metallic In confirms that there is no excess unreacted crystalline In on the surface/bulk or at the tip of the NRs, which is also well corroborated by FESEM and XPS studies. Fig 7.9(a) and (b) give the epitaxial relationship of InN with respect to the GaN NWN and c-Sapphire, as InN[0001] ||GaN[0001] ||Al_2O_3[0001] and InN[10$\bar{1}$0] ||GaN[10$\bar{1}$0] ||Al_2O_3[11$\bar{2}$0], revealing

that c-oriented InN and GaN unit cells are azimuthally rotated by 30° with respect to the sapphire substrate, to minimize the lattice mismatch between GaN template and c-sapphire. Fig 7.9(c) is the phi-scan that is obtained from asymmetric plane InN($10\bar{1}1$) for the InN NRs, exhibiting six equally spaced peaks characteristic of the six fold symmetry of the wurtzite InN. Absence of any other random peak in the phi-scan suggests that the NRs predominantly grow along the c-direction. From symmetric and asymmetric scans, the calculated high precision lattice parameters (c, a) for the InN NRs (5.7058Å, 3.5372Å) are very close to the unstrained values[218] revealing that the InN NRs are relaxed. Fig 7.9(d) shows the ω-scans (rocking curves) obtained around the InN(0002) and InN($10\bar{1}1$) reflections for InN NRs. The FWHM values for InN(0002) and InN($10\bar{1}1$) are 0.38° and 0.82°, respectively. These higher broadening values are due to the Gaussian distribution of angular spread of the mosaicity caused by slight tilt and twist in the nano rods with respect to the surface normal as also seen in Fig 7.7(c), thus these broader FWHM values are not useful in evaluating the dislocation density for NR configuration.

TEM studies: Zero dislocation density

Fig 7.10 (a) and (b) show bright field and dark field TEM images of a typical InN NR while **g** vectors are setup along [$11\bar{2}0$] and [0002], respectively. It is evident from Fig 7.10(a) and (b) that the NR has a uniform diameter of $\approx$ 140 nm along the rod length of $\approx$ 750 nm and a tapering at the apex with a small c-plane terrace. Fig 7.10(c) and (d) show the Selected Area Electron Diffraction (SAED) pattern for bright field image Fig 7.10(a) taken along the <$11\bar{2}0$> and <$10\bar{1}0$> zone axis which indicates that the wurtzite InN NRs grow along the [0002] direction where the top c-plane plateau is bound by m-planes ($10\bar{1}0$) as the six side walls. The apex of the InN NRs has truncated pyramidal r-plane ($10\bar{1}2$) facets with an inclination angle of $\approx$ 58° with respect to the top c-plane. Fig 7.10(a-b) show some stacking faults but the absence of any dislocation lines in InN NRs is notable. Fig 7.10(b) exhibits fringes and contours in dark field image, which are attributed to the slight bend and thickness variation at edges of NR, respectively.[271] Thus, the InN NRs that form inside the GaN NW cavities, are single crystalline and free of dislocations and grow strain free along the c-direction. After observing the various stages of growth and analyzing the structural properties by

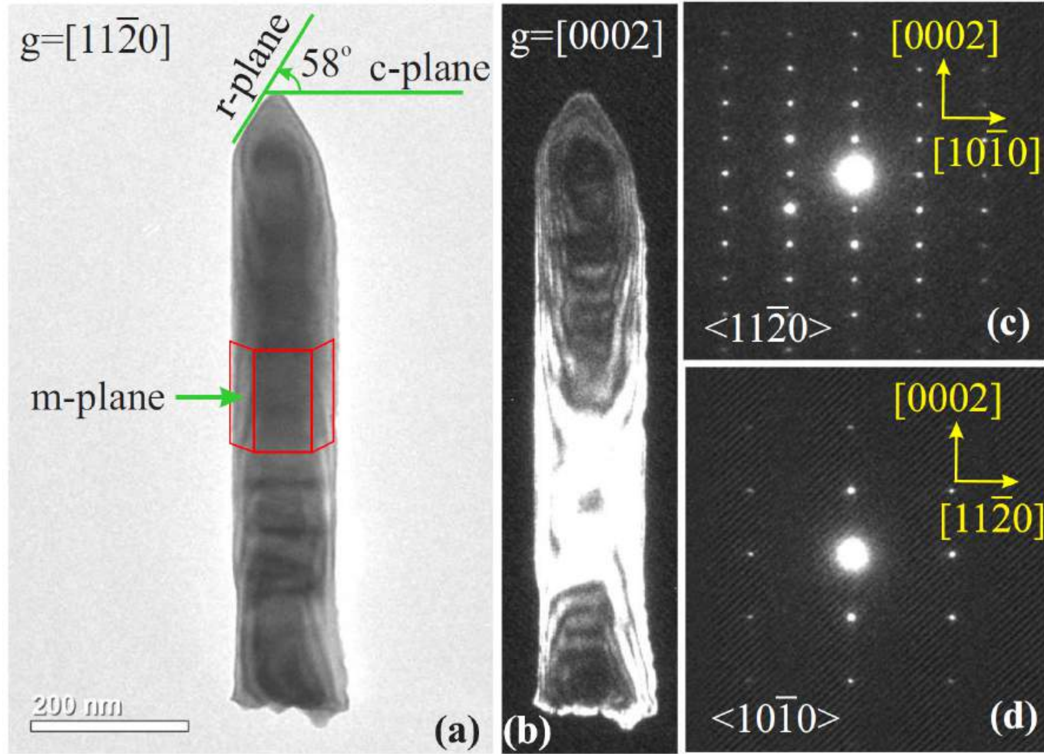

Figure 7.10: (a) is the bright field and (b) the dark field TEM images of an InN NR along [11$\bar{2}$0] and [0002], respectively. 7.10(c) and (d) show the SAED pattern acquired on InN NR along zone axis <11$\bar{2}$0> and <10$\bar{1}$0>. All facets are marked according to SAED pattern.

different techniques, we try to understand the possible mechanism involved in the InN NR growth. The impinged III and V group atoms on to the GaN NWN, bound by r-planes have a low sticking coefficient[272] and are funneled into the cavities. Contrary to the dislocation mediated NR formation in GaN[273] the InN NRs appear to adopt the vapor-solid (V-S,[274]) or the droplet epitaxy[275] route. At this temperature the adatoms do not spend much time in smaller cavities, and thus leads to super-saturation only in larger cavities where they nucleate and get nitrided by the N_2* plasma into m-faceted hexagonal NRs. Thus, the InN NRs grow spontaneously along the c-direction with non polar m-plane side facets, due to the low diffusion barrier (E_{diff}) of In adatoms along m-plane ($E_{diff}^{||c-axis} = 0.06eV$) than along the c-plane ($E_{diff}^{\perp c-axis} = 1.30eV$) which results in higher sticking coefficient ($\Gamma \sim exp(-E_{diff}/k_BT)$ where k_B the Boltzmann constant and T the absolute temperature) of In atoms on c-plane than that on the m-plane at the growth temperature employed[276–278]. Thus, In adatoms having low sticking coefficient on the m-plane InN walls and r-plane GaN facets, creep along the sides and nucleate on the c-terraces, promoting the NR growth of InN. The high quality of the spontaneously formed

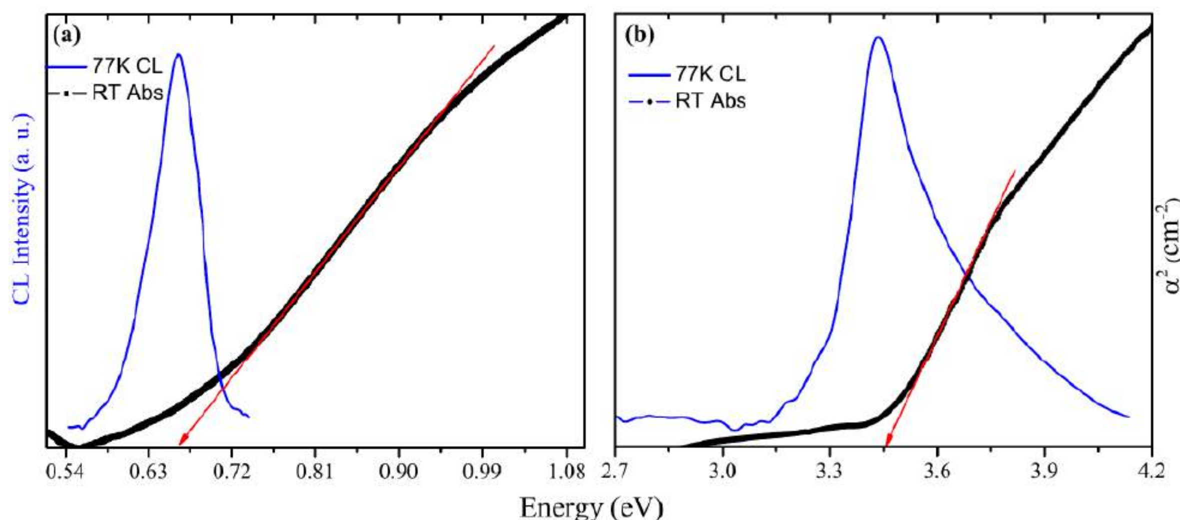

Figure 7.11: (a) and (b) show CL emission and optical absorption spectra acquired on InN NRs and GaN NWN.

self assembled isolated InN NRs in the GaN NWN matrix, prompted us to look at the resulting optical properties, by UV-VIS-IR absorption and cathode-luminescence. The absorption coefficient is determined from transmission measurements. Fig 7.11 shows CL (normal y-axis) and absorption (alternate y-axis) measurements for InN NRs and GaN NWN where the CL band edge emission is obtained at liquid nitrogen temperature (77K). The emission peaks and absorption edges, at 0.65eV and 3.44eV, corresponding to the InN NRs and the GaN NWN template.

7.4.2 Hall and transport measurements on a single InN NR

In order to measure the electron mobility and carrier concentration of InN NRs, Hall measurements are carried out on a single NR. Using masking technique, four isolated In(20nm)/Ag(20nm) pads having separation of $\approx 20\mu$m are deposited on the sapphire substrate by e-beam evaporation. The InN NRs are deposited on sapphire substrate in middle of the four In/Ag pads by drop casting. The Platinum (Pt) connecting wires are deposited in FESEM environment having high vacuum conditions, followed by annealing at 200 °C for 60 mins in UHV conditions 5×10^{-10} Torr. Fig 7.12(a) shows the FESEM image of the NR after depositing Pt connecting wires. The respective inset is the schematic representation of the contacts where Pt connecting wires electrically connect the NR and In/Ag pads. The Hall measurements are performed within the ohmic region of the contacts by assuming rectangular bar geometry using Van der Pauw

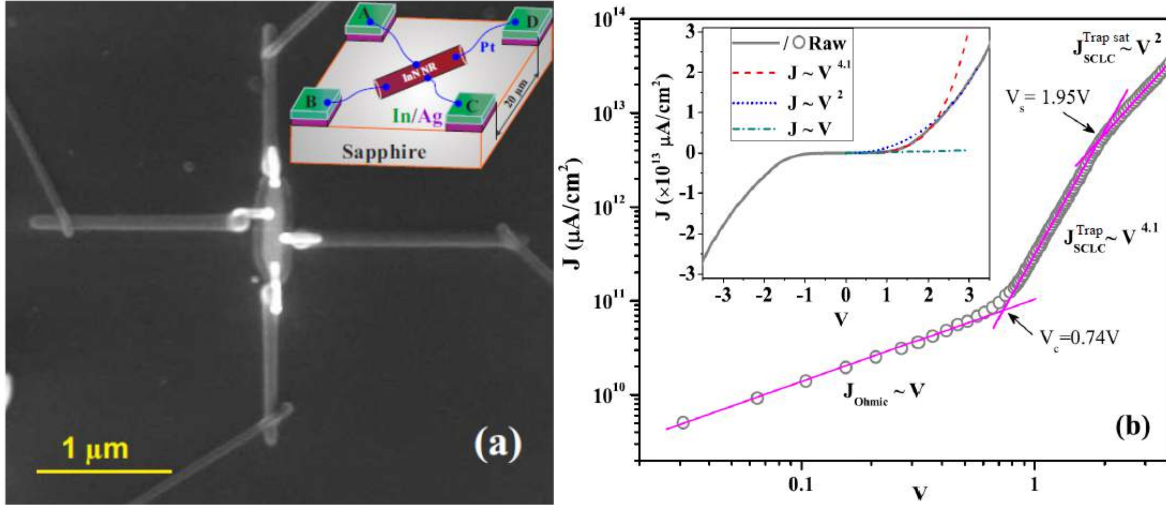

Figure 7.12: (a) shows the InN NR having four Pt contacts and the respective inset shows the schematic representation of the InN NR with four metal contacts Pt/In/Ag. (b) and respective inset show non-linear J-V characteristics in logarithmic and linear scale. Inset also describes the dependence of J on V, V^2 and $V^{4.1}$ in the forward bias region.

method, which can be used for any arbitrary disc shape to measure resistivity and Hall voltage.[279] The carrier concentration is found to be 3.1×10^{17} cm^{-3} and the mobility is 4263 cm^2/V-sec.

Further confirmation of measured mobility and carrier concentration is achieved by employing space charge limited current (SCLC) formalism to J-V characteristics that are performed on InN NR across the contacts B and D. Fig 7.12(b) shows log-log plot of J-V characteristics, where increasing forward bias switches ohmic region J$\sim$V to SCLC region J$\sim V^{\beta+2}$, where $\beta \approx$2.1, due to the space charge limited currents,[280] associated with charged traps like unavoidable native point defects,[243] which starts over the voltage value of $V_c \approx 0.74$V. Further increasing bias leads to the saturation of the charged traps and thus SCLC region $V_s \geq 1.95$V holds J$\sim V^2$, which consequently result in non-linear J-V characteristics. Inset shows J-V characteristics in linear scale along with the fitted curves which depicts the dependence of J on forward bias V, $V^{4.1}$ and V^2. The SCLC for nano-wires/rods[281] can be described by the following modified Mott and Gurney expression.[282]

$$J_{SCLC}^{NR} = \left(\frac{R}{L}\right)^{-2} \frac{\epsilon\mu\xi}{L^3} V^2 \tag{7.4}$$

where J is current density, R is radius, L is length of NR, ϵ is static dielectric constant, μ is electron mobility, $\xi = \xi_0(V/V_c)^\beta$ and V_c is cross over voltage, ξ_0 is constant[280]. When

$V = V_s$, $\xi \longrightarrow 1$ and $\xi_0 \sim (V_c/V_s)^{\beta}$. The mobility thus extracted from SCLC region in J-V characteristics using Eq. (7.4) is $\approx$ 4453 cm^2/V-sec. For the NR geometry, the expression[281,283] for the carrier concentration is $n = \epsilon V_c/eR^2$, which yields a value of $\approx 1.1\times10^{17}$cm^{-3} for InN NR. The carrier concentration (mobility) obtained from SCLC model is lower (higher) than that of the value obtained from Hall measurements, which could be due to the assumption of rectangular bar geometry with volume of 1.3 times larger than the cylinder and asymmetry in the larger contacts.

The obtained high mobility and low carrier concentration values agree well with earlier Monte Carlo simulations[115] performed by Polyakov *et al.* for defect free InN material and also dislocation density dependent mobility calculations by Miller *et al.*, where it has been shown that when the dislocation density reaches $\leq 10^7$ cm^{-2}, electron mobility of InN attains $\approx$4000 cm^2/V-sec.[257]. The mobility of the dislocation free degenerate pristine InN NR is higher than that of state-of-the-art InN epilayers ($\approx$ 3000 cm^2/V-sec)[128] having the dislocation density in the range of 10^9 to 10^{10} cm^2. Very recently, Zhao *et al.*[284] have shown very high mobility in the range of 8000 - 12000 cm^2/V-sec for intrinsic InN Nano wires with carrier concentration in the range of 10^{13} to 10^{15}cm^{-3} from I-V measurements, where any effect of dislocation density on mobility has not been considered. In our study, mobility and carrier concentration values are measured directly using Hall measurements for degenerate NRs, which are also confirmed by SCLC analysis. Thus, this study clearly shows the method to obtain dislocation free InN NRs, which exhibit very low band-gap and high electron mobility.

7.5 Native point defects and dislocations as scattering centers

7.5.1 Charge neutrality condition

Considering the process of full ionization of both donors and acceptor like impurities in semiconducting material, where donor (acceptor) atoms are doped in the material donate (accept) electrons and become positively (negatively) charged ions having the concentration of N_D (N_A). There are negatively charged electrons and positively

charged holes present in the material with concentrations of n and p, respectively. As the semiconducting material is always electrically neutral, the total positive charge concentration in the material must be equal to the total negative charge concentration in the material. Therefore, the charge neutrality condition for semiconductors turns into the following equation.

$$N_A^- + n = N_D^+ + p \tag{7.5}$$

In case of MBE grown InN, there is significant evidence in literature that the dominant defects are In vacancies probed by the positron annihilation measurements[47,225,285] and the nitrogen related point defects probed by Raman spectroscopy and X ray Photoelectron Spectroscopy[136,212,243] as well as the threading dislocations probed by HRXRD and TEM measurements .[45,91,254] The In vacancies are found to be triply charged acceptors[104,285] and the other nitrogen related defects act as the donors in n-type InN.[48] The hole concentration (p) is negligible in degenerate unintentionally doped n-type InN having the electron concentration of n. The values of carrier concentration (n) from Hall measurements are determined to be 6.1×10^{17} and 8.4×10^{17} cm^{-3} for samples InN/NWN and InN/epi, respectively (values for other samples see Table 7.1). The concentration of the V_{In} native defects $[V_{In}]$ = C exp($-E_f/k_BT$), depends on the energy that is required for the Indium vacancy to be created in the lattice, generally known as formation energy E_f that relies on the Fermi Level position.[210,244] In case of the narrow band gap semiconductors, Fermi level position varies from the bottom of the conduction band to the Fermi Level stabilization energy (pinning level) due to the strong band filling effects ,[116] thus the concentration of Indium vacancies are evaluated within the amphoteric defect model, where the native point defects act as donors or acceptors based on the Fermi level position.[286] The dislocation density is also evaluated using HRXRD measurements as described in above section. It is known in the literature it has been shown that the charge can be distributed continuously along the dislocation line at the rate of one electron per c lattice distance for III nitrides.[257] The only unknown parameter is the concentration of nitrogen related donor like defects. Therefore, the following simplified charge neutrality condition is used to estimate the donor concentration in n-type InN,

$$n + 3[V_{In}^-] = N_D^+ + \frac{N_{dis}}{c} \tag{7.6}$$

7.5.2 Matthiessen's rule

In order to calculate the resultant number of native point defects ($N_{npd}= N_D + 3[V_{In}]$) which act as charge scattering centers in InN, using above charge neutrality condition. In heavily doped semiconductors, electron mobility is remarkably limited by the scattering phenomena due to the native point defects (charge centers), dislocations and the small contribution from the phonons. The resultant electron mobility (μ) limited by all these dominating scattering mechanisms can be expressed by employing the Matthiessen's rule:

$$\mu = \left(\frac{1}{\mu_{npd}} + \frac{1}{\mu_{dis}} + \frac{1}{\mu_{ph}} \right)^{-1} \tag{7.7}$$

where μ_{npd}, μ_{dis} and μ_{ph} are the mobility of electrons scattered by charged native point defects, dislocations and phonons at room temperature. Walukiwiez *et al.*, have shown that the phonon limiting mobility at room temperature for InN is ≈7000 cm^2/V-sec.[287] As deduced by Walukiwiez *et al.*[288] and Look *et al.*,[91] the expressions for mobility of electrons associated with charged native point defects and dislocations respectively, are

$$\mu_{npd} = \frac{e\tau_{npd}(E_F)}{m^*} = \frac{3\pi}{2} \frac{\epsilon_0^2 \hbar^3}{e^3} \frac{n}{N_{npd} \left(m^*\right)^2 F_{npd}} \tag{7.8}$$

$$\mu_{dis} = \frac{e\tau_{dis}(E_F)}{m^*} = \frac{4 \times 3^{2/3} e c^2 n^{2/3}}{\pi^{8/3} \hbar N_{dis}} [1+\gamma]^{3/2} \tag{7.9}$$

where ϵ_0 is static dielectric constant, n is carrier concentration, $\hbar$ is reduced Planck's constant, e is electron charge, m* is energy dependent effective mass of electron for a non-parabolic conduction band which is described in Fig 7.13, $F_{npd} = \ln(\gamma+1) - \frac{\gamma}{\gamma+1}, \gamma = (2k_F/\lambda)^2, k_F = (3\pi^2 n)^{1/3}$ is electron wave vector at Fermi level and $\lambda = \frac{2e}{\hbar}\left(\frac{\pi}{3n}\right)^{1/6}\left(\frac{m^*}{\epsilon_0}\right)^{1/2}$ is the Thomas Fermi screening vector and c is lattice constant of InN. Equation (7.9) is used here in CGS units, divided by 4π.

From equation (7.7), electron mobility of InN is calculated for the experimentally obtained dislocation density values in the effective range of carrier concentration 5×10^{17} - 5×10^{19} cm^{-3}. Fig 7.14 shows the experimental results along with the calculated mobility versus carrier concentration plots for different dislocation density values that

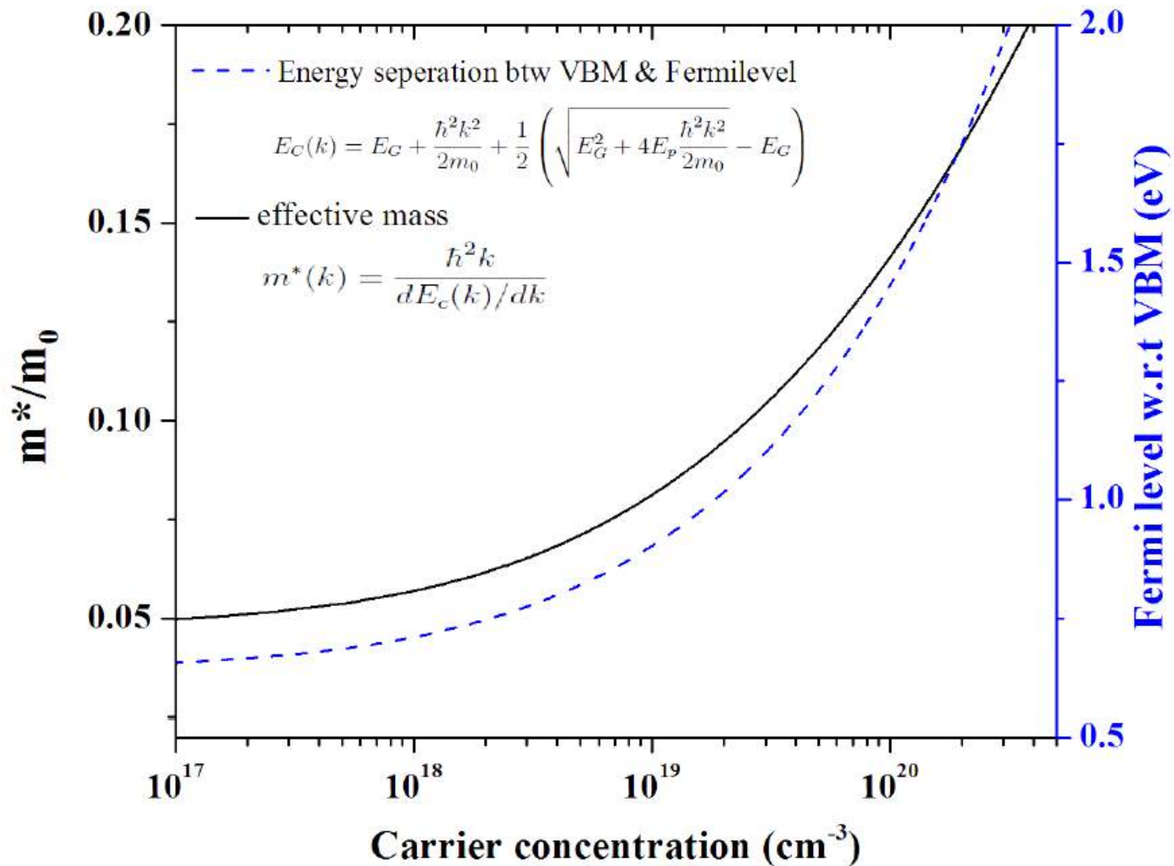

Figure 7.13: shows the energy dependent effective mass (solid line) of electron for a non-parabolic conduction band along with the Moss-Burstein curve (dashed line).

were obtained from the HRXRD measurements for the films A-D, E and F. Variation of the mobility is ascribed to the scattering of electrons mainly at the charge centers, dislocations and phonons. As the carrier concentration increases, effect of scattering at dislocation lines is less significant since the dislocation lines are screened by the free electrons of the ionized native point defects. Dislocation scattering plays a dominant role at low carrier concentration values, and below this specific value of carrier concentration, the mobility increases with decreasing dislocation density. Inset also shows that the calculated mobility attains its maximum value at a certain value of carrier concentration, which relies solely on the dislocation density. The mobility calculated is maximum for the film grown on GaN NWN having dislocation density value of $7.5\times10^{9}\text{cm}^{-2}$ at carrier concentration value of $\approx 6.1\times10^{17}\text{cm}^{-3}$. The experimental values of mobility more or less agree with the calculated ones, since the dislocation and point defect scattering mechanisms are playing a crucial role in limiting electron transport in n-type InN. Maximum attainable calculated mobility for InN, having the dislocation density of zero

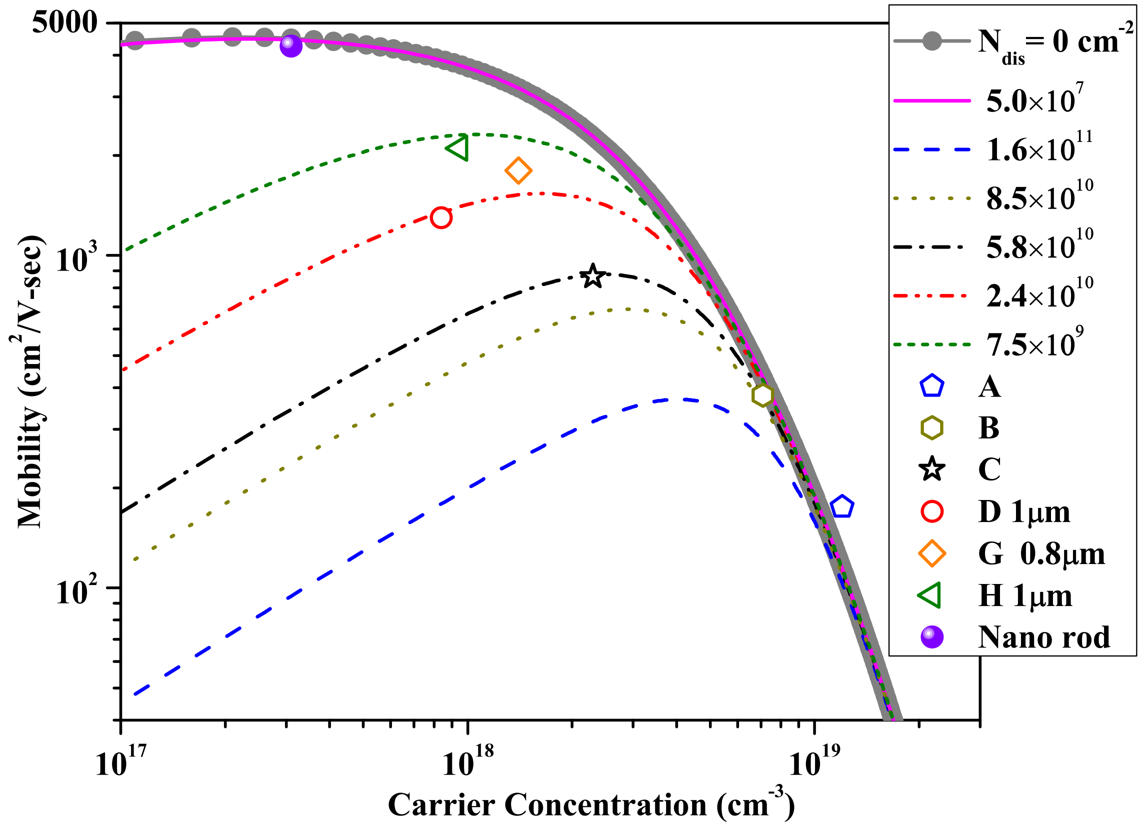

Figure 7.14: The inset shows calculated mobility as a function of carrier concentration for the experimentally obtained dislocation density values and the open symbols are from this study.

or $\leq 5\times10^7$ cm^{-2} is $\approx$4400 cm^2/V-sec for carrier concentration of $\approx1\times10^{17}$cm^{-3} which agrees well with the earlier Monte Carlo simulation results.[128] Thus, dislocation related scattering is negligible when the dislocation density in InN material is less than or equal to $\approx5\times10^7$ cm^{-2}. In our experiments GaN NWN template enables the reduction of the dislocation density in over-grown InN layer to attain high mobility of 2121cm^2/V-sec for the film thickness of 1μm.

7.6 Inferences

In summary, InN compact films are grown on GaN epilayer and NWN templates deposited on c-sapphire. The careful experiments are directed towards obtaining high mobility InN layers having low band gap and improved crystal quality. The dislocation

density measured from HRXRD rocking curve broadening values for the films of InN/GaN NWN is less than that of the films InN/GaN epilayer which can be due to the presence of voids at the interface of InN/GaN NWN. Thus, this new adaptation of the Nano ELOG growth process enable us to obtain high mobility InN layers. This obtained high hall mobility 2121 cm^2/V-s for 1μm thick InN/GaN NWN. The self-induced and self-assembled vertically aligned (c-oriented) high quality InN NRs are grown on GaN NWN template deposited on c-sapphire at slightly higher temperature of 450 °C with In K-cell temperature of 750 °C. The TEM and XRD studies reveal that InN NRs are observed to be dislocation free, m-faceted and with a relaxed wurtzite structure. The method is a simple single growth, two-step MBE process, that enables the growth of very high quality pristine InN NRs exhibiting good structural, optical and electrical properties. The rods display a sharp and low band edge emission at 0.65eV with low Hall carrier concentration of $\approx 3.1\times10^{17}$ cm^{-3} and a very high electron mobility of ≈ 4263 cm^2/V-sec. By employing SCLC formalism to J-V characteristics allow us to measure low carrier concentration of $\approx 1.1\times10^{17}$ cm^{-3} and high electron mobility of ≈ 4453 cm^2/V-sec. The value of electron mobility of 1μm thick InN thin films (2121 cm^2/V-sec) is the highest reported in the literature, to the best of our knowledge.

Chapter 8

Conclusions

This chapter summarizes briefly the contents of the present thesis, lists the highlights of the work and draws conclusions from the observed results. Overall, the thesis is a systematic approach to understand InN formation, inherent defects and means to reduce them and to obtain high quality and reliable material. We have methodically narrowed the kinetic growth paths towards obtaining high structural, optical and electrical quality thin films and nano-structures with very high electron mobility values. This chapter also gives a brief outlook for the future work.

Though InN is a highly potential candidate for electronic and opto-electronic devices, it has not yet been exploited due to its low dissociation temperature which has resulted in ambiguous values of experimentally obtained material parameters. Literature shows a wide scatter of values for different fundamental properties such as band gap, electron effective mass and electron mobility of this material. One of the aims of the thesis is to design experiments to obtain high mobility InN layers and to evaluate the various suggested reasons in the literature for the measured band gap of InN grown on c-Al_2O_3(0001) substrate. InN is also proposed to exhibit phenomenon like surface electron accumulation which has not yet been comprehensively understood. The incorporation of III nitrides into the well established Si industry is another major challenge. In the literature attempts in this direction is quite nominal especially for InN. Si surfaces are endowed with fascinating surface reconstructions induced by metal adsorption, which offers the possibility of using them as matching templates for foreign adsorbents. Thus, we

have carefully studied the formation of different superstructural phases of group III metals on Si surfaces so as to find a lattice matched template for the growth of good quality InN. On the other hand, achieving high mobility InN layers on c-sapphire has remained challenging as experimentally obtained mobility values are far below the theoretically estimated ones. In order to get high mobility, InN films are grown by a novel adaptation of the nano ElOG process using GaN nano wall network as template. The summary of the work carried out and the results obtained are given below:

8.1 Summary and Conclusions

8.1.1 Unintentional doping in InN: Band gap controversy

Unintentional degenerate doping of InN layers is attributed due to its low dissociation temperature and high vapor pressure of nitrogen during growth, which consequently makes preparing high quality material very difficult. Literature showed a wide scatter of the InN band gap values in the range of 0.6-2eV and several reasons have been provided to account and discount the different observations. To look at the reasons for the observed high band gap of InN, we have carried out a set of kinetically controlled growth of experiments, to form InN films at different growth temperatures and nitrogen flux rates, on bare c-sapphire (0001) substrates using MBE. The formed films have been characterized using several complementary characterization tools to relate structure and properties. We observe high band gap values ($>$0.65eV)for all the samples studied. Our results clearly exclude stoichiometry and quantum size effects as reasons for the observed high band gap for InN. The XRD measurements on all samples show a strong dependence of InN orientation on the growth temperature. One of the contentious reasons given in the literature, for the observed high band gap, is the formation of indium oxide or indium oxynitride which have higher band gap values. Using core-level XPS measurements, we show that the band gap values observed from absorption and PL studies were similar to that of all the other samples. This enabled us to rule out the role of oxides on the observed band gap. Hall effect measurement on all the samples measured by the Van der Pauw method showed a degenerate level of unintentional doping with a carrier concentration 10^{20}cm^{-3}. We observe that all the experimental data agreed well with

the theoretical prediction of Moss-Burstein shift with a non-parabolic behavior of the observed band edge with carrier concentration. In other experiment, in order to find the reasons behind formed degenerate films, N_2^* flux is varied from 2 to 8 sccm in steps of 2sccm, where the degeneracy in the samples is attributed the nitrogen related native point defects that contribute to the carrier concentration. Thus, on the basis of analysis by several parametrically controlled growth experiments coupled with complementary characterization tools, we confirm that the high band gap is due to the high unintentional doping in InN which results from the native point defects.

We performed another set of experiments to grow InN on 2μm thick GaN epilayer at different growth temperatures to isolate the sapphire interface and look into the low band gap region of the reported InN band-gap values. In this set of experiments, the growth parameters remained the same except the growth temperature, but two of the samples were grown at temperatures of 400 °C and 470 °C yielding high band gap values of 1.25 and 1.05eV, while the samples grown at intermediate temperatures of 430 °C and 450 °C showed a lower band-gap values of 0.75 and 0.70eV, respectively. This demonstrated the criticality of the role of the substrate temperature in determining the InN film properties. One of the arguments among the previously attributed reasons for the low band gap observed for InN was Mie-resonances, resulting from distributed metallic In clusters in InN which can shift the absorption edge to the infrared region of the electromagnetic spectrum. Our XRD and SAED measurements clearly rule out the presence of metallic crystalline/amorphous unreacted indium in low band-gap InN samples, and thus, discounting the possibility of Mie-resonance as the reason for the observed low band gap for InN. The base pressure of our MBE chamber is $<5\times10^{-11}$ torr and the oxygen partial pressure is beyond the detection limit of residual gas analyzer attached to the chamber ($<10^{-12}$ torr). This, as observed by XPS studies also rules out oxygen having any role in the observed high band gap in these experiments. However, we have carried out core-level XPS measurements to verify the presence of oxide due to the diffusion of oxygen from the oxide substrate (Al_2O_3) in all our samples. A native oxide is found to be formed on the surface of the films due to atmospheric exposure of the samples, but we show that it does not effect the band gap values of InN. We have studied the variation in the observed band edge values with carrier concentration

in the present experiments and understood them in the context of the data existing in the literature. A non-linear curve fit for the experimental data using theoretically calculated Moss-Burstein relation with parabolic conduction band approximation for InN, yielded unacceptable value for the effective mass of InN. However, a fit of the various experimental data values assuming a non-parabolic conduction band yielded us better fit and an effective mass of $\approx 0.07 m_0$ at the bottom of the conduction band. Thus, based on systematic experiments and a comprehensive analysis we observe a band gap value of InN $\approx$0.7eV grown on c-sapphire by sheer control of the kinetic growth parameters. Our studies show a narrow band gap ($\approx$0.7eV) for InN with a non-parabolic conduction band with carrier concentration dependent electron effective mass, and for a parabolic conduction band the effective mass of electrons is constant.

8.1.2 Surface charge accumulation

Literature shows several reports on the presence of a surface electron accumulation layer for InN (0001), which manifests as an increase in the carrier concentration near the surface of the film, which results in surface downward band-bending. To study this phenomenon in our samples, we have performed XPS valence band measurements on InN samples grown on GaN epi-layer having different values of carrier concentration. Prior to the XPS measurements, low energy Ar^+ ions are used to remove adventitious contaminants from the atmospheric exposure. XPS In 3d core level analysis reveals that the near surface charge is due to the In adatoms which act as donor like states and contribute electrons to the conduction band. The band bending values calculated using both optical absorption and XPS valence band studies reveal that the poly-crystalline films having high band gap exhibit the absence of band-bending and the low band gap films have the band-bending upto $\approx$1eV. Thus, our results clearly show the presence of surface accumulation layer for InN (0001) surface.

8.1.3 Super Lattice Matching Epitaxy of InN on Si(111)

Since the interfacial lattice mismatch between the InN films and the substrate play a critical role in determining the morphology and structure of the films, we have used the phase diagram of In metal adsorption on Si(111)-7$\times$7 surfaces as a guidance to obtain

different metal-induced superstructures as growth templates. We perform careful thermal desorption of about 2ML of In deposited on the Si(111)-7×7 surface to obtain different superstructural phases viz., $\sqrt{3} \times \sqrt{3}$, 4×1,$\sqrt{31} \times \sqrt{31}$ and 1×1 in the MBE system. Five different growths of InN are performed under similar growth conditions on these structurally modified substrate surfaces and followed them by evaluating the quality of the formed InN film using several complementary characterization tools. InN grown on 4×1 and 1×1 surfaces are seen to show superior optical, structural and electronic quality compared to the films grown on other superstructural interfaces. Further improved crystal quallity is achieved by using these layers as intermediate buffer layers. We explain the results using the lattice matching epitaxy of the unit cells of these reconstructions with that of InN. The observed PL band edge emission on these samples again are explained by the Moss-Burstein shift in InN and propose a non-parabolic conduction band for InN. The films far away from the stoichiometric ratio do not exhibit any PL emission. The auto doping by Si atoms into the InN over grown layer is discounted by systematic and careful XPS Si core level measurements. Our results show lattice matching epitaxy as a novel and simple growth process to grow InN at much lower temperatures than usually employed, which displays better optical, structural and electronic properties.

8.1.4 Towards high mobility InN films

In our experiments of GaN growth on c-sapphire we have found a unique Nanowall Network morphology that is seen to be defect and strain free. The role of native point defects and dislocations in limiting the electron mobility of InN layers has been carefully studied. Using charge neutrality condition and Matthiessens rule various charge scattering mechanisms are studied and the resultant mobility which is limited by various scattering mechanism is calculated and compared with experimentally obtained mobility values. As the carrier concentration increases, effect of scattering at dislocation lines is less significant since they screened by the free electrons that stem from the ionized native point defects. Consequently, charged native point defects play a dominant role at low carrier concentration values, where as at lower carrier concentration, dislocations play a dominant role in limiting the mobility of InN. Thus, In order to get high mobility layers, dislocation density has to be reduced. We have used nano ELOG process where

InN films having thickness upto 1μm are grown on GaN nano wall network templates. In order to reduce dislocation density, in our InN films, we have carried out a set of systematic experiments where the films are grown under optimized growth conditions on GaN epilayer and GaN NWN templates for different growth durations.

Table 8.1: Consolidated values of carrier concentration and band gap for all the samples used in this thesis

	Sample	Carrier concentration n (cm^{-3})	Bandgap / Method $E_g \pm 0.05$ (eV)
Chp 4	InN/Sapphire	$\approx 7.00\times10^{20}$	1.78 / CL
	2sccm	3.10×10^{20}	1.29 / Abs
	4sccm	4.30×10^{20}	1.62 / Abs
	6sccm	5.70×10^{20}	1.72 / Abs
	7sccm	6.10×10^{20}	1.93 / Abs
Chp 5	A	4.00×10^{20}	1.54 / Abs
	B	5.20×10^{19}	0.82 / Abs
	C	2.40×10^{19}	0.74 / Abs
	D	1.50×10^{20}	1.25 / Abs
Chp 6	A2	3.00×10^{20}	1.32 / PL
	A3	6.30×10^{20}	2.00 / PL
	A5	1.20×10^{20}	1.12 / PL
	A6	6.00×10^{19}	0.74 / PL
	B1	4.20×10^{19}	0.72 / PL
	B2	8.10×10^{19}	0.80 / PL
Chp 7	D	8.40×10^{17}	0.65 / Abs
	C	2.30×10^{18}	0.68 / Abs
	B	7.10×10^{18}	0.73 / Abs
	H	6.10×10^{17}	0.63 / Abs
	G	1.40×10^{18}	0.67 / Abs
	F	6.00×10^{18}	0.68 / Abs

Dislocation density of InN epilayers is measured from HRXRD ω-scan broadening while carrier concentration and mobility values are measured using Hall system in the Van der Pauw geometry. The InN films having different thickness values have shown different values of electron carrier concentration and mobility. In this set of experiments, consistently we have obtained low band gap and Hall carrier concentration, than in our earlier experiments on bare sapphire. The obtained mobility values of InN grown on NWN are much higher than those obtained for films grown on GaN epi-layer. The films of 1 μm thickness, show high mobility value of 2121 cm^2/V-sec which is the highest value reported in the literature to-date. These mobility values are still lower than the

theoretical prediction, which is due to the defects that are present and which act as scattering centers to limit the electron mobility. In order to obtain the electron mobility in dislocation free material, and measure their mobility, we have formed self-assembled vertically aligned (c-oriented) high quality InN NRs on the GaN NWN template, under optimized growth conditions. By making *in-situ* electrical contacts on individual rods, we have measured their transport properties. The rods display a sharp and low band edge emission at 0.65eV with a low Hall carrier concentration of $\approx 3.1\times10^{17}$ cm^{-3} and high electron mobility of ≈ 4263 cm^2/V-sec. Also employing SCLC formalism to J-V characteristics, we are able to re-confirm the low carrier concentration of $\approx 1.1\times10^{17}$ cm^{-3} and high electron mobility of ≈ 4453 cm^2/V-sec. Thus, this uniquely formed dislocation free material exhibits an unprecedented mobility of ≈ 4453 cm^2/V-sec, which equals the earlier theoretical predictions for 10^{17} cm^{-3} carrier concentration.

The bandgap and carrier concentration values which are listed in Table 8.1 from all the chapters for all the films discussed in this thesis are summarized in the plot of carrier concentration vs bandgap as shown in Fig 8.1

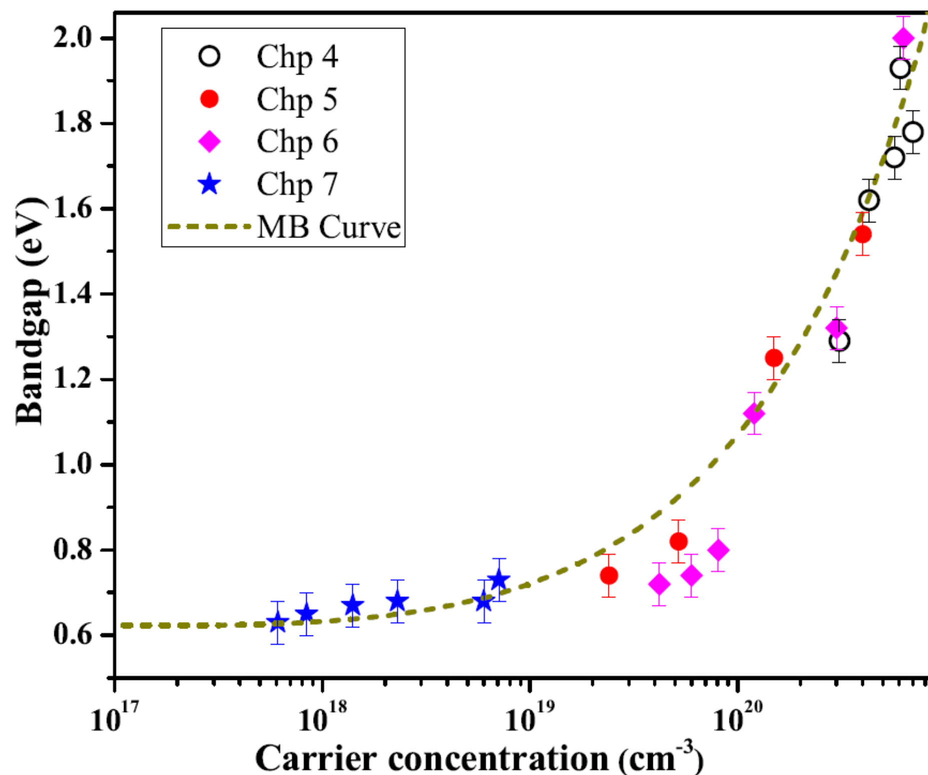

Figure 8.1: shows the plot of carrier concentration vs bandgap for all the films discussed in the thesis.

8.2 Highlights of the work

We list here the significant observations and inferences that have resulted from the present work:

① Nitrogen related native point defects are the reason for unintentionally doped degenerate InN films.

② Causes for high band gap and low band gap are studied, and a non-parabolic conduction band model is found essential to evaluate the variation in band gap of InN. We observe PL band-edge peaks at RT, which testify the high crystallinity of films.

③ Surface charge accumulation is studied on inert gas sputter cleaned InN surface. The downward band bending is attributed to donor like In adatoms that present on surface.

④ The fascinating reconstructions of Si(111) upon In adsorption, are found to give excellent lattice matched substrates for growth of single crystalline InN films at relatively low growth temperatures. We have called this approach as Super Lattice Matching Epitaxy.

⑤ Adapting the sophisticated, lithography dependent Epitaxial Lateral Overlayer Growth (ELOG) in a novel way, we have used defect free GaN Nano Wall Network (NWN) configuration as a template for growing high quality InN films. High electron mobility of $\approx$ 2121 cm^2/V-sec is obtained for 1μm InN layers by this approach, which is the highest value in literature to-date.

⑥ To study mobility in dislocation free material, InN Nano Rods (NRs) are grown on GaN Nano wall Network (NWN) template under certain MBE growth conditions. Measuring electron transport in individual rods, we have observed the highest mobility of $\approx$ 4453 cm^2/V-sec, which is the value theoretically expected for defect free InN for a carrier concentration of $\approx 10^{17}$ cm^{-3}.

8.3 Future directions

InN is a material with enormous potential, but its applications have been limited due to difficulties in the formation of high quality films, which have been attributed to

several ambiguous reasons in the literature. We have carried out several experiments to lift the ambiguity concerning its basic material parameters like band gap and carrier concentration. We believe that our results will be of significant use in the direction of attaining the definitive and potent basic attributes of this material. Though we have demonstrated routes to obtain very high quality InN, further improvements and optimization can enable standardization of optimal growth parameters and schemes for reliable device fabrication. Theoretical calculations based on the results of the present experimental results are essential to pin-point the mechanism understanding the speculations made in this work. Another important concern of the surface electron accumulation layer in InN which can hinder device application of polar surfaces has to be tackled by more experiments to find ways to overcome such barriers and reach a good understanding of this phenomenon. If the novel method of 'super lattice matching epitaxy' proposed here to grow high quality InN on Si surfaces at lower temperatures, can be optimized a general growth technique, to form epitaxial III-nitride films on Silicon surfaces, can be significant in integrating the III-V and Silicon technologies. Our study hints at the possibility of employing the faceted Si(5 5 12) surface and its metal induced reconstructions as good templates to grow III-nitrides as they may promote nucleation in its grooved facets, followed by lateral over-layer growth, with reduced defect densities. Our device quality 1μm thick InN layers on GaN Nano Wall Network and GaN epilayers displaying unprecedented high mobility, shows promise as channel layers for the high mobility transistors. The high electron mobility of InN among all nitrides makes it very important as the channel region of high electron mobility transistors. The consequence of its high mobility and low effective mass, InN-based HEMTs may be recorded as high performance devices among III-N transistors which could be possible by replacing the GaN with InN channel, even though the growth of InN heterostructures is still in the immature stage. Moreover, high quality Indium nitride (InN) is identified as a promising material for terahertz (THz) emission. This THz region of the electromagnetic spectrum ranges from microwave frequencies (100 GHz) to photonic frequencies (30 THz) which is a potentially region for Army applications such as identification of explosive devices. On the other hand, Ga into these high quality InN layers, InGaN alloy can be formed, which is very useful material for the state of art of LED applications. This approach can be adapted for InGaN layer formation, which we predict will give extremely stable

alloy compositions, with significantly reduced 'green-droop' effects that have limited the extent of LED and Laser Diode applications for Solid State Lighting and opto-electronic communication. The formation of self organized InN nanorods inside the nanowall network appear to provide a coupled band-gap crystal and tunable plasmonic crystals with periodic variation of refractive indices of GaN, InN and air, in the entire UV to IR range. These applications need to be seriously explored.

Bibliography

[1] Z. C. Feng, *III-Nitrides Semiconductor Materials*, Vol. 203 (Imperial College Press, 2006).

[2] H. Morkoç, *Handbook of Nitride Semiconductors and Devices, Vol. 1* (WILEY-VCH Verlag GmbH & Co. KGaA, 2008).

[3] B. G. Clarendon, ed., *Group III Nitride Semiconductor Compounds*, April (Oxford, 1998).

[4] P. Ruterana, M. Albrecht, and J. Neugebauer, *Nitride Semiconductors: Hand book on Materials and Devices* (Wiley-VCH Verlag GmbH & Co. KGaA, Weinheim, FRG, 2003).

[5] S. Nakamura, Science **281**, 956 (1998).

[6] L. Liu and J. H. Edgar, Mater. Sci. Eng. R Reports **37**, 61 (2002).

[7] I. Akasaki, J. Cryst. Growth **300**, 2 (2007).

[8] P. Gibart, Reports Prog. Phys. **67**, 667 (2004).

[9] S. Nakamura, T. Mukai, and M. Senoh, Jpn. J. Appl. Phys. **30**, L1998 (1991).

[10] S. Nakamura, M. Senoh, and T. Mukai, Jpn. J. Appl. Phys. **32**, L8 (1993).

[11] J. F. Geisz, D. J. Friedman, J. S. Ward, A. Duda, W. J. Olavarria, T. E. Moriarty, J. T. Kiehl, M. J. Romero, A. G. Norman, and K. M. Jones, Appl. Phys. Lett. **93**, 123505 (2008).

[12] $http://www-opto.e-technik.uni-ulm.de/lehre/cs/$.

[13] E. Tiede, M. Thimann, and K. Sensse, Chem. Berichte **61**, 1568 (1928).

[14] R. Juza and H. Hahn, Anorg. Allgem. Chem. **239**, 282 (1938).

[15] H. P. Maruska, Appl. Phys. Lett. **15**, 327 (1969).

[16] J. I. Pankove, E. A. Miller, and J. E. Berkeyheiser, RCA Rev **383**, 383 (1971).

[17] H. Amano, M. Kito, K. Hiramatsu, and I. Akasaki, Jpn. J. Appl. Phys. **28**, L2112 (1989).

[18] M. A. Khan, J. M. Van Hove, J. N. Kuznia, and D. T. Olson, Appl. Phys. Lett. **58**, 2408 (1991).

[19] J. Kuzmík, Electron Device Lett. **22**, 510 (2001).

[20] S. C. Jain, M. Willander, J. Narayan, and R. V. Overstraeten, J. Appl. Phys. **87**, 965 (2000).

[21] A. G. Bhuiyan, A. Hashimoto, and A. Yamamoto, J. Appl. Phys. **94**, 2779 (2003).

[22] J. Wu, J. Appl. Phys. **106**, 011101 (2009).

[23] K. S. A. Butcher and T. L. Tansley, Superlattices Microstruct. **38**, 1 (2005).

[24] B. Monemar, P. Paskov, and A. Kasic, Superlattices Microstruct. **38**, 38 (2005).

[25] Y. Nanishi, Y. Saito, and T. Yamaguchi, Jpn. J. Appl. Phys. **42**, 2549 (2003).

[26] V. Y. Davydov, A. A. Klochikhin, R. P. Seisyan, V. V. Emtsev, S. V. Ivanov, F. Bechstedt, J. Furthmüller, H. Harima, A. V. Mudryi, J. Aderhold, O. Semchinova, and J. Graul, Phys. Status Solidi B **3**, R1 (2002).

[27] J. Wu, W. Walukiewicz, K. M. Yu, J. W. Ager III, E. E. Haller, H. Lu, W. J. Schaff, Y. Saito, and Y. Nanishi, Appl. Phys. Lett. **80**, 3967 (2002).

[28] B. E. Foutz, S. K. OLeary, M. S. Shur, and L. F. Eastman, J. Appl. Phys. **85**, 7727 (1999).

[29] V. W. L. Chin, T. L. Tansley, and T. Osotchan, J. Appl. Phys. **75**, 7365 (1994).

[30] S. K. OLeary, B. E. Foutz, M. S. Shur, U. V. Bhapkar, and L. F. Eastman, J. Appl. Phys. **83**, 826 (1998).

[31] E. Bellotti, B. K. Doshi, K. F. Brennan, J. D. Albrecht, and P. P. Ruden, J. Appl. Phys. **85**, 916 (1999).

[32] J. Black, H. Lockwood, and S. Mayburg, J. Appl. Phys. **34**, 178 (1963).

[33] R. D. Dupuis, IEEE Quant. Electr. **QE-23**, 651 (1987).

[34] M. G. Craford, *Circuit Devices*, Vol. 8 (IEEE, 1992).

[35] S. Nakamura and G. Fasol, *The Blue Laser Diode* (Springer-Verlag Berlin Heidelberg GmbH, 1997).

[36] D. B. Nicol, *Ph. D Thesis,*, Ph.D. thesis, Georgia Institute Of Technology (2006).

[37] *http://www.blue-ray.com/*.

[38] M.-S. Hu, G.-M. Hsu, K.-H. Chen, C.-J. Yu, H.-C. Hsu, L.-C. Chen, J.-S. Hwang, L.-S. Hong, and Y.-F. Chen, Appl. Phys. Lett. **90**, 123109 (2007).

[39] G. D. Chern, E. D. Readinger, H. Shen, M. Wraback, C. S. Gallinat, G. Koblmuller, and J. S. Speck, Appl. Phys. Lett. **89**, 141115 (2006).

[40] V. Gru inskis, P. Shiktorov, E. Starikov, L. Reggiani, L. Varani, and J. C. Vaissière, Semicond. Sci. Technol. **19**, S173 (2004).

[41] R. Ascazubi, I. Wilke, K. Denniston, H. Lu, and W. J. Schaff, Appl. Phys. Lett. **84**, 4810 (2004).

[42] E. Starikov, Phys. B Condens. Matter **314**, 171 (2002).

[43] X. Wang and A. Yoshikawa, Prog. Cryst. Growth Charact. Mater. **48-49**, 42 (2004).

[44] R. Chierchia, T. Bottcher, H. Heinke, S. Einfeldt, S. Figge, and D. Hommel, J. Appl. Phys. **93**, 8918 (2003).

[45] V. Srikant, J. S. Speck, and D. R. Clarke, J. Appl. Phys. **82**, 4286 (1997).

[46] W. D. Callister, *Materials science and engineering*, Vol. 30 (Jr John Wiley & Sons , New York, 2007).

[47] F. Reurings, F. Tuomisto, C. S. Gallinat, G. Koblmuller, and J. S. Speck, Appl. Phys. Lett. **97**, 251907 (2010).

[48] X. M. Duan and C. Stampfl, Phys. Rev. B **77**, 115207 (2008).

[49] A. Terentjevs, A. Catellani, and G. Cicero, Appl. Phys. Lett. **96**, 171901 (2010).

[50] Z. Feng-Qi, S. Jun-Jie, and Y. Mao, Commun. Theor. Phys. **53**, 145 (2010).

[51] Y. Ishitani, K. Kato, H. Ogiwara, S.-B. Che, A. Yoshikawa, and X. Wang, J. Appl. Phys. **106**, 113515 (2009).

[52] K. Yagi, N. Miyamoto, and J.-i. Nishizawa, Jpn. J. Appl. Phys. **9**, 246 (1970).

[53] März, *High Resolution X-Ray Diffraction: User guide manual* (Walter Schottky Institut, 2009).

[54] D. Holec, *Multi-scale modelling of III-nitrides: from dislocations to the electronic structure*, Ph.D. thesis, University of Cambridge (2008).

[55] M. J. Hordon and B. L. Averbach, Acta Metall. **9**, 237 (1961).

[56] D. Zakharov, Z. Liliental-Weber, B. Wagner, Z. Reitmeier, E. Preble, and R. Davis, Phys. Rev. B **71**, 235334 (2005).
[57] W. K. Liu and M. B. Santos, *Thin Films: Heteroepitaxial Systems*, Series on Directions in Condensed Matter Physics, Vol. 15 (World Scientific Publishing Co. Pte. Ltd., 1999).
[58] Edik U. Rafailov, *The Physics and Engineering of Compact Quantum Dot based Lasers for Biophotonics* (John Wiley & Sons, Weinheim, Germany, 2014).
[59] A. Yamamoto, Y. Yamauchi, M. Ohkubo, and A. Hashimoto, J. Cryst. Growth **174**, 641 (1997).
[60] H. Naoi, F. Matsuda, T. Araki, A. Suzuki, and Y. Nanishi, J. Cryst. Growth **269**, 155 (2004).
[61] A. G. Bhuiyan, A. Yamamoto, A. Hashimoto, and Y. Ito, J. Cryst. Growth **236**, 59 (2002).
[62] C. S. Gallinat, G. Koblmuller, J. S. Brown, and J. S. Speck, J. Appl. Phys. **102**, 064907 (2007).
[63] Q. Guo, O. Kato, and A. Yoshida, J. Appl. Phys. **73**, 7969 (1993).
[64] Yoshinao Kumagaia, J. Kikuchi, Y. Nishizawa, H. Murakami, and A. Koukitu, J. Cryst. Growth **300**, 57 (2007).
[65] J. W. Trainor and K. Rose, J. Electron. Mater. **3**, 821 (1974).
[66] T. L. Tansley and C. P. Foley, Electron. Lett. **20**, 1066 (1984).
[67] T. Matsuoka, H. Tanaka, and A. Katsui, in *Int. Symp. GaAs Relat. Compd. Karuizawa, Japan* (1989).
[68] A. Wakahara and A. Yoshida, Appl. Phys. Lett. **54**, 709 (1989).
[69] W. Hoke, P. Lemonias, and D. Weir, J. Cryst. Growth **111**, 1024 (1991).
[70] J. B. MacChesney, P. M. Bridenbaugh, and P. B. O'connor, Mater. Res. Bull. **5**, 783 (1970).
[71] H. J. Hovel and J. J. Cuomo, Appl. Phys. Lett. **20**, 71 (1972).
[72] L. A. Marasina, I. G. Pichugin, and M. Tlaczala, Krist. Tech. **12**, 541 (1977).
[73] A. Wakahara, T. Tsuchiya, and A. Yoshida, J. Cryst. Growth **99**, 385 (1990).
[74] T. Inushima, V. V. Mamutin, V. A. Vekshin, S. V. Ivanov, T. Sakon, M. Motokawa, and S. Ohoya, J. Cryst. Growth **227-228**, 481 (2001).
[75] V. Y. Davydov, A. A. Klochikhin, V. V. Emtsev, D. A. Kurdyukov, S. V. Ivanov, V. Vekshin, F. Bechstedt, J. Furthmüller, J. Aderhold, J. Graul, A. V. Mudryi, H. Harima, A. Hashimoto, A. Yamamoto, and E. E. Haller, Phys. Status Solidi B **234**, 787 (2002).
[76] J. Wu, W. Walukiewicz, W. Shan, K. M. Yu, J. W. Ager III, E. E. Haller, H. Lu, and W. J. Schaff, Phys. Rev. B **66**, 201403 (2002).
[77] M. Higashiwaki and T. Matsui, J. Cryst. Growth **269**, 162 (2004).
[78] A. A. Klochikhin, V. Y. Davydov, V. V. Emtsev, A. V. Sakharov, V. A. Kapitonov, B. A. Andreev, H. Lu, and W. J. Schaff, Phys. Rev. B **71**, 195207 (2005).
[79] H. Lu, W. J. Schaff, and L. F. Eastman, Mater. Res. Soc. Symp. Proc. **9**, 693 (2002).

[80] N. Dietz, M. Straß burg, and V. Woods, J. Vac. Sci. Technol. A **23**, 1221 (2005).
[81] T. L. Tansley and C. P. Foley, J. Appl. Phys. **59**, 3241 (1986).
[82] K. Osamura, S. Naka, and Y. Murakami, J. Appl. Phys. **46**, 3432 (1975).
[83] B. Natarajan, A. Eltoukhy, J. Greene, and T. Barr, Thin Solid Films **69**, 201 (1980).
[84] B. T. Sullivan, R. R. Parsons, K. L. Westra, and M. J. Brett, J. Appl. Phys. **64**, 4144 (1988).
[85] V. V. Mamutin, V. a. Vekshin, V. Y. Davydov, V. V. Ratnikov, T. V. Shubina, S. V. Ivanov, P. S. Kopev, M. Karlsteen, U. Söderwall, and M. Willander, Phys. Status Solidi A **176**, 247 (1999).
[86] H. Lu, W. J. Schaff, J. Hwang, H. Wu, W. Yeo, A. Pharkya, and L. F. Eastman, Appl. Phys. Lett. **77**, 2548 (2000).
[87] V. V. Mamutin, T. V. Shubina, V. A. Vekshin, V. V. Ratnikov, A. A. Toropov, S. V. Ivanov, M. Karlsteen, U. Sodervall, and M. Willander, Appl. Surf. Sci. **166**, 87 (2000).
[88] J. Aderhold, V. Y. Davydov, F. Fedler, H. Klausing, D. Mistele, T. Rotter, O. Semchinova, J. Stemmer, and J. Graul, J. Cryst. Growth **222**, 701 (2001).
[89] H. Lu, W. J. Schaff, J. Hwang, H. Wu, G. Koley, and L. F. Eastman, Appl. Phys. Lett. **79**, 1489 (2001).
[90] A. Kasic, M. Schubert, Y. Saito, Y. Nanishi, and G. Wagner, Phys. Rev. B **65**, 115206 (2002).
[91] D. C. Look, H. Lu, W. J. Schaff, J. Jasinski, and Z. Liliental-Weber, Appl. Phys. Lett. **80**, 258 (2002).
[92] Z. G. Qian, W. Z. Shen, H. Ogawa, and Q. X. Guo, J. Appl. Phys. **92**, 3683 (2002).
[93] Y. Saito, T. Yamaguchi, H. Kanazawa, K. Kano, T. Araki, Y. Nanishi, N. Teraguchi, and A. Suzuki, J. Cryst. Growth **237-239**, 1017 (2002).
[94] Y. Saito, H. Harima, E. Kurimoto, T. Yamaguchi, N. Teraguchi, A. Suzuki, T. Araki, and Y. Nanishi, Phys. Status Solidi B **234**, 796 (2002).
[95] F.-H. Yang, J.-S. Hwang, Y.-J. Yang, K.-H. Chen, and J.-H. Wang, Jpn. J. Appl. Phys. **41**, L1321 (2002).
[96] A. G. Bhuiyan, K. Sugita, K. Kasashima, A. Hashimoto, A. Yamamoto, and V. Y. Davydov, Appl. Phys. Lett. **83**, 4788 (2003).
[97] M. Higashiwaki and T. Matsui, J. Cryst. Growth **252**, 128 (2003).
[98] K. Sugita, H. Takatsuka, A. Hashimoto, and A. Yamamoto, Phys. Status Solidi B **240**, 421 (2003).
[99] J. Wu, W. Walukiewicz, W. Shan, K. M. Yu, J. W. Ager III, S. X. Li, E. E. Haller, H. Lu, and W. J. Schaff, J. Appl. Phys. **94**, 4457 (2003).
[100] V. Cimalla, C. Förster, G. Kittler, I. Cimalla, R. Kosiba, G. Ecke, O. Ambacher, R. Goldhahn, S. Shokhovets, A. Georgakilas, H. Lu, and W. Schaff, Phys. Status Solidi C **0**, 2818 (2003).
[101] M. Higashiwaki and T. Matsui, J. Cryst. Growth **251**, 494 (2003).
[102] M. Wintrebert-Fouquet, K. S. A. Butcher, and Motlan, Phys. Status Solidi **2789**,

2785 (2003).

[103] C.-A. Chang, C.-F. Shih, N.-C. Chen, P.-H. Chang, and K.-S. Liu, Phys. Status Solidi **1**, 2559 (2004).

[104] J. Oila, A. Kemppinen, A. Laakso, K. Saarinen, W. Egger, L. Liszkay, P. Sperr, H. Lu, and W. J. Schaff, Appl. Phys. Lett. **84**, 1486 (2004).

[105] V. M. Naik, R. Naik, D. B. Haddad, J. S. Thakur, G. W. Auner, H. Lu, and W. J. Schaff, Appl. Phys. Lett. **86**, 201913 (2005).

[106] K. Scott, A. Butcher, P. P.-T. C. Marie Wintrebert-Fouquet, K. E. Prince, H. Timmers, S. K. Shrestha, T. V. Shubina, S. V. Ivanov, R. Wuhrer, M. R. Phillips, and B. Monemar, Phys. Status Solidi C **2**, 2263 (2005).

[107] K. M. Yu, Z. Liliental-Weber, W. Walukiewicz, W. Shan, J. W. Ager III, S. X. Li, R. E. Jones, E. E. Haller, H. Lu, and W. J. Schaff, Appl. Phys. Lett. **86**, 071910 (2005).

[108] H.-Y. Chen, H.-W. Lin, C.-H. Shen, and S. Gwo, Appl. Phys. Lett. **89**, 243105 (2006).

[109] R. E. Jones, S. X. Li, L. Hsu, K. M. Yu, W. Walukiewicz, Z. Liliental-weber, J. W. Ager III, E. E. Haller, H. Lu, and W. J. Schaff, Phys. B Condens. Matter **376-377**, 436 (2006).

[110] G. Koblmüller, C. S. Gallinat, S. Bernardis, J. S. Speck, G. D. Chern, E. D. Readinger, H. Shen, and M. Wraback, Appl. Phys. Lett. **89**, 071902 (2006).

[111] V. Lebedev, F. Morales, V. Cimalla, J. Lozano, D. Gonzalez, M. Himmerlich, S. Krischok, J. Schaefer, and O. Ambacher, Superlattices Microstruct. **40**, 289 (2006).

[112] D. Muto, H. Naoi, T. Araki, S. Kitagawa, M. Kurouchi, H. Na, and Y. Nanishi, Phys. Status Solidi **203**, 1691 (2006).

[113] L. F. J. Piper, T. D. Veal, C. F. McConville, H. Lu, and W. J. Schaff, Phys. Status Solidi (C) **3**, 1841 (2006).

[114] L. F. J. Piper, T. D. Veal, C. F. McConville, H. Lu, and W. J. Schaff, Appl. Phys. Lett. **88**, 252109 (2006).

[115] V. M. Polyakov and F. Schwierz, Appl. Phys. Lett. **88**, 032101 (2006).

[116] W. Walukiewicz, J. W. Ager III, K. M. Yu, Z. Liliental-Weber, J. Wu, S. X. Li, R. E. Jones, and J. D. Denlinger, J. Phys. D. Appl. Phys. **39**, R83 (2006).

[117] K. R. Wang, L. W. Tu, S. J. Lin, Y. L. Chen, Z. W. Jiang, M. Chen, C. L. Hsiao, K. H. Cheng, J. W. Yeh, and S. K. Chen, Phys. Status Solidi **243**, 1461 (2006).

[118] C. L. Wu, C. H. Shen, H. Y. Chen, S. J. Tsai, H. W. Lin, H. M. Lee, S. Gwo, T. F. Chuang, H. S. Chang, and T. M. Hsu, J. Cryst. Growth **288**, 247 (2006).

[119] V. Cimalla, V. Lebedev, C. Y. Wang, M. Ali, G. Ecke, V. M. Polyakov, F. Schwierz, O. Ambacher, H. Lu, and W. J. Schaff, Appl. Phys. Lett. **90**, 152106 (2007).

[120] B. Arnaudov, T. Paskova, P. P. Paskov, B. Magnusson, E. Valcheva, B. Monemar, H. Lu, W. J. Schaff, H. Amano, and I. Akasaki, Phys. Rev. B **69**, 115216 (2004).

[121] J. C. Lin, Y. K. Su, S. J. Chang, W. H. Lan, W. R. Chen, Y. C. Cheng, W. J. Lin, Y. C. Tzeng, H. Y. Shin, and C. M. Chang, Opt. Mater. (Amst). **30**, 517 (2007).

[122] I. Gherasoiu, M. OSteen, T. Bird, D. Gotthold, A. Chandolu, D. Y. Song, S. X. Xu, M. Holtz, S. A. Nikishin, and W. J. Schaff, J. Vac. Sci. Technol. A **26**, 399 (2008).
[123] N. Khan, A. Sedhain, J. Li, J. Y. Lin, and H. X. Jiang, Appl. Phys. Lett. **92**, 172101 (2008).
[124] A. Knübel, R. Aidam, V. Cimalla, L. Kirste, M. Baeumler, C.-C. Leancu, V. Lebedev, J. Wallauer, M. Walther, and J. Wagner, Phys. Status Solidi **6**, 1480 (2009).
[125] T. A. Komissarova, M. A. Shakhov, V. N. Jmerik, T. V. Shubina, R. V. Parfeniev, S. V. Ivanov, X. Wang, and A. Yoshikawa, Appl. Phys. Lett. **95**, 012107 (2009).
[126] G. P. Dimitrakopulos, T. Kehagias, A. Ajagunna, J. Kioseoglou, I. Kerasiotis, G. Nouet, A. P. Vajpeyi, P. Komninou, and T. Karakostas, Phys. Status Solidi **207**, 1074 (2010).
[127] W. Liu, R. J. N. Tan, C. B. Soh, and S. J. Chua, Appl. Phys. Lett. **97**, 042110 (2010).
[128] X. Wang, S. Liu, N. Ma, L. Feng, G. Chen, F. Xu, N. Tang, S. Huang, K. J. Chen, S. Zhou, and B. Shen, Appl. Phys. Express **5**, 015502 (2012).
[129] K. Wang, T. Araki, M. Takeuchi, E. Yoon, and Y. Nanishi, Appl. Phys. Lett. **104**, 032108 (2014).
[130] D. Bagayoko and L. Franklin, J. Appl. Phys. **97**, 123708 (2005).
[131] Abdul Kadir, T. Ganguli, M. R. Gokhale, A. P. Shah, S. S. Chandvankar, B. M. Arora, and A. Bhattacharya, J. Cryst. Growth **298**, 403 (2007).
[132] A. Nikolaev, I. Nikitina, A. Zubrilov, M. Mynbaeva, Y. Melnik, , and V. Dimitriev, Mater. Res. Soc. Symp. Proc. **595**, W6.5 (2000).
[133] Y. Kumagai, T. Yamane, and A. Koukitu, J. Cryst. Growth **281**, 62 (2005).
[134] A. Yamamoto, H. Miwa, Y. Shibata, and A. Hashimoto, Thin Solid Films **494**, 74 (2006).
[135] M. Alevli, G. Durkaya, A. Weerasekara, A. G. U. Perera, N. Dietz, W. Fenwick, V. Woods, and I. Ferguson, Appl. Phys. Lett. **89**, 112119 (2006).
[136] K. S. A. Butcher, A. J. Fernandes, P. P. T. Chen, M. Wintrebert-Fouquet, H. Timmers, S. K. Shrestha, H. Hirshy, R. M. Perks, and B. F. Usher, J. Appl. Phys. **101**, 123702 (2007).
[137] J. Tauc, *The Optical Properties of Solids*, edited by F. Abeles (North-Holland, Amsterdam, 1971).
[138] M. Alevli, R. Atalay, G. Durkaya, A. Weesekara, A. G. U. Perera, N. Dietz, R. Kirste, and A. Hoffmann, J. Vac. Sci. Technol. A **26**, 1023 (2008).
[139] J. Wu, W. Walukiewicz, S. X. Li, R. Armitage, J. C. Ho, E. R. Weber, E. E. Haller, H. Lu, W. J. Schaff, A. Barcz, and R. Jakiela, Appl. Phys. Lett. **84**, 2805 (2004).
[140] E. Kane, J. Phys. Chem. Solids **1**, 249 (1957).
[141] I. Mahboob, T. D. Veal, L. F. J. Piper, C. F. McConville, H. Lu, W. J. Schaff, J. Furthmüller, and F. Bechstedt, Phys. Rev. B **69**, 201307(R) (2004).
[142] L. O. Olsson, C. B. M. Andersson, M. C. Hå kansson, J. Kanski, L. Ilver, and U. O. Karlsson, Phys. Rev. Lett. **76**, 3626 (1996).

[143] T. D. Veal, L. F. J. Piper, M. R. Phillips, M. H. Zareie, H. Lu, W. J. Schaff, and C. F. McConville, Phys. Status Solidi **204**, 536 (2007).

[144] P. D. C. King, T. D. Veal, P. H. Jefferson, S. A. Hatfield, L. F. J. Piper, C. F. McConville, F. Fuchs, J. Furthmüller, F. Bechstedt, H. Lu, and W. J. Schaff, Phys. Rev. B **77**, 045316 (2008).

[145] P. D. C. King, T. D. Veal, D. J. Payne, A. Bourlange, R. G. Egdell, and C. F. McConville, Phys. Rev. Lett. **101**, 116808 (2008).

[146] W. M. Linhart, *Electron accumulation and doping in InN and InGaN alloys*, Ph.D. thesis, The University of Warwick.

[147] V. Y. Aristov, V. M. Zhilin, C. Grupp, A. Taleb-Ibrahimi, H. J. Kim, P. S. Mangat, P. Soukiassian, and G. Le Lay, Appl. Surf. Sci. **166**, 263 (2000).

[148] M. Noguchi, K. Hirakawa, and T. Ikoma, Phys. Rev. Lett. **66**, 2243 (1991).

[149] H. Yamaguchi, J. Sudijono, B. Joyce, T. Jones, C. Gatzke, and R. Stradling, Phys. Rev. B **58**, R4219 (1998).

[150] I. Mahboob, T. D. Veal, C. F. McConville, H. Lu, and W. J. Schaff, Phys. Rev. Lett. **92**, 036804 (2004).

[151] P. D. C. King, T. D. Veal, C. F. McConville, F. Fuchs, J. Furthmüller, F. Bechstedt, P. Schley, R. Goldhahn, J. Schörmann, D. J. As, K. Lischka, D. Muto, H. Naoi, Y. Nanishi, H. Lu, and W. J. Schaff, Appl. Phys. Lett. **91**, 092101 (2007).

[152] C.-L. Wu, H.-M. Lee, C.-T. Kuo, C.-H. Chen, and S. Gwo, Phys. Rev. Lett.. **101**, 106803 (2008).

[153] D. Segev and C. G. V. D. Walle, Eur. Lett. **76**, 305 (2006).

[154] L. Colakerol, T. D. Veal, H.-K. Jeong, L. Plucinski, A. DeMasi, T. Learmonth, P.-A. Glans, S. Wang, Y. Zhang, L. F. J. Piper, P. H. Jefferson, A. Fedorov, T.-C. Chen, T. D. Moustakas, C. F. McConville, and K. E. Smith, Phys. Rev. Lett. **97**, 237601 (2006).

[155] A. Y. Cho, M. B. Panish, and I. Hayashi, in *Gall. Arsenide Relat. Compd.*, Vol. 18 (1970) p. 18.

[156] J. E. Davey and Titus Pankey, J. Appl. Phys. **39**, 1941 (1968).

[157] J. R. A. Jr., J. Appl. Phys. **39**, 4032 (1968).

[158] A. Cho, Am. Inst. Physcis (1994).

[159] G. M. Uddin, Z. Cai, K. S. Ziemer, A. Zeid, and S. Kamarthi, J. Manuf. Sci. Eng. **132**, 030913 (2010).

[160] S. L. Wright, H. Kroemer, and M. Inada, J. Appl. Phys. **55**, 2916 (1984).

[161] W. Paul and H. Steinwedel, Zeitschrift für Naturforsch. **8A**, p448 (1953).

[162] K. Ploog, 27th Int. Conf. Phys. Semicond. Tutorials (2004).

[163] E. Doktorgrades, *Epitaktische Heterostrukturen aus dotierten Manganaten*, Ph.D. thesis (2001).

[164] W. Braun, *Applied RHEED* (Springer, New York, 1999).

[165] A. Ichimiya and P. I. Cohen, *Reflection High Energy Electron Diffraction* (Cambridge University Press, 2004).

[166] K. Siegbahn, Philos. Trans. R. Soc. London Ser. A Math. Phys. Sci. **268**, 33 (1970).

[167] D. Briggs and M. P. Seah, *Practical surface analysis by Auger and X-ray photo electron spectroscopy* (John Willey & Sons, New York, 1987).

[168] D. P. Woodruff and T. A. Delchar, *Modern techniques of surface science* (University press, Cambridge, 1999).

[169] M. Prutton, *Introduction to surface physics* (Oxford science publications, Clarendon Press, 1994).

[170] Stefan Hüfner, *Photoelectron Spectroscopy: Principles and Applications* (3rd Edition Springer Verlag, Berlin., 2003).

[171] J. H. Scofield, J. Electron Spectrosc. **8**, 129 (1976).

[172] *CasaXPS Software: User manuals, Copyright 2009 Casa Software Ltd.* (http://www.casaxps.com/, 2009).

[173] J. F. Watts and J. Wolstenholme, *An introduction to surface analysis by XPS and AES* (J. Wiley, 2003).

[174] D. A. Shirley, Phys. Rev. B **5**, 4709 (1972).

[175] B. Hermsmeier, J. Osterwalder, D. J. Friedman, B. Sinkovic, T. Tran, and C. S. Fadley, Phys. Rev. B **42**, 11895 (1990).

[176] B. D. Cullity, *Elements of X ray Diffraction* (Addison - Wesley Publishing Company, Inc., 1956).

[177] N. W. Ashcroft and N. D. Mermin, *Solid State Physics* (Saunders College, Philadelphia, 1976).

[178] M. A. Moram and M. E. Vickers, Reports Prog. Phys. **72**, 036502 (2009).

[179] A. Kadir, *MOVPE Growth and Characterization of InN and InN/GaN Heterostructures*, Ph.D. thesis, Tata Institute of Fundamental Research (2008).

[180] S. A. Speakman, *X ray Diffraction: Standard Operating Procedures* (MIT).

[181] O. Stenzel, *The Physics of Thin Film Optical Spectra* (Springer, 2005).

[182] J. Tauc, Mater. Res. Bull. **3**, 37 (1968).

[183] J. Tauc, R. Grigorovici, and A. Vancu, Phys. Status Solidi B **15**, 627 (1966).

[184] S. Perkowitz, *Optical Characterization Of Semiconductors: Infrared, Raman, and Photoluminescence Spectroscopy* (Academic Press, 1993).

[185] B. Monemar, J. Mater. Sci. Mater. Electron. **10**, 227 (1999).

[186] Joseph F. Becker, *MAGNETIC FIELD & MAGNETIC FORCES, Chapter 27* (Physics Department, San Jose State University).

[187] L. J. Van der Pauw, Philips Tech. Rev. **20**, 220 (1958).

[188] J. Horkstra and L. J. Van Der Pauw, J. Electron. Control **7**, 169 (1959).

[189] S. M. Sze and K. K. Ng, *Physics of Semiconductor Devices , 3rd Edition* (John Wiley & Sons, Inc., Hoboken, New Jersey., 2007).

[190] H. A. Lorentz, Amsterdammer Akad. Der Wet. **4**, 176 (1986).

[191] F. J. Giessibl, Rev. Mod. Phys. **75**, 949 (2003).

[192] C. E. Lyman, D. E. Newbury, J. I. Goldstein, D. B. Williams, A. D. Romig, J. T. A. Jr., P. Echilin, C. E. Fiori, D. C. Joy, E. Lifshin, and K.-R. Peters, *Scanning Electron Microscopy, X-Ray Microanalysis, and Analytical Electron Microscopy* (Plenum Press, New York, 1990).

[193] R. Cusco, N. Domenech-Amador, L. Artus, T. Gotschke, K. Jeganathan, T. Stoica, and R. Calarco, Appl. Phys. Lett. **97**, 221906 (2010).

[194] J. Segura-Ruiz, A. Molina-Sánchez, N. Garro, A. García-Cristóbal, A. Cantarero, F. Iikawa, C. Denker, J. Malindretos, and A. Rizzi, Phys. Rev. B **82**, 125319 (2010).

[195] J. Kamimura, K. Kishino, and A. Kikuchi, Appl. Phys. Lett. **97**, 141913 (2010).

[196] C.-K. Chao, H.-S. Chang, T.-M. Hsu, C.-N. Hsiao, C.-C. Kei, S.-Y. Kuo, and J.-I. Chyi, Nanotechnology **17**, 3930 (2006).

[197] T.-T. Kang, A. Hashimoto, and A. Yamamoto, Appl. Phys. Lett. **92**, 111902 (2008).

[198] I. Hamberg and C. G. Granqvist, J. Appl. Phys. **60**, 123 (1986).

[199] T. Yodo, H. Yona, H. Ando, D. Nosei, and Y. Harada, Appl. Phys. Lett. **80**, 968 (2002).

[200] A. L. Yang, H. P. Song, H. Y. Wei, X. L. Liu, J. Wang, X. Q. Lv, P. Jin, S. Y. Yang, Q. S. Zhu, and Z. G. Wang, Appl. Phys. Lett. **94**, 163301 (2009).

[201] T. Yodo, Y. Kitayama, K. Miyaki, H. Yona, Y. Harada, K. E. Prince, and K. S. A. Butcher, J. Cryst. Growth **269**, 145 (2004).

[202] D. Alexandrov, K. Scott, A. Butcher, and M. Wintrebert-Fouquet, J. Vac. Sci. Technol. A **22**, 954 (2004).

[203] John F. Moulder, W. F. Stickle, P. E. Sobol, and K. D. Bomben, *Handbook of X-ray Photoelectron Spectroscopy*, edited by J. Chastain and J. Roger C. King (Published by ULVAC-PHI, Japan and Physical Electronics, USA, 1978).

[204] T. V. Shubina, S. V. Ivanov, V. N. Jmerik, D. D. Solnyshkov, V. A. Vekshin, P. S. Kopev, A. Vasson, J. Leymarie, A. Kavokin, H. Amano, K. Shimono, A. Kasic, and B. Monemar, Phys. Rev. Lett. **92**, 117407 (2004).

[205] E. Burstein, Phys. Rev. **93**, 632 (1954).

[206] T. S. Moss, Proc. Phys. Soc. London B **67**, 775 (1954).

[207] A. Kadir, T. Ganguli, R. Kumar, M. R. Gokhale, A. P. Shah, S. Ghosh, B. M. Arora, and A. Bhattacharya, Appl. Phys. Lett. **91**, 111913 (2007).

[208] P. Specht, R. Armitage, J. Ho, E. Gunawan, Q. Yang, X. Xu, C. Kisielowski, and E. Weber, J. Cryst. Growth **269**, 111 (2004).

[209] C. Stampfl, C. Van de Walle, D. Vogel, P. Krüger, and J. Pollmann, Phys. Rev. B **61**, R7846 (2000).

[210] X. M. Duan and C. Stampfl, Phys. Rev. B **79**, 174202 (2009).

[211] K. S. A. Butcher, P. P.-T. Chen, and J. E. Downes, Appl. Phys. Lett. **100**, 011913 (2012).

[212] K. S. a. Butcher, J. Appl. Phys. **95**, 6124 (2004).

[213] J. T. Chen, C. L. Hsiao, H. C. Hsu, C. T. Wu, C. L. Yeh, P. C. Wei, L. C. Chen, and K. H. Chen, J. Phys. Chem. A **111**, 6755 (2007).

[214] J. Kuyyalil, M. Tangi, and S. M. Shivaprasad, J. Appl. Phys. **109**, 093513 (2011).

[215] J. Kuyyalil, M. Tangi, and S. M. Shivaprasad, J. Appl. Phys. **112**, 083521 (2012).

[216] Q. Guo, T. Tanaka, M. Nishio, and H. Ogawa, Jpn. J. Appl. Phys. **42**, L141 (2003).

[217] T. Chen, C. Thomidis, J. Abell, W. Li, and T. Moustakas, J. Cryst. Growth **288**, 254 (2006).

[218] M. F. Wu, S. Q. Zhou, A. Vantomme, Y. Huang, H. Wang, and H. Yang, J. Vac. Sci. Technol. A **24**, 275 (2006).

[219] E. Dimakis, E. Iliopoulos, K. Tsagaraki, A. Adikimenakis, and A. Georgakilas, Appl. Phys. Lett. **88**, 191918 (2006).

[220] T. Sasaoka, M. Mori, T. Miyazaki, and S. Adachi, J. Appl. Phys. **108**, 063538 (2010).

[221] B. Bansal, A. Kadir, A. Bhattacharya, and V. V. Moshchalkov, Appl. Phys. Lett. **93**, 021113 (2008).

[222] W. C. Ke, C. P. Fu, C. Y. Chen, L. Lee, C. S. Ku, W. C. Chou, W.-H. Chang, M. C. Lee, W. K. Chen, W. J. Lin, and Y. C. Cheng, Appl. Phys. Lett. **88**, 191913 (2006).

[223] T. D. Veal, I. Mahboob, L. F. J. Piper, C. F. McConville, H. Lu, and W. J. Schaff, J. Vac. Sci. Technol. B **22**, 2175 (2004).

[224] P. D. C. King, T. D. Veal, H. Lu, S. A. Hatfield, W. J. Schaff, and C. F. McConville, Surf. Sci. **602**, 871 (2008).

[225] a. Laakso, J. Cryst. Growth **269**, 41 (2004).

[226] S. X. Li, K. M. Yu, J. Wu, R. E. Jones, W. Walukiewicz, J. W. Ager III, W. Shan, E. E. Haller, H. Lu, and W. J. Schaff, Phys. Rev. B **71**, 161201(R) (2005).

[227] L. F. J. Piper, T. D. Veal, M. J. Lowe, and C. F. McConville, Phys. Rev. B **73**, 195321 (2006).

[228] C.-T. Kuo, S.-C. Lin, K.-K. Chang, H.-W. Shiu, L.-Y. Chang, C.-H. Chen, S.-J. Tang, and S. Gwo, Appl. Phys. Lett. **98**, 052101 (2011).

[229] T. Ohashi, Y. Saito, T. Maruyama, and Y. Nanishi, J. Cryst. Growth **237-239**, 1022 (2002).

[230] H. Lu, W. J. Schaff, L. F. Eastman, and C. E. Stutz, Appl. Phys. Lett. **82**, 1736 (2003).

[231] Y.-L. Chang, Z. Mi, and F. Li, Adv. Funct. Mater. **20**, 4146 (2010).

[232] S. Zhao, S. Fathololoumi, K. H. Bevan, D. P. Liu, M. G. Kibria, Q. Li, G. T. Wang, H. Guo, and Z. Mi, Nano Lett. **12**, 2877 (2012).

[233] G. Pettinari, F. Masia, M. Capizzi, A. Polimeni, M. Losurdo, G. Bruno, T. H. Kim, S. Choi, A. Brown, V. Lebedev, V. Cimalla, and O. Ambacher, Phys. Rev. B **77**, 125207 (2008).

[234] S. J. Pearton, C. R. Abernathy, F. Ren, and J. R. Lothian, J. Appl. Phys. **76**, 1210 (1994).

[235] S. P. Fu, T. T. Chen, and Y. F. Chen, Semicond. Sci. Technol. **21**, 244 (2006).

[236] M. Millot, Z. M. Geballe, K. M. Yu, W. Walukiewicz, and R. Jeanloz, Appl. Phys. Lett. **100**, 162103 (2012).

[237] R. Swanepoel, J. Phys. E Sci. Instrum. **16**, 1214 (1983).

[238] T. Tansley and C. Foley, J. Appl. Phys. **60**, 2092 (1986).

[239] V. Y. Davydov, A. A. Klochikhin, and V. V. Emtsev, Phys. Status Solidi B **230**,

R4 (2002).
[240] B. R. Nag, Phys. Status Solidi B **237**, R1 (2003).
[241] K. Levenberg, Q. Appl. Math. **2**, 164 (1944).
[242] D. Marquardt, SIAM J. Appl. Math. **11(2)**, 431 (1963).
[243] M. Tangi, J. Kuyyalil, and S. M. Shivaprasad, J. Appl. Phys. **112**, 073510 (2012).
[244] C. G. Van de Walle, J. L. Lyons, and A. Janotti, Phys. Status Solidi **207**, 1024 (2010).
[245] T. Yamaguchi, Y. Saito, C. Morioka, K. Yorozu, T. Araki, a. Suzuki, and Y. Nanishi, Phys. Status Solidi **240**, 429 (2003).
[246] J. Grandal, M. A. Sainchez-Garcia, F. Calle, and E. Calleja, Phys. Status Solidi C **2**, 2289 (2005).
[247] J. Grandal, M. A. Sanchez-Garcia, E. Calleja, E. Luna, and A. Trampert, Appl. Phys. Lett. **91**, 021902 (2007).
[248] C. L. Wu, C.-H. Shen, H.-W. Lin, H.-M. Lee, and S. Gwo, Appl. Phys. Lett. **87**, 241916 (2005).
[249] P. Kumar, J. Kuyyalil, and S. M. Shivaprasad, Appl. Phys. Lett. **97**, 221913 (2010).
[250] H. Ofner, S. L. Surney, Y. Spapira, and F. P. Netzer, Phys. Rev. B **48**, 940 (1993).
[251] J. Kuyyalil, M. Kumar, and S. Shivaprasad, Surf. Sci. **604**, 1972 (2010).
[252] K. Jithesh, U. V. Waghmare, and S. M. Shivaprasad, Appl. Surf. Sci. **256**, 348 (2009).
[253] J. Kuyyalil, M. Tangi, and S. M. Shivaprasad, Mater. Res. Bull. **48**, 256 (2013).
[254] S. R. Lee, A. M. West, A. A. Allerman, K. E. Waldrip, D. M. Follstaedt, P. P. Provencio, D. D. Koleske, and C. R. Abernathy, Appl. Phys. Lett. **86**, 241904 (2005).
[255] T. D. Veal, P. D. C. King, P. H. Jefferson, L. F. J. Piper, C. F. McConville, H. Lu, W. J. Schaff, P. A. Anderson, S. M. Durbin, D. Muto, H. Naoi, and Y. Nanishi, Phys. Rev. B **76**, 075313 (2007).
[256] M. Tangi, J. Kuyyalil, and S. M. Shivaprasad, J. Appl. Phys. **114**, 153501 (2013).
[257] N. Miller, E. E. Haller, G. Koblmüller, C. Gallinat, J. S. Speck, W. J. Schaff, M. E. Hawkridge, K. M. Yu, and J. W. Ager III, Phys. Rev. B **84**, 075315 (2011).
[258] C. S. Gallinat, G. Koblmuller, J. S. Brown, S. Bernardis, J. S. Speck, G. D. Chern, E. D. Readinger, H. Shen, and M. Wraback, Appl. Phys. Lett. **89**, 032109 (2006).
[259] E. Dimakis, J. Domagala, A. Delimitis, P. Komninou, A. Adikimenakis, E. Iliopoulos, and A. Georgakilas, Superlattices Microstruct. **40**, 246 (2006).
[260] I. P. Seetoh, C. B. Soh, L. Zhang, K. H. Patrick Tung, E. a. Fitzgerald, and S. Jin Chua, Appl. Phys. Lett. **103**, 121903 (2013).
[261] S. Li and A. Waag, J. Appl. Phys. **111**, 071101 (2012).
[262] F. Qian, Y. Li, S. Gradecak, D. Wang, C. J. Barrelet, and C. M. Lieber, Nano Lett. **4**, 1975 (2004).
[263] S. K. Lim, M. J. Tambe, M. M. Brewster, and S. Gradecak, Nano Lett. **8**, 1386 (2008).
[264] Z. X. Yan and A. G. Milnes, J. Electrochem. Soc. **129**, 1353 (1982).

[265] S. H. Oh, K. V. Benthem, S. I. Molina, A. Y. Borisevich, W. Luo, P. Werner, N. D. Zakharov, D. Kumar, S. T. Pantelides, and S. J. Pennycook, Nano Lett. **8**, 1016 (2008).

[266] J. Noborisaka, J. Motohisa, and T. Fukui, Appl. Phys. Lett. **86**, 213102 (2005).

[267] J. Park, P. A. Grudowski, C. J. Eiting, and R. D. Dupuis, Appl. Phys. Lett. **73**, 333 (1998).

[268] K. Tomioka, K. Ikejiri, T. Tanaka, J. Motohisa, S. Hara, K. Hiruma, and T. Fukui, J. Mater. Res. **26**, 2127 (2011).

[269] M. Kesaria, S. Shetty, and S. M. Shivaprasad, Cryst. Growth Des. **11**, 4900 (2011).

[270] P. Kumar, M. Tuteja, M. Kesaria, U. V. Waghmare, and S. M. Shivaprasad, Appl. Phys. Lett. **101**, 131605 (2012).

[271] B. Fultz and J. M. Howe, *Transmission Electron Microscopy and Diffractometry of Materials*, 3rd ed. (Springer Berlin Heidelberg, New York, 2008).

[272] V. Darakchieva, M.-Y. Xie, N. Franco, F. Giuliani, B. Nunes, E. Alves, C. L. Hsiao, L. C. Chen, T. Yamaguchi, Y. Takagi, K. Kawashima, and Y. Nanishi, J. Appl. Phys. **108**, 073529 (2010).

[273] M. Kesaria and S. M. Shivaprasad, Appl. Phys. Lett. **99**, 143105 (2011).

[274] R. S. Wagner and W. C. Ellis, Appl. Phys. Lett. **4**, 89 (1964).

[275] B. J. Ohlsson, M. T. Bjork, M. H. Magnusson, K. Deppert, L. Samuelson, and L. R. Wallenberg, Appl. Phys. Lett. **79**, 3335 (2001).

[276] A. Aliano, A. Catellani, and G. Cicero, Appl. Phys. Lett. **99**, 193106 (2011).

[277] V. Jindal and F. Shahedipour-Sandvik, J. Appl. Phys. **107**, 054907 (2010).

[278] K. A. Bertness, A. Roshko, L. M. Mansfield, T. E. Harvey, and N. A. Sanford, J. Cryst. Growth **310**, 3154 (2008).

[279] L. J. Van der Pauw, Philips Res. Repts. **13**, 1 (1958).

[280] A. Rose, Phys. Rev. **97**, 1538 (1955).

[281] A. A. Talin, F. Léonard, B. S. Swartzentruber, X. Wang, and S. D. Hersee, Phys. Rev. Lett. **101**, 076802 (2008).

[282] N. F. Mott and R. W. Gurney, *Electronic processes in ionice crystals* (Oxford University Press, New York, 1940).

[283] A. A. Talin, B. S. Swartzentruber, F. Leonard, X. Wang, and S. D. Hersee, J. Vac. Sci. Technol. B **27**, 2040 (2009).

[284] S. Zhao, O. Salehzadeh, S. Alagha, K. L. Kavanagh, S. P. Watkins, and Z. Mi, Appl. Phys. Lett. **102**, 073102 (2013).

[285] C. Rauch, I. Makkonen, and F. Tuomisto, Phys. Rev. B **84**, 125201 (2011).

[286] W. Walukiewicz, Appl. Phys. Lett. **54**, 2094 (1989).

[287] L. Hsu, R. E. Jones, S. X. Li, K. M. Yu, and W. Walukiewicz, J. Appl. Phys. **102**, 073705 (2007).

[288] W. Walukiewicz, Phys. Rev. B **41**, 10218 (1990).

List of Publications

1. Jithesh Kuyyalil, **Malleswararao Tangi** and S. M. Shivaprasad, *Dependence of crystal orientation and bandgap on substrate temperature of molecular-beam epitaxy grown InN on bare Al_2O_3 (0001)* **Journal of Applied Physics** 109, 093513, (2011).

2. **Malleswararao Tangi**, Jithesh Kuyyalil and S. M. Shivaprasad, *Role of native defects in nitrogen flux dependent carrier concentration of InN films grown by molecular beam epitaxy* **Journal of Applied Physics** 112, 073510, (2012).

3. Jithesh Kuyyalil, **Malleswararao Tangi** and S. M. Shivaprasad, *Effect of interfacial lattice mismatch on bulk carrier concentration and band gap of InN* **Journal of Applied Physics** 112, 083521, (2012).

4. Praveen Kumar, **Malleswararao Tangi**, Satish Shetty, Manoj Kesaria, and S. M. Shivaprasad, *Growth of aligned wurtzite GaN nanorods on Si(111): Role of Silicon nitride intermediate layer* **MRS Proc.**, 1411, mrsf11-1411-ee09-24, (2012).

5. **Malleswararao Tangi**, Jithesh Kuyyalil and S. M. Shivaprasad, *Optical bandgap and near surface band bending in degenerate InN films grown by Molecular Beam Epitaxy* **Journal of Applied Physics** 114, 153501, (2013).

6. Jithesh Kuyyalil, **Malleswararao Tangi** and S.M. Shivaprasad, *In induced reconstructions of Si(1 1 1) as superlattice matched epitaxial templates for InN*

growth **Materials Research Bulletin** 48, 256-259, (2013)

7. **Malleswararao Tangi**, Arpan De and S. M. Shivaprasad, *Lowering of growth temperature of epitaxial InN by superlattice matched intermediate layers* **Physica Status Solidi (A)** 210, 2409-2415, (2013).

8. Arpan De, Nagaraja K K, **Malleswararao Tangi**, and S. M. Shivaprasad, *Spontaneous growth of $In_xGa_{1-x}N$ nanostructures directly on c-plane Sapphire by Plasma Assisted Molecular Beam Epitaxy* **Materials Research Express** 1, 035019 (2014).

9. **Malleswararao Tangi**, Arpan De, Jay Ghatak, and S. M. Shivaprasad, *Electron mobility of self-assembled and dislocation free InN nano rods grown on GaN Nano Wall Network template* **Applied Physics Letters** under revision

10. **Malleswararao Tangi**, Arpan De and S. M. Shivaprasad, *Growth of high quality InN films and nano-rods grown on GaN nano wall network* **Accepted** in IEEE conference proceedings

11. **Malleswararao Tangi**, Arpan De and S. M. Shivaprasad, *Role of defects in limiting electron mobility of InN epilayers* **under preparation**

12. **Malleswararao Tangi**, Arpan De and S. M. Shivaprasad, *Effect of nitridation of the Si(111) substrates on the growth of InGaN nano rods* **under preparation**